Impulse Generation by Detonation Tubes

Thesis by

Marcia Ann Cooper

In Partial Fulfillment of the Requirements

for the Degree of

Doctor of Philosophy

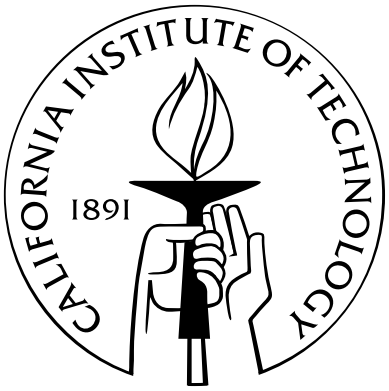

California Institute of Technology

Pasadena, California

2004

(Defended May 20, 2004)

© 2004
Marcia Ann Cooper
All Rights Reserved

Acknowledgements

My biggest and warmest thank you goes to my advisor Dr. Joseph Shepherd. With his mentoring, my time at Caltech has been more rewarding than I ever could have imagined. His incredible work ethic and enthusiam are two of his traits that I most admire. I am especially grateful for being given the opportunity to work on multiple projects, only a portion of which are described in this thesis. Another warm thank you goes to Professor Hans Hornung who generously gave me access to the dump tank of T5 and served on my doctoral committee. I also thank the remaining two members of my doctoral committee, Professors Melany Hunt and David Goodwin.

I thank the past and present members of the Explosion Dynamics Laboratory for helpful discussions and assistance including Eric Schultz, Joanna Austin, Eric Wintenberger, Tony Chao, Scott Jackson, and Daniel Lieberman. A special thank you goes to Joanna, a friend and confidant, who made working in a lab group full of boys bearable. And to Scott, thank you for being my best friend.

The staff of the Aero machine shop deserve a big thank you for their machining assistance on my many projects. I very much appreciate the help given to me by the GALCIT administrative assistants, in particular, Suzy Dake.

A final thank you goes to my family. I especially thank my parents and grandparents for sharing this experience with me by celebrating my milestones, supporting me during the intermediate times, and giving me the tenacity to make it through.

This research was sponsored by a Multidisciplinary University Research Initiative from the Office of Naval Research *"Multidisciplinary Study of Pulse Detonation Engine."*

Abstract

Impulse generation with gaseous detonation requires conversion of chemical energy into mechanical energy. This conversion process is well understood in rocket engines where the high pressure combustion products expand through a nozzle generating high velocity exhaust gases. The propulsion community is now focusing on advanced concepts that utilize non-traditional forms of combustion like detonation. Such a device is called a pulse detonation engine in which laboratory tests have proven that thrust can be achieved through continuous cyclic operation. Because of poor performance of straight detonation tubes compared to conventional propulsion systems and the success of using nozzles on rocket engines, the effect of nozzles on detonation tubes is being investigated. Although previous studies of detonation tube nozzles have suggested substantial benefits, up to now there has been no systematic investigations over a range of operating conditions and nozzle configurations. As a result, no models predicting the impulse when nozzles are used exist. This lack of data has severely limited the development and evaluation of models and simulations of nozzles on pulse detonation engines.

The first experimental investigation measuring impulse by gaseous detonation in plain tubes and tubes with nozzles operating in varying environment pressures is presented. Converging, diverging, and converging-diverging nozzles were tested to determine the effect of divergence angle, nozzle length, and volumetric fill fraction on impulse. The largest increases in specific impulse, 72% at an environment pressure of 100 kPa and 43% at an environment pressure of 1.4 kPa, were measured with the largest diverging nozzle tested that had a 12° half angle and was 0.6 m long. Two regimes of nozzle operation that depend on the environment pressure are responsible

for these increases and were first observed from these data. To augment this experimental investigation, all data in the literature regarding partially filled detonation tubes was compiled and analyzed with models investigating concepts of energy conservation and unsteady gas dynamics. A model to predict the specific impulse was developed for partially filled tubes. The role of finite chemical kinetics in detonation products was examined through numerical simulations of the flow in nonsteady expansion waves.

Contents

List of Figures

List of Tables

Nomenclature

Roman characters

Δx	maximum horizontal displacement
$\tilde{R}$	universal gas constant
A	area
C	combustible mixture mass
c	damping constant
$C^{\pm}$	characteristics, left- and right-facing families
c_0	environment sound speed
c_1	initial combustible mixture sound speed
c_2	CJ sound speed
c_3	sound speed in products behind Taylor wave
c_e	equilibrium sound speed
c_f	frozen sound speed
C_p	specific heat at constant pressure
c_p	specific heat at constant pressure per unit mass
D	diameter

Da	Damkohler number, t_{chem}/t_{flow}
E	Gurney energy
F	force
F_D	force provided by diaphragm
g	gravitational acceleration
h	enthalpy
h_t	total enthalpy
I	impulse
I_{sp}	mixture-based specific impulse
J^-	Riemann invariant on a left-facing characteristic
K	model proportionality constant
K_{LP}	variable model constant K for low environment pressures
L	tube length filled with the combustible mixture
L°	total tube length
L_p	pendulum arm length
M	tube mass
m	mass
M_1	Mach number at state 1 (reactants)
M_2	Mach number at state 2 (products)
M_p	pendulum mass
N	tamper mass

P	pressure
P_0	environment pressure
P_1	initial combustible mixture pressure
P_3	plateau pressure behind the Taylor expansion wave
P_{CJ}	equilibrium pressure at rear of CJ detonation
P_{CV}	constant volume combustion pressure
q	effective energy release per unit mass calculated from M_{CJ}
s	entropy per unit mass
T	temperature
t	time
t^*_{chem}	largest value of the characteristic times for chemical reaction
t_1	time taken by the detonation wave to reach the mixture interface
t_2	time taken by the first reflected characteristic to reach the thrust surface
t_3	time associated with pressure decay period
t_{chem}	characteristic timescale of chemical reaction
t_{flow}	characteristic timescale of fluid motion
t_{TW}	time required for a particle to travel through the Taylor wave
u	velocity
U_{CJ}	CJ detonation velocity
V	tube volume filled with the initial combustible mixture
V°	total tube volume

w velocity in wave fixed coordinates

x distance

Y mass fraction

$\mathbf{I}$ Identity matrix

$\mathbf{Y}$ matrix of mass fractions

$\mathcal{J}$ Jacobian matrix, $\sum \partial\Omega_i/\partial Y_k$

Greek characters

α non-dimensional parameter corresponding to time t_2

β non-dimensional parameter corresponding to pressure decay period

β_{LP} variable model constant β describing pressure decay in low environment pressures

η similarity variable in Taylor wave $\eta = x/c_3 t$

γ specific heat ratio

γ_0 ratio of specific heats in environment

γ_e ratio of specific heats at equilibrium composition

γ_f ratio of specific heats at frozen composition

γ_{CV} ratio of specific heats in constant volume combustion products

λ eigenvalues

ω_d damped frequency

ω_n natural frequency

Φ products state in steady flow analysis $T_i/\mathcal{W}$

Π	non-dimensional pressure
ρ	density
τ_d	damped period
v	specific volume
$\mathbf{\Omega}$	matrix of chemical reaction rates
$\mathcal{W}$	molecular weight

Acronyms

CJ	Chapman-Jouguet
DDT	deflagration-to-detonation transition
LTE	local thermodynamic equilibrium
PDE	pulse detonation engine
TW	Taylor wave

Subscripts

0	environment conditions
CJ	pertaining to detonation traveling at CJ velocity
CV	constant volume
i	corresponding to species i
i	nozzle inlet state
sp	normalization by the explosive mixture mass
1	initial combustible mixture state
2	CJ state

3	state behind Taylor wave

Superscripts

eq	equilibrium state

Accents

$\dot{}$	time derivative

Chapter 1

Introduction

1.1 Overview

This work is an experimental study aimed at understanding impulse generation in detonation tubes. The tubes are closed at one end, open at the other, and are filled with a gaseous reactive mixture that is combusted by means of an unsteady detonation wave. The impulse is determined by the chemical energy released by detonation and the transfer of this energy into accelerating the tube, detonation products, and gas in the surrounding environment. For the case of a fully filled detonation tube exhausting into atmospheric air, the impulse has been experimentally (Cooper and Shepherd, 2002, Zitoun and Desbordes, 1999, Kiyanda et al., 2002, Zhdan et al., 1994, Falempin et al., 2001) determined for a wide range of initial mixtures and can be analytically (Wintenberger et al., 2003, Wu et al., 2003) predicted by one-dimensional gas dynamics within 10% of these measured values. However, addition of an exit nozzle or variation in the environment conditions alters the distribution of energy between the tube, product gases, and environment gases such that the impulse is significantly affected. Because of the inherently unsteady and multi-dimensional flow which may also contain complicated shock wave interactions, standard one-dimensional gas dynamic analysis methods are of limited value. Currently, there are no experimental or analytical studies quantifying detonation tube impulse in environments of varied pressure and composition. Previous studies with exit nozzles have been single-point designs, not systematic investigations. The purpose of the present research is to conduct a

systematic experimental investigation of detonation tube impulse for a wide range of conditions varying the pressure of the environment surrounding the detonation tube and the exit nozzle shape (converging, diverging, and converging-diverging) in order to obtain performance bounds at an arbitrary operating condition. We also address the lack of unifying relationships in the literature by generating a single relationship from which the impulse of partially filled tubes can be predicted and a relationship to predict the impulse of tubes exhausting into low environment pressures.

1.2 Motivation: pulse detonation engines

In recent years, a novel propulsive device called a pulse detonation engine (PDE) has been the focus of many experimental (Cooper and Shepherd, 2002, Falempin et al., 2001, Zitoun and Desbordes, 1999, Kiyanda et al., 2002, McManus et al., Zhdan et al., 1994), numerical (Morris, 2004, Cambier and Tegner, 1998, Eidelman and Yang, 1998, Li and Kailasanath, 2003), and analytical (Wintenberger et al., 2003, Wu et al., 2003) modeling efforts by both academics and industry which are reviewed in Kailasanath and Patnaik (2000) and Kailasanath (2001). A PDE is a propulsive device that is based on intermittent detonation and borrows concepts from rocket engines and air-breathing propulsion. Figure 1.1 illustrates a conceptual PDE developed at Caltech that is based on the results of our research efforts.

In this conceptual stand-alone propulsion system, ram air enters the device through the inlet at the left end of the figure, flowing through a swirler and/or inlet valve. Fuel enters and mixes with the air stream via a fuel injector creating a combustible mixture that travels into the main combustion chamber. Mixture ignition is achieved by means of an annular initiator (Jackson et al., 2003) which uses a unique technique of an imploding detonation to generate a region of high temperature and pressure that is capable of initiating a detonation in the flowing combustible mixture within the main chamber. The detonation propagates through the device, processing the combustible mixture into products, and emerges from the device through the exit nozzle at the right end of the figure. The momentum of the exhausting detonation

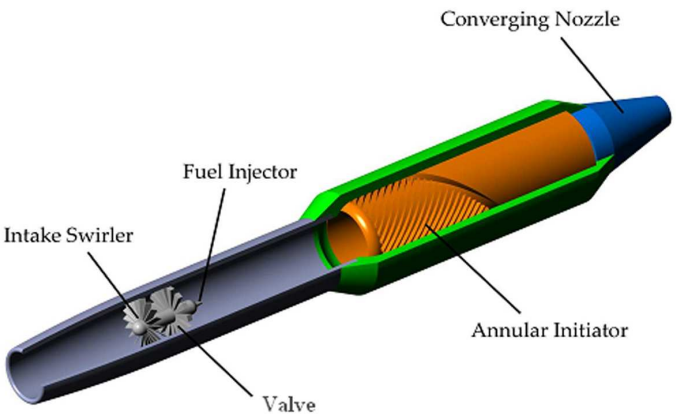

Figure 1.1: Illustration of a conceptual PDE device.

products and the pressure differential across the internal components result in thrust.

The time duration of this thrust force is on the order of $0.01L$ s, where L is the tube length in meters, and repetitive operation is required in order to obtain quasi-steady thrust levels. The basic operating cycle must consist of at least four main steps which are illustrated in Fig. 1.2 for the simplest PDE device formed from a cylinder that is closed at one end forming the "thrust surface" and open at the other. A more complex operating cycle containing a step for filling with a purge gas has been analyzed by Wintenberger (2004).

The first step of the operating cycle consists of initiating a detonation at or near the thrust surface of the tube. A detonation is a supersonic combustion wave that consists of a leading shock wave followed by a region of chemical reaction (Fickett and Davis, 1979). The shock wave processes the reactants to temperatures and pressures sufficiently high to initiate chemical reactions after an induction period. The energy release and volumetric expansion that occurs as a result of these chemical reactions support the leading shock wave. This coupling between the shock wave and reaction zone occurs on length scales that are orders of magnitude smaller than our experimental facilities eliminating the need to resolve the internal wave structure for our study. Associated with such detonations are propagation velocities on the order of

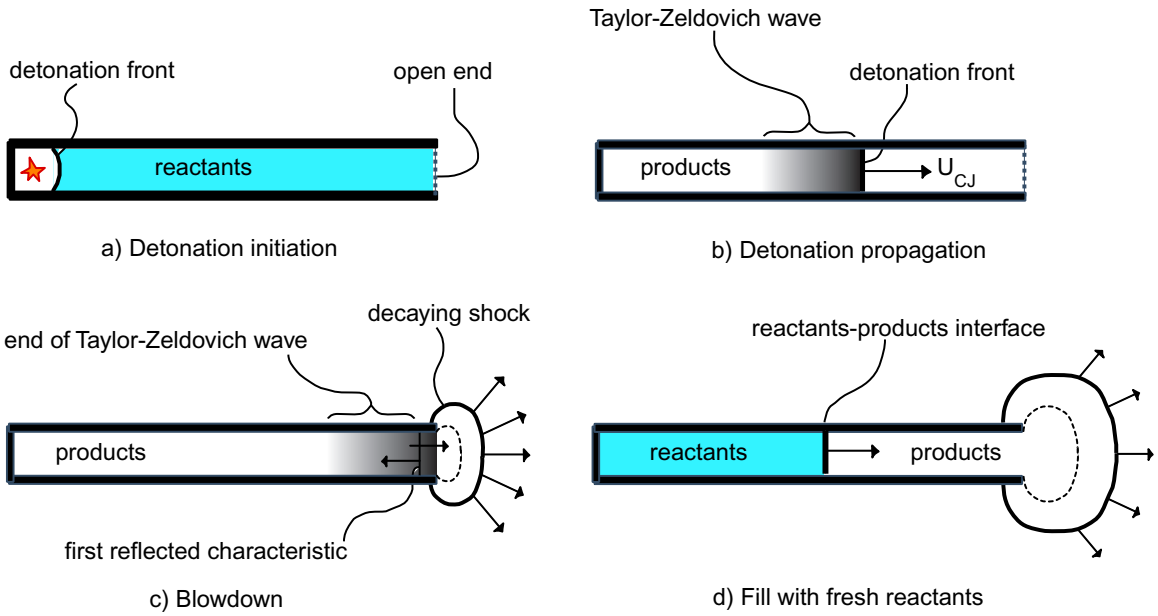

Figure 1.2: Illustration of a PDE operating cycle.

2 km/s and peak overpressures on the order of 10-20 bar.

After the detonation is initiated, it propagates down the tube towards the open end during the second step. An unsteady expansion called the Taylor-Zeldovich wave (Fickett and Davis, 1979) sets up behind the detonation wave, expanding the products from high pressure and velocity just behind the detonation wave to lower pressure and zero velocity matching the boundary condition at the thrust surface. The blow down process of step three starts when the detonation wave reaches the open end of the tube transmitting a decaying shock wave into the surrounding environment. A reflected wave, propagating back through the product gases to the thrust surface, is generated due to interaction with the simultaneous area change and mixture interface at the open end. The fourth step involves filling the tube with a fresh combustible mixture after completion of the blow down process. Repeating this cycle on the order of 100 Hz has been experimentally demonstrated and can be used to generate, on the average, net thrust (Schauer et al., 2001, McManus et al., Hinkey et al., 1997, Brophy and Netzer, 1999, Farinaccio et al., 2002).

Estimates (Wintenberger, 2004, Wu et al., 2003) of performance for a multi-cycle,

air-breathing PDE are shown in Fig. 1.3 for the simplest device of a fully filled, straight tube open directly to the environment. From these results, it is apparent that these devices are inefficient since, without further expansion of the exit flow, only a relatively modest amount of the chemical energy is converted into thrust. In order to obtain performance comparable to existing propulsion systems, it has been proposed that some type of exit nozzle be used on PDEs. Although there have been extensive studies on the role of nozzles on steady flow propulsion systems, relatively little is known about the propagation of detonations and subsequent unsteady flow development in nozzles. This forms the motivation behind the present study.

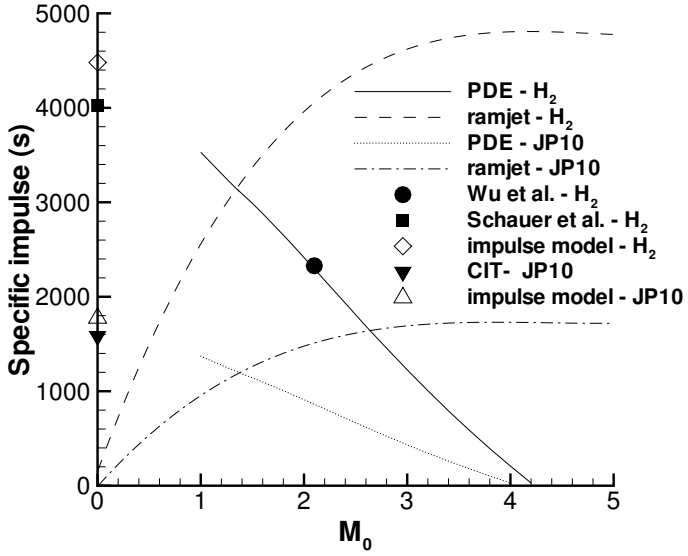

Figure 1.3: Specific impulse of a single-tube, air-breathing PDE compared to the ramjet operating with stoichiometric hydrogen-air and JP10-air. Predictions from multi-cycle numerical simulations by Wu et al. (2003) for $M_0 = 2.1$ at 9,300 m altitude are shown as well as control volume model of multi-cycle operation by Wintenberger (2004). Experimental data from Schauer et al. (2001) and Wintenberger et al. (2002) and impulse model predictions by Wintenberger et al. (2003) are also given as a reference for the static case. See Wintenberger (2004) for model specifics.

1.3 Detonation basics

A detonation wave is commonly described by the ZND model based on the independent contributions of Zel'dovich (1940), von Neumann (1942), and Doering (1943). This model neglects transport processes, assumes one-dimensional flow, and resolves the thermochemical state throughout the thickness of the wave. The head of the detonation wave is a shock wave that propagates through an unreacted mixture causing a discontinuous increase in fluid temperature and pressure sufficient to initiate chemical reactions. The chemical reactions progress through the reaction zone to a near-equilibrium final state at the end of the detonation front. Together, the shock wave and reaction zone propagate at a constant speed known as the detonation velocity, commonly written as U_{CJ}.

The reaction zone specifics depend on the chemical kinetics of the reactions along with the equation of state of the reaction products which are utilized to fully determine the final state. Following the flow from the front to a position well behind the detonation, a specified rear boundary condition must be satisfied. It is this boundary condition that determines the thermochemical flow field behind the detonation wave. In this analysis, we consider only the case of a tube that has one end open and the other end closed. This implies a rear boundary condition of zero flow velocity at the closed tube end which must be satisfied by the presence of an unsteady expansion wave called the Taylor-Zeldovich expansion wave (Fickett and Davis, 1979). The head of the Taylor wave lies at the final state of the reaction zone and travels at the detonation velocity. The tail of the Taylor wave lies at some distance down the tube behind the detonation wave and is followed by a region of fluid at a constant state with zero flow velocity (measured in the lab-fixed coordinates).

Predictions (Wintenberger et al., 2003) of the impulse are obtained by determining the flow field within the tube between the initial state upstream of the detonation wave and the rear boundary condition. There is no need to resolve the state changes within the detonation wave itself, so a simplified model of a detonation called the Chapman-Jouguet (CJ) model is used. This simplest theory assumes the flow is one-

dimensional, the detonation wave is a discontinuity where the shock and chemical reactions occur instantaneously, and the final state just behind the detonation (called the CJ state) is in thermochemical equilibrium. The CJ model and the more detailed ZND model yield identical results for the final state and the detonation velocity since they both depend only on the equation of state of the reaction products. Thus, it is important to emphasize that high levels of agreement between model and experiment require the use of an accurate and realistic product equation of state regardless of which detonation model is used.

Use of the CJ model enables the entire solution for a steadily-propagating detonation in a tube that is closed only at one end to be constructed piecewise with three regions, shown on Fig. 1.4: the stationary reactants ahead of the detonation mixture at pressure P_1, the expansion wave behind the detonation that begins to expand the flow from the CJ pressure, and the stationary products next to the closed end of the tube at pressure P_3. A detailed discussion of how the different states of Fig. 1.4 are defined is given in Chapter 6.

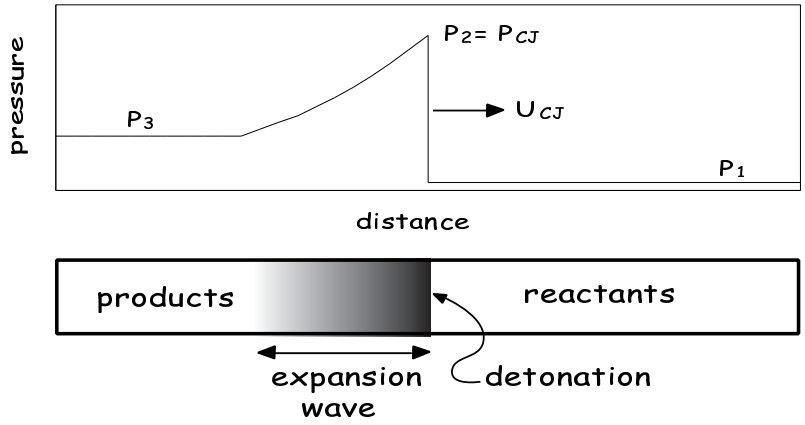

Figure 1.4: Detonation propagation in tube with a closed end.

1.4 Impulse generation

Impulse is defined as the time integral of a force.

$$I(t) = \int_0^t F dt \tag{1.1}$$

In common propulsive devices, such as rocket engines, guns, grenades, and other munitions, the force is generated by converting the stored chemical energy within an explosive into mechanical energy for the sole purpose of imparting motion to either the device or a projectile (Corner, 1950, Robinson, 1943). The processes involved in the conversion of the chemical energy into mechanical energy are of interest to this work.

The impulse is often normalized by the weight of the explosive to yield the mixture-based specific impulse which is a measure of impulse per unit mass of the propellant. The factor g, acceleration of gravity on Earth's surface, is traditionally included in order to give specific impulse in units of time.

$$I_{sp} = \frac{\int_0^t F dt}{g \int_0^t \dot{m} dt} \tag{1.2}$$

Note that for steady flow devices, $I_{sp} = F/g\dot{m}$.

1.4.1 Steady combustion

This section considers impulse generation by steady combustion followed by steady, isentropic product gas expansion. This is the process that occurs in an ideal rocket engine consisting of a combustion chamber and an exit nozzle (Fig. 1.5). Inside the combustion chamber, a propellant is burned generating a uniform mixture of gaseous products with molecular weight $\mathcal{W}$ and specific heat ratio γ. The products are initially at an elevated temperature T_i and pressure P_i at the nozzle inlet and are expanded through the exit nozzle to a lower pressure P_x and a high velocity u_x.

A control volume drawn around the device is used to calculate the force F applied

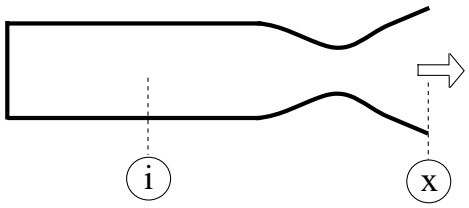

Figure 1.5: Schematic of idealized, steady rocket engine flying in a uniform environment.

to the engine by the momentum $\dot{m}u_x$ of the exhausting products (Sutton, 1992, Hill and Peterson, 1992).

$$F = \dot{m}u_x + (P_x - P_0)A \tag{1.3}$$

The engine is assumed to operate in a uniform environment with pressure P_0, and the reactant momentum in the combustion chamber is assumed to be negligible compared to the momentum of the exhaust products. Steady operation implies that the mass flow rate $\dot{m}$ is constant,

$$\dot{m} = \rho_x u_x A_x \tag{1.4}$$

and steady, adiabatic flow implies that the total enthalpy h_t at any position within the nozzle remains constant.

$$h_t = h + u^2/2 = \text{constant} \tag{1.5}$$

With these relations and a final assumption that the product gases are perfect, the specific impulse of the engine can be calculated as a function of the state of the products at the nozzle inlet.

$$u_x = \sqrt{2(h_i - h_x + u_i^2)} \tag{1.6}$$

Rewriting enthalpy as

$$\Delta h = c_p \Delta T = \gamma R \Delta T/(\gamma - 1) \tag{1.7}$$

where $R = \tilde{R}/\mathcal{W}$ and substituting into Eq. 1.6 for the exit velocity yields

$$u_x = \sqrt{\frac{2\gamma}{\gamma - 1} RT_i \left[1 - \left(\frac{P_x}{P_i} \right)^{(\gamma-1)/\gamma} \right] + u_i^2} \; . \tag{1.8}$$

This exit velocity applies to the particular case where the area ratio across the nozzle equals the *optimum expansion ratio* resulting in full expansion of the product gases to ambient pressure $P_0 = P_x$. From Eq. 1.3, the thrust force then depends entirely on the momentum of the exhaust gases enabling calculation of the specific impulse for an arbitrary nozzle inlet state $T_i/\mathcal{W} = c^2/\gamma\tilde{R} = \Phi$ (Fig. 1.6).

$$I_{sp} = \frac{u_x}{g} \tag{1.9}$$

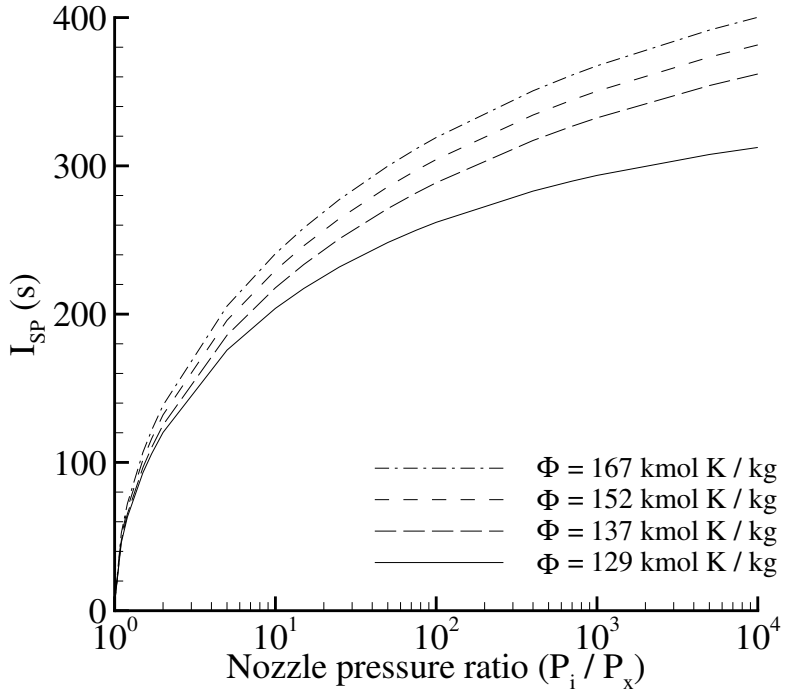

Figure 1.6: Ideal specific impulse as a function of the conditions in the combustion chamber.

While steady, isentropic expansion of the product gases to perfectly matched con-

ditions at the exit is possible, it is generally not the case when considering practical engine operation over a range of altitudes. Conditions may arise where the exhaust gases become either over- or under-expanded within the nozzle causing the impulse to vary from these theoretical predictions (Romine, 1998, Welle et al., 2003, Arens, 1963, Arens and Spiegler, 1963, Lawrence and Weynand, 1968, Frey and Hagemann, 2000, Chen et al., 1994). This issue, along with the presence of unsteady nozzle flow, must also be addressed when analyzing nozzles on detonation tubes. We compare the specific impulse from this steady, isentropic analysis to our values measured from detonation tubes with nozzles operating at varying pressure ratios.

1.4.2 Explosive systems

Military applications and weapons research are the primary motivations to study explosive systems (Davis, 1998). An exhaustive number of studies involving projectile and early propulsion systems exist that are of historical significance. However, just a few of the more recent studies relevant to PDEs are highlighted.

A simplified PDE is a cylindrical tube containing an explosive mixture so an obvious comparison should be made to gunnery. The field of interior ballistics is concerned with the flow field inside the gun barrel that is responsible for accelerating the bullet (Robinson, 1943, Cooper, 1996). Explosion of the charge, typically in a powder form, produces a high pressure gas which applies a force to the backside of the bullet causing it to accelerate. As the bullet travels down the chamber, the volume contained by the product gases increases, decreasing the pressure (Fig. 1.7). At the same time, the gases are working to accelerate the bullet, further expanding the gases. To completely analyze this situation, the ignition process, rate of explosion of the propellant, the temperature, species and pressure of the products over time, and the bullet position must be determined simultaneously because of their interrelation.

A simpler and more versatile model of estimating projectile motion by explosives was developed by Gurney (1943). His model, derived and discussed in more detail in Chapter 3, is based on the assumption that before detonation, the explosive charge

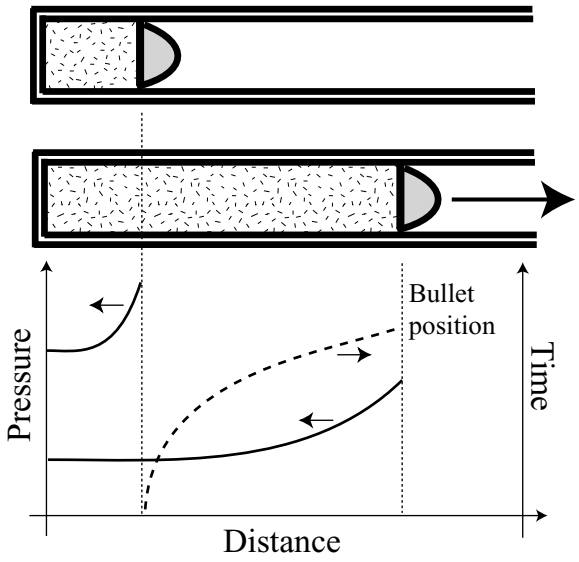

Figure 1.7: Interior ballistics of a gun.

contains chemical energy that is converted into kinetic energies of the product gases and metal fragments (Fig. 1.8). The Gurney model assumes that the wave reflections

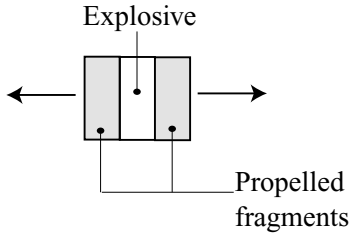

Figure 1.8: Situation considered by Gurney model

within the expanding detonation products occur very fast compared to the fragment velocities resulting in a linear velocity profile and spatially uniform density in the products. Models like the Gurney model that consider energy conservation have been applied to predicting fragments from rock blasting, bombs and shells, and explosive welding (Davis, 1998).

A detonation tube is a combination of these two explosive systems. Physically, the tube represents the gun barrel but the goal is not to propel a lighter bullet but to instead propel the barrel! In other words, the recoil is to be maximized the recoil (Fig. 1.9). Previous research in cannons and guns has sought to eliminate the barrel

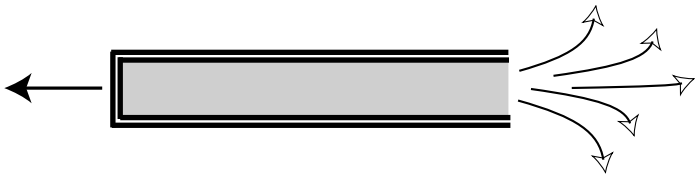

Figure 1.9: Situation of a detonation tube.

recoil in order to maximize the projectile velocity (Corner, 1950, Ahmadian et al., 2003).

Early work carried out by Robbins (1805) initially measured muzzle velocities from cannons before he became interested in trying to measure the velocity of the gunpowder exhaust gases. These are the first impulse experiments in a tube closed at one end and open at the other, hung in a ballistic pendulum arrangement. Later studies by Hoffman (1940) and Nicholls et al. (1958) measured the impulse by gaseous detonation in tubes with explosive mixtures like those of contemporary facilities. Recently, PDE researchers sought to promote detonation initiation in fuel-air mixtures, construct operational multi-cycle facilities, and quantify the maximum impulse for the range of intended operating conditions.

A number of approaches have been investigated regarding detonation initiation and they can be categorized as studies of mixture sensitization, shock/detonation wave focusing, and deflagration-to-detonation transition (DDT). The detonation properties of fuel additives such as methane, acetylene, ethers, and nitrates for sensitizing the main fuel component were carried out by Austin and Shepherd (2003), Hitch (2002) and Akbar et al. (2000). Fuel sensitization by catalytic cracking, thermal cracking, and partial oxidation has been conducted in bench-top reactors (Cooper and Shepherd, 2003, Green et al., 2001, Davidson et al., 2001). Shock wave and detonation wave focusing have been investigated by Jackson et al. (2003) for PDE applications. Similar to these studies are detonation initiation by imploding jets. These methods seek to generate regions of high temperature and pressure capable of initiating detonations under the correct conditions. The effect of DDT for different internal obstacle configurations was carried out by Cooper and Shepherd (2002) in

1 m tubes. Fundamental studies of the DDT mechanism appear in Knystautas et al. (1998) and Lindstedt and Michels (1989).

Several research groups have made significant advancements in the development of multi-cycle facilities. This work has helped to advance the fields of fluid-structure and fracture mechanics (Chao, 2004) in order to understand the structural response due to the repetitive traveling loads experienced by the tubes during extended operation. Advanced concepts are now being investigated such as hybrid engines in which the PDE replaces the inner stage of a turbojet. In this case, the ability of the detonation tube exhaust to drive the turbomachinery is investigated (Rasheed et al., 2004).

All of these studies have dealt with different aspects of PDE operation while addressing the main issue of impulse measurement and optimization. For example, DDT studies were used to determine the effect of late or no transition to detonation on the impulse (Cooper and Shepherd, 2002); the effect of a poor inlet valve timing (modeled as a porous thrust surface) on impulse was investigated (Cooper and Shepherd, 2004); the effect of the initial pressure, dilution amount, and fuel type on impulse have been measured. Many unresolved issues affecting the impulse still exist. We have chosen to address the issue of exit nozzles and environment pressure in this study.

Currently, several studies (Cooper and Shepherd, 2002, Eidelman and Yang, 1998, Falempin et al., 2001) involving nozzles on detonation tubes have been completed but they were all carried out in 1 atm pressure environments. This is the first study to address the effect of changing the environment pressure on impulse from plain tubes and tubes with exit nozzles. In addition to completing a systematic experimental study, the existing ideas of energy conservation from Gurney (1943) and one-dimensional gas dynamics are used to analyze the data, providing insight into the factors that affect and ways to maximize the impulse in tubes with nozzles operating in various environments.

1.5 Outline

An overview of this work, the motivating concept of a PDE, and background concepts regarding detonations and impulse generation are presented in Chapter 1.

The experiments presented here consist of single-cycle impulse measurements obtained with a simplified detonation tube hung in a ballistic pendulum arrangement. The tube was either hung in a blast-proof room where it exhausted into atmospheric conditions or hung in a large pressure vessel that could be evacuated so the tube exhausted into sub-atmospheric conditions. A series of different nozzle types including a cylindrical extension, converging nozzles, diverging nozzles, and converging-diverging nozzles were tested. Both facilities and supporting equipment are discussed in Chapter 2.

Impulse measurements from partially filled detonation tubes exhausting into standard conditions are the subject of Chapter 3. A compilation of existing data from other researchers is presented and a unifying relationship between the impulse as a function of the explosive mixture mass fraction in the tube is proposed. An analytical model to predict the maximum specific impulse of an infinitely long tube for a given explosive-inert gas combination is presented.

Experimental data for fully filled tubes exhausting into sub-atmospheric pressures appear in Chapter 4 and for tubes with an exit nozzle exhausting into sub-atmospheric pressures appear in Chapter 5. These chapters present the first experimental measurements of impulse under varying environment conditions in plain tubes and in tubes with exit nozzles. The systematically obtained data generate a substantial database from which unifying relationships are derived.

Chapter 7 discusses how the reacting flow behind a detonation wave should be modeled when it is expanded by the Taylor wave. The thermodynamic states of the gas through the Taylor wave are analyzed considering finite rate chemical kinetics.

Chapter 2

Experimental setup

This chapter describes experiments carried out to measure the single-cycle impulse of a tube containing a gaseous mixture. The experimental method consisted of hanging the detonation tube in a ballistic pendulum arrangement. This apparatus was originally invented by Robbins (1805) who carried out many experiments studying early explosives, characterizing the forces imparted to projectiles, and measuring muzzle velocities. The device he invented consisted of a vertical bar to which he had bolted a block of wood onto its bottom end. The bar, pinned at its top end to a support structure, was able to swing freely when a force was applied to the block of wood. Robbins deduced projectile velocities by launching projectiles of known mass towards the pendulum, embedding them into the block of wood and measuring the resulting deflection. His device enabled him to make many contributions to the field of ballistics because his measuring technique generated data with uncertainties that were orders of magnitude less than other methods used at the time. He continued using the concept of a ballistic pendulum for other studies, eventually fixing the canon directly on the end on the pendulum in the same fashion as done in the experiments reported here. Others have since borrowed the idea of hanging munitions in a ballistic pendulum arrangement in order to "tune" recoilless guns.

Several research groups within the PDE community began using the ballistic pendulum in their laboratories in order to agree upon the maximum single-cycle impulse obtainable from a simplified detonation tube and combustible mixture at a given set of initial conditions. The tube, which is the oscillating mass, is suspended from above

by steel wires and is free to oscillate in a periodic fashion. A measure of the impulse imparted to the tube is obtained by igniting the initial mixture, allowing the combustion products to expand out the open end, and recording the tube's maximum deflection. Because of the relative simplicity in the experimental setup as compared with other measuring techniques, such as with damped thrust stands or measuring the time-varying exhaust flow at the exit plane, the impulse values generated have made significant contributions in recent years to the PDE development effort. Damped thrust stands are being used primarily for multi-cycle test facilities where a ballistic pendulum is not practical due to the gas, electrical, and cooling attachments that are required. For single-cycle impulse measurements however, the damped thrust stand is difficult to design in order to generate data within the same uncertainty values of the ballistic pendulum. Measuring the flow at the exit plane and using the control volume methods of traditional rocket engine analysis is difficult due to the time-varying flow of the detonation and unsteady Taylor expansion wave.

A control volume analysis with a different control volume, drawn around just the walls (Figure 2.1), has been used with some success. This eliminates the need of

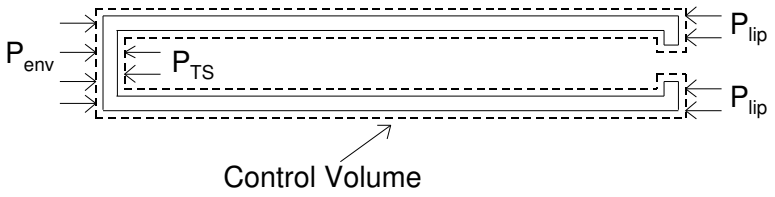

Figure 2.1: Illustration of detonation tube with control volume.

characterizing the momentum and velocity of the exhausting detonation products which are difficult to measure. The force balance is written in the direction of the tube axis.

$$F = (P_{env} - P_{TS})A_{TS} + \sum_{obstacles} \int P\mathbf{n} \cdot \mathbf{x}\, dA + \int \tau\, dS + (P_{env} - P_{lip})A_{lip} \qquad (2.1)$$

The first term on the right side of the equation is the force on the thrust surface, the second term is the drag (due to pressure differentials) over internal obstacles (if

installed) or rough tube walls, the third term is the viscous drag, and the last term represents the force over the tube wall thickness. The effect of heat transfer from the combustion products to the tube walls could also reduce the impulse due to a reduction of pressure internal to the detonation tube (Radulescu et al., 2004). The impulse is obtained by integrating this force over a cycle (Eq. 1.1). Unfortunately, calculating the forces due the shear wall stresses, pressure losses due to internal obstacles or rough tube walls, forces due to shock diffraction on the wall thickness, just to name a few, is very difficult.

To calculate the impulse from the measured deflection, consider a pendulum initially at rest in its natural position. Applying an impulsive force to the pendulum mass causes it to move with an initial velocity that depends on the magnitude of the applied force. The pendulum deflects and at the height of its swing reaches a position of maximum deflection where it momentarily comes to rest before changing direction to pass back through its initial position. In the detonation tube, the force applied to the pendulum mass is generated by the high-pressure, detonation products exhausting from the tube. In these experiments, each support wire was about 1.0 m in length so that the natural period of oscillation was about 2.0 s. During free oscillations, the maximum horizontal deflection occurs at a time equal to one-quarter of the period or 500 ms. The time over which the force is applied can be estimated (Wintenberger et al., 2001) as $10t_1$, where $t_1 = L/U_{CJ}$ is the time required for the detonation to propagate the length of the tube. For the tube 1 m in length, the time over which the force is applied is approximately 4.2 ms, which is significantly less than one-quarter of the oscillation period. Therefore, the classical analysis of an impulsively-created motion can be applied and the conservation of energy can be used to relate the maximum horizontal deflection to the initial velocity of the pendulum.

From elementary mechanics, the impulse is given by

$$I = M_p \sqrt{2gL_p \left(1 - \sqrt{1 - \left(\frac{\Delta x}{L_p}\right)^2}\right)} \tag{2.2}$$

This expression is exact given the assumptions discussed above and there are no limits on the values of Δx. Actual values of Δx observed in our experiments were between 39 and 292 mm. The impulse I measured in this fashion is referred to as the *ballistic* impulse, and is specific to a given tube size. Two measures of the impulse that are independent of tube size are the impulse per unit volume

$$I_V = I/V \tag{2.3}$$

and the specific impulse based on the total explosive mixture mass (fuel and oxidizer)

$$I_{sp} = \frac{I}{g\rho_1 V} \tag{2.4}$$

If all of the terms making up F of Eq. 2.1 can be computed or measured, the ballistic impulse and the impulse computed from this control volume integration should be identical. Previous studies by Zitoun and Desbordes (1999) have used Eq. 2.1 to analyze data from unobstructed tubes neglecting all but the first contribution to the force. This is a reasonable approximation when fast transition to detonation occurs; however, in the case of obstacles or very rough tube walls, the net contribution of the two drag terms may be substantial and using the first term alone can result (Cooper et al., 2000) in overestimating the force and impulse by up to 50%. Since it is difficult to estimate or accurately measure all of the terms in Eq. 2.1, direct measurement of the impulse is the only practical method for tubes with obstructions or other unusual features such as exit nozzles.

Impulse measurements were carried out with the tube hung in two different facilities which enabled variation of the external environment conditions. The first facility consisted of the detonation tube hung in a blast-proof room. The second facility consisted of the detonation tube hung in a large tank. The discussion begins with a description of the tube followed by a detailed discussion of the tube arrangement and the supporting equipment comprising each facility. The tested exit nozzles are also described along with a discussion estimating the experimental uncertainties.

2.1 Detonation tube

The detonation tube is a cylinder made of 6061-T6 aluminum that is 1.014 m in length, has an inner diameter of 76.2 mm, and a wall thickness of 12.7 mm. The dimension of the inner diameter was chosen based on the need to run experiments with JP-10 and propane (Cooper et al., 2002) mixtures which have cell sizes on the order of 60 mm at atmospheric initial pressures. The length of the tube was chosen based on the relationship of Dorofeev et al. (2000) that correlates the mixture's cell size to the minimum distance required for deflagration to detonation transition. While internal obstacles can be installed inside the tube to promote deflagration to detonation transition (Cooper et al., 2002), the experiments discussed here were all carried out in a smooth tube.

One end of the tube (Fig. 2.2) is sealed with a plate called the "thrust surface" and contains the spark plug, a pressure transducer, and a gas-inlet fitting. The other

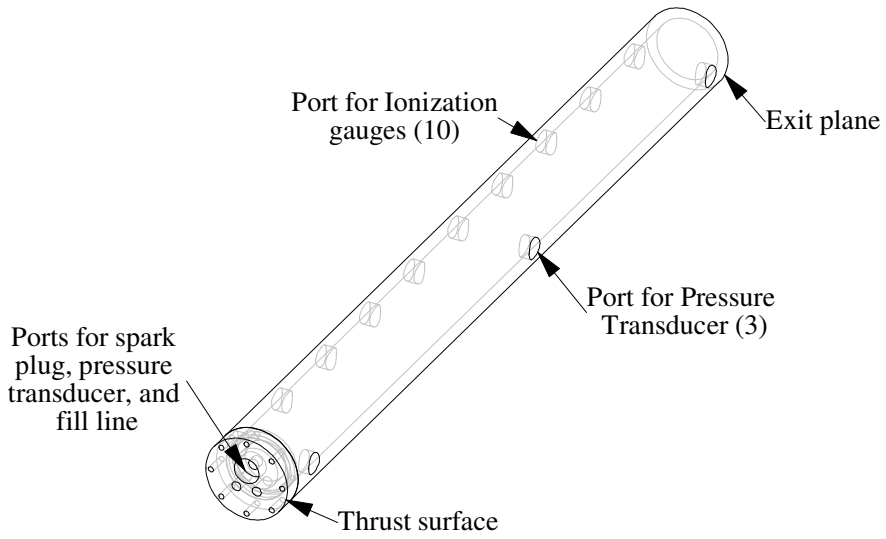

Figure 2.2: Illustration of the experimental detonation tube.

end of the tube is open, but is initially sealed with a Mylar diaphragm to contain the combustible mixture prior to ignition. In addition to the pressure transducer mounted in the thrust surface, two more pressure transducers located 0.58 m and

0.99 m from the thrust surface and ten ionization gauges (spaced 10.4 cm apart) were installed. These diagnostics measured wave arrival times and pressure histories at specific locations within the tube. The pressure transducers were purchased from PCB (model 113A26) and the ionization gauges were constructed from Swagelok fittings, teflon inserts, and long sewing needles. See Cooper et al. (2000) for details of the ionization gauge construction.

2.2 Ignition system

Mixture ignition occurs by discharging a 5μF capacitor charged to 110 V through a standard aircraft spark plug. This system has a discharge energy of 30 mJ. The critical energy for direct ignition of hydrocarbon mixtures is on the order of 10-100 kJ (Shepherd and Kaneshige, 1997, rev. 2001). Thus, the low ignition energy provided by the spark plug results in igniting an initial deflagration that must transition to a detonation after propagating some distance down the tube. Previous research of Kiyanda et al. (2002) has shown that the impulse measured between mixtures in which a detonation was achieved via the mechanism of deflagration to detonation transition or via direct initiation are the same as long as all of the combustible mixture burns within the tube. In cases with late or no transition to detonation, the propagating deflagration compresses the unburned gas ahead of the flame. This unburned gas compression is sufficient to rupture the thin diaphragm causing a considerable part of the mixture to be ejected outside the tube. Observations made by Jones and Thomas (1991) clearly demonstrate the gas motion and compression waves ahead of an accelerating deflagration. This effect was observed in these experiments and is discussed later in Chapter 4.

2.3 Facility I: Blast proof room

The first impulse facility consisted of hanging the detonation tube from the ceiling of a blast-proof room which has an inner volume of approximately 50 m^3. Four steel

wires located the tube 1.5 m below the ceiling. The detonation products were free to expand from the tube's open end into the room which contained atmospheric air.

In this facility, two methods were used to fill the detonation tube with the combustible mixture. The first method used two gas lines attached to the tube. The method of partial pressures was then used to fill the fuel, oxidizer, and diluent directly into the tube from the gas bottles. A circulation pump located on the gas line outside the tube was operated for at least 5 minutes to ensure homogeneity. After mixing, the fill lines were removed and the tube was ready for mixture ignition.

The second fill method used a single gas line attached to the tube and an external vessel containing the mixed fuel, oxygen, and diluent. The pressure vessel was filled directly from the gas bottles by the method of partial pressures and subsequently mixed with a brushless fan located inside the vessel to ensure homogeneity. The resulting premix was then plumbed to the tube directly, eliminating the need for an external circulation pump. The pressure vessel was constructed from a cylinder of A106B seamless pipe with a XXH wall thickness (2.2 cm). It had an outer diameter of 16.8 cm (6.625 in) and a length of 76.2 cm (30 in). Two 680 kg (1500 lb) weld-on flanges, onto which a 680 kg (1500 lb) blind flange with a metal o-ring was bolted, were attached to each end. One of the blind flanges had through-holes drilled for the attachment of a gas line, an electrical feed-through to power the brushless fan, and a connection to a static pressure gauge (Ashcroft Precision Digital Test Gauge Type 2089, Model 30-2089-SD-02L-Abs 3.5 Bar). The vessel was certified to 6.9 MPa (1000 psi). In general, the vessel was filled with the combustible mixture to an initial pressure of 3 bar. Because its internal volume is 9.25 L, the detonation tube could be filled approximately four times to an initial pressure of one bar before the premix vessel had to be evacuated and refilled with a fresh batch of the combustible mixture. After the tube was filled, the gas line was removed and the tube was ready for mixture ignition.

Although the gas fill line(s) were removed from the tube prior to ignition, the spark plug cable, ionization wires, and pressure gauge cables were still attached. The added resistance to the tube's periodic motion provided a damping force that reduced

the maximum measured deflection. An experimental analysis was carried out (§2.6.1) to quantify this error.

2.4 Facility II: Large tank

The second series of single-cycle impulse measurements were carried out in a large tank. The tank, actually the test section and dump tank of Caltech's T5 hypersonic wind tunnel facility, contained the hanging detonation tube as illustrated in Fig. 2.3.

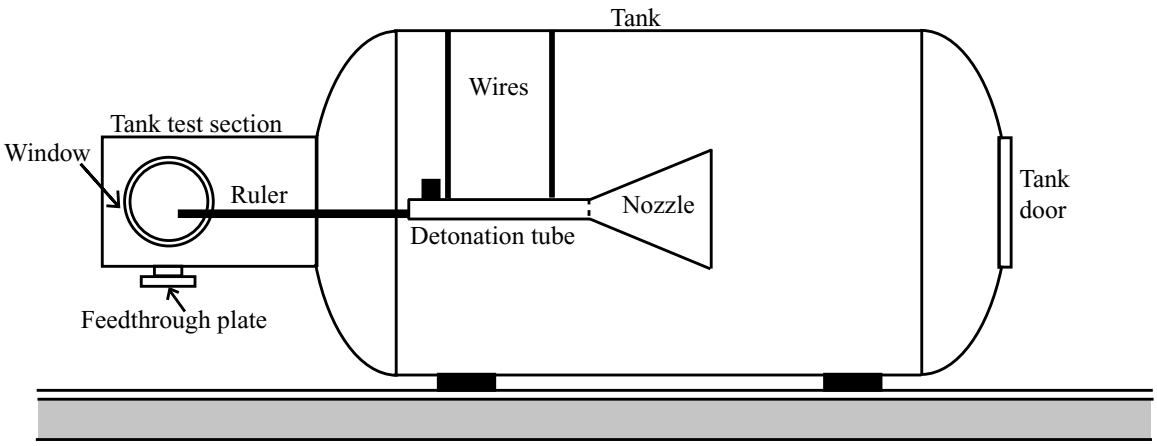

Figure 2.3: Schematic of Facility II.

The detonation tube could be sealed within the tank. The volume internal to the tank but external to the detonation tube is referred to as the "environment" and is air at pressure P_0 while the initial pressure of the combustible mixture is at pressure P_1. The environment pressure could be varied between 100 and 1.4 kPa, thus extending the capabilities of the ballistic pendulum method to obtain accurate single-cycle impulse measurements at a variety of operating conditions. The diaphragm separated the environment gases from the combustible mixture and is denoted in Fig. 2.3 by a dashed line separating the detonation tube from the nozzle (if attached).

The tank has an internal volume of approximately 12,500 L and is roughly the shape of a horizontal cylinder with an inner diameter of 2 m and a length of 4 m.

The attached test section (labeled in Fig. 2.3) is a cylinder approximately 0.7 m in diameter and 1.3 m in length. It contained two windows on each side through which the tube's motion was observed. A ruler extending off the front of the detonation tube and into view of the test section windows was filmed by a digital camera situated outside the tank (Fig. 2.4). From this recording of the tube's periodic motion, the maximum deflection was converted into impulse. A door on the end of the tank downstream of the detonation tube exhaust was used for access inside the tank to install a new diaphragm between each experiment.

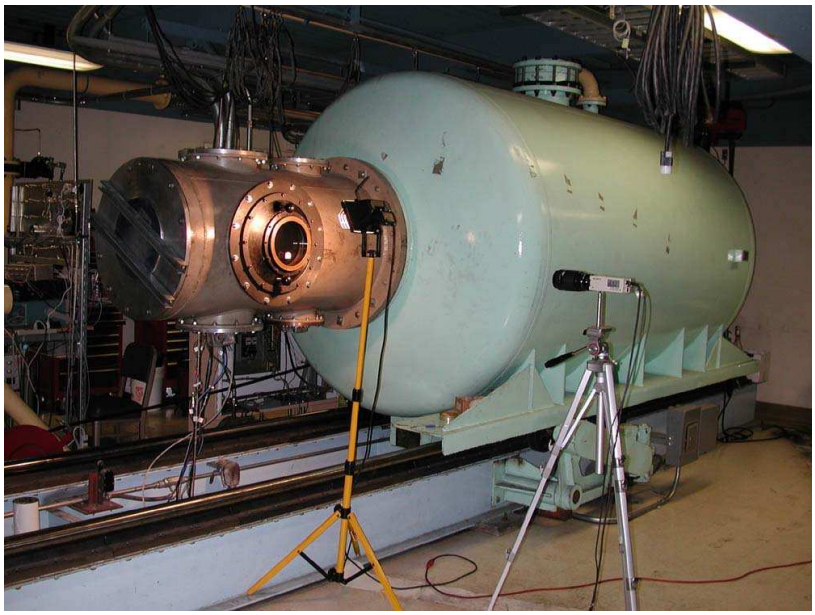

Figure 2.4: Photograph of the outside of the tank and attached test section.

2.4.1 Support structure

The inner surface of the large tank was smooth and so a support structure was built from which the detonation tube could be hung. It was fabricated out of unistrut bars and aluminum plates cut into triangular shapes for stability at the corners.

The support structure consisted of two faces, each forming a six-sided polygon (Fig. 2.5). One of the six-sided, unistrut polygons was positioned in the tank close to the attached test section. It was secured by extending four threaded rods that

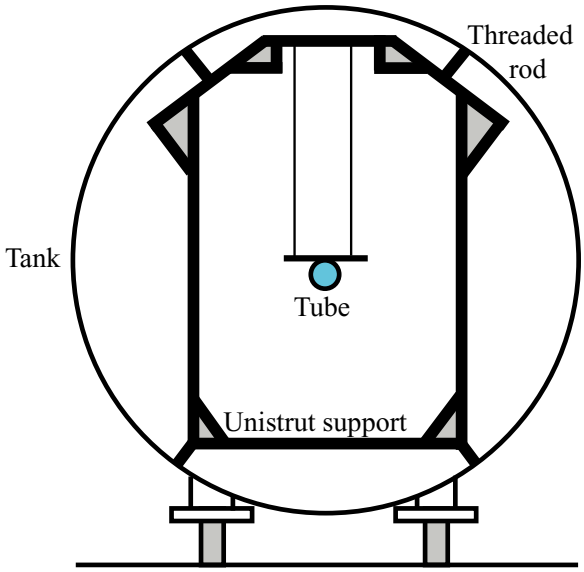

Figure 2.5: Schematic of unistrut support structure used to hang detonation tube within tank.

were attached to the unistrut such that they pressed against the tank's inner surface. A second six-sided, unistrut polygon was positioned approximately halfway down the length of the tank. It was again secured by extending four threaded rods that were attached to the unistrut against the tank's inner surface. Three long unistrut bars running parallel to the axis of the tank were used to connect the two polygon faces together. Two of these bars were bolted to the top horizontal bar of Fig. 2.5 and were used for attaching the wires from which the tube was hung. A single bar was bolted to the bottom horizontal bar of Fig. 2.5 to provide additional rigidity to the structure.

Figure 2.6 shows the detonation tube hanging within the tank from the support structure with the exhaust end of the tube in the foreground. The ionization gauges can be seen extending off the left side of the tube and the solenoid valve is seen mounted on the tube at the top of the image. Portions of the unistrut frame are also visible.

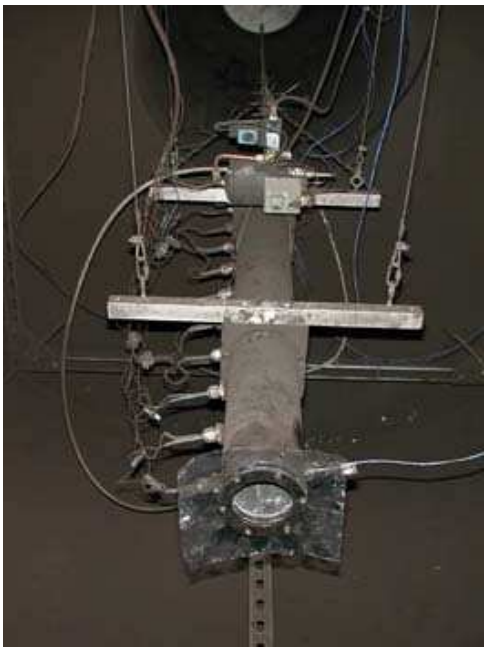

Figure 2.6: Photograph of detonation tube hanging in the ballistic pendulum arrangement within the T-5 dump tank. The exhaust end of the tube is located in the foreground.

2.4.2 Fill station

A fill station consisting of stainless steel tubing, pressure gauges, and valves was built to manage the filling of the premix vessel and the evacuation and filling of the detonation tube. A schematic of the gas plumbing for the facility appears in Fig. 2.7. The components that make up the fill station, detonation tube, and large tank are noted. One vacuum pump, attached to the large tank, was used to reduce its internal air pressure. A bleed-up valve on the tank enabled fine tuning of the environment pressure. A second vacuum pump was attached to the detonation tube and mixing vessel via the fill station.

2.4.3 Feed-through plate

A feed-through plate located on the bottom of the tank's test section (Fig. 2.3) was used to connect the gas lines and electrical connections through the tank wall to the detonation tube. One gas line connected the building air supply to the solenoid valve

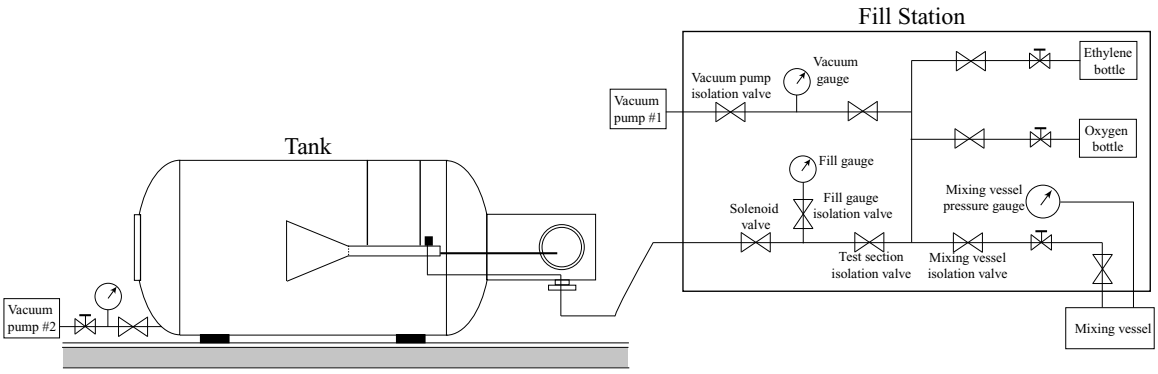

Figure 2.7: Schematic of fill station and plumbing connections to the tube.

mounted on the tube and was used to cycle the valve. A second gas line connected the fill station to the gas inlet fitting on the detonation tube through the solenoid valve. The electrical connections through the feed-through plate consisted of low voltage connections that powered the solenoid valve and diagnostics, while a high voltage feed-through was used to fire the spark plug. A teflon insert with two terminals made out of copper rods were used to pass the high voltage spark signal through the feed-through plate.

2.4.4 Test procedure

The initial combustible mixture was created in the external mixing vessel. From the fill station, the vacuum pump was applied to the premix vessel and its contents were evacuated until a pressure of at least 0.003 bar. The vacuum pump isolation valve is closed and the fill valves to the ethylene and oxygen bottles are opened individually. The premix vessel is filled with the ethylene and oxygen gases based on the partial pressure of the desired mixture. The attached pressure gauge is monitored and final pressure is recorded. The mixing vessel isolation valve is closed and mixing fan is turned on to mix the contents, ensuring homogeneity. This mixture is filled into the detonation tube over multiple tests until it was emptied, after which the vessel is evacuated and the above steps were repeated to refill the premix vessel.

With the mixture prepared and stored in the premix vessel, the tank and deto-

nation tube are prepared for a test. Preparation involves aligning the camera and light source such that the ruler is clearly visible and the VCR is ready for recording. The back door of the tank is opened and a new diaphragm is installed on the tube. The back door is sealed and the tube solenoid valve is opened. If a low environment pressure experiment is to be conducted, the tank vacuum pump is turned on and the tank contents are evacuated until the desired tank pressure is reached. The test section isolation valve is closed during this process to ensure the diaphragm properly seals. Once the tank has reached the desired pressure and no leak occurs at the diaphragm, the vacuum pump isolation valve is opened and the external vacuum pump is applied to the detonation tube via the fill station. The detonation tube and associated plumbing is evacuated to 133 Pa.

The vacuum isolation valve is turned off and the mixing vessel isolation valve is opened such that the premixed ethylene-oxygen gases flow directly through the fill station plumbing into the detonation tube. A fill gauge is used to monitor the increase in tube pressure. The mixing vessel isolation valve and tube solenoid valve are closed when the desired pressure is reached within the detonation tube. The vacuum pump isolation valve is again opened to evacuate the combustible mixture from the fill station plumbing between the two isolation valves. The test is initiated by starting the visual recording of the detonation tube's ruler and powering up the ignition system. The spark is fired to ignite the mixture. After the detonation event is complete. The VCR is stopped, the contents of the tank are purged, and preparations for the next test begin.

2.5 Extensions

The exit condition of the detonation tube was modified by attaching a nozzle or extension on the end of the tube opposite of the thrust surface. The diaphragm was positioned between the exit plane of the tube and the inlet to the nozzle so that the nozzle contained air at the environment conditions. Impulse measurements were carried out with four types of extensions attached to the tube; conical converging nozzles, conical diverging nozzles, conical converging-diverging nozzles, and a cylindrical extension. Descriptions of the extensions follow.

2.5.1 Converging nozzles

Two conical converging nozzles were constructed of equal length and varying exit area. The general shape of the nozzle is illustrated in Fig. 2.8 and the specific dimensions appear in Table 2.1. The area ratios (A_{exit}/A_{inlet}) varied between the most

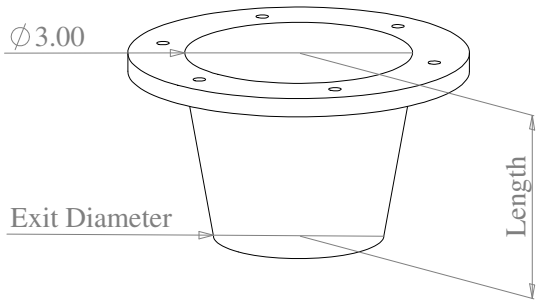

Figure 2.8: Schematic of a general converging nozzle. Refer to Table 2.1 for the exact dimensions.

Description	Length (mm)	ϕ (°)	D_{exit} (mm)	A_{exit}/A_{inlet}
Noz-0.50	63.5	10	54.0	0.50
Noz-0.75	63.5	5	66.0	0.75

Table 2.1: Dimensions of the tested converging nozzles. Refer to Fig. 2.8 for the corresponding labels.

restrictive value of 0.50 to the least restrictive value of 0.75.

Although the converging nozzles are short relative to the tube length, a finite mass of the environment air is contained within the nozzle volume. Impulse experiments with the converging nozzles were carried out in a tube that exhausted into atmospheric pressure only.

2.5.2 Diverging nozzles

Three conical diverging nozzles were constructed by rolling 6061-T6 aluminum sheet with a thickness of 0.16 cm into the general shape illustrated in Fig. 2.9 and the seam was welded shut. The corresponding dimensions for each nozzle appear in Table 2.2.

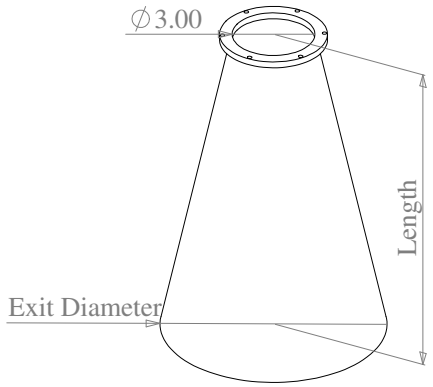

Figure 2.9: Schematic of a general diverging nozzle. Refer to Table 2.2 for the exact dimensions.

Description	Length (m)	ϕ (°)	D_{inlet} (mm)	D_{exit} (mm)	A_{exit}/A_{inlet}
8°-0.3 m	0.3	8	63.5	152.0	5.7
12°-0.3 m	0.3	12	76.2	194.0	6.5
12°-0.6 m	0.6	12	76.2	311.0	16.7

Table 2.2: Dimensions of the diverging nozzles. Refer to Fig. 2.9 for the corresponding labels.

A mounting flange containing through-holes for bolts to attach the nozzle to the detonation tube was welded to the small end of the nozzle. Rings with a thickness of 0.64 cm and different inner diameters were constructed and spot welded to the

outer surface of the nozzle. These rings provided rigidity to the welded seam and maintained the nozzle's shape under the transient gas dynamic loads. The rings and spot welds are visible in the photographs of Fig. 2.10.

(a) (b)

Figure 2.10: Photographs of the three diverging nozzles; a) left: 12° - 0.3 m, right: 8° - 0.3 m; b) left: 12° - 0.3 m, right: 12° - 0.6 m

The nozzles differed in terms of their length (either 0.3 m or 0.6 m) and in terms of their half angle (either 8° or 12°), the combination of which determines the exit area and the corresponding area ratio. The nozzle inlet area was held constant at an area equal to the tube cross-sectional area.

2.5.3 Converging-diverging nozzles

The effect of a throat restriction upstream of a diverging nozzle was tested by attaching a separate throat section onto the diverging nozzles with a 12° half angle. Each throat section had an inlet area that equal to the detonation tube cross-sectional area, followed by a decrease in area to the throat area. After the throat, the area increased until it equaled the tube cross-sectional area (also equal to the inlet area of the diverging nozzles). This created a single converging-diverging nozzle that had a

continuous increase in area from the throat to the nozzle exit. An illustration of the general shape of the converging-diverging throat section appears in Fig. 2.11 and the exact dimensions are tabulated in Table 2.3.

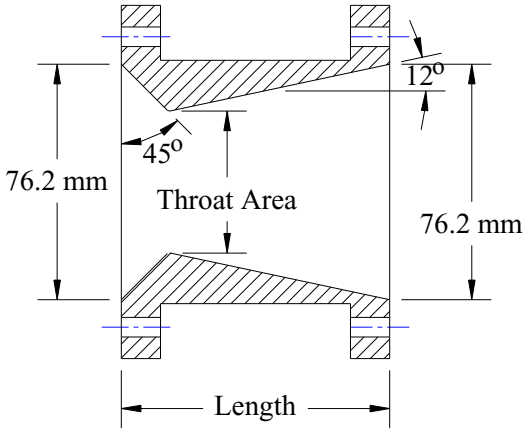

Figure 2.11: Illustration of a general converging-diverging throat section that was attached between the detonation tube exit and the diverging nozzle inlet. Refer to Table 2.3 for the exact dimensions.

Description	Length (mm)	D_{throat} (mm)	A_{throat}/A_{inlet}
CD-0.75	29.0	66.0	0.75
CD-0.54	57.9	55.9	0.54
CD-0.36	86.9	45.7	0.36

Table 2.3: Dimensions of the converging-diverging throat sections. Refer to Fig. 2.11 for the corresponding labels.

The converging part of the throat had a 45° half angle while the half angle after the throat was 12° to match the diverging nozzles. This enabled the three different converging-diverging sections to be installed on the two diverging nozzles with a 12° half angle for a total of 6 test configurations. A photograph of one of the throat sections installed on the 12°-0.6 m nozzle appears in Fig. 2.12.

Because the inlet and exit half angles of the converging-diverging section were fixed, the length of each fixture varied in order to obtain the desired throat area. Thus, the section with the smallest throat area had the longest length as illustrated in Table 2.3.

Figure 2.12: Photograph of 12°-0.6 m nozzle with a converging-diverging throat section installed.

2.5.4 Straight extension

A cylinder with the same cross-sectional area as the detonation tube was also examined. It had a length of 0.6 m and is referred to as either the straight extension or a diverging nozzle with a 0° half angle. Figure 2.13 is a photograph of the hanging tube with the straight extension attached. Because the cross-sectional area of the detonation tube and extension are equal, the entire device can be thought of as a long detonation tube that is only partially filled with the explosive mixture.

2.6 Analysis of experimental uncertainties

A number of sources of uncertainty exist due to the experimental facility, initial conditions, and procedure. These are discussed and when possible, are quantified using the standard method for estimating error propagation. As discussed in Bevington (1969), the variance $\Delta\mathcal{X}$ associated with the measured quantity $\mathcal{X}(x_1, ...x_n)$ can be

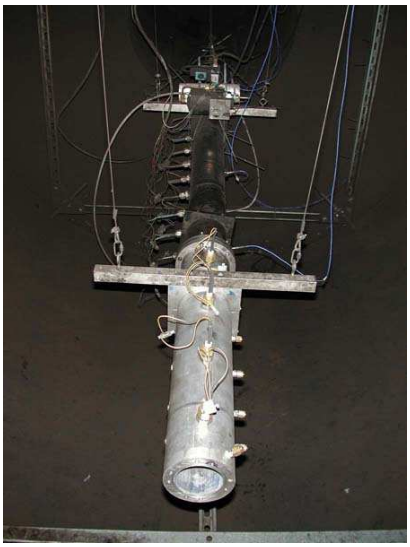

Figure 2.13: Photograph of the detonation tube with the straight extension (or 0°-0.6 m nozzle) installed.

estimated as

$$\Delta\mathcal{X} = \sqrt{\left(\frac{\partial\mathcal{X}}{\partial x_1}\right)^2 (\Delta x_1)^2 + ... \left(\frac{\partial\mathcal{X}}{\partial x_n}\right)^2 (\Delta x_n)^2} \; .$$

2.6.1 Ballistic pendulum technique

Using the expression for ballistic impulse in Eq. 2.2, the uncertainty in the direct experimental measurements of the impulse per unit volume can be quantified. The estimated uncertainties in the pendulum arm length, measured pendulum deflection, pendulum mass, and the tube volume are given in Table 2.4. From this analysis, the total uncertainty in the direct impulse measurements due to the experimental setup was calculated to be at most ±1.3%.

Quantity	Range of values	Uncertainty
L_p	1.0-1.55 m	±0.0016 m
Δx	39-292 mm	±0.5 mm
M_p	12.808-31.558 kg	±0.001 kg
V	4.58×10^{-3} m^3	$\pm4.5\times10^{-8}$ m^3

Table 2.4: Uncertainties used in determining the error for experimentally measured impulse.

The ballistic pendulum arrangement is a popular method (Cooper et al., 2002, Zhdan et al., 1994, Harris et al., 2001, Kiyanda et al., 2002) with which accurate impulse measurements from a detonation tube can be obtained due to its simplicity as compared to measurements made with damped thrust stands. But to the author's knowledge, the error in the impulse measurements due to non-ideal processes within the pendulum itself have not been quantified in its contemporary use to measure detonation tube impulse. While this measure of ballistic impulse includes all the gas dynamic processes acting on the tube to change its displacement, a real experiment is never ideal and a fraction of these forces are lost due to losses associated with the pendulum. Experiments of the pendulum motion were carried out and are discussed in the next section.

2.6.1.1 Fundamentals of pendulum motion

The motion of a pendulum is periodic in time and can be characterized by its natural frequency. This frequency depends only on the pendulum's arm length L_p and gravity g.

$$\omega_n = \sqrt{g/L_p} \tag{2.5}$$

An ideal pendulum, once in motion, would continue to swing forever, passing by a stationary observer every $2\pi/\omega_n$ seconds. However, the real pendulums used in our laboratory experiments experience frictional forces or damping that decrease the maximum deflection over time and eventually bring the pendulum to rest. The rate at which the maximum deflection of the pendulum decreases over time depends on the amount of damping in the device.

The published experimental impulse values of Cooper et al. (2002), Zhdan et al. (1994), Harris et al. (2001), and Kiyanda et al. (2002) gave no mention to the amount of damping that existed in each experimental setup. It must be assumed that the reported impulse data were measured from a damped system and actually underestimate the initial impulsive force imparted to the tube by the detonation process. For an exact measurement of the impulse, the pendulum damping should be zero such

that all the gas-dynamic energy goes into changing the location of the tube. For the two facilities described in §2.3 and in §2.4, a potential source of damping are the fill lines and electrical connections that remain attached to the tube during its motion.

The pendulum's response to a general force $F(t)$ is represented by

$$M_p y'' + cy' + ky = F(t) \tag{2.6}$$

where M_p is the pendulum mass, c is the damping, and k is a constant. This is a constant coefficient, second-order differential equation in which an exponential solution for the deflection $y(t)$ of the form $A\exp(\lambda t)$ is assumed. Three types of system responses are possible depending on the level of damping; an underdamped system, an overdamped system and a critically damped system. The value of λ dictates the system's response. For the application discussed here, we are only concerned with the case of an underdamped system and a system with no damping.

When the system has no damping ($c = 0$ in Eq. 2.6), the value of λ has only an imaginary part and the deflection is written in terms of a sine function.

$$y_{c=0}(t) = C\sin(\omega_n t + \phi) \tag{2.7}$$

The constant C and the phase shift ϕ are determined from the initial conditions. When the system is underdamped ($c > 0$ in Eq. 2.6), the value of λ has a real and imaginary part which enables the deflection to be written in terms of an decaying exponential factor and a sine term.

$$y_{c>0}(t) = C\exp(-\beta\omega_n t)\sin(\omega_d t + \phi) \tag{2.8}$$

The constant C and the phase shift ϕ depend on the initial conditions as before. The period of the system now depends on the damped frequency ω_d instead of the natural frequency ω_n as in Eq. 2.7. These two frequencies are related to each other by the

damping factor β.

$$\omega_n = \frac{\omega_d}{\sqrt{(1-\beta^2)}} \tag{2.9}$$

The unknown parameters of the underdamped expression Eq. 2.8 can be experimentally determined from the pendulum position recorded over time.

2.6.1.2 Experiments measuring pendulum motion

While the tube was hung in Facility II (§2.4), its pendulum motion was recorded during several separate experiments. The motion was recorded from the tube only (no extension or nozzle was attached), the tube with the 0°-0.6 m straight extension, and the tube with the 12°-0.6 m diverging nozzle. All electrical connections and plumbing connections were attached as in the actual experiment. The camera and VCR recorded the deflection through the test section windows over time.

The procedure for each experiment began by starting the VCR to record. The tube was initially stationary at a deflection of zero from its neutral or natural resting position. The back of the tube was given a sharp push and allowed to swing for several oscillations. The force imparted to the tube varied between tests. Data was obtained by re-playing the video tape frame by frame and recording the ruler measurement and frame number at the point of maximum positive displacement from its neutral position. Because of the camera's field of view, only half of the pendulum's periodic motion was observable. Since 1/30th of a second elapses between each frame, the number of elapsed frames between successive maximum deflections could be converted into an equivalent time.

The experimental data from all tests appears in Fig. 2.14.

The elapsed time between the data points is the damped natural period τ_d and was used to calculate the damped frequency.

$$\omega_d = \frac{2\pi}{\tau_d} \tag{2.10}$$

An estimate of β was obtained from the experimental data by determining its loga-

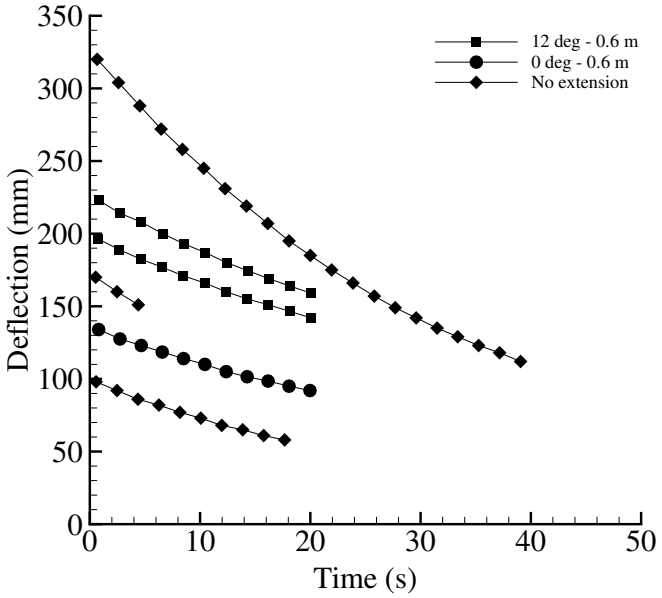

Figure 2.14: Experimental data of pendulum motion.

Parameter	Tube only	Tube and 0°-0.6 m extension	Tube and 12°-0.6 m nozzle
C	325.37	135.00	224
β	0.0085	0.0059	0.0052
ω_n	3.220116	3.230056	3.230042
ω_d	3.22	3.23	3.23

Table 2.5: Parameters of Eq. 2.8 characterizing each pendulum configuration.

rithmic decrement as discussed in Ginsberg and Genin (1995),

$$\beta = \frac{\ln(y_1/y_2)}{\sqrt{\ln(y_1/y_2)^2 + 4\pi^2}} \tag{2.11}$$

where y_1 and y_2 are two successive maximum deflections. Now the natural frequency of the system was calculated from β and ω_d by Eq. 2.9 and was found to equal, within the experimental uncertainty, the value calculated from Eq. 2.5 based on the measured pendulum arm length. The constant C in Eq. 2.8 varied with the value of the initial impulse force $F(t)$ to match the initial maximum deflection. The phase shift ϕ in Eq. 2.8 equaled zero since the pendulum always started its motion from the neutral position. Table 2.5 shows the resulting parameters for each tube configuration.

These parameters are substituted into Eq. 2.8 to yield a continuous function de-

scribing the pendulum motion over time. Similarly, these parameters can be used in Eq. 2.7 to yield a continuous function describing the ideal pendulum motion over time if there is no damping.

Plots of the motion $y_{c>0}(t)$ and the experimental data for the three tube configurations appear in Figs. 2.15, 2.16, and 2.17. Additional experiments with the same tube configuration that had a smaller maximum initial deflection were time shifted to fit onto the analytical curve of the system. After matching this initial point for all tests, the other data points for the successive pendulum oscillations were found to match the curve well.

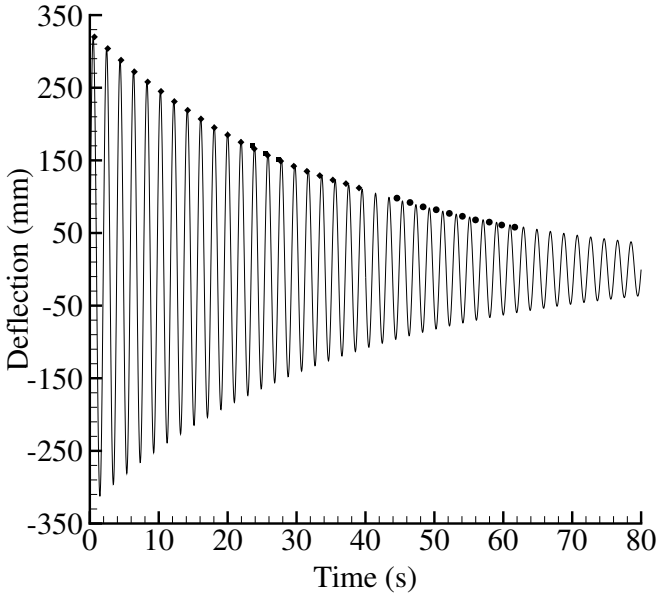

Figure 2.15: Experimental pendulum motion data for the tube only plotted with the solution of the damped second-order differential equation Eq. 2.8 using the parameters listed in Table 2.5.

The original second-order differential equation Eq. 2.6 of each case can also now be determined if the pendulum's mass is known. The resulting equations are tabulated in Table 2.6. The corresponding second order equation for the undamped case follows since c must equal zero (Table 2.7). The constant k is calculated from the natural

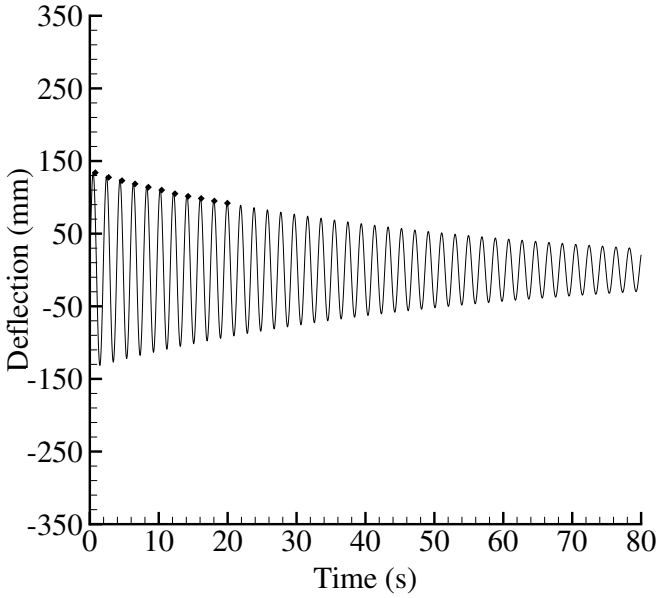

Figure 2.16: Experimental pendulum motion data for the tube with the 0°-0.6m straight extension plotted with the solution of the damped second-order differential equation Eq. 2.8 using the parameters listed in Table 2.5.

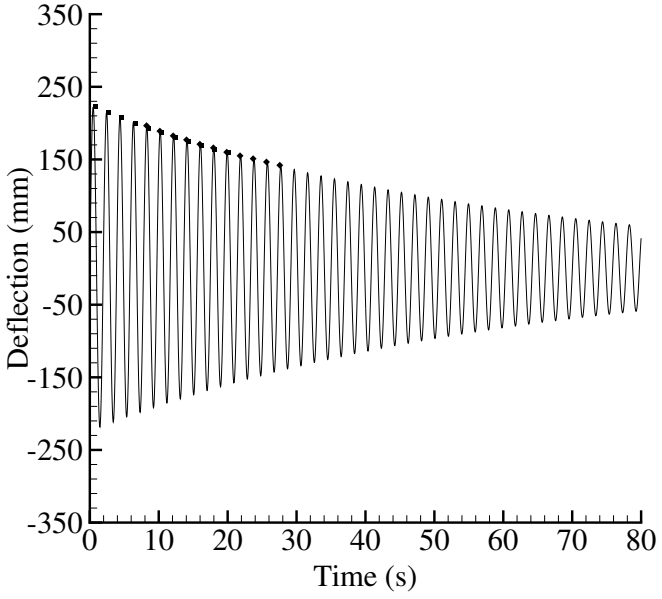

Figure 2.17: Experimental pendulum motion data for the tube with the 12°-0.6m nozzle plotted with the solution of damped second-order differential equation Eq. 2.8 using the parameters listed in Table 2.5.

Configuration	Damped equation
Tube only	16.417 y" + 0.8987 y' + 170.230 y = 0
Tube and 0°-0.6 m extension	31.171 y" + 1.1881 y' + 325.215 y = 0
Tube and 12°-0.6 m nozzle	23.556 y" + 0.7913 y' + 245.764 y = 0

Table 2.6: Second-order differential equation of underdamped periodic motion.

Configuration	Undamped equation
Tube only	16.417 y" + 170.230 y = 0
Tube and 0°-0.6 m extension	31.171 y" + 325.215 y = 0
Tube and 12°-0.6 m nozzle	23.556 y" + 245.764 y = 0

Table 2.7: Second-order differential equation of undamped periodic motion.

frequency and the mass while the damping c is calculated from k, M, and β.

$$k = \omega_n^2 M_p \quad and \quad c = 2\sqrt{kM_p}\beta \tag{2.12}$$

2.6.1.3 Evaluating the deflection for each case

The difference between the impulse values obtained in an ideal and non-ideal experiment is determined by evaluating the difference in the maximum initial deflections predicted by the undamped solution $y_{c=0}$ and the underdamped solution $y_{c>0}$. The difference is calculated by evaluating each solution at the time of maximum deflection given the same initial conditions. Because of the damping in the non-ideal case, the time of maximum deflection t_{max} occurs earlier as compared to the undamped case. We evaluate t_{max} by setting the derivative of the deflection $y'(t)$ equal to zero.

$$\begin{aligned} y'_{c>0}(t_{max}) &= -C\beta\omega_n \exp(-\beta\omega_n t_{max}) \sin(\omega_d t_{max}) \\ &\quad + \omega_d C \exp(-\beta\omega_n t_{max}) \cos(\omega_d t_{max}) = 0 \\ \beta\omega_n \sin(\omega_d t_{max}) &= \omega_d \cos(\omega_d t_{max}) \\ (t_{max})_{c>0} &= \frac{1}{\omega_d} \tan^{-1}\left(\frac{\omega_d}{\beta\omega_n}\right) \end{aligned} \tag{2.13}$$

This same procedure is followed for the undamped equation $y_{c=0}(t)$.

$$\begin{aligned} y'_{c=0}(t_{max}) &= C\omega_n \cos(\omega_n t_{max}) = 0 \\ (t_{max})_{c=0} &= \frac{\pi}{2\omega_n} \end{aligned} \tag{2.14}$$

The constant C for each system is calculated based on the same initial velocity imparted to the pendulum.

$$\begin{aligned} y'_{c>0}(0) &= -C\beta\omega_n \exp(-\beta\omega_n * 0)\sin(\omega_d * 0) \\ &\quad + \omega_d C \exp(-\beta\omega_n * 0)\cos(\omega_d * 0) \\ C_{c>0} &= \frac{y'_{c>0}(0)}{\omega_d} \end{aligned} \tag{2.15}$$

This same procedure is followed for the undamped equation $y_{c=0}(t)$.

$$\begin{aligned} y'_{c=0}(0) &= C\omega_n \cos(\omega_n * 0) \\ C_{c=0} &= \frac{y'_{c=0}(0)}{\omega_n} \end{aligned} \tag{2.16}$$

We use the deflection relationship Eq. 2.8 with the desired parameters that model the experimental system from Table 2.5 to evaluate the initial velocity $y'(t)$ as the pendulum passes through the neutral position $y(t) = 0$ that must have been imparted to the pendulum to yield a maximum deflection $y(t + \tau_d/4)$ one quarter of a period later.

This initial velocity is now used with Eqs. 2.8, 2.13, and 2.15 to evaluate the maximum deflection for the damped system and Eqs. 2.7, 2.14, and 2.16 and for the undamped system. The results are plotted in Fig. 2.18 as a function of the maximum measured deflection for each tube configuration. The difference in the maximum deflection for the damped and undamped system should be applied to the experimental data to correct for the non-ideal, dissipative effects in the pendulum (Fig. 2.19). The slope of these lines are 0.0134 for the tube only, 0.0093 for the

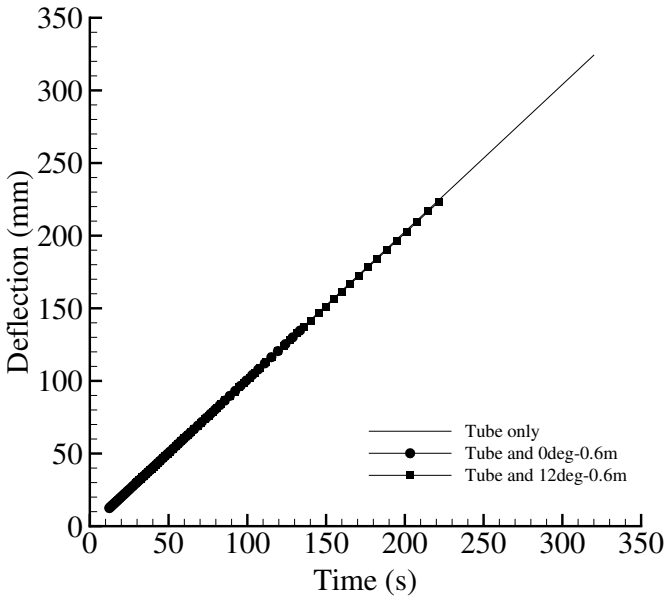

Figure 2.18: The maximum deflection of the damped system versus the maximum deflection of the undamped system for the same initial conditions.

0°-0.6 m straight extension, and 0.0082 for the 12°-0.6 m nozzle. Thus, the effect of damping results in an error of 1.34%, 0.93%, and 0.82% in the deflection measurement for the different tube configurations tested in our laboratory. The corresponding error in the normalized impulse is calculated by evaluating Eq. 2.2 and is shown in Fig. 2.20. The slope of these lines are 0.1522 for the tube only, 0.2011 for the 0°-0.6 m straight extension, and 0.1105 for the 12°-0.6 m nozzle.

Thus, the error in the impulse measurement due to dissipative forces in the experimental pendulum can be determined by characterizing the system with a second-order differential equation. This error in the normalized impulse is at most 2% for our impulse facility and depends only slightly on the pendulum mass.

Combining the error due to the damping forces with the uncertainty in the ballistic pendulum measurement, we determine a total uncertainty in the normalized impulse measurement of 2.8%.

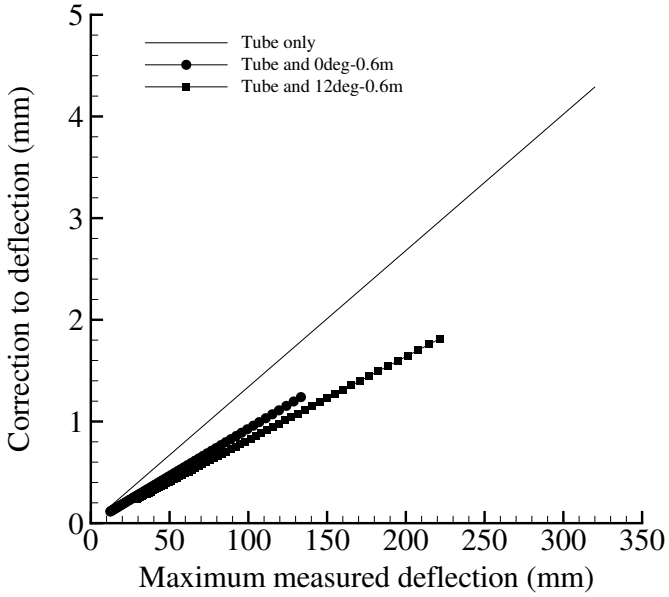

Figure 2.19: The correction in the deflection to correct the experimental data to represent an undamped system.

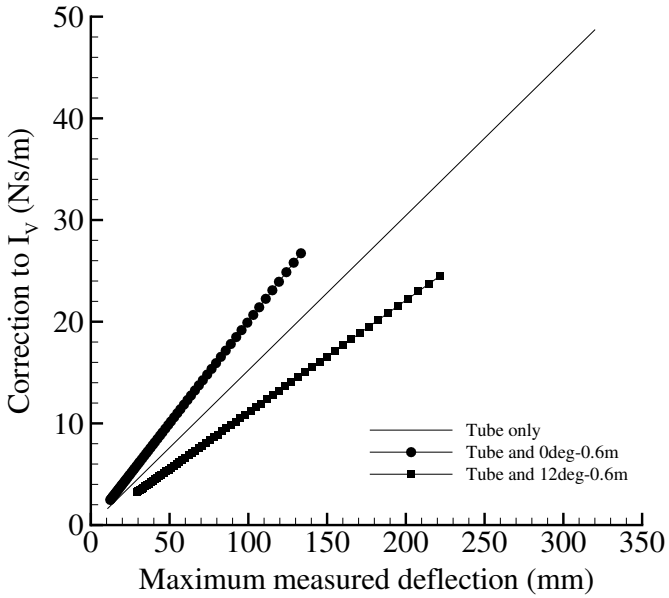

Figure 2.20: The correction in the normalized impulse to correct the experimental data to represent an undamped system. This is the correction for the experimental setup of the low-environment-pressure impulse facility.

2.6.2 Measured U_{CJ} and P_3 values

Measured data also included the CJ velocity and plateau pressure P_3. The CJ velocity was calculated from the ionization gauge data at each initial mixture pressure. The average measured velocity, the difference between the maximum and the minimum measured values, the standard deviation from the mean, and the value predicted by Stanjan (Reynolds, 1986) appear in Table 2.8. The relative differences between the

P_1 (kPa)	U_{CJ} from Stanjan (m/s)	Average U_{CJ} Exps. (m/s)	Max - Min U_{CJ} Exps. (m/s)	Std. Dev. of U_{CJ} Exps. (m/s)
100	2376	2375	63	24
80	2365	2366	63	21
60	2351	2350	90	32
40	2331	2351	12	6
30	2317	2352	221	93

Table 2.8: Measured U_{CJ} data tabulated for different initial mixture pressures.

measured and predicted detonation velocities are less than 0.05% for the mixtures with an initial pressure 60 kPa and greater. Larger differences are observed for the mixtures with lower initial pressures, but this is expected due to the longer time required for transition to detonation.

The same procedure was followed for the measured plateau pressures P_3 at the thrust surface. Experimental values were obtained by averaging the measured pressure histories. The relative difference between the measured and predicted plateau

P_1 (kPa)	P_3 from Model (MPa)	Average P_3 Exps. (MPa)	Max - Min P_3 Exps. (MPa)	Std. Dev. of P_3 Exps. (MPa)
100	1.222	1.202	0.046	0.016
80	0.970	0.982	0.035	0.012
60	0.720	0.746	0.048	0.015
40	0.472	0.523	0.009	0.004
30	0.351	0.398	0.056	0.024

Table 2.9: Measured P_3 data tabulated for different initial mixture pressures. The model values correspond to the predictions of Wintenberger et al. (2003).

pressures is less than 4% for the mixtures with an initial pressure of 60 kPa and

greater. The difference is less than 14% for the mixtures with a smaller initial pressure.

The average measured values for the detonation velocity and plateau pressure were used to normalize the experimental impulse data and were found to be independent of the environment pressure.

2.6.3 Mixture preparation

Uncertainties in the initial conditions were also quantified. Uncertainty in the initial pressure P_1 is due to the gauge precision of ± 0.1 kPa and uncertainty in the environment pressure P_0 is due to the gauge precision of ± 0.345 kPa. The largest measured leak rate was 200 Pa/min from an initial pressure of 133 Pa. Because a premix vessel was used to fill the tube, less than 5 s elapsed between removing the vacuum pump from to tube and filling the tube with the combustible mixture. Mixture contamination due to incomplete evacuation of the tube results in a worst-case air contamination of 133 Pa. Mixture contamination due to incomplete evacuation of the premix vessel results in a worst-case air contamination of 150 Pa. Before refilling the mixing vessel at most 0.003 bar air could not be evacuated. A total of 4 experiments could be run from each batch of the ethylene-oxygen mixture in the premix vessel. Combining, the total worst-case air contamination is approximately 280 Pa.

A study to identify the mixture most affected by this leak rate found stoichiometric ethylene-oxygen at an initial pressure of 30 kPa and initial temperature of 295 K to be the most sensitive case. An error analysis was then performed for this mixture to find the maximum uncertainty in initial conditions for all experiments. The analytical model of Wintenberger et al. (2003) can be used to express I_V as a function of U_{CJ}, P_3, and c_3. The quantity ΔU_{CJ} is the difference in the Chapman-Jouguet velocity for a mixture containing an additional 280 Pa of air. STANJAN (Reynolds, 1986) was used to calculate U_{CJ} in each case. ΔP_3 and Δc_3 can then be found from differences in P_3 and c_3 for the two mixtures, where P_3 and c_3 are given by the relationships below, which are derived by using the method of characteristics to relate flow properties on

either side of the Taylor wave (Wintenberger et al., 2003),

$$\frac{P_3}{P_2} = \left(\frac{c_3}{c_2}\right)^{\frac{2\gamma}{\gamma-1}} = \left(\frac{\gamma+1}{2} - \frac{\gamma-1}{2}\frac{U_{CJ}}{c_2}\right)^{\frac{2\gamma}{\gamma-1}} . \tag{2.17}$$

Table 2.10 lists the calculated maximum changes in the flow parameters due to the leak rate. Also shown are the largest possible contributions due to uncertainty in the initial pressure because of gauge precision (±0.1 kPa) and due to uncertainty in the initial temperature (295-298 K). All uncertainties shown are calculated for comparison with the same ideal case specified above.

	Ideal	Dilution	Pressure	Temperature
P_1 (kPa)	30.0	30.0	30.1	30.0
T_1 (K)	295	295	295	298
U_{CJ} (m/s)	2317.9	2311.7	2307.5	2317.3
P_2 (kPa)	970.2	964.3	965.4	960.0
c_2 (m/s)	1249.	1245.	1243.	1249.
γ	1.14	1.14	1.14	1.14
P_3 (kPa)	354.8	352.2	352.7	351.2
c_3 (m/s)	1174.	1170.	1168.	1174.
ΔU_{CJ}(m/s)	-	6.2	10.4	0.6
ΔP_3 (Pa)	-	2577	2008	3525
Δc_3 (m/s)	-	4.	6.	0.
ΔI_V	-	0.9%	0.9%	1.1%

Table 2.10: Variations in flow parameters resulting from uncertainty in initial conditions due to error in dilution (leak rate), initial pressure, and initial temperature as described in the text. The mixture chosen is stoichiometric C_2H_4-O_2 at an initial pressure of 30 kPa, which corresponds to the worst case of all the mixtures considered in experiments. The percentage error in I_V is based on the model predicted impulse.Wintenberger et al. (2001)

Combining the results in Table 2.10, the uncertainty in the impulse measurement due to the initial conditions is found to contribute at most ±2.9%, resulting in an overall maximum uncertainty of ±3.8% in ballistic measurements of the impulse (including damping error of 2% and uncertainty in ballistic impulse of 1.3%).

Experimental repeatability was also considered. For experiments in which fast transition to detonation occurred, the impulse was repeatable to within ±0.7%. In

cases where late DDT or fast flames were observed, the impulse in repeat experiments varied by as much as $\pm 17\%$ due to the turbulent nature of the flow during the initiation process. Additional experiments were conducted to verify that no out-of-plane motion existed during the initial pendulum swing.

Chapter 3

Partially filled tubes at standard conditions

3.1 Introduction

The impulse from a partially filled detonation tube is investigated. A detonation tube is considered to be partially filled if a portion of the tube near the thrust surface contains the combustible mixture while the remaining portion of the tube contains an inert mixture. This chapter studies cylindrical tubes that are closed at one end, open at the other, and partially filled with an inert gas at standard pressure of 1 atm. Chapter 5 discusses the partial fill effect in non-cylindrical tubes, such as tubes with nozzles.

In the laboratory, there are several ways to construct a partially filled detonation tube. The most common method is to add cylindrical extensions of varying lengths onto a cylinder of constant length. The constant-length cylinder is filled with the combustible mixture which is initially sealed inside by a diaphragm. On the other side of the diaphragm and attached onto this tube are extensions of varying length. Thus, the distance separating the thrust surface and diaphragm is held constant while the total tube length varies depending on the extension's length. A second method uses a constant length tube comprised of many shorter segments. This enables the diaphragm location to be varied while the total tube length remains constant. A third method, used in multi-cycle facilities, is to dynamically fill the tube by switching the

inlet gas stream between the combustible mixture and the inert gas (Schauer et al., 2001). In all of these situations, the volume fraction of the tube filled with the combustible mixture and the volume fraction of the tube filled with the inert mixture can be used as a quantitative measure of comparison between different facilities.

A number of researchers have previously studied the partial fill effect. The pioneering experiments in partially filled detonation tubes were carried out by Zhdan et al. (1994) with acetylene-oxygen mixtures at standard conditions in detonation tubes having an inner diameter of 0.107 m. They added cylindrical extensions to a constant-length tube containing the combustible mixture so that the total tube length varied between 0.125 m and 1.00 m. An initiation tube and reflector was used to initiate a detonation. Direct impulse measurements were obtained with a ballistic pendulum arrangement and their findings were extended with two-dimensional numerical modeling of the nonsteady gas dynamics assuming chemical equilibrium to predict the thrust wall pressure history.

Zitoun and Desbordes (1999) carried out experiments with four tubes of different lengths all having an inner diameter of 0.05 m and containing ethylene-oxygen mixtures at standard conditions. Cylindrical extensions 0.011 m in length were added to the four tubes so that the total tube lengths varied from 0.061 m to 0.436 m. Detonations were directly initiated with approximately 35 J of energy and they calculated the impulse by integrating the thrust surface pressure differential.

Cooper et al. (2001) and Falempin et al. (2001) both used a ballistic pendulum to experimentally measure the single-cycle impulse of ethylene-oxygen mixtures ignited with a weak spark. Both studies used a constant length tube containing the combustible mixture and added extensions of varying length. The total tube lengths varied between 0.065 m and 0.439 m and had an inner diameter of 0.05 m in the facilities of Falempin et al. (2001) whereas the total tube lengths varied between 1.014 m and 1.614 m and had an inner diameter of 0.0762 m in the facilities of Cooper et al. (2001). Cooper et al. (2001) extended their tests to study the effect of diluent amount in the combustible mixture.

Eidelman and Yang (1998) numerically studied the partial-fill effect in acetylene-

air mixtures at standard conditions. The modeled a 6 cm diameter tube with variations in the total length from 15 cm to 30 cm. Their model solved the nonsteady gas dynamic equations using a one-step Arrhenius law equation model for the chemical reactions and heat release. The increase in impulse they predict for the partially filled tubes is approximately 50% greater than the other studies. This is attributed to their numerical method of detonation initiation and as a result we do not consider their data in the following analyzes.

Li and Kailasanath (2003) numerically modeled the partial fill effect in tubes with a constant length of 1350 mm filled with ethylene-oxygen mixtures and tubes with a constant length of 1000 mm filled with ethylene-air mixtures. They investigated a wide range of lengths filled with the combustible mixture which enabled them to obtain data at small fill fractions where experimental data is not available. An exponential curve fit was applied to their data relating the fuel-based specific impulse to the amount of the tube length filled with the explosive mixture.

Sato et al. (2004) numerically predict the impulse of partially filled tubes with mixtures of hydrogen-air and ethylene-oxygen at standard conditions. They varied the equivalence ratio, inert gas amount and type (Air, He, Ar) at 1 atm, and inert gas temperature. They present a mass-based model of partial-filling. A faster pressure decay rate at the thrust surface was observed with an inert gas of helium as compared to inert gases of air or argon due to its higher sound speed. As will be discussed later in §3.4.2 the critical parameters that affect the pressure decay rate are the sound speed ratio for the explosive-inert gas combination.

Endo et al. (2004) analytically predict the impulse of partially filled tubes by calculating an equivalent homogeneous mixture representative of the explosive and inert mixtures. With the redefined homogeneous mixture, they predict the impulse for a fully filled tube with their analytical model. The resulting impulse values are comparable within 25% of their two-dimensional hydrogen-oxygen simulations with inert gases of helium or air, but there is no correlation between the predicted thrust surface pressure histories. This leads them to conclude that the impulse of a partially filled detonation tube is dominated only by the mixture energetics.

The general conclusions of these studies are that adding a constant-area extension onto a constant length tube filled with the combustible mixture will increase the mixture-based specific impulse. The impulse will continue to increase until the maximum value for the specific explosive-inert combination is reached. This maximum impulse has not been conclusively determined for any of the mixtures. If the total tube length remains constant and the amount of combustible mixture filling the tube decreases, the total impulse also decreases. The unsteady gas dynamics indicate that the internal flow field is affected by wave reflections from the mixture interface and the open tube end which in turn affect the thrust surface pressure history and the observed impulse. Experimental and numerical data from previous researchers along with new analysis presented here are used to evaluate the effect of partially filling a detonation tube. The limiting case of an infinite length tube is studied to predict the maximum specific impulse possible for a given explosive-inert gas combination.

3.2 Experimental and numerical data

The experimental data published prior to 2002 and the numerical data of Li and Kailasanath (2003) are plotted in Fig. 3.1 as a function of the fractional tube volume filled with the combustible mixture. This volume fraction V/V° is defined as the fill fraction, where V is the tube volume filled with the combustible mixture and V° is the total tube volume. To non-dimensionalize, the impulse I is divided by the impulse I° for a tube of equal total length and fully filled with the combustible mixture. The predictions of our single-cycle impulse model (Wintenberger et al., 2003) for a fully filled tube were used to normalize the experimental data of Zitoun and Desbordes (1999) since experimental data for I° were not available. In all cases, the tubes exhaust into air at 1 atm.

Sample pressure traces appear in Fig. 3.2(a) for a fully filled tube and in Fig. 3.2(b) for a partially filled tube with $V/V^0 = 0.625$. The y-axis of Figs. 3.2(a) and 3.2(b) are in units of pressure and distance. In each experiment, the pressure from the thrust surface and two intermediate distances along the tube length were recorded. These

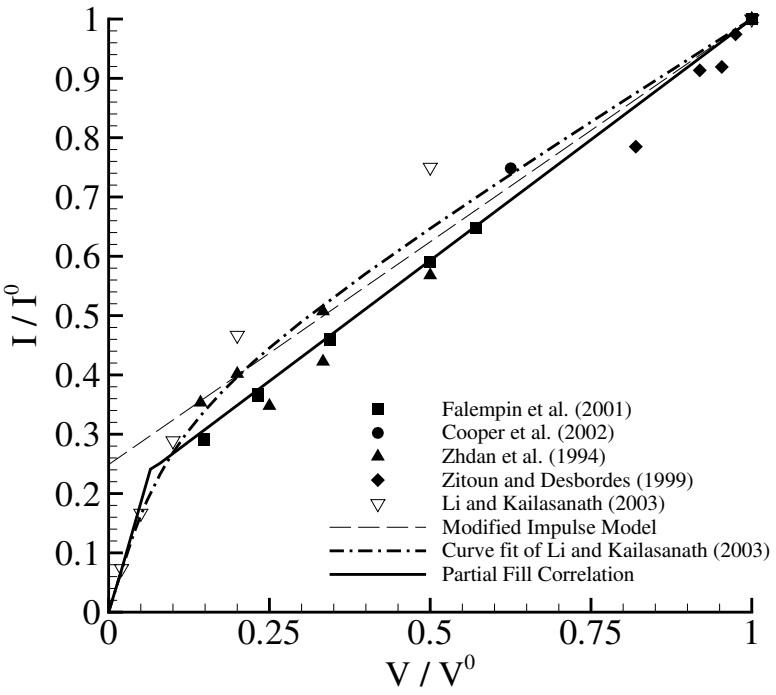

Figure 3.1: Normalized impulse I/I^0 from published data of Falempin et al. (2001), Cooper et al. (2002), Zhdan et al. (1994), Zitoun and Desbordes (1999), and Li and Kailasanath (2003) versus the fill fraction V/V^0 for tubes with constant cross-sectional area. The partial fill correlation discussed in §3.3.1.1, the curve fit of Li and Kailasanath (2003) discussed in §3.3.1.2, and the modified impulse model discussed in §3.3.2 are also plotted.

three different pressure histories have been offset along the y-axis by a distance equal to their location from the thrust surface in the experimental setup. Thus, the bottom trace corresponds the thrust surface pressure history, the middle trace corresponds to the pressure history approximately in the middle of the tube, and the top trace corresponds to the pressure just before the tube exit. The black squares correspond to time of combustion wave arrival at the ten ionization gauge locations down the tube length.

As shown in Fig. 3.1, the maximum impulse from a detonation tube is obtained by completely filling it with the explosive mixture. In other words, filling only a fraction of the tube volume with the explosive mixture results in obtaining only a fraction of the maximum possible impulse for that length tube. This total impulse I is affected by

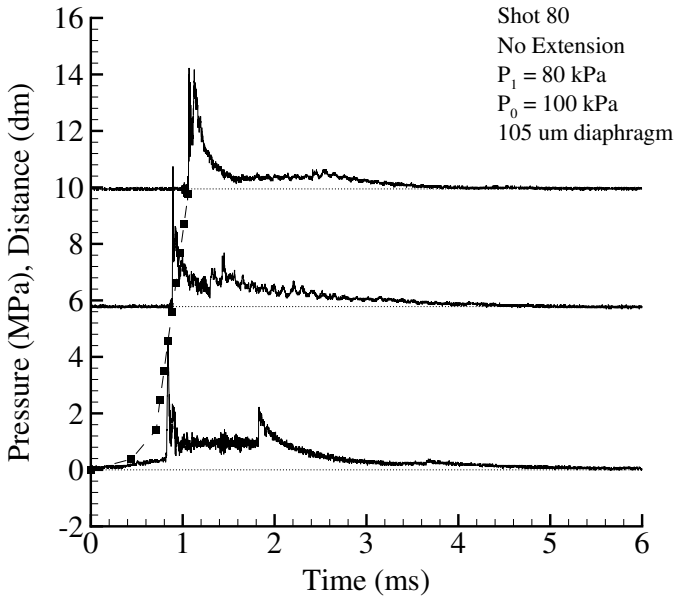

(a) Tube with no extension.

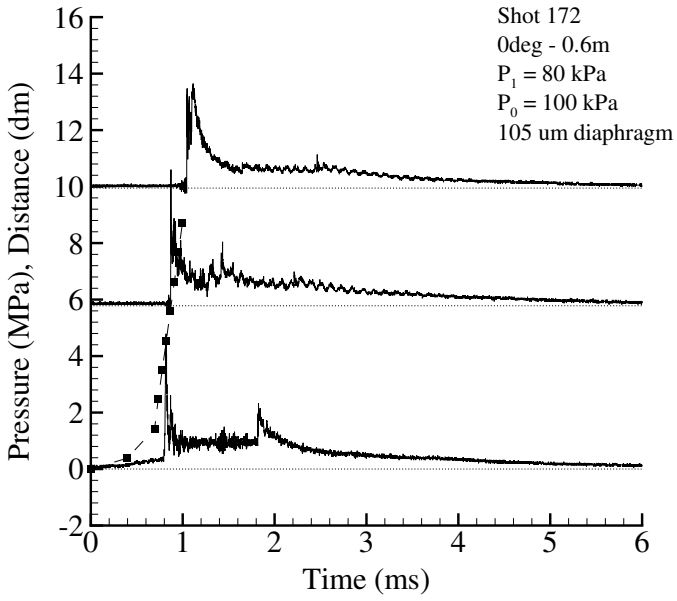

(b) Tube with a straight extension (0°-0.6 m).

Figure 3.2: Experimental pressure traces in ethylene-oxygen mixtures with an initial pressure of 80 kPa, environment pressure of 100 kPa and a 105 μm diaphragm. The black squares correspond to the combustion wave arrival time at each ionization gauge location.

the combined masses of the combustible mixture and the inert gases contained in the tube which vary as the fill fraction varies depending on their relative initial densities, $n = \rho_{mix}/\rho_{inert}$. For the experimental data discussed above, the densities of the combustible mixture (ethylene-oxygen or acetylene-oxygen at standard conditions) and inert gas (atmospheric air) are approximately equal ($n \approx 1$). This means that the total mass within a constant-length tube remains approximately constant regardless of fill fraction. By decreasing the amount of combustible mixture in the tube, a corresponding decrease in the stored chemical energy occurs decreasing the impulse imparted to the tube. A tube containing only inert gases (V/V^0=0) produces zero impulse since the stored chemical energy equals zero. A fully filled tube produces the maximum impulse since the useful stored chemical energy is maximized.

The impulse data of Fig. 3.1 are plotted in terms of the specific impulse in Fig. 3.3. The specific impulse is found to increase as the explosive mixture mass decreases indicating a specific performance increase even though the total impulse decreases. In the limit as the explosive mass tends to zero, the specific impulse ratio tends to a constant value as indicated by the numerical data of Li and Kailasanath (2003). This increase in specific impulse is attractive to designers who are concerned about fuel consumption and not concerned about device size limitations.

3.3 Models

In an effort to develop a unifying relationship for the impulse of a partially filled detonation tube, two correlations, modifications to our impulse model, and a mass-based model have been developed.

3.3.1 Curve fit to data

3.3.1.1 Partial Fill correlation

The partial-fill correlation shown in Figs. 3.1 and 3.3 is a piece-wise linear fit of the plotted data. It should be noted that the data on which this correlation is based

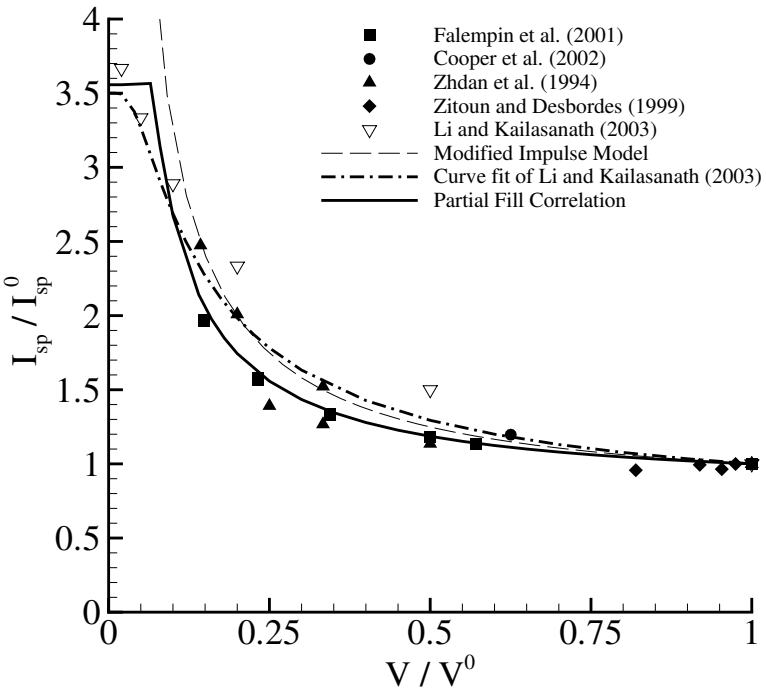

Figure 3.3: Normalized impulse I_{sp}/I^0_{sp} from published data of Falempin et al. (2001), Cooper et al. (2002), Zhdan et al. (1994), Zitoun and Desbordes (1999), and Li and Kailasanath (2003) versus the fill fraction V/V^0 for tubes with constant cross-sectional area. The partial fill correlation discussed in §3.3.1.1, the curve fit of Li and Kailasanath (2003) discussed in §3.3.1.2, and the modified impulse model discussed in §3.3.2 are also plotted.

were obtained in ethylene-oxygen mixtures except that of Zhdan et al. (1994) which were obtained in acetylene-oxygen mixtures. Zhdan et al. (1994) first suggested the existence of a correlation between impulse and fill fraction, but it was not until several years later that enough experimental data was available to fully validate the claim. The following discussion follows that of Cooper et al. (2002).

For the range of experimentally tested fill fractions ($0.15 < V/V^\circ < 1$), a linear relationship exists between the impulse fraction and the fill fraction

$$I/I^\circ = 0.814\,(V/V^\circ) + 0.186 \tag{3.1}$$

The experimental data lie within 15% of this line for that range of fill fractions.

Numerical simulations by Li and Kailasanath (2003) were used to determine the

behavior of the partial-fill correlation at fill fractions close to zero ($V/V^\circ < 0.15$) where experimental data was not available. They found that the impulse behavior near the origin in Fig. 3.1 can be approximated as

$$I/I^\circ = 3.560\,(V/V^\circ) \tag{3.2}$$

The intersection of these two linear relations, Eqs. (3.1) and (3.2), occurs at a fill fraction of 0.0676 determining the range of applicability for each equation.

Equations (3.1) and (3.2), written in terms of impulse, can be rewritten as the mixture-based specific impulse $I_{sp} = I/g\rho_1 V$ normalized by the specific impulse I°_{sp} of the fully filled tube (Fig. 3.3). The initial explosive mixture density is represented by ρ_1 and g is the standard gravitational acceleration. For $0.0676 < V/V^\circ < 1$

$$I_{sp}/I^\circ_{sp} = 0.814 + 0.186\,(V^\circ/V) \tag{3.3}$$

and for $0 < V/V^\circ < \ 0.0676$

$$I_{sp}/I^\circ_{sp} = 3.560 \tag{3.4}$$

Our partial-fill correlation in terms of specific impulse is compared to multi-cycle experiments by Schauer et al. (2001) in hydrogen-air mixtures (Fig. 3.4). Data were obtained for a variety of tube dimensions, fill fractions, and cycle frequencies. Impulse and thrust measurements were taken with a damped thrust stand and, for our correlation, we assume that multi-cycle operation is equivalent to a series of ideal single cycles. This data were not considered in the development of the partial fill correlation enabling an independent test to experimental data for validation purposes.

The fill fractions in Fig. 3.4 greater than one correspond to over-filling the detonation tube, and in this case, the *specific* impulse is reduced since only the mixture within the tube contributes to the impulse. The impulse I of an over-filled tube is equal to the impulse I° of a fully filled tube. This can be simply accounted for by

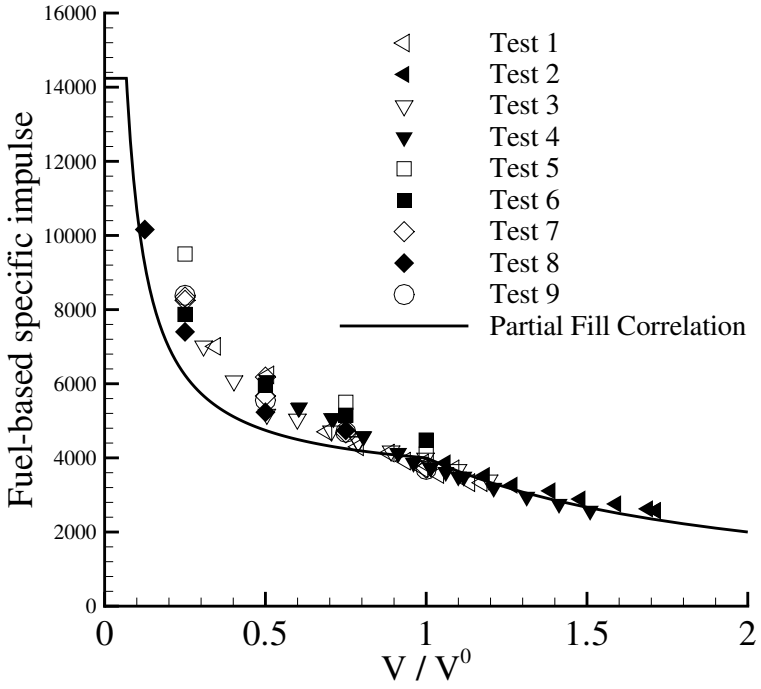

Figure 3.4: Comparisons between the fuel-based specific impulse for the partial-fill correlation and multi-cycle experimental data (Schauer et al., 2001) are plotted as a function of the volumetric fill fraction V/V^0.

computing the specific impulse as

$$I_{sp}/I^{\circ}_{sp} = \frac{I}{V}\frac{V^{\circ}}{I^{\circ}} = V^{\circ}/V \tag{3.5}$$

when $V/V^{\circ} > 1$. This relation is precise and valid for all fill fractions greater than one. The hydrogen-air experimental data is within 25% of the partial fill correlation for fill fractions less than one and within 10% for fill fractions greater than one.

The partial-fill correlation consists of the two relationships, Eqs. (3.1) and (3.2) for impulse or alternatively, Eqs. (3.3) and (3.4) for specific impulse. This correlation is empirical in nature and is derived from a limited amount of experimental and numerical data. However, it compares well with multi-cycle data over a wide range of fill fractions. Its advantages are that it is simple and in conjunction with our previous models of fully filled tubes (Wintenberger et al., 2003), provides a rapid means of estimating the ideal impulse of partially filled detonation tubes exhausting

into 1 atm air and $n \approx 1$.

3.3.1.2 Li and Kailasanath (2003)

Li and Kailasanath (2003) proposed a correlation for the specific impulse of partially filled tubes based on an exponential curve fit with data from their numerical simulations in ethylene-oxygen and ethylene-air mixtures

$$I_{spf}/I^{\circ}_{spf} = a - \frac{(a-1)}{exp\left(\frac{L^{\circ}/L - 1}{8}\right)} \tag{3.6}$$

The constant a is determined to have values between 3.2 and 3.5. They attribute these values to the maximum specific impulse available in the ethylene mixtures they analyzed as the value of L goes to zero. Their curve fit is based on a length ratio and not a volume ratio, but this difference is not important since presently we are analyzing only tubes with a constant cross-sectional area.

Equation (3.6) in terms of the volumetric fill fraction is compared with our partial-fill correlation in Fig. 3.1. Both relationships predict zero impulse at a fill fraction of zero as expected, and both tend to a constant specific impulse value in the limit of zero explosive mixture.

3.3.2 Modified impulse model

Previously, an impulse model that predicts the one-dimensional, unsteady gas dynamics within a fully filled detonation tube was developed by Wintenberger et al. (2003). An idealized thrust surface pressure history is calculated for the case where the environment pressure P_0 equals the initial combustible mixture pressure P_1 (Fig. 3.5) and the impulse is determined by integrating the area under the curve.

$$I = A\left[(P_3 - P_0)t_1 + (P_3 - P_0)t_2 + \int_{t_1+t_2}^{\infty} \Delta P(t)dt\right] \tag{3.7}$$

The terms of this integral are considered for the case of a partially filled detonation

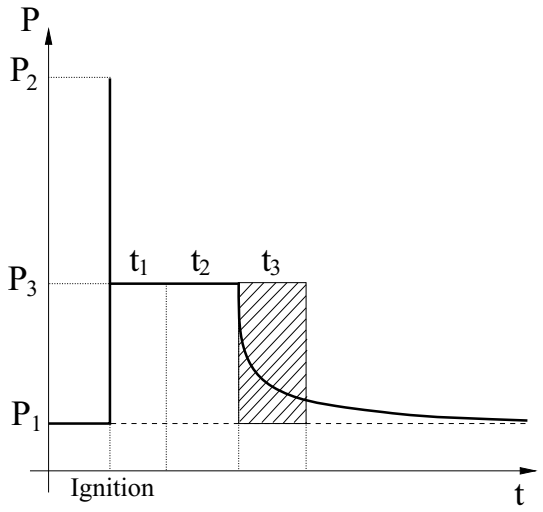

Figure 3.5: Idealized thrust surface pressure history modeled by Wintenberger et al. (2003) where the initial mixture pressure equals the environment pressure.

tube. The time $t_1 = L/U_{CJ}$ corresponds to the time required by the detonation wave to travel through the combustible mixture filling a length L of the tube with total length L^0.

$$I_{0\rightarrow t_1} = A(P_3 - P_0)L/U_{CJ} \tag{3.8}$$

The time t_2 corresponds to the time for the reflected wave from the mixture interface to reach the thrust surface. Because this time depends on the length of the tube filled with the combustible mixture L and the product sound speed behind the Taylor wave c_3, it can be scaled with a non-dimensional parameter α.

$$t_2 = \alpha L/c_3 \Rightarrow I_{t_1\rightarrow t_2} = A(P_3 - P_0)\alpha L/c_3 \tag{3.9}$$

This value of α can be analytically determined by tracking the first reflected characteristic of the Taylor wave and was found to be approximately 1.1 (Wintenberger et al., 2003) for a wide range of fuels and compositions.

After time t_2 the rate of pressure decay at the thrust surface is determined by the

environment pressure and the relative sound speeds in the gases.

$$I_{t_1+t_2\to\infty} = \int_{t_1+t_2}^{\infty} (P(t) - P_0)dt \tag{3.10}$$

As was previously done in the original impulse model, this pressure integral is non-dimensionalized in terms of c_3, $(P_3 - P_0)$, and here the total tube length L^0.

$$\int_{t_1+t_2}^{\infty} (P(t) - P_0)dt = \frac{(P_3 - P_0)L^0}{c_3} \int_{\tau_1+\tau_2}^{\infty} \Pi(\tau)d\tau \tag{3.11}$$

The non-dimensional integral on the right-hand side of Eq. 3.11 depends on the other non-dimensional parameters of the flow and is defined to equal β. In particular, in §3.4.2 we determine that both the ratio of the product sound speed to the environment sound speed, and the ratio of the product γ to the environment γ affect the pressure decay. Additionally, in §4.2 we determine that the pressure ratio P_3/P_0 affects the pressure decay.

$$\beta = \int_{\tau_1+\tau_2}^{\infty} \Pi(\tau)d\tau \tag{3.12}$$

For simplicity, we use the value of $\beta = 0.53$, determined (Wintenberger et al., 2003) by integrating the pressure decay history from experimental data of Zitoun and Desbordes (1999) for tubes containing an initial mixture of stoichiometric ethylene-oxygen exhausting into atmospheric air. It is assumed a constant value of β suffices for fuel-air detonations over a limited range of compositions close to stoichiometric (Wintenberger et al., 2003) and this assumption is revised in the next chapter.

With the value of β, a characteristic time t_3 is defined and represents the hatched region in Fig. 3.5 where

$$\int_{t_1+t_2}^{\infty} (P(t) - P_0)dt = (P_3 - P_0) = (P_3 - P_0)\beta\frac{L^0}{c_3} \tag{3.13}$$

The components of the impulse integral, Eq. 3.8 from $0 < t < t_1$ and Eq. 3.9 from $t_2 < t < t_2$ and Eq. 3.13 from $t_1 + t_2 < t < t_3$, are summed to yield the total impulse as a function of the tube length filled with the combustible mixture L and the total

tube length L^0.

$$I = \frac{V(P_3 - P_0)}{U_{CJ}} \left[1 + \alpha \frac{U_{CJ}}{c_3} + \beta \frac{L^0}{L} \frac{U_{CJ}}{c_3} \right] \tag{3.14}$$

Here the volume V is the tube volume filled with the combustible mixture. For constant cross-sectional tubes as considered here, the length fraction L/L^0 in Eq. 3.14 can be replaced with the volumetric fill fraction V/V^0.

The terms in the brackets of Eq. 3.14 are labeled as the model parameter K. In the original impulse model, K is a constant value of 4.3 (Wintenberger et al., 2003). In the case of a partially filled tube, the value of K changes with the fill fraction (Fig. 3.6).

$$K = \left[1 + \alpha \frac{U_{CJ}}{c_3} + \beta \frac{U_{CJ}}{c_3} \frac{L^0}{L} \right] \tag{3.15}$$

The initial mixture pressure and environment pressure are equal in this calculation as is the case with the experimental data considered in this chapter. In Chapter 4 we evaluate the behavior of K when $P_0 \neq P_1$.

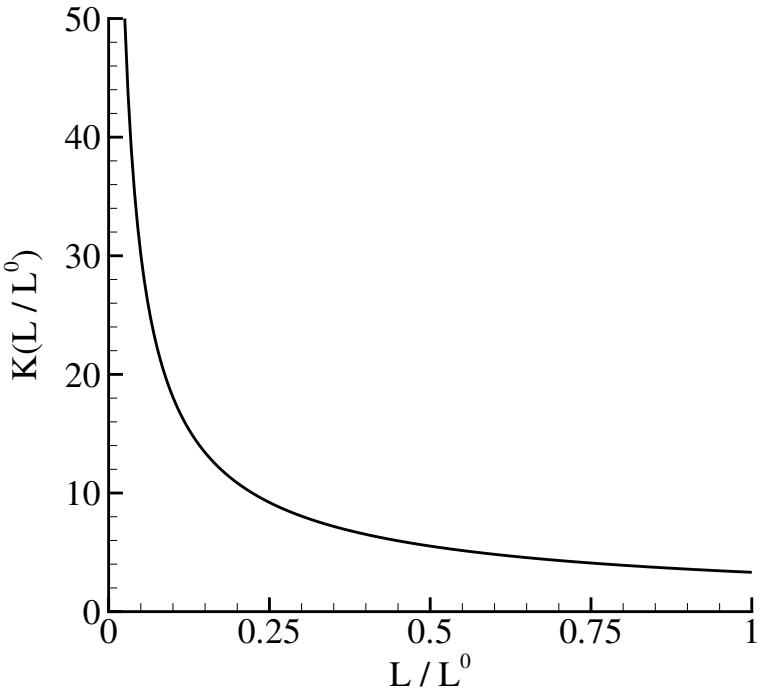

Figure 3.6: Variation of model parameter K for partially filled tubes that have $P_0 = P_1$ exhausting into atmospheric pressure as a function of the fill fraction.

The impulse Eq. 3.14 is divided by the original impulse model (Wintenberger et al., 2003) and is plotted in Fig. 3.1.

$$I/I^0 = \frac{V}{V^0}\frac{\left[1+\alpha\frac{U_{CJ}}{c_3}+\beta\frac{U_{CJ}}{c_3}\frac{L^0}{L}\right]}{\left[1+(\alpha+\beta)\frac{U_{CJ}}{c_3}\right]} \tag{3.16}$$

The model represents the decrease in impulse as the fill fraction decreases. However, the model predicts a value of $I/I^0 \approx 0.2$ at a fill fraction of zero which is clearly not correct.

The mixture-based specific impulse is determined in the usual fashion.

$$I_{sp} = \frac{I}{V\rho_1 g} = \frac{(P_3 - P_0)}{\rho_1 g U_{CJ}}\left[1+\alpha\frac{U_{CJ}}{c_3}+\beta\frac{U_{CJ}}{c_3}\frac{L^0}{L}\right] \tag{3.17}$$

Dividing by the original impulse model (Wintenberger et al., 2003) for a fully filled tube, the specific impulse fraction is determined and is plotted in Fig. 3.3.

$$I_{sp}/I^0_{sp} = \frac{\left[1+\alpha\frac{U_{CJ}}{c_3}+\beta\frac{U_{CJ}}{c_3}\frac{L^0}{L}\right]}{\left[1+(\alpha+\beta)\frac{U_{CJ}}{c_3}\right]} \tag{3.18}$$

The model represents the increase in the mixture-based specific impulse as the fill fraction decreases. However, the model approaches infinity as the fill fraction approaches zero. Numerical simulations indicate that the specific impulse should become finite as the fill fraction approaches zero. To understand the partial fill effect better, we consider energy conservation in the following sections.

3.3.3 Energy considerations

While the previous correlations and impulse model do characterize trends in the data, more insight can be gained by applying some elementary principles of mechanics. A control volume is drawn around the partially filled tube (Fig. 3.7) and we predict the impulse from the average velocity of the exhaust gases. As labeled in Fig. 3.7, the

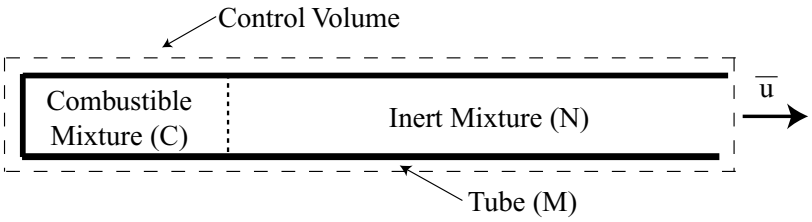

Figure 3.7: Illustration of partially filled detonation tube with a control volume.

initial mass of the combustible mixture is C, the mass of the inert gas, also called the tamper, is N and the tube mass is M. From these three masses, two mass ratios can be defined and are used in the following discussions. The tamper mass ratio N/C is the ratio of the tamper mass to the combustible mixture mass and the tube mass ratio M/C is the ratio of the tube mass to the combustible mixture mass.

The combustible mixture has a constant amount of stored chemical energy E per unit mass. We assume that all of this chemical energy is converted into kinetic energy of the exhaust gases. The exhaust gases consist of the product gases and the inert gases.

$$CE = (N + C)\overline{u}^2/2 \tag{3.19}$$

Analysis of the x-direction forces on the control volume equate the impulse to the momentum of the exhaust gases if they are assumed to be pressure matched to the ambient conditions.

$$I = \int F dt = (N + C)\overline{u} \tag{3.20}$$

As in the rocket engine analysis of § 1.4.1, the specific impulse is related to the velocity of the exhaust gases.

$$I_{sp} = \frac{\overline{u}}{Cg} = [\sqrt{2E(N/C + 1)}]/g \tag{3.21}$$

This simple analysis based on first principle for the specific impulse of a partially filled tube (Eq. 3.21) is observed to depend on two quantities. The first is a parameter $\sqrt{2E}$ that is a measure of the useful stored chemical energy in the system and has units of velocity. The quantity E is commonly referred to as the Gurney energy

(Gurney, 1943). The Gurney energies of high explosives are well known from carefully conducted experiments and can be easily approximated with simple relations that depend on the explosive's detonation parameters (Kennedy, 1998). However, these relations are not applicable for the gaseous mixtures used in PDE situations. To further complicate matters, the energy available for mechanical work is often sensitive to variations in initial density, temperature, and degree of confinement (Cooper, 1996). Several analytical methods have been proposed to predict the energy E for gaseous detonations. One method uses traditional thermodynamic cycle analysis with the Jacobs cycle (Fickett and Davis, 1979) for a detonation to predict the maximum possible work. A second method analyzes a detonation and associated Taylor wave expansion after it has propagated an arbitrary distance down a tube that is closed at one end. Summing the total thermal and kinetic energy of the fluid particles from the closed tube end to the instantaneous detonation location yields the total energy of the detonation. Both of these methods were first proposed by Jacobs (1956) and are discussed in greater detail in Cooper and Shepherd (2002) and Wintenberger (2004). The second parameter of importance in Eq. 3.21 is the explosive mass fraction $C/(N+C)$. This parameter is used in §3.3.4 to correlate the experimental data and models into a single relationship for the effect of partial filling.

A similar relationship to Eq. 3.21 was obtained by Back and Varsi (1974) in analyzing their experimental results detonating a charge of high explosive in nozzles filled with inert substances of different densities and pressures. They studied the feasibility of detonative propulsion in the high-pressure environments of other planets. Unlike the constant cross-sectional area detonation tubes we consider, they measured the impulse imparted to a conical diverging nozzle with a flat end wall. The entire nozzle assembly was submerged in a tank so that the type and pressure of the substance surrounding their device could be varied. Gaseous environments of nitrogen, helium, air, and carbon dioxide with pressures ranging from 1 bar up to 69 bars were tested. The impulse measurements were obtained by measuring the maximum vertical displacement of the device due to the exhausting product and inert gases. They observed an increase in specific impulse as the environment pressure increased for the higher

molecular weight gases (CO_2, N_2, Air). At the lower environment pressures tested, the difference in the specific impulse values for the different gases were negligible.

The specific impulse for these two limiting cases can be evaluated with Eq. 3.21. One limit is reached when the mass of the inert environment is significantly smaller than the explosive mass, as in the case of a near fully filled tube or a partially filled detonation tube containing a low-density inert gas. The tamper mass fraction approaches zero ($N/C \rightarrow 0$), the average exhaust gas velocity is maximized (from Eq. 3.19),

$$\overline{u}_{(N/C \rightarrow 0)} = \sqrt{2E} \tag{3.22}$$

and the specific impulse approaches a constant (from Eq. 3.21).

$$I_{sp_{(N/C \rightarrow 0)}} = \sqrt{2E}/g \tag{3.23}$$

A different limit exists when the inert gas mass is significantly greater than the initial explosive mass, as in the case of a near empty tube or a partially filled detonation tube containing a high-density inert gas. The tamper mass fraction N/C becomes large causing the average exhaust gas velocity to become small (from Eq. 3.19).

$$\overline{u}_{(N/C \text{ large})} = \sqrt{2EC/N} \tag{3.24}$$

Although the exhaust gas velocity becomes small, it is the exhaust gas momentum that influences the impulse and as the tamper mass increases, so does their momentum.

$$(N + C)\overline{u} \approx N\overline{u} = \sqrt{2ENC} \tag{3.25}$$

When considered on a unit mass basis, the specific impulse increases as the tamper mass increases.

$$I_{sp_{(N/C \text{ large})}} = \sqrt{2EN/C}/g \tag{3.26}$$

If we consider the extreme limiting case where the tamper mass fraction approaches infinity, the average exhaust gas velocity approaches zero, and the specific impulse

approaches infinity. We will show later in §3.4.2 that the specific impulse actually does not approach infinity but in fact reaches a finite value. Understanding the tamper compressibility is crucial to finding the limiting specific impulse in this case.

3.3.3.1 Gurney model

The previous energy considerations are extremely simplified for application to a partially filled detonation tube, and in particular do not account for motion of the tube. The chemical energy released by detonation not only goes into accelerating the product gases and the tamper, but also into accelerating the tube mass. The ideas previously developed can be extended to cover this case. This derivation follows the work of Gurney (1943) who used both energy and momentum conservation to predict the terminal velocities of metal fragments propelled by detonation of high explosives. Gurney's original ideas have been applied to many different geometries including open-faced, symmetric, and asymmetric sandwiches, cylindrical, spherical, and grazing detonation which are discussed in Kennedy (1998) and Henry (1967).

The situation we consider for application to a partially filled detonation tube is that which contains three masses; the explosive mixture mass C, the tamper mass N, and the tube mass M. The explosive is sandwiched between the tube and tamper as illustrated in Fig. 3.8 and has an initial density ρ_0. The explosive contains a constant

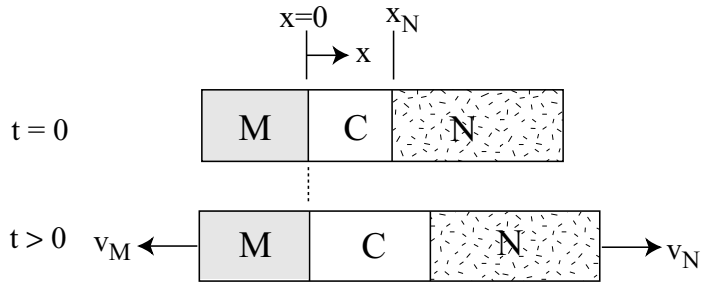

Figure 3.8: Schematic of asymmetric sandwich.

amount of chemical energy E per unit mass. To simplify the analysis, the tube and tamper mass are modeled as rigid plates (Gurney, 1943) so that simultaneously solving the energy and momentum equations will yield their terminal velocities.

For times greater than zero, the high-pressure detonation products expand, applying a force to the tube and the tamper "plates," driving them apart (Fig. 3.8). The numerous wave reflections within the expanding product gases are assumed (Kennedy, 1998) to occur very fast as compared to the plate velocities resulting in a constant velocity gradient and spatially uniform, but time-dependent density $\rho = \rho(t)$. After a long time, the plates reach their terminal velocities v_M and v_N.

The conservation of momentum is

$$0 = -Mv_M + Nv_N + \rho_0 \int_0^{x_N} v(x')dx' \tag{3.27}$$

and the approximate conservation of energy is

$$CE = 1/2Mv_M^2 + 1/2Nv_N^2 + 1/2\rho_0 \int_0^{x_N} v(x')^2 dx' \tag{3.28}$$

where the internal energy of the detonation product gas is neglected. The velocity profile in the detonation products is assumed (Kennedy, 1998) to be a linear function of position between the tube and tamper masses.

$$v(x) = (v_M + v_N)x/x_N - v_M \tag{3.29}$$

Solving Eqs. 3.27-3.29 yields the terminal velocity v_M of the tube mass which is found to be a function of the previously defined Gurney velocity $\sqrt{2E}$, the tamper mass ratio N/C, and the tube mass ratio M/C (Kennedy, 1998). This is also equal to the impulse normalized by the tube mass which is plotted as a function of the two mass ratios in Fig. 3.9.

$$\frac{v_M}{\sqrt{2E}} = \frac{I}{M\sqrt{2E}} = \left[\sqrt{(1+A^3)/[3(1+A)] + (N/C)A^2 + (M/C)}\right]^{-1} \tag{3.30}$$

where

$$A = (1 + 2M/C)/(1 + 2N/C) \tag{3.31}$$

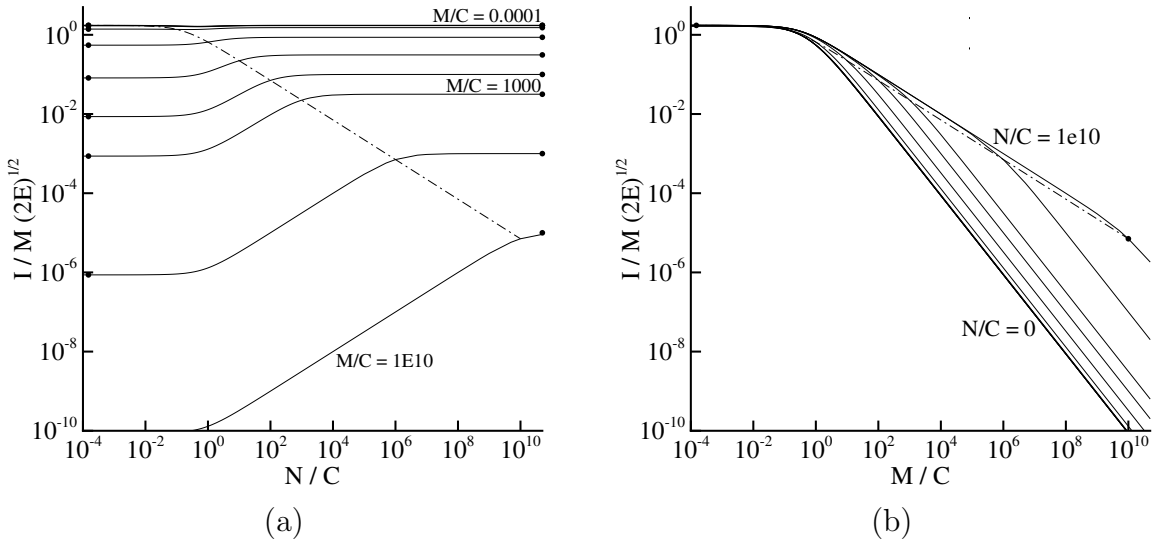

Figure 3.9: Impulse $I/M\sqrt{2E}$ predictions with the Gurney model versus (a) the tamper mass ratio N/C and (b) the tube mass ratio M/C.

The effect of increasing the tamper mass ratio N/C while the tube mass ratio M/C remains constant is shown. Starting from very small values of the tamper mass ratio N/C in Fig. 3.9a, increasing N/C does not affect the impulse until this ratio is approximately one. When the tamper mass ratio N/C increases above a value of one, the impulse increases to a value which depends on the tube mass fraction M/C. For example, increasing the tamper mass ratio N/C from 1 to 100 causes a greater increase in impulse if the tube mass ratio M/C is large (i.e., > 1000) whereas a very small (negligible) increase in impulse is observed if the tube mass ratio is small (i.e., < 1000). Once the tamper mass ratio N/C has increased to equal the tube mass ratio M/C, resulting in the situation of a symmetric sandwich, no additional gains in impulse occur if the tamper mass ratio continues to increase. In other words, for a given tube mass ratio, the impulse can be increased by adding tamper mass but the impulse is maximized when the tamper is large enough such that its mass ratio N/C equals the tube mass ratio M/C. These same observations can be made through inspection of Fig. 3.9b plotted as a function of the tube mass ratio M/C.

The maximum value for the impulse in the limit of infinite N/C and fixed M/C

ratios is evaluated from Eq. 3.30. From the definition of A,

$$A \approx (M/C)/(N/C) \rightarrow 0 \quad \text{as} \quad N/C \rightarrow \infty \tag{3.32}$$

and a Taylor series expansion of Eq. 3.30 about $A = 0$ yields a finite maximum value.

$$I/M\sqrt{2E} \cong (1/3 + M/C)^{-1/2} \tag{3.33}$$

We compare Eq. 3.33 to the symmetric sandwich solution for the impulse (Eq. 3.34), which can be derived from Eqs. 3.27-3.29 assuming that $M = N$.

$$I/M\sqrt{2E} = (1/3 + 2M/C)^{-1/2} \tag{3.34}$$

The impulse for a symmetric sandwich (Eq. 3.34) is plotted as the dashed line Fig. 3.9a,b. The maximum impulses for infinitely tamped asymmetric sandwiches (Eq. 3.33) are plotted as dots for the different M/C ratios in Fig. 3.9a.

The other limit for the impulse occurs at $N/C = 0$ and is plotted as dots in Fig. 3.9a for very small N and the different tube mass ratios. A final limiting case to consider is when both mass ratios, N/C and M/C, approach infinity simultaneously. In this case A approaches one and a Taylor expansion of the impulse equation for an assymetrical sandwich yields a leading order solution of

$$I/M\sqrt{2E} = (1/3 + N/C + M/C)^{-1/2} \tag{3.35}$$

Equation 3.35 is plotted as a single point at a mass ratio of $N/C = M/C = 1E10$ in Fig. 3.9b and is only slightly different than the above limit of infinite N/C at fixed M/C (Eq. 3.33).

The impulse plots of Fig. 3.9 are plotted in Fig. 3.10 in terms of specific impulse.

$$I_{sp}/\sqrt{2E} = I/C\sqrt{2E} = I/M\sqrt{2E}(M/C) \tag{3.36}$$

This scaling reorders the relationship of impulse in Fig. 3.10 as compared to

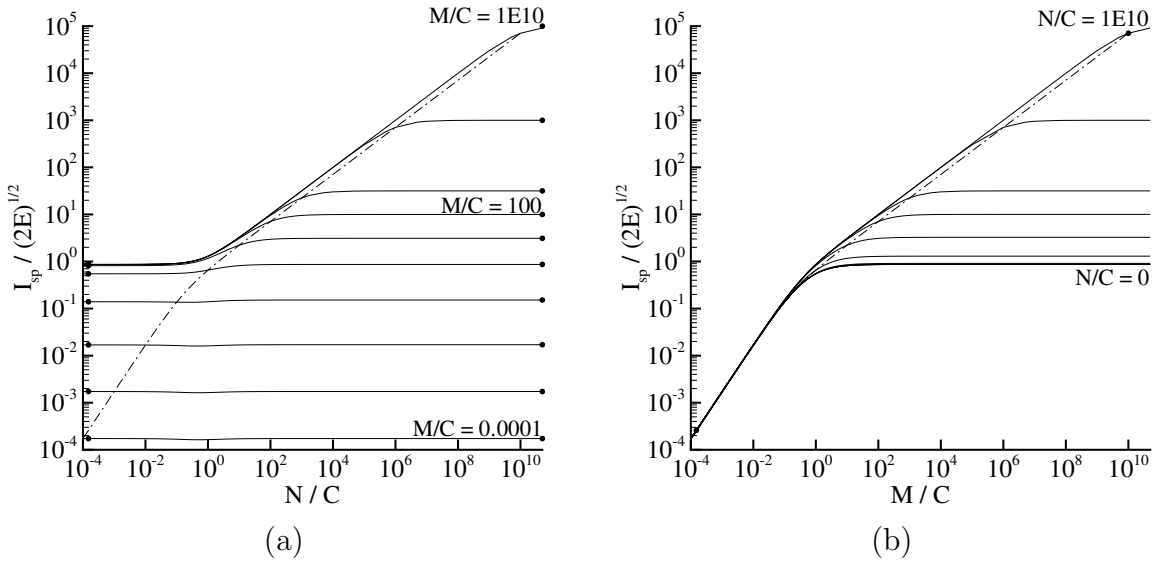

Figure 3.10: Specific impulse $I_{sp}/\sqrt{2E}$ predictions with the Gurney model versus (a) the tamper mass ratio N/C and (b) the tube mass ratio M/C.

Fig. 3.9. The symmetric sandwich solution is plotted by dashed line and the limiting values at N/C ratios of zero and infinity at the different values of M/C are shown by the solid dots. The specific impulse is unaffected by changes in N/C until it exceeds a value of one. For larger N/C ratios, the specific impulse increases until N/C equals the tube mass ratio M/C. When the two mass ratios are equal, the specific impulse is maximized at a value that agrees with the Taylor series analysis at infinite N/C and fixed M/C.

In the plots of impulse (Fig. 3.9) and specific impulse (Fig. 3.10), the results depend on the constant energy per unit mass of the explosive E. This dependence on the explosive's energy can be removed by normalizing the impulse (specific impulse) by the impulse I^0 (specific impulse I^0_{sp}) when the tamper mass equals zero. The results of this normalization appear in Fig. 3.11 as a function of the different mass ratios.

The results of Fig. 3.11 show that the normalized impulse fraction I/I^0 and the specific impulse fraction I_{sp}/I^0_{sp} are identical and the dependence on M/C and N/C is interchangeable. Increasing the tamper mass, increasing the tube mass, or decreasing the explosive mass have no effect of the impulse until the mass ratios N/C or M/C

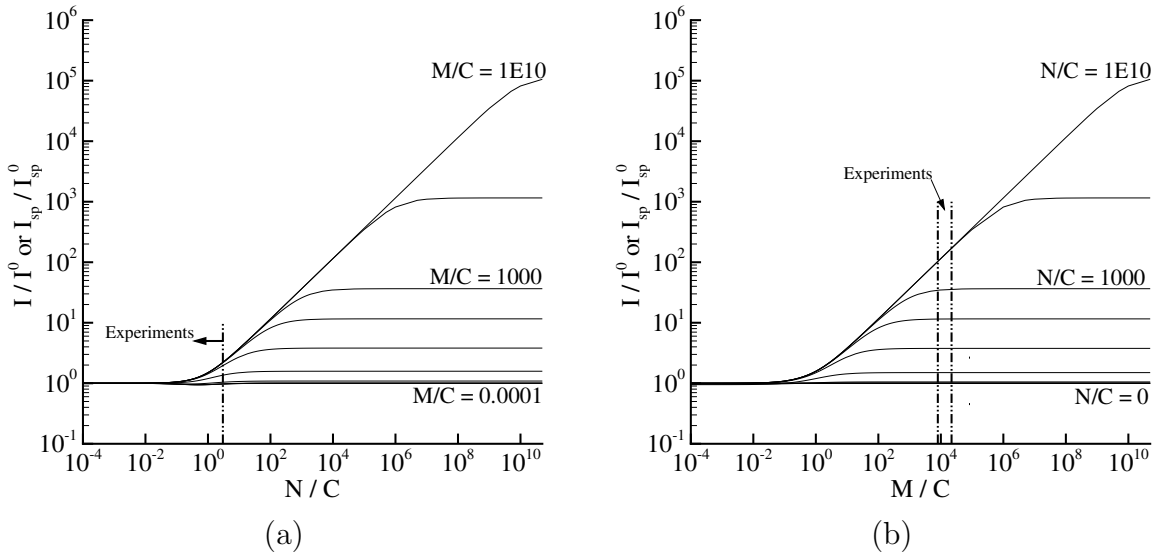

Figure 3.11: I/I^0 and I_{sp}/I°_{sp} predictions with the Gurney model versus (a) the tamper mass ratio N/C and (b) the tube mass ratio M/C.

are greater than one. At a constant tamper mass ratio (Fig. 3.11a) or a constant tube mass ratio (Fig. 3.11b), the largest gains in impulse are achieved for the largest mass ratios. In our experiments, the tube mass varied between approximately 12 kg and 32 kg. The explosive mixture mass of the stoichiometric ethylene-oxygen mixtures varied between approximately 1.5 g to 5.8 g depending on its initial pressure. This implies tube mass ratios M/C were between approximately 8,000 and 22,000. In our experiments, an extension 0.6 m in length was used with atmospheric air as the tamper. Thus, the tamper mass ratios N/C varied between 0 and 3.

Values of N/C and their effect on the specific impulse fraction are tabulated in Table 3.1 for our experimental range in tube mass ratios M/C. For either value of

M/C	N/C	I/I^0 or I_{sp}/I^0_{sp} (Fig. 3.11)	M/C	N/C	I/I^0 or I_{sp}/I^0_{sp}(Fig. 3.11)
8000	∞	103	22000	∞	171
8000	7E4	98	22000	2E5	162
8000	75	10	22000	75	10
8000	18.5	5	22000	18.5	5
8000	2.5	2	22000	2.5	2

Table 3.1: Specific impulse fraction predicted with Gurney model for range of M/C ratios in our experiments.

M/C, the impulse can be increased up to 10 times by adding a tamper with a mass of 75 times C. The more reasonable tamper mass ratios (up to $N/C \approx 2.5$) that could be obtained with air at standard conditions in a modest length extension (3 m) added to our tube would result in only doubling the impulse over the case without a tamper. So while the partial fill effect seems to have limited benefit for the smaller scale laboratory facilities, the concept is important to propulsive applications where sufficiently large tamper mass ratios are possible. Detonation propulsion in high-density environments would benefit from higher tamper mass ratios N/C without requiring large nozzles or extensions to contain the tamper. This is the motivation behind the work by Back and Varsi (1974) in which they studied detonative propulsion in very high pressure environments in order to predict engine performance in the atmosphere of Jupiter.

For the situations of moderately sized laboratory detonation tubes and the gaseous explosive mixtures, the M/C ratios are essentially infinite when compared to realistic tamper mass ratios (Table 3.1).

3.3.4 Comparison of models

Figures 3.9 through 3.11 were generated by varying one independent mass ratio while the other independent mass ratio is fixed. Varying both mass ratios simultaneously and independently defines a three-dimensional surface. To apply these results to the situation of a detonation tube, both the tube mass ratio and the tamper mass ratio vary as the volumetric fill fraction varies. It is the relative changes of these two mass ratios that defines a path on this three-dimensional surface enabling a direct comparison of the mass-based models to the partial fill data in terms of volumetric fill fraction.

The relationship between the masses and fill fractions depend on the density ratio

$n = \rho_{mix}/\rho_{inert}$ between the combustible and inert gases.

$$C = \rho_{mix} V \tag{3.37}$$

$$M/C = \left(\frac{M}{\rho_{mix} V^{\circ}}\right) \frac{V}{V^{\circ}} \tag{3.38}$$

$$N/C = \frac{\rho_{air}}{\rho_{mix}} \left(\frac{V^{\circ}}{V} - 1\right) = n \left(\frac{V^{\circ}}{V} - 1\right) \tag{3.39}$$

Because in this chapter we analyze only the data of partially filled tubes exhausting into an inert gas environment at 1 atm, different density ratios n are obtained for a given explosive mixture by changing the tamper type (i.e. helium, nitrogen, air, or carbon dioxide). For the experimental data mentioned in §3.1, the relative density ratios are approximately one (Table 3.2).

Explosive	Inert gas	n
C_2H_4-O_2	Air	1.08
C_2H_2-O_2	Air	1.06
C_2H_4-Air	Air	1.00
C_2H_2-Air	Air	1.00
H_2-O_2	He	3.00
H_2-O_2	Air	0.42

Table 3.2: Density ratios for several explosive-inert gas combinations currently investigated. All explosive and inert gases were considered to be at 1 atm, 300 K.

The mass-based Gurney model is plotted (Fig. 3.12) in terms of the equivalent volumetric fill fraction for different values of n and compared to the initial results of Fig. 3.1. Also shown are additional numerical (Sato et al., 2004) and experimental (Kasahara, 2003) data that have recently become available. The scatter in the experimental data, numerical data, and the predicted curves for different values of n clearly shows that a correlation based on the volumetric fill fraction is only valid for one specific explosive-inert gas combination. The original volumetric partial fill correlation was primarily based on experimental data of ethylene-oxygen mixtures exhausting into atmospheric air but some data used in the correlation were from acetylene-oxygen mixtures exhausting into air. From Table 3.2, the two explosive-inert combinations have a density ratio of 1.0 and so the dependence of the partial

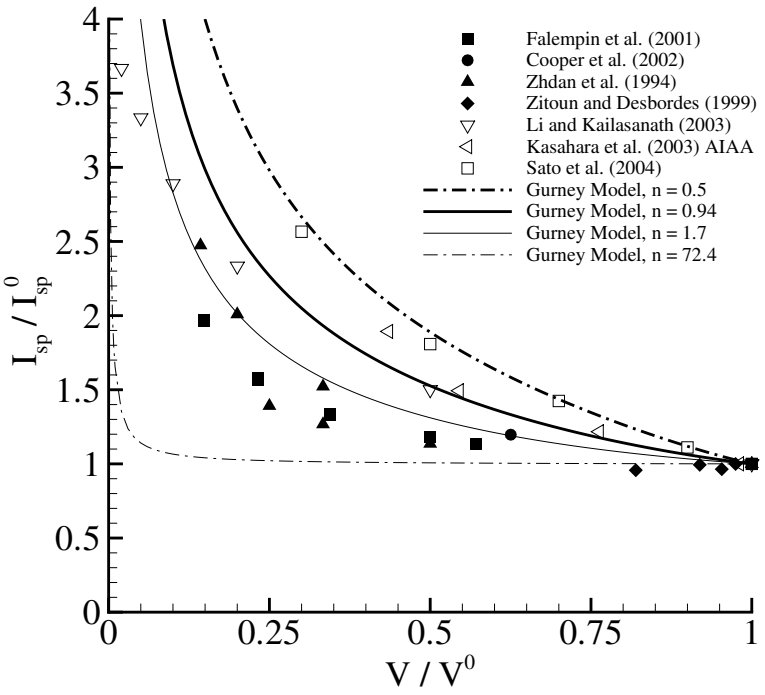

Figure 3.12: Specific impulse fraction versus fill fraction for all mixtures.

fill effect on the explosive-inert gas *combination* was not initially identified.

Instead of plotting in terms of a volume fraction, the same data of Fig. 3.12 is plotted in Fig. 3.13 in terms of the mass fraction $C/(N+C)$ using Eqs. 3.37-3.39 for the conversion. Also plotted is the Gurney model where now the curves for different values of n collapse onto a single curve. The scatter in the experimental data is reduced but not eliminated and all the data lie below the ideal curve of the Gurney model. In the laboratory experiments, heat transfer to the tube walls and other unsteady gas dynamic processes not accounted for in the Gurney model act to reduce the impulse below the ideal case.

The Gurney model is a useful correlation but fails in the limit where the volumetric fill fraction and the mass fraction approach zero. This deficiency is corrected in the next section.

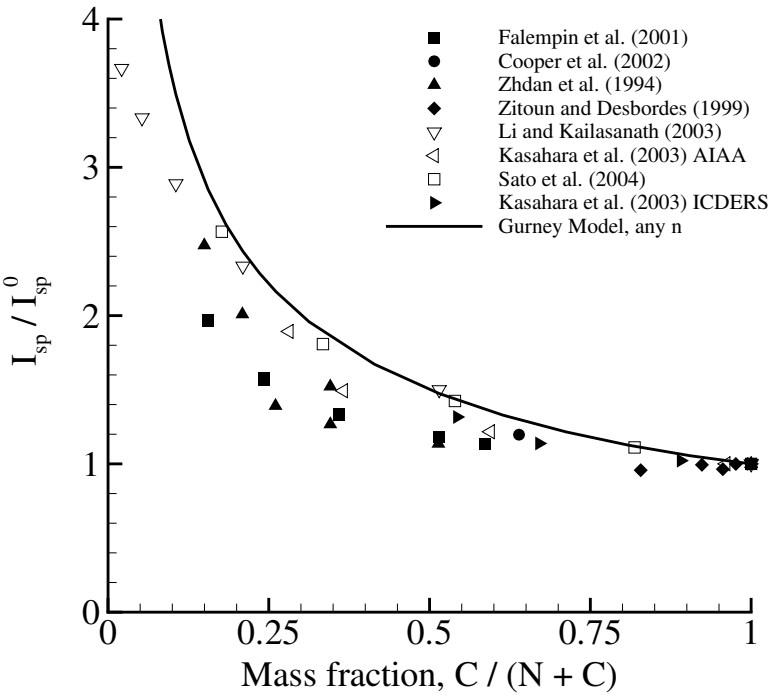

Figure 3.13: Specific impulse fraction versus mass fraction

3.4 Gas dynamic effects

The previous models do not correctly predict the partial fill effect in the limit as $N/C \rightarrow 0$. The failure occurs because nonsteady gas dynamics and relative gas compressibility dominate in this regime. Several previous studies have attempted to modify the Gurney model to account for gas compressibility, but these have only been applied to open sandwiches where the one-dimensional wave dynamics are solved for in the high explosive. Jones et al. (1980) extended the initial work of Gurney to include the product gas equation of state in the energy equation. An ordinary differential equation for the plate motion could be derived and solved for the acceleration and plate position over time. These results for an open sandwich configuration can be compared to an exact analytical solution by Aziz et al. (1961). In his study, a block of high explosive is bounded on one end by a plate. The detonation is initiated at the other end. Aziz et al. (1961) analyzes the one-dimensional gas dynamics of the detonation reflecting off of the explosive-plate interface assuming a product equation

of state equal to $E = Pv/(\gamma - 1)$ where an exact solution using the method of characteristics is found for a γ of 3. A finite difference calculation is conducted for other values of γ between 2.5-3.5. Comparison between the exact solution of Aziz et al. (1961) and the simplified calculation of the Gurney model by Jones et al. (1980), both for a product γ of 3, yield similar histories for the plate motion but a difference of approximately 15% in the predicted terminal velocity. Jones et al. (1980) conclude that, for the case of an open sandwich, the assumptions regarding the product gas energy are at least as good as the Gurney model assumptions to obtain the terminal velocity.

The conclusions of Aziz et al. (1961) are similar to the initial conclusions of Gurney in that the plate motion does not depend strongly on the detonation parameters or product gas gamma. The final plate velocity is found to depend almost entirely on the initial chemical energy of the explosive and the ratio of explosive mass to plate mass. Fickett (1987) rescaled the equations of Aziz et al. (1961) in order to determine a simpler explicit solution for all values of gamma. He observed the same effect of the detonation parameters, product gamma, and explosive mass to plate mass ratio.

A study by Duvall et al. (1969) analyzed a similar open sandwich, explosive-plate configuration but in their case the plate to be driven was spaced an arbitrary distance from the high explosive and was of variable size. The gas dynamics were analyzed using the method of characteristics and the force on the plate was determined from a simple drag formula. The terminal velocity of the plate was found to increase as the acceleration parameter Q increased. When a rigid backing was applied to the side of the explosive opposite of the plate, the terminal velocity of the plate increased over the case with no backing on the explosive.

In the present application, it is more important to include the wave processes in the tamper. We do that in the next section with the development of an analytical model of an expanding bubble that highlights the effect of the tamper compressibility. Special attention is paid to determining the specific impulse in the limit of zero explosive.

3.4.1 Modeling a compressible tamper

To effectively model the situation of a partially filled detonation tube, the compressibility of both the explosive products and tamper gas in an asymmetric sandwich must be considered. To do this, we use a simplified analysis of the unsteady gas dynamics in the explosive products and tamper gas. The goal of this model is to predict the thrust surface pressure decay as a function of the product and inert gas thermodynamic states.

Consider an infinitely long tube that is partially filled to a distance X_{CV} from the thrust surface with the initial explosive substance as illustrated in Fig. 3.14. This

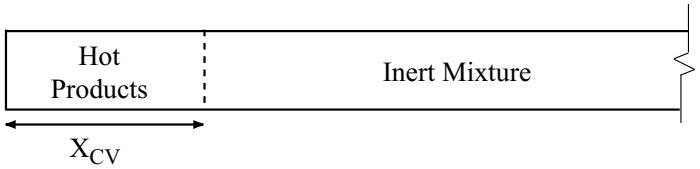

Figure 3.14: Schematic for analysis of an expanding "bubble" of hot products in an infinite length tube.

situation models the limit of a nearly empty tube where the open end is far from the mixture interface or equivalently, a very thin layer of explosive in a finite length tube; $N/C \rightarrow \infty$ in either case. This configuration eliminates the reflections from the open end such that the dynamics of the expanding products are independent of the events associated with the area change at the tube exit. We refer to this as the "bubble" model in analogy to the one-dimensional models of gas bubbles in liquids (Brennen, 1995, Shepherd, 1980), which are the inspiration for this approach. A characteristic length scale is determined from the initial length X_{CV} filled with the explosive mixture. A characteristic time T is defined by scaling with the inert gas sound speed c_0.

$$T = X_{CV}/c_0 \tag{3.40}$$

This can be used to define a non-dimensionalized time $\tau = t/T$.

An additional simplification is to assume the combustion products are obtained by constant volume combustion instead of a propagating detonation wave. If a deto-

nation wave propagates through a closed volume, after multiple wave reflections the products have no fluid motion and have thermal energy equal to that of constant volume combustion. This was verified with Amrita (Quirk, 1998) simulations carried out by Wintenberger (2004). We apply this to our bubble situation assuming that multiple wave reflections have occurred, yielding constant volume combustion conditions before significant motion of the contact surface begins. Thus, a large pressure difference ΔP between the combustion products and the inert gas mixture initially exists and the product gas expansion can be written as a function of this initial pressure difference as it decays in time.

$$P(\tau) = \Delta P f(\tau) \tag{3.41}$$

Evaluating the impulse requires integrating the pressure decay over time

$$I = A \int_0^\infty P(t)dt = AT \int_0^\infty P(\tau)d\tau = AT\Delta PF \tag{3.42}$$

where

$$F = \int_o^\infty f(\tau)d\tau \ . \tag{3.43}$$

The specific impulse is determined by normalizing the impulse with the initial mass of the combustible mixture.

$$I_{sp} = \frac{\Delta PF}{g\rho_{CV}c_0} \tag{3.44}$$

As long as $P(t)$ decays faster than $1/t$, the integrated pressure decay function F and the specific impulse will be finite. If this is the case, then this model will enable us to determine a finite value for impulse in the limit of zero fill fraction, unlike the results of the Gurney model or the modified impulse model.

3.4.2 Analysis of expanding bubble with 1-D gas dynamics

The situation of an expanding "bubble" of products is analyzed in more detail with one-dimensional nonsteady gas dynamics. The hot products just after constant vol-

ume combustion are defined to be at pressure P_{CV}, density ρ_{CV}, and have a specific heat ratio of γ_{CV}. The inert gas initial conditions are pressure P_0, density ρ_0, and specific heat ratio γ_0. The initial position of the mixture interface is located a distance X_{CV} from the tube's thrust surface which is located at $X = 0$.

As time increases, the hot products expand into the region previously filled with the inert gases. This process is illustrated on the distance-time diagram of Fig. 3.15. Acoustic waves are assumed to reverberate sufficiently rapidly between the solid thrust

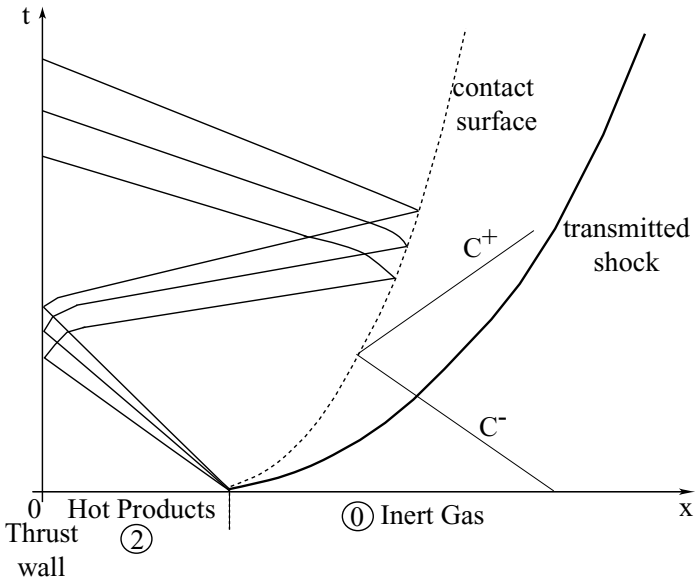

Figure 3.15: Distance-time diagram for expanding hot products from constant volume combustion in a partially filled tube.

surface and the contact surface, so that the pressure in the hot products is assumed to be spatially uniform. After time $t = 0$, the hot products expand, transmitting a shock wave into the inert mixture. The contact surface between the post-shock inert gas and the hot products follows behind the shock wave, slowing down at a faster rate than the shock decays. An expansion wave, centered at the initial location of the mixture interface, propagates towards the thrust surface accelerating the hot products away from the thrust surface. We assume that the transmitted shock is weak so that the Riemann invariant remains constant on the C^- characteristic from the undisturbed inert mixture ahead of the shock to the contact surface behind the

shock.

The speed of the propagating contact surface is related to the thermodynamic state at the interface by the Riemann invariant J^- on the C^- characteristic.

$$u - 2c/(\gamma_0 - 1) = -2c_0/(\gamma_0 - 1) \tag{3.45}$$

Assuming a weak leading shock, we approximate the compression as isentropic in order to relate the sound speed to the pressure at the interface.

$$P/P_0 = (c/c_0)^{2\gamma_0/(\gamma_0 - 1)} \tag{3.46}$$

Substituting back into Eq. 3.45 results in an ordinary differential equation for the contact surface position as a function of the hot gas pressure.

$$u = \frac{dx}{dt} = \frac{2c_0}{\gamma_0 - 1}\left[\left(\frac{P/P_{CV}}{P_0/P_{CV}}\right)^{2\gamma_0/(\gamma_0 - 1)} - 1\right] \tag{3.47}$$

To relate the time-varying pressure P at the contact surface to the initial pressure of the expanding hot products P_{CV}, we assume isentropic expansion of the hot products.

$$Px^{\gamma_{CV}} = P_{CV}X_{CV}^{\gamma_{CV}} \tag{3.48}$$

Substituting this into Eq. 3.47 for P/P_{CV} results in a differential equation for the instantaneous contact surface location x.

$$dx/dt = 2c_0/(\gamma_0 - 1)\left[(x/X_{CV})^{\gamma_{CV}(1-\gamma_0)/2\gamma_0}\,(P_{CV}/P_0)^{(\gamma_0 - 1)/2\gamma_0} - 1\right] \tag{3.49}$$

This equation is scaled based on the non-dimensional parameters $\mathcal{X} = x/X_{CV}$ and $\tau = c_0 t/X_{CV}$ to obtain

$$d\mathcal{X}/d\tau = 2/(\gamma_0 - 1)\left[\mathcal{X}^{\gamma_{CV}(1-\gamma_0)/2\gamma_0}\,(P_{CV}/P_0)^{(\gamma_0 - 1)/2\gamma_0} - 1\right] \tag{3.50}$$

The solution $\tau(x)$ can be written in terms of an integration since the variables are

separable.

$$\tau = \int_0^{\tau} d\tau' = (\gamma_0 - 1)/2 \int_1^{\mathcal{X}} \frac{d\mathcal{X}'}{(\mathcal{X}')^{\gamma_{CV}(1-\gamma_0)/2\gamma_0} \left(P_{CV}/P_0\right)^{(\gamma_0-1)/2\gamma_0} - 1} \tag{3.51}$$

Equation 3.51 was numerically integrated using Mathematica for all times until the contact surface remains stationary. This is represented as a vertical line in the distance-time plane. Sample contact surface trajectories are shown in Fig. 3.16 for initial pressure ratios P_{CV}/P_0 of 13 and 25 between the hot products and inert gases. Also investigated were variations in γ_{CV}. The γ_0 in the inert gas was always assumed to be that of air and equal to 1.4. A total of 36 cases were analyzed where γ was either 1.0, 1.1396, or 1.4 and the initial pressure ratios varied between 2 and 100. The

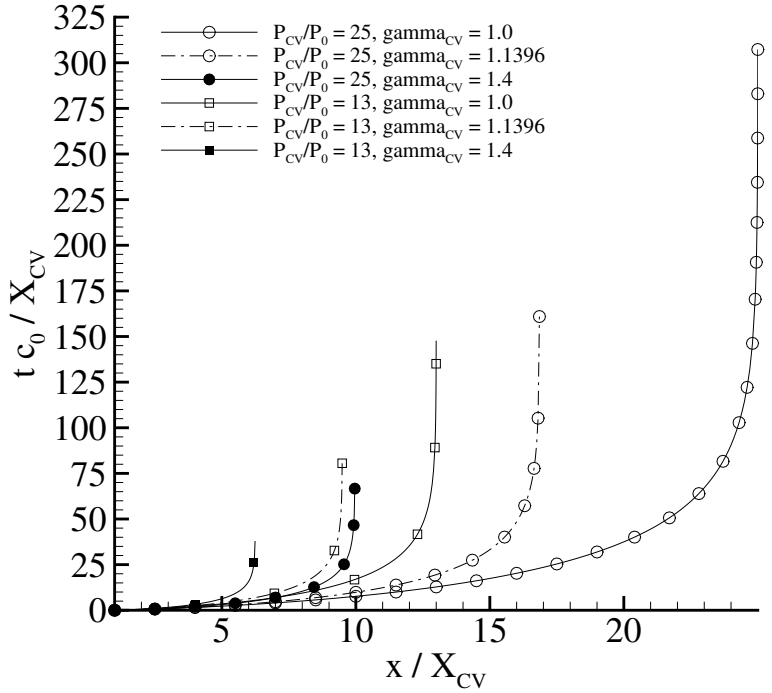

Figure 3.16: Distance-time diagram illustrating contact surface trajectory of the boundary between the expanding hot products and the inert gases.

pressure decay as a function of time plotted for the initial pressure ratios of 13 and 25 appear in Fig. 3.17 and were determined from Eq. 3.48 once the contact surface trajectory is known.

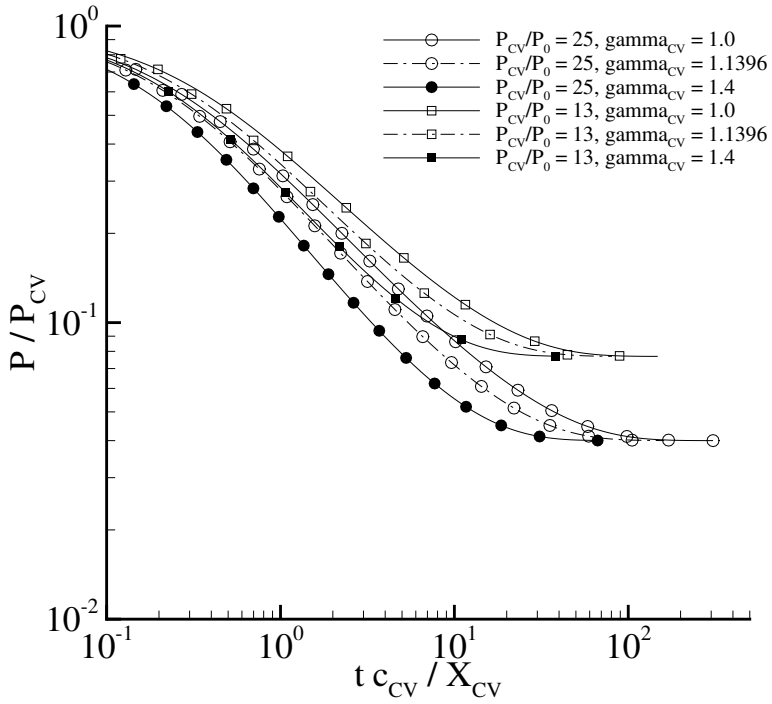

Figure 3.17: Pressure-time diagram illustrating pressure decay of hot products as a function of initial pressure ratio and product gamma.

Integration of this pressure decay over time yields the predicted impulse.

$$\begin{aligned} I &= P_{CV} A \int_0^\infty (P/P_{CV} - P_0/P_{CV})\, dt \\ &= \frac{P_{CV} A X_{CV}}{c_0} \int_0^\infty (P/P_{CV} - P_0/P_{CV})\, d\tau \end{aligned} \tag{3.52}$$

$$I_{sp} = \frac{P_{CV}}{c_0 \rho_{CV} g} \int_0^\infty (P/P_{CV} - P_0/P_{CV})\, d\tau \tag{3.53}$$

The integral in Eq. 3.53,

$$F(\infty) = \int_0^\infty (P/P_{CV} - P_0/P_{CV})\, d\tau \tag{3.54}$$

is plotted as a function of the initial pressure ratio P_{CV}/P_0 for values between 1 and 100 and values of γ_{CV} of 1.0, 1.1396, and 1.4 in Fig. 3.18. In all cases, $F(\infty)$ is finite. It is noted that Eq. 3.53 for the specific impulse has the same functional form

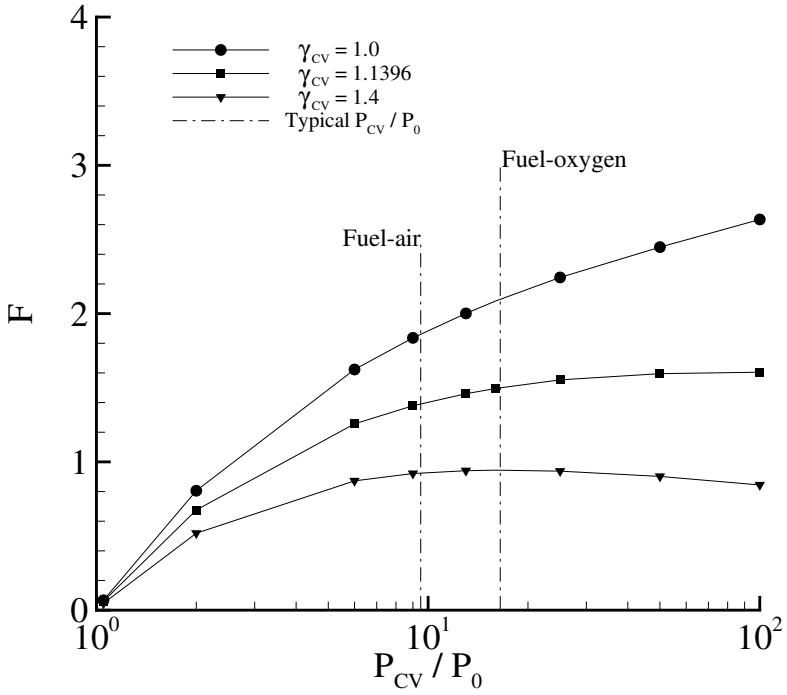

Figure 3.18: Non-dimensional pressure integral as a function of the initial pressure ratio and product gamma.

as the dimensional analysis result of Eq. 3.44 given earlier. Because of the sound speed relation $c^2 = \gamma P/\rho$, the maximum specific impulse in the limit of an infinitely long tube can be expressed in terms of the sound speed ratio between the products and inert gases.

$$I_{sp} = \frac{c_{CV}}{c_0} \cdot \frac{c_{CV}}{g} \frac{1}{\gamma_{CV}} F(\infty) \tag{3.55}$$

Increasing the tamper gas sound speed relative to the product gas sound speed results in decreasing the maximum specific impulse because the pressure decays at a faster rate. If the combustion products and tamper are initially at the same pressure $P_{CV} = P_0$, then Eq. 3.55 can be written in terms of densities.

$$I_{sp} = \frac{\rho_0}{\rho_{CV}} \cdot \frac{F(\infty)}{g} \sqrt{\frac{P_0}{\gamma_0 \rho_0}} \tag{3.56}$$

Now, we see the same dependence on impulse due to the relative densities as in the

Gurney model analysis where an increase in the density of the tamper results in increasing the maximum specific impulse.

To determine the limiting specific impulse for an arbitrary explosive-inert combination, the relationship of Eq. 3.55 is used along with Fig. 3.18 for the non-dimensional pressure integrals. The constant volume combustion parameters, c_{CV} and γ_{CV}, for the mixtures considered were calculated with Stanjan (Reynolds, 1986) and the results are tabulated in Table 3.3. The predictions of the maximum specific impulse for a given

Explosive	Inert gas	c_{CV}/c_0	γ_{CV}	P_{CV}/P_0	$F(\infty)$	I_{sp}/I°_{sp}
C_2H_4-O_2	Air	3.55	1.132	16.6	1.53	3.68
C_2H_2-O_2	Air	3.63	1.144	17.0	1.49	3.65
C_2H_4-Air	Air	2.78	1.163	9.34	1.36	2.73
C_2H_2-Air	Air	2.83	1.155	9.71	1.37	2.77
H_2-O_2	Air	4.29	1.124	9.56	1.45	4.46

Table 3.3: Limiting fraction of specific impulse as the explosive mixture mass goes to zero for partially filled tubes exhausting into 1 atm air. The explosive initial conditions were pressure 100 kPa, 300 K. The inert gas was air at 1 atm, 300 K. The predictions of Wintenberger et al. (2003) were used for the fully filled impulse value I°_{sp}.

explosive-inert gas combination are plotted in Figs. 3.19-3.21 for ethylene-oxygen, ethylene-air, and hydrogen-oxygen combustible mixtures with available experimental and numerical data. It should be noted that the maximum impulse predictions from the "bubble" model are valid for the limit when $C/(N+C) \rightarrow 0$. However, in Figs. 3.19-3.21 the maximum impulse predictions are shown to span the range of explosive mass fractions from zero until reaching the Gurney model predictions. This method results in overestimating the impulse for a small range of mass fractions for the mixtures investigated, as illustrated by comparisons with the numerical predictions of Li and Kailasanath (2003) in Fig. 3.19. However, extending the range of application for the "bubble" model predictions enables a prediction to be made for all explosive mass fractions from zero to one.

These tabulated values of the maximum specific impulse are the limiting results for the impulse when the effect of gas compressibility dominates. In the other regime,

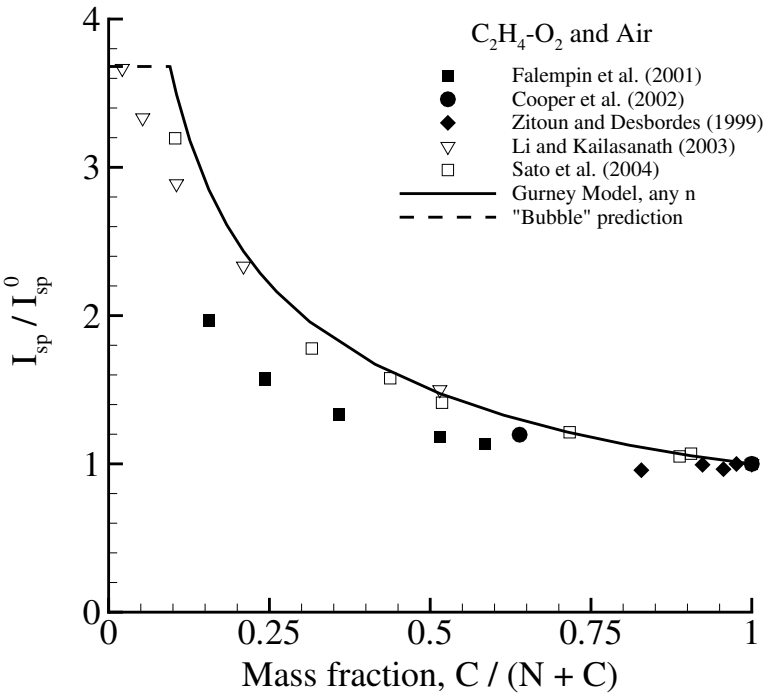

Figure 3.19: Comparison of "bubble" model predictions with the available experimental and numerical data for ethylene-oxygen mixtures exhausting into air.

the momentum and energy conservation dominate and the Gurney model can be used for estimates. There is some transition region at low mass fractions (and also low fill fractions) where the impulse lies somewhere between the two cases. This can be determined by full gas dynamic simulations or experiments.

3.5 Summary

This chapter has examined the issue of predicting the impulse of partially filled detonation tubes with a constant cross-sectional area exhausting into 1 atm environments. Using experimental and numerical data for tubes partially filled with a variety of fuel and oxidizer combinations, the effect of partial filling can be correlated to the relative densities of the explosive mixture and the inert mixture. Estimates of the impulse imparted to the detonation tube as a function of the tube mass, explosive mass, and inert gas mass were generated using the energy and momentum conservation and

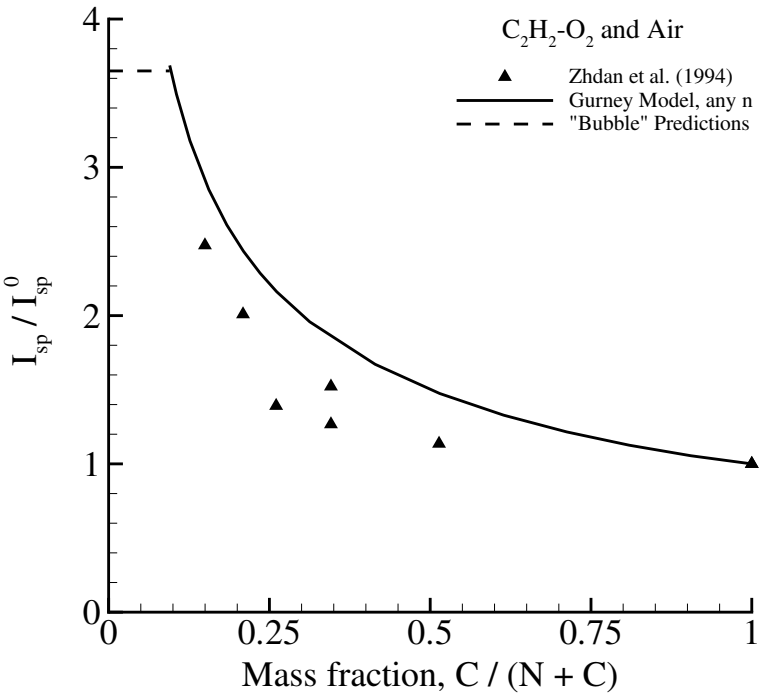

Figure 3.20: Comparison of "bubble" model predictions with the available experimental and numerical data for acetylene-oxygen mixtures exhausting into air.

following the analysis of Gurney (1943). A unifying relationship exists between the predictions of the Gurney model and the experimental data when plotted on a mass basis. Different explosive and inert combinations can be represented by a single value of the density ratio and for an arbitrary initial mass fraction within the tube, the impulse can be predicted. This model successfully correlates data over a range of explosive and inert gas mixtures. While we have currently only considered partially filled tubes exhausting into atmospheric conditions, it is possible that the analysis could be extended to treat higher or lower pressure environments.

The Gurney model does fail in the limit of zero explosive mixture, where the nonsteady gas dynamics and the compressibility of the inert gas should be considered. An analytical model of an expanding "bubble" of products demonstrates that the specific impulse reaches a limiting value for a range of product γ's and initial pressure ratios expected in detonation tubes. To accurately determine the maximum specific impulse, this value would have to be numerically simulated or experimentally

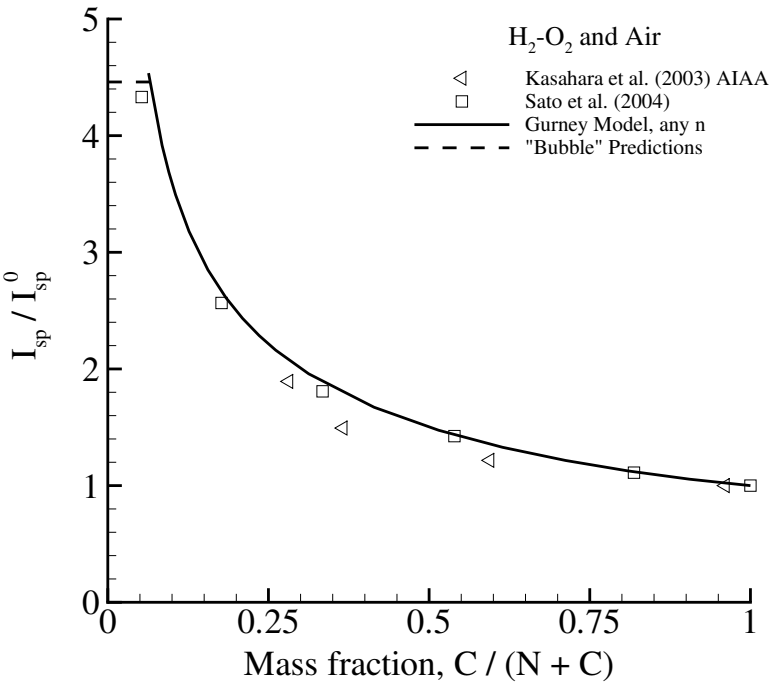

Figure 3.21: Comparison of "bubble" model predictions with the available experimental and numerical data for hydrogen-oxygen mixtures exhausting into air.

measured under these conditions and will depend on the specific explosive-inert gas combination. An upper bound to this value was predicted with the bubble analysis for partially filled tubes exhausting into atmospheric air and matches very well with the available experimental and numerical data.

Chapter 4

Fully filled tubes at sub-atmospheric conditions

4.1 Introduction

The impulse of a fully filled detonation tube exhausting into sub-atmospheric environments is experimentally investigated. The tube was filled with a stoichiometric mixture of ethylene-oxygen and no extension or nozzle was attached. These experiments measured impulse as a function of environment pressure in order to establish the baseline performance for the later purpose of quantifying the effect of nozzles.

Operation of a practical PDE is expected to extend over a range of altitudes implying that the detonation products will exhaust into sub-atmospheric pressures. Variations in pressure between 100 kPa and 1.4 kPa simulates altitudes from sea level up to 29 km. Under these varying environment conditions, the nozzle is expected to affect the detonation tube impulse but quantitative data are lacking. Historically, single-cycle ballistic pendulum experiments have been instrumental in quantifying the maximum impulse obtained for a specific operating condition which, until now, have only investigated in-tube parameters such as the initial pressure, equivalence ratio and diluent of the explosive mixture, internal obstacle configurations, and ignition sources. We have carried out the first experimental study to measure single-cycle impulse as a function of the environment pressure. This contribution to the PDE community supplies critical data demonstrating the effect of the environment conditions on the

impulse.

4.2 Modified impulse model

We return to our previous discussion of the modified impulse model in §3.3.2, now considering cases where the tube is fully filled $L = L^0$ and the initial mixture pressure P_1 does not equal the environment pressure P_0. The idealized thrust surface pressure history is illustrated in Fig. 4.1 and the impulse is determined by integrating the area under the curve but the result differs from that of Eq. 3.14.

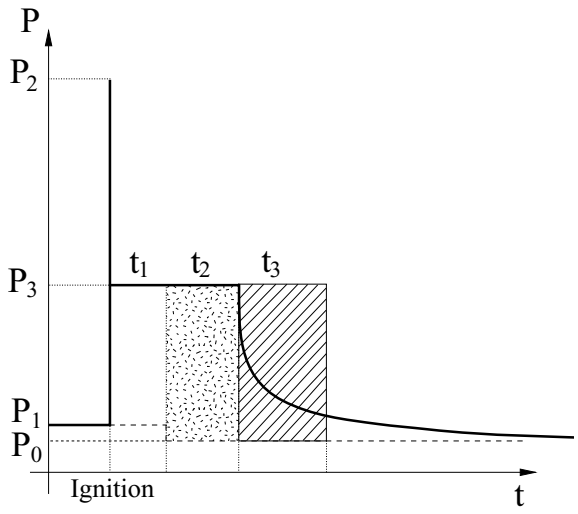

Figure 4.1: Idealized thrust surface pressure history for tubes with P_1 not equal to P_0.

To understand, we return to the control volume analysis from which the impulse integral is derived and analyze it with regard to our laboratory experiments. We consider the same control volume as before (Fig. 4.2) where a time varying pressure $P(t)$ is applied to one side of the thrust surface and the environment pressure P_0 is applied to the other side. In the laboratory setup, a diaphragm is used to seal the combustible mixture inside the tube. The control surface passes through this diaphragm, which will have a pressure differential across it if $P_1 \neq P_0$.

Before mixture ignition, the tube is not moving so the impulse must be zero.

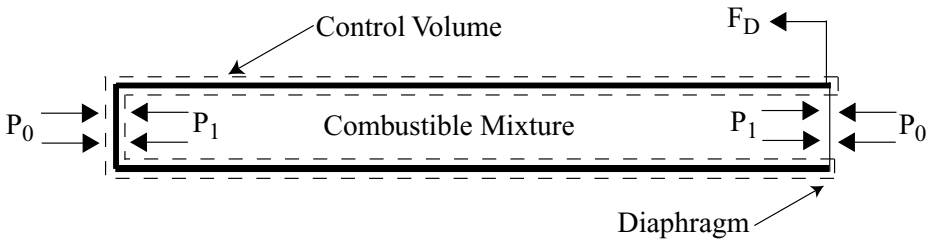

Figure 4.2: Illustration of detonation tube control volume when the initial combustible mixture is sealed inside the tube with a diaphragm at the open end.

Integration of the thrust surface pressure differential alone yields a non-zero impulse. This discrepancy is because of the force provided by the diaphragm that must be considered. When the diaphragm is present, it generates a force on the control volume that is equal to the pressure differential acting across the thrust surface.

$$I = 0 = \int (P_1 - P_0)dt + F_D \qquad \Rightarrow \qquad F_D = -\int (P_1 - P_0)dt \tag{4.1}$$

Even after mixture ignition, the force F_D still acts on the control volume until the detonation wave reaches the open end and bursts the diaphragm. The time $t_1 =$

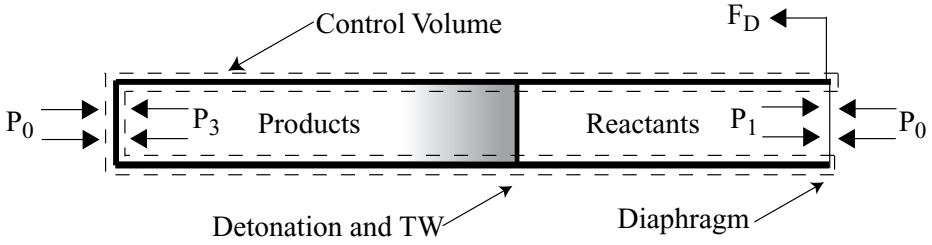

Figure 4.3: Illustration of detonation tube control volume when the initial combustible mixture is sealed inside the tube with a diaphragm and the detonation wave has not reached the open end.

L/U_{CJ} corresponds to the time required by the detonation wave to travel through the combustible mixture. So, the impulse integral from ignition at $t = 0$ to the time when the diaphragm breaks is

$$I_{t_1} = \int_0^{t_1} (P_3 - P_0)dt + F_D = \int_0^{t_1} (P_3 - P_1)dt \tag{4.2}$$

After time t_1 and before the time t_2, the thrust surface pressure history can be integrated directly.

$$I_{t_1 \rightarrow t_1+t_2} = \int_{t_1}^{t_1+t_2} (P_3 - P_0)dt = (P_3 - P_0)t_2 \tag{4.3}$$

The time t_2 corresponds to the time for the reflected wave from the mixture interface (also the open end of the tube) to reach the thrust surface and is scaled with a non-dimensional parameter α as was done in §3.3.2.

$$t_2 = \alpha L / c_3 \tag{4.4}$$

The value of α depends only on the parameters behind the Taylor wave which are not affected by changes in P_0 (see §2.6.2) so the constant value of 1.1 (Wintenberger et al., 2003) previously determined for a wide range of fuels and compositions is still valid here.

After time t_2 the rate of pressure decay at the thrust surface is determined by the environment pressure and the relative sound speeds in the gases.

$$I_{t_1+t_2 \rightarrow \infty} = \int_{t_1+t_2}^{\infty} (P(t) - P_0)dt \tag{4.5}$$

As was previously done in the original impulse model, this pressure integral is non-dimensionalized in terms of c_3, $P_3 - P_0$, and the length L.

$$\int_{t_1+t_2}^{\infty} (P(t) - P_0)dt = \frac{(P_3 - P_0)L}{c_3} \int_{\tau_1+\tau_2}^{\infty} \Pi(\tau)d\tau \tag{4.6}$$

The non-dimensional integral on the right-hand side of Eq. 4.6 depends on the other non-dimensional parameters of the flow and is defined to equal β_{LP}.

$$\int_{t_1+t_2}^{\infty} (P(t) - P_0)dt = (P_3 - P_0)\beta_{LP}\frac{L}{c_3} = (P_3 - P_0)t_3 \tag{4.7}$$

With the value of β_{LP}, a characteristic time t_3 is defined that represents the hatched

region in Fig. 4.1. In §3.3.2 the pressure decay integral was assumed to have a constant value of $\beta = 0.53$ (Wintenberger et al., 2003). As the environment pressure decreases, the blow down time should increase. To account for this increase in time t_3, the corresponding values β_{LP}, and K_{LP} should also increase. Our experimental data in this chapter shows this to be the case.

The components of the impulse integral, Eq. 4.2 from $0 < t < t_1$ and Eq. 4.3 from $t_1 < t < t_1 + t_2$ and Eq. 4.7 from $t_1 + t_2 < t < t_1 + t_2 + t_3$, are summed to yield the total impulse as a function of P_3/P_1 and P_0/P_1.

$$I = \frac{V(P_3 - P_0)}{U_{CJ}} \left[\frac{(P_3 - P_1)}{(P_3 - P_0)} + \alpha \frac{U_{CJ}}{c_3} + \beta_{LP} \frac{U_{CJ}}{c_3} \right] \tag{4.8}$$

Here the volume $V = AL$ is the tube volume filled with the combustible mixture.

The terms in the brackets of Eq. 4.8 are labeled as the model parameter K_{LP}.

$$K_{LP} = \left[\frac{(P_3 - P_1)}{(P_3 - P_0)} + \alpha \frac{U_{CJ}}{c_3} + \beta_{LP} \frac{U_{CJ}}{c_3} \right] \tag{4.9}$$

The measured impulse values from Fig. 4.7 and 4.9 were used along with the measured values of U_{CJ} and P_3 from Tables 2.8 and 2.9 to determine the relationship of K_{LP}. The values of K_{LP} are plotted in Fig. 4.4 without error bars and in Fig. 4.5 with error bars.

$$K_{LP} = \frac{I_V U_{CJ}}{(P_3 - P_0)} \tag{4.10}$$

Also plotted by the dotted curve is the previously documented constant value of $K = 4.3$ determined by Wintenberger et al. (2003).

The scatter in the data of Figs. 4.4 and 4.5 correspond to the different diaphragm thicknesses. The open symbols correspond to the 25 μm diaphragm, the solid black symbols correspond to the 51 μm diaphragm, and the grey symbols correspond to the 105 μm diaphragm. A curve fit through the data of Fig. 4.4(a) yields a relationship between K_{LP} and the pressure ratio P_0/P_1 which is plotted by the solid line. Alternatively, a relationship between K_{LP} and the pressure ratio P_3/P_0 is shown in

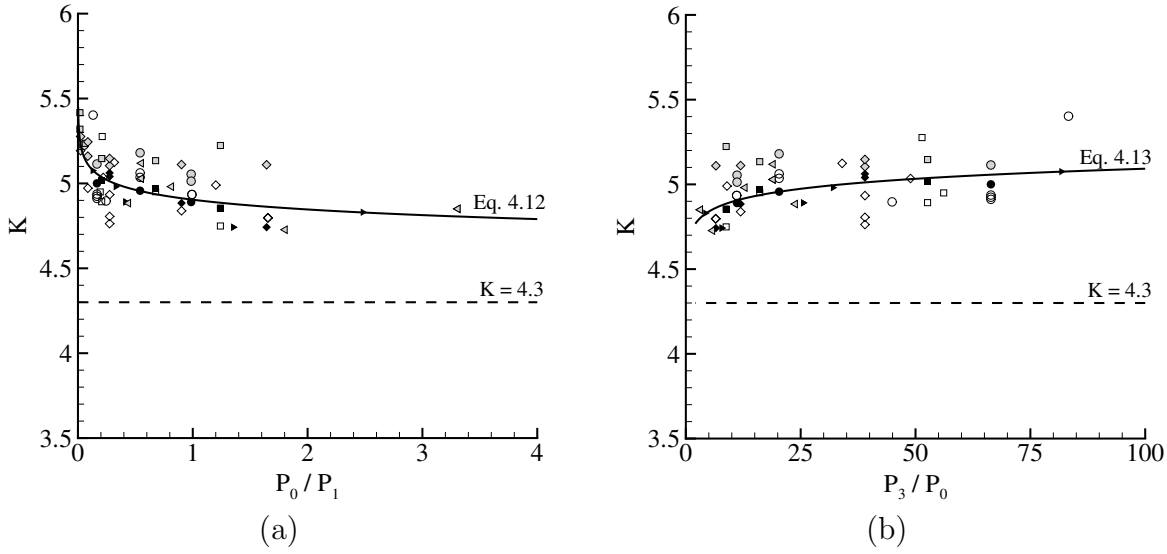

Figure 4.4: Determination of model factor K_{LP} as a function of (a) P_0/P_1 and (b) P_3/P_0. Solid lines are the curve fit equations. Open symbols correspond to 25 μm diaphragm, solid black symbols correspond to 51 μm diaphragm, and solid grey symbols correspond to 105 μm diaphragm.

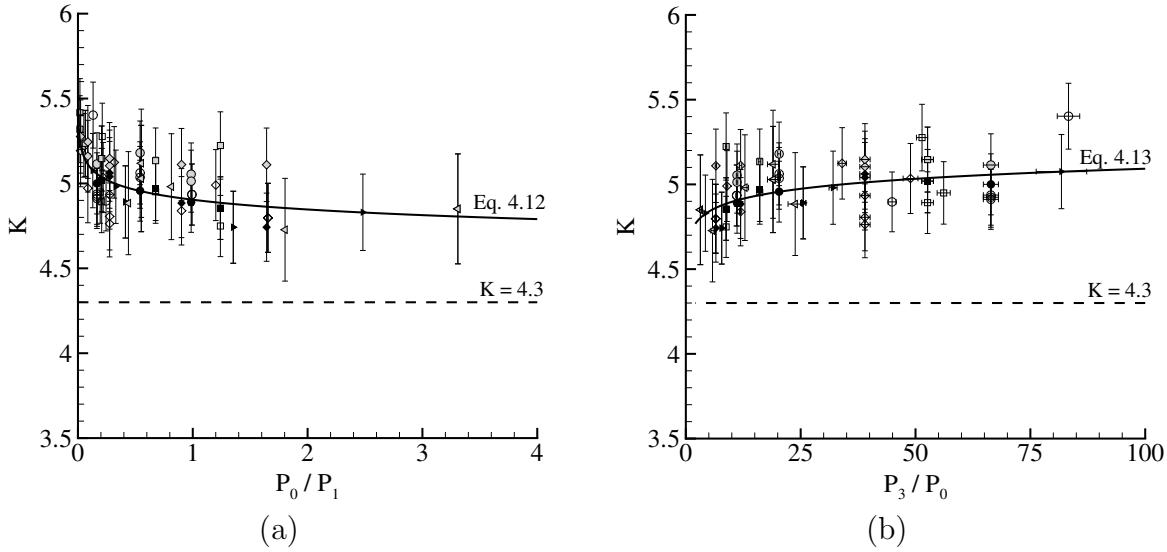

Figure 4.5: Determination of model factor K_{LP} as a function of (a) P_0/P_1 and (b) P_3/P_0 with error bars. Solid lines are the curve fit equations. Open symbols correspond to 25 μm diaphragm, solid black symbols correspond to 51 μm diaphragm, and solid grey symbols correspond to 105 μm diaphragm.

Figs. 4.4(b) and 4.5(b).

$$K_{LP} = 4.904\,(P_0/P_1)^{-0.017} \tag{4.11}$$

$$K_{LP} = 4.904\,[(P_3/P_0) \times (P_1/P_3)]^{0.017} \tag{4.12}$$

With Eq. 4.9, the value of β_{LP} is calculated from the experimental data of K_{LP} and is plotted in Fig. 4.6 with the experimental data. By substituting this new

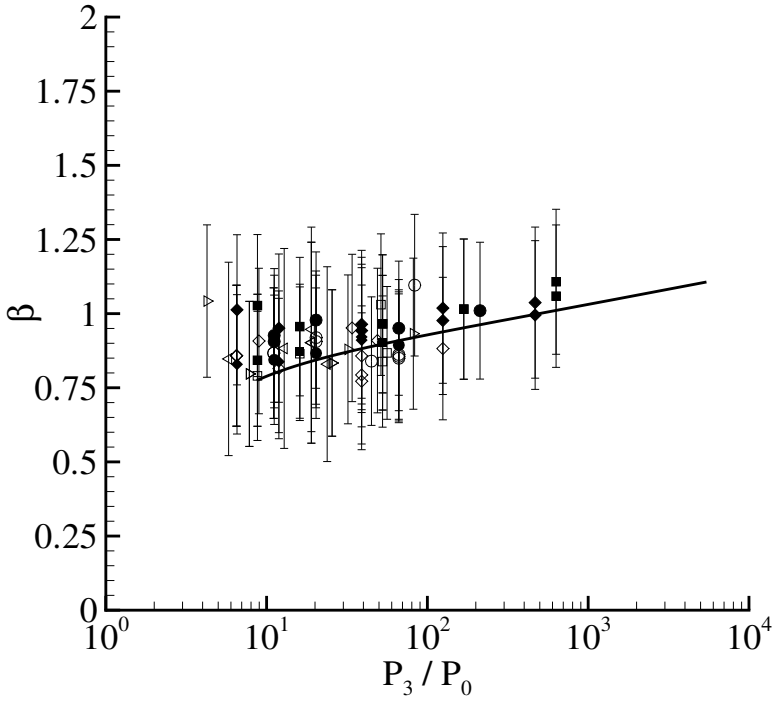

Figure 4.6: β_{LP} as a function of P_3/P_0. Open symbols correspond to 25 μm diaphragm, solid black symbols correspond to 51 μm diaphragm, and solid grey symbols correspond to 105 μm diaphragm.

relationship for β_{LP} into the impulse model of Eq. 4.8 the mixture-based specific impulse is determined in the usual fashion.

$$I_{sp} = \frac{I}{V\rho_1 g} = \frac{(P_3 - P_0)}{\rho_1 g U_{CJ}} \left[\frac{(P_3 - P_1)}{(P_3 - P_0)} + \alpha\frac{U_{CJ}}{c_3} + \beta_{LP}\frac{U_{CJ}}{c_3}\right] \tag{4.13}$$

4.3 Experimental data

The detonation tube without a nozzle was hung in a ballistic pendulum arrangement within Facility II (§2.4). The initial combustible mixture pressure P_1 was varied between 100 kPa and 30 kPa. The environment pressure P_0 outside the tube varied between 100 kPa and 1.4 kPa. Mylar diaphragms with thicknesses of 25, 51, and 105 μm were used to separate the initial combustible mixture from the surrounding air in the tank.

4.3.1 Specific impulse versus P_1

4.3.1.1 Data obtained with 25 and 51 μm diaphragms

Impulse data obtained with the 25 and 51 μm thick diaphragms are plotted in Fig. 4.7 as a function of P_1. Appearing in the figure is a series of data obtained at an environment pressure of 100 kPa. This data are comparable to previous experimental data (Cooper et al., 2002) obtained from the same detonation tube in Facility I (§2.3). Two additional series of data are shown for environment pressures of 54.5 kPa and 16.5 kPa. The lines are polynomial curve fits to the data at each environment pressure.

At an environment pressure of 100 kPa, the specific impulse decreases as the initial mixture pressure decreases. This trend is well-known (Cooper et al., 2002, Wintenberger et al., 2003) and can be attributed to the increasing importance of dissociation as the initial pressure decreases. Experimental pressure traces are plotted in Fig. 4.8 to illustrate the effect of the initial pressure on the DDT process.

As stated in the experimental setup, all mixtures were ignited by a spark with a discharge energy (30 mJ) less than the critical energy required for direct initiation of a detonation (approximately 56 kJ for ethylene-air mixtures (Shepherd and Kaneshige, 1997, rev. 2001) at 100 kPa). Thus, detonations were obtained only by transition from an initial deflagration. The presence of a deflagration is denoted by a gradual rise in the pressure histories as the unburned gas ahead of the flame is compressed due

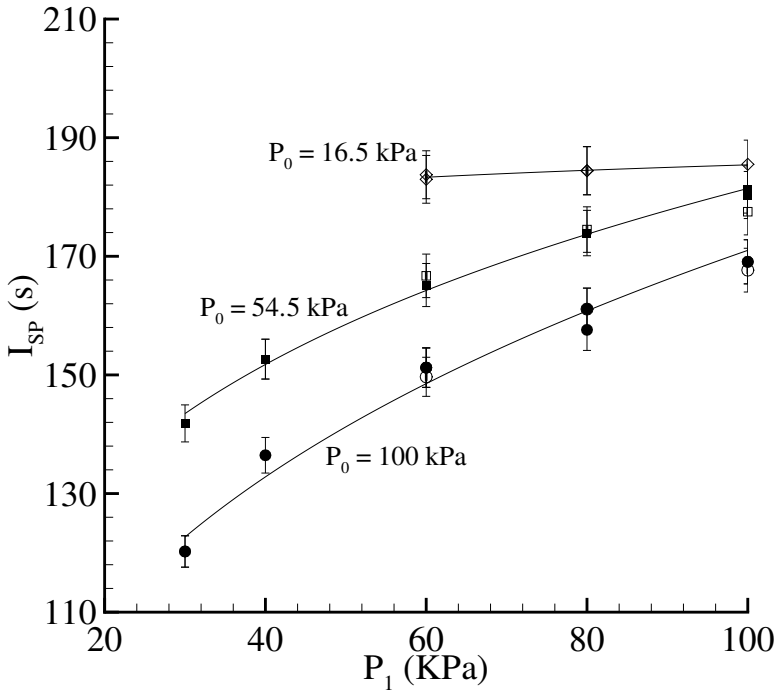

Figure 4.7: Specific impulse data in tubes with a 25 (solid symbols) or 51 μm (open symbols) thick diaphragm. The initial mixture pressure varied between 100 and 30 kPa and the environment pressure was 100 kPa, 54.5 kPa, or 16.5 kPa.

to the expansion of the burned gases behind the flame. If the correct conditions exist, this initial deflagration can transition to a detonation wave. Otherwise, transition will not occur and the deflagration wave will travel the entire length of the tube. An abrupt pressure jump ($\Delta P > 2$ MPa for hydrocarbon fuels) is indicative of this transition which can be quantified in terms of both the DDT time (from spark firing) and DDT distance (axial distance from ignition source location) required for the event to occur.

Previous studies (Cooper et al., 2002) have quantified DDT times and distances with experiments varying the initial mixture and internal obstacles within the tube. Several combustion regimes including the DDT process were identified. As in the previous work (Cooper et al., 2002), the pressure transducers were protected by a layer of thermally-insulating vacuum grease. While this delays the onset of heating of the gauge surface, our experience is that eventually thermal artifacts will be produced

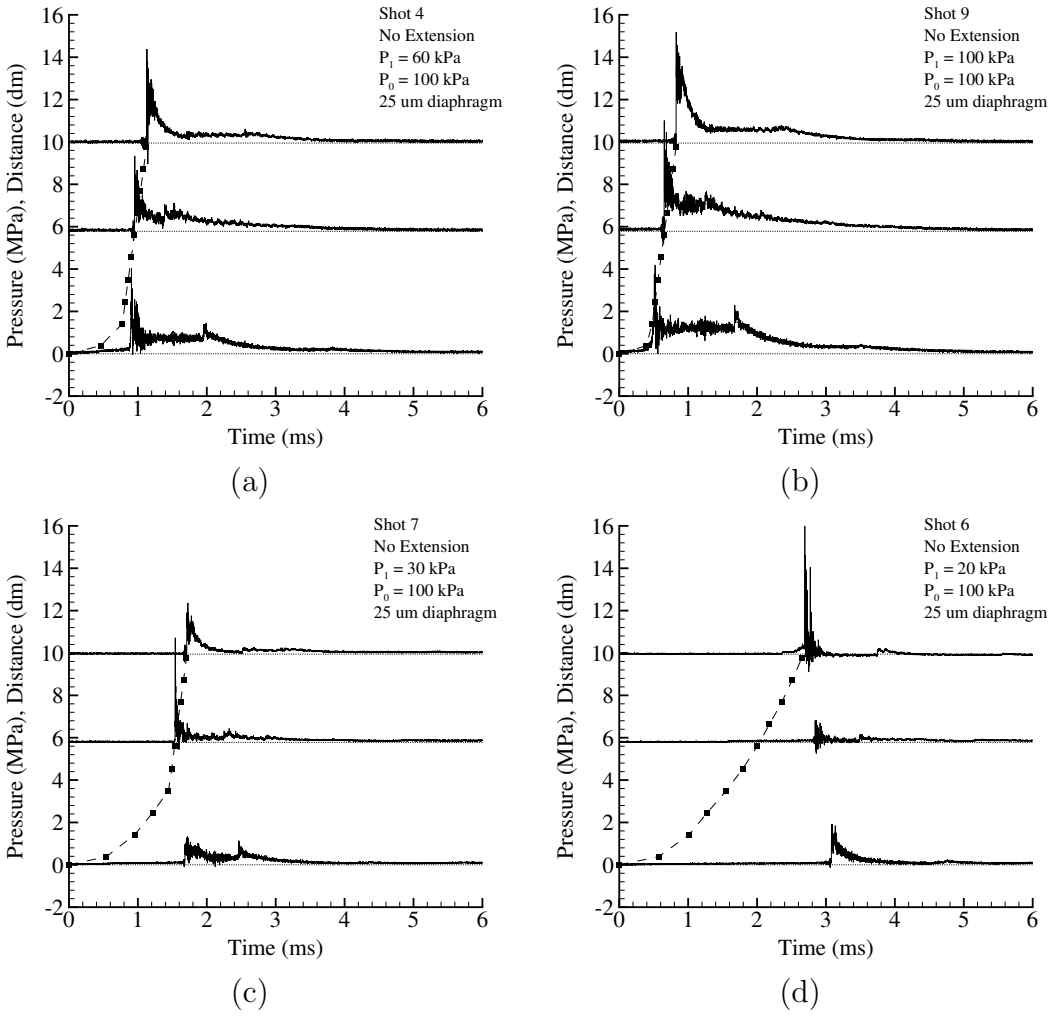

Figure 4.8: Experimental pressure traces illustrating different regimes of (a) and (b) fast DDT, (c) slow DDT, and (d) fast flames.

in the signal. Although we have not quantified this for the present experiments, the pressure signals are reproducible and physically reasonable.

These different combustion regimes are categorized as fast transition to detonation (Fig. 4.8a, b), slow transition to detonation (Fig. 4.8c), and fast flames (Fig. 4.8d). Figures 4.8(a, b) illustrate the case of fast transition to detonation, defined by an abrupt pressure increase before the first pressure transducer along the tube axis and the low DDT time. Figure 4.8(c) illustrates a slow transition to detonation case. An accelerating flame produces a gradual increase in pressure with time at the first pressure transducers, and transition to a detonation occurs before the second pressure

transducer. In this case, the transition occurs late in the tube resulting in a longer DDT time. Figure 4.8(d) illustrates the case of a fast flame. The flame speed is fast enough to create significant compression waves. Transition does occur, only in the last 10 cm of the tube after the last pressure transducer.

For cases when transition to detonation did occur, the slope of the ionization gauge data in Fig. 4.8 equals the Chapman-Jouguet detonation velocity, U_{CJ}. When the detonation wave passes by the location of each individual ionization gauge, the time is recorded and plotted as a black square. This method illustrates the combustion wave trajectory over time for cases of slow acceleration in Fig. 4.8(d) and prompt transition to a detonation in Figs. 4.8(a, b). The relative ability of the mixture to transition to detonation can be related to (Dorofeev et al., 2000, 2001) mixture properties such as the detonation cell size, expansion ratio, and deflagration speed. Necessary conditions for DDT are that the cell width be smaller than a specified fraction of the tube or obstacle dimensions, the expansion ratio (ratio of burned to unburned gas volume) must be larger than a minimum value, and that the deflagration speed exceeds a minimum threshold. For cases of an unobstructed straight tube, transition to detonation is possible only if the detonation cell width is smaller than the tube diameter. We observed DDT in our unobstructed tube for mixtures with initial pressures between 30 and 100 kPa. Since cell size increases with decreasing initial pressure, the largest cell size was about 0.5 mm (Shepherd and Kaneshige, 1997, rev. 2001) corresponding to ethylene-oxygen at 30 kPa. Because the purpose of this study was not to investigate DDT phenomena, all the tests were carried out with values of P_1 greater than and equal to 60 kPa where transition to a detonation occurred within the first 4 cm of the tube. The reader is referred to the work of Dorofeev et al. (2000, 2001) and Lindstedt and Michels (1989) for investigations of the DDT process in tubes.

Impulse data does not appear in Fig. 4.7 for initial mixture pressures below 60 kPa at an environment pressure of 16.5 kPa due to poor experimental repeatability. At the lower initial mixture pressures, transition to detonation occurs later in the tube after a period of flame acceleration and the leading compression waves cause the

diaphragm to rupture, spilling some of the unburned mixture outside of the tube. This effect has been previously observed (Cooper et al., 2002) for initial pressures below 30 kPa, but here we observed this effect for initial pressures below 60 kPa when the environment pressure was reduced. In an effort to prevent early diaphragm rupture as the environment pressure is reduced further, a thicker diaphragm of 105 μm was used.

4.3.1.2 Data obtained with 105 μm diaphragms

Impulse data obtained in tubes sealed with a 105 μm thick diaphragm as a function of the initial mixture pressure appear in Fig. 4.9. The data at $P_1 = 100$ kPa with a

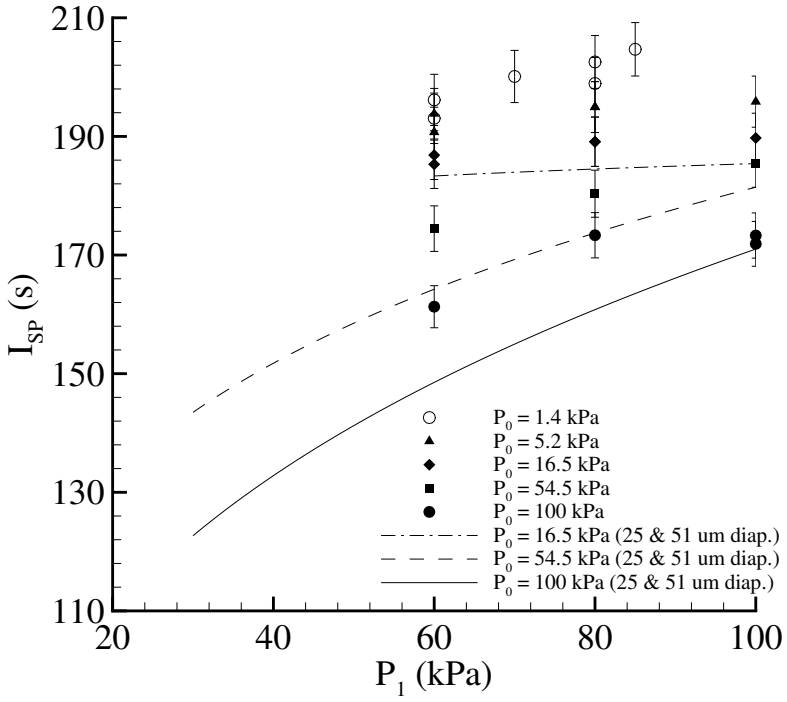

Figure 4.9: Specific impulse data in tubes with a 105 μm diaphragm as a function of the initial mixture pressure. Data is plotted for environment pressures between 100 kPa and 1.4 kPa.

105 μm thick diaphragm does not follow the same trend as shown in Fig. 4.7. This is due to the thicker diaphragm which does not break quickly when the environment pressure is not low. The additional time required by the combustion wave to rupture

the diaphragm results in an energy loss due to heat transfer to the tube walls affecting the shot-to-shot repeatability. Evidence of diaphragm melting was observed after the experiments at $P_0 = 100$ kPa by examining the remaining diaphragm material that did not get destroyed by the detonation wave but appeared to be melted at the edges. At the lower environment pressures, evidence of diaphragm melting disappeared and repeated shots generated impulse values within the range of experimental uncertainty.

4.3.2 Specific impulse versus P_0

The impulse data at initial pressures of 100, 80, and 60 kPa in Figs. 4.7 and 4.9 is plotted in Fig. 4.10-4.12 as a function of the environment pressure. For each initial pressure, the impulse increases as the environment pressure decreases. Also plotted are the model predictions of Eq. 3.14 with a constant value of $\beta = 0.53$ as predicted by Wintenberger et al. (2003). From Eq. 4.8, the specific impulse can be written as

$$I_{sp} = \frac{1}{\rho_1 g U_{CJ}} \left[(P_3 - P_1) + \frac{U_{CJ}}{c_3}(\alpha + \beta)(P_3 - P_0) \right] \tag{4.14}$$

A constant β implies that I_{sp} varies linearly with P_0 for a fixed P_3 and P_1. This is what is being tested by plotting the model with a new, constant value of β to match the experimental data at $P_0 = 100$ kPa. The values of β to match the experimental data are 0.73 for $P_1 = 100$ kPa, 0.70 for $P_1 = 80$ kPa, and 0.66 for $P_1 = 60$ kPa. The experimental data clearly shows an increase in the specific impulse greater than what is predicted if the blow down time t_3 or equivalent β is kept constant. The experimental data is predicted if a variable β_{LP} is used in the model. Sample experimental pressure traces appear in Fig. 4.13 for environment pressures of 100 kPa and 1.4 kPa but differences are difficult to distinguish.

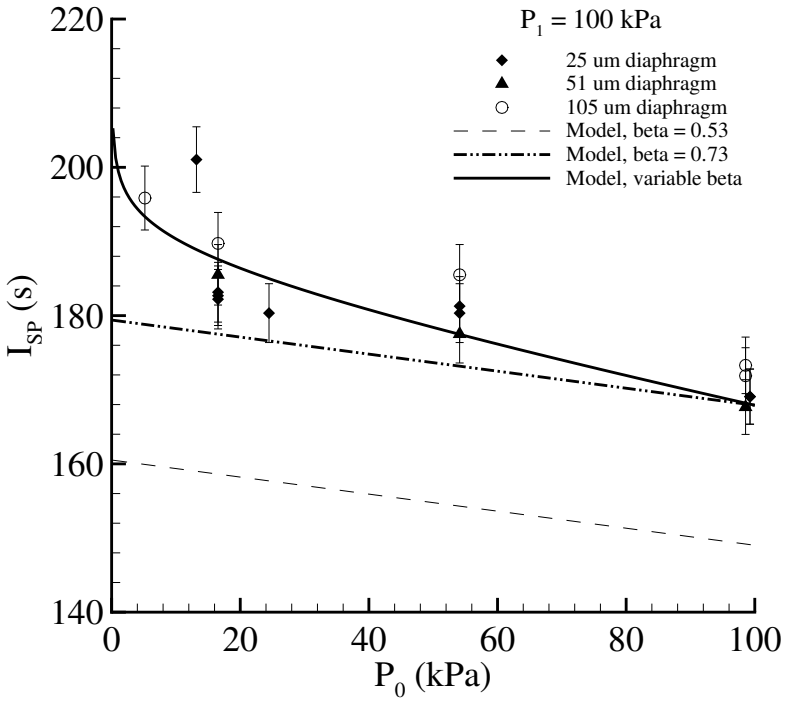

Figure 4.10: Specific impulse data as a function of P_0 for an initial mixture pressure of 100 kPa.

4.4 Non-dimensionalized impulse data

A non-dimensionalization of the experimental data arises from the key relationship of the impulse model (Eq. 4.8).

$$I_V = K_{LP}\,(P_1/U_{CJ})\,[(P_3/P_2)(P_2/P_1) - P_0/P_1] \tag{4.15}$$

where the non-dimensional group $I_V U_{CJ}/P_1$ appears. The ratio P_3/P_2 has been shown to have an average value of 0.35 for a wide range of compositions and initial conditions (Wintenberger et al., 2003). The Chapman-Jouguet pressure ratio P_2/P_1 and detonation velocity U_{CJ} depend on the initial mixture parameters (Table 4.1). This scaling results in a single relationship plotted as a function of the pressure ratio P_0/P_1 in Fig. 4.14.

All data of Figs. 4.7 and 4.9 are shown in Fig. 4.14 and the scatter in the data is due to the different diaphragm thicknesses. Alternatively to Eq. 4.15, the impulse

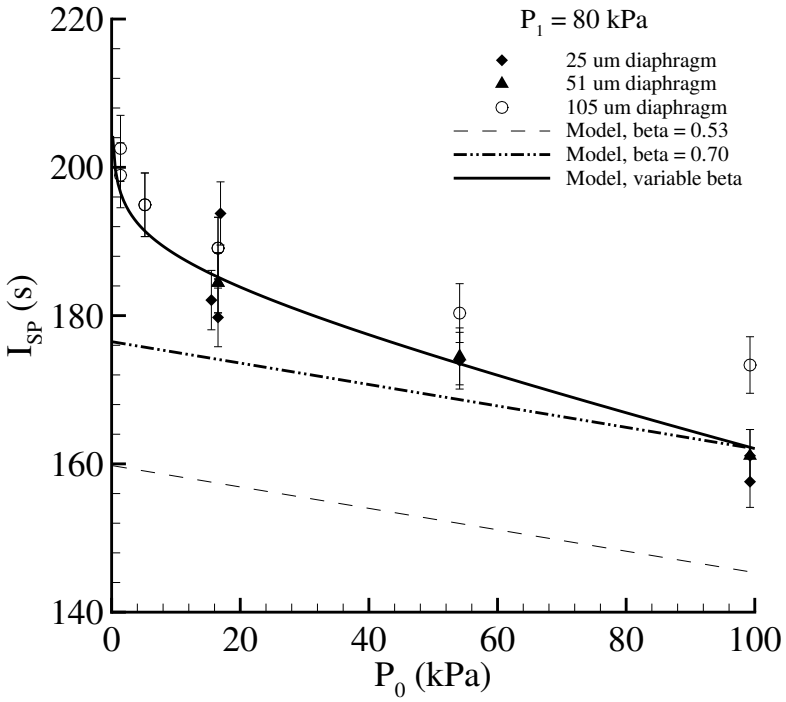

Figure 4.11: Specific impulse data as a function of P_0 for an initial mixture pressure of 80 kPa.

can be written as

$$\begin{aligned} I &= K\,(VP_1/U_{CJ})\,[(P_3/P_0)(P_0/P_1) - P_0/P_1] \\ &= K\,(VP_1/U_{CJ})\,(P_0/P_1)\,[(P_3/P_0) - 1] \end{aligned} \tag{4.16}$$

where the non-dimensional group $I_V U_{CJ}/P_1$ again appears along with an important

P_1 (kPa)	P_3 from Model (MPa)	P_2 Stanjan (MPa)	P_3/P_2	P_2/P_1
100	1.222	3.327	0.367	3.327
80	0.970	2.640	0.367	4.159
60	0.720	1.959	0.368	3.265
40	0.472	1.286	0.367	3.215
20	0.23	0.626	0.367	3.13

Table 4.1: Pressure ratios of P_3/P_2 and P_2/P_1 for ethylene-oxygen mixtures tabulated for different initial pressures. Values of P_3 are from the original impulse model of Wintenberger et al. (2003).

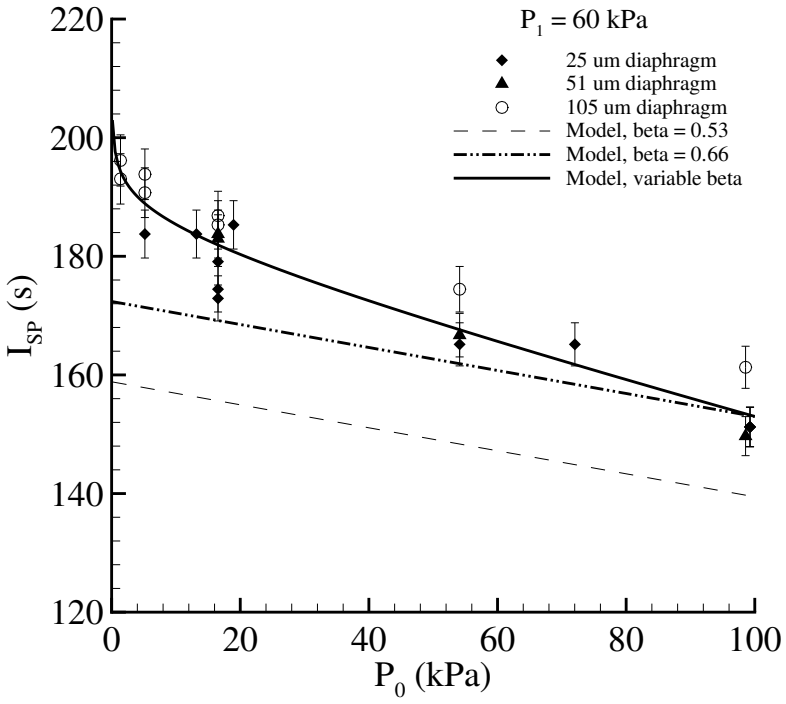

Figure 4.12: Specific impulse data as a function of P_0 for an initial mixture pressure of 60 kPa.

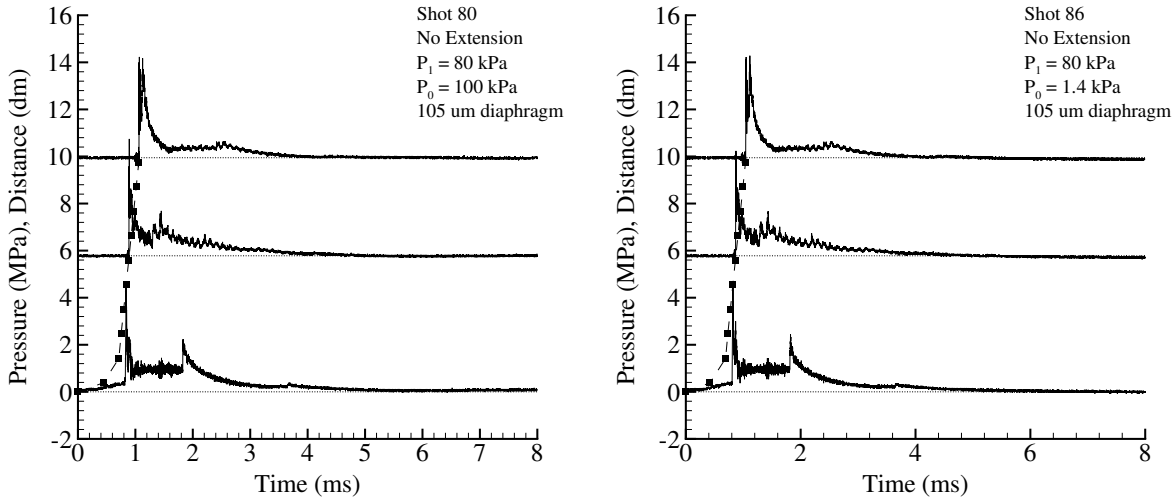

Figure 4.13: Experimental pressure traces obtained in a tube with a 105 μm diaphragm and at environment pressures of (a) 100 kPa and (b) 1.4 kPa.

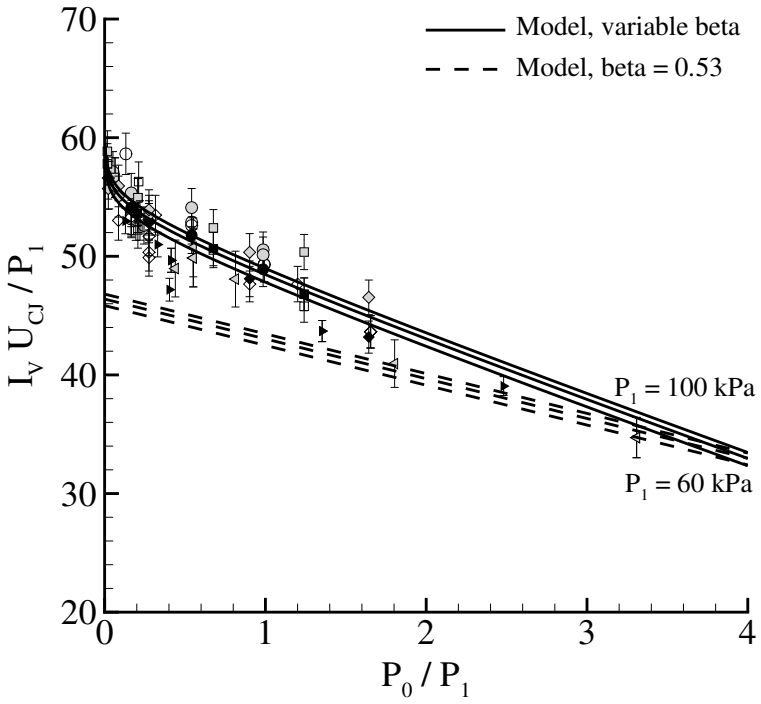

Figure 4.14: Non-dimensionalized impulse data plotted as a function of P_0/P_1. Data correspond to initial mixture pressures between 100 and 30 kPa, environment pressures between 100 kPa and 1.4 kPa, and diaphragm thickness of 25 (open symbols), 51 (solid black symbols), and 105 μm (solid grey symbols).

pressure ratio P_3/P_0. We replot the data of Fig. 4.14 as a function of P_3/P_0 in Fig. 4.15. Also plotted in this figure are numerical simulations performed using AMRITA (Quirk, 1998). The simulation solved the nonreactive Euler equations using a Kappa-MUSCL-HLLE solver in the two-dimensional (cylindrical symmetry) computational domain, consisting of a tube of length L closed at the left end and open to a half-space at the right end. The Taylor wave similarity solution (Fickett and Davis, 1979) was used as an initial condition, assuming the detonation has just reached the open end of the tube when the simulation is started. This solution was calculated using a one-γ model for detonations (Fickett and Davis, 1979) for a non-dimensional energy release $q/RT_1 = 112$ across the detonation and $\gamma = 1.1396$ for the reactants and products. This value of the non-dimensional energy release was chosen to match the plateau pressure P_3 measured in the experiments, however this resulted in a cal-

culated CJ velocity of approximately 12% greater than the measured values.

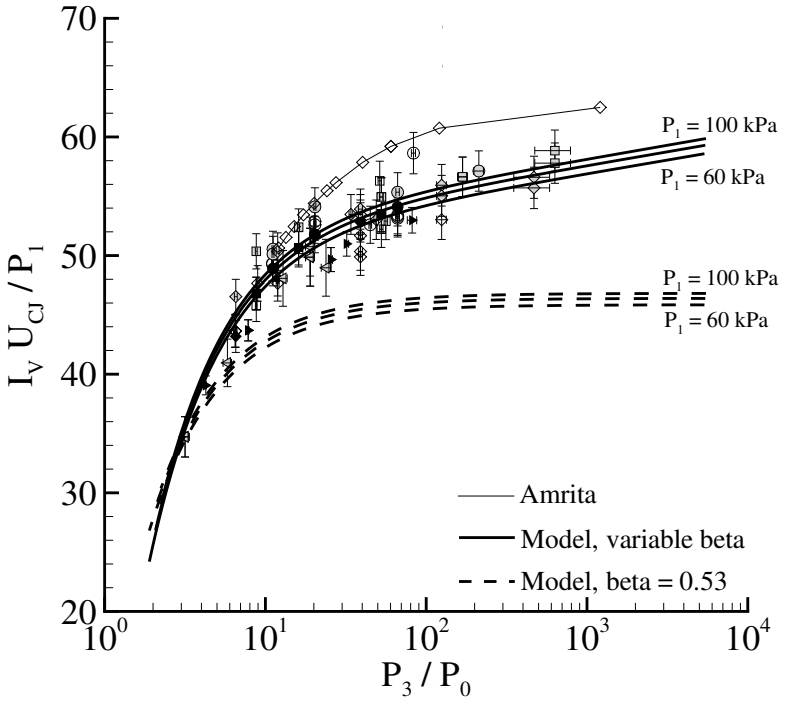

Figure 4.15: Non-dimensionalized impulse data plotted as a function of P_3/P_0. Data correspond to initial mixture pressures between 100 and 30 kPa, environment pressures between 100 kPa and 1.4 kPa, and diaphragm thickness of 25 (open symbols), 51 (solid black symbols), and 105 μm (solid grey symbols).

The difference between the model curve and the AMRITA predictions does not exceed 8% over the range of P_3/P_0 tested. The AMRITA simulations do exhibit a greater increase in impulse for a given increase in the pressure ratio and this can be attributed to the fact that a single value for γ is used for both the products and environment gases in the simulations. In reality, the inert gas has a γ equal to 1.4 whereas the detonation products have a γ equal to 1.1396. The previously discussed "bubble" model shows that at large pressure ratios, the effect of the inert gas γ can have in some cases a significant effect on the normalized pressure integration. While we do not expect this effect to significantly affect a fully filled tube because of the sonic outflow condition at the open end, the experiments are not accurately represented by the simulations using the one-γ detonation model.

Plotting the non-dimensional impulse data as a function of the pressure ratio P_3/P_0 more clearly shows the effect of environment pressure. In Fig. 4.14, it is difficult to distinguish the individual data points at pressure ratios $P_0/P_1 < 0.5$. With our intention of studying the effect of nozzles on detonation tubes, we compare the pressure ratio P_3/P_0 in a detonation tube to the pressure ratio P_i/P_x across a steady flow nozzle. For a lack of any other comparison of nozzle performance for unsteady devices, we propose a comparison between the detonation tube impulse and the impulse obtained from at theoretical, ideal steady flow rocket engine with an ideal nozzle. This ideal impulse of Fig. 1.6 is plotted with the experimental data from the plain detonation tube in Fig. 4.16 for two values of Φ. For $\Phi = 152$, the nozzle inlet conditions are representative of state 3 in the detonation tube for an initial pressure of 80 kPa. As the pressure ratio across the nozzle increases, the difference between the experimental data and the ideal steady flow impulse curve increase indicating the lack of full product gas expansion to the lower environment pressures. This experimental data of a detonation tube at different environment pressures serves as a baseline from which the effect of adding a nozzle can be quantified.

4.5 Summary

This study obtained the first experimental data quantifying the effect of environment pressure on the single-cycle impulse of a fully filled detonation tube. The data was obtained for stoichiometric mixtures of ethylene-oxygen at initial pressures between 100 and 30 kPa and environment pressures between 100 kPa and 1.4 kPa. The specific impulse increased as the environment pressure decreased at a constant initial mixture pressure. This increase in impulse was not predicted by the original impulse model (Wintenberger et al., 2003) which used a constant value of K and β. At the lowest environment pressures, the increased time required to blow down the tube caused the impulse to increase approximately 11% greater than the predictions. New model parameters K_{LP} and β_{LP} were defined to be functions of the environment pressure and were determined from the experimental data. The pressure ratio P_3/P_0, if compared

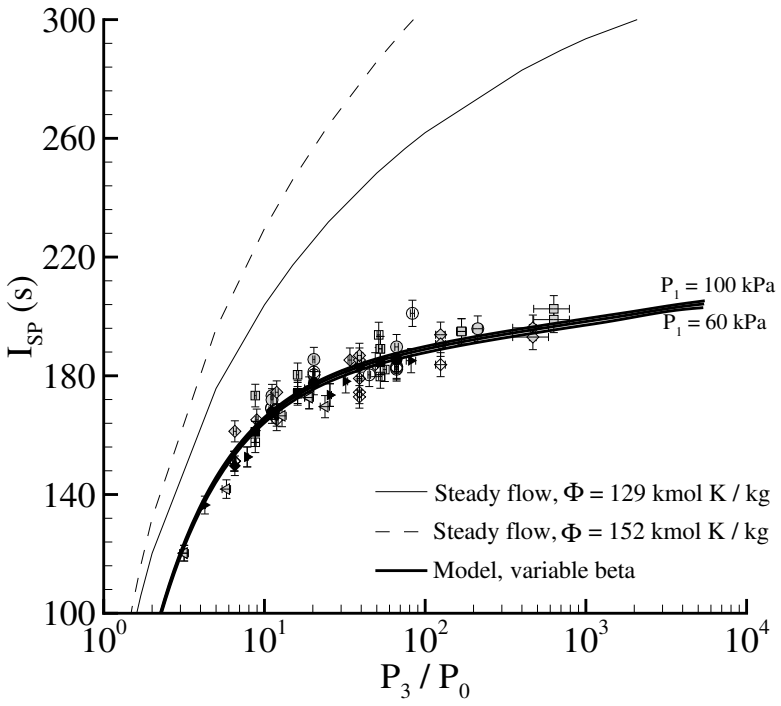

Figure 4.16: Specific impulse data plotted as a function of P_3/P_0. Data correspond to initial mixture pressures between 100 and 30 kPa, environment pressures between 100 kPa and 1.4 kPa, and diaphragm thickness of 25 (open symbols), 51 (solid black symbols), and 105 μm (solid grey symbols). Thin solid curves corresponds to ideal impulse from a steady flow nozzle for values of $\Phi = 129$ and 152. Thick solid curve corresponds to the model predictions with variable β_{LP}.

to the nozzle pressure ratio in the steady flow case, enables a direct comparison between the detonation tube impulse data and the theoretical ideal maximum impulse based on isentropic, steady-flow expansion. These results indicate the detonation products are underexpanded, motivating further research into the effect of nozzles, which is the subject of the next chapter.

Chapter 5

Variable-area nozzles

5.1 Introduction

The previous chapter presented single-cycle impulse data from fully filled detonation tubes exhausting into sub-atmospheric environments. Comparisons of the data to the steady flow impulse predictions based on isentropic expansion showed that the products exhausting from a straight tube are underexpanded. In an effort to promote additional gas expansion and hopefully recover some of the lost energy, experiments with nozzles were carried out. Each nozzle was attached to the end of the detonation tube which was hung in a ballistic pendulum arrangement within Facility II (described in §2.4). A Mylar diaphragm separated the combustible mixture inside the tube from the environment air in the nozzle. The tested nozzles included conical converging nozzles, conical diverging nozzles, and conical converging-diverging nozzles. A straight extension, categorized as a "diverging" nozzle with a 0° half angle, was also tested.

Previous experimental and numerical studies have investigated nozzles on detonation tubes. The first study was carried out by Cambier and Tegner (1998) who numerically studied contoured diverging nozzles on detonation tubes. The effect on the impulse was quantified in hydrogen-oxygen mixtures at 1 atm and 350 K. Eidelman and Yang (1998) carried out a numerical calculations to study the effect of converging and diverging nozzles on tubes with a 6 cm inner diameter and a length of 15 cm in acetylene-air mixtures at 1 atm pressure. The nozzles contained air at

standard conditions. The converging nozzles were found to cause multiple shock reflections and longer blow down times. A relatively long converging nozzle with a small half angle increased the impulse over the baseline case of a plain tube, but this is most likely due to the partial fill effect. Very short converging nozzles showed no significant increase in impulse. Two conical diverging nozzles and a bell shaped nozzle with an area ratio of 5, designed for full expansion to atmospheric conditions, were examined. However, the flow overexpanded in the nozzle decreasing the impulse below the ideal value.

Yang et al. (2001) carried out numerical calculations studying the impulse for a converging, diverging, and plug nozzle in hydrogen-air mixtures at 0.29 atm and 228 K. The nozzle contained air at the same conditions. The conical converging and diverging nozzles had 10° half angles and area ratios of A_{exit}/A_{tube} of 1.25 and 0.75, respectively. They observed a limited performance gain with the diverging nozzle over the case of a straight extension.

Guzik et al. (2002) carried out a numerical study using the method of characteristics to solve the flow field within a detonation tube containing a fixed area nozzle and a variable area nozzle. They assume the detonation products for the propane-oxygen mixture, initially at 1 atm and 295 K, are frozen at the CJ equilibrium conditions. The variable area nozzle was a diverging nozzle with "flexible" cross section in order to fully expand the flow. The fixed area nozzle had an exit area equal to the tube cross-sectional area and a converging-diverging throat section. For a detonation initiated at the thrust surface, they found that the optimum area ratio A_{throat}/A_{tube} was 0.54. The throat restriction was observed to delay the time at which the maximum impulse was observed over that of the plain tube. They concluded that a variable nozzle can always be added to extract more thrust.

Morris (2004) carried out a numerical investigation using a quasi-one-dimensional, finite-rate chemistry computational fluid dynamics model for pulse detonation rocket engines in hydrogen-oxygen mixtures. Four different geometries were analyzed including a plain detonation tube, a straight extension, and two converging-diverging nozzles with different throat restrictions and 15° half angles for the converging and

diverging sections. The converging-diverging nozzles were found to always be more effective than at straight extension at increasing the impulse for initial pressure ratios P_1/P_0 between 10 and 1000. This is contrary to the findings of this study.

Cooper et al. (2002) previously carried out an experimental investigation measuring impulse from a 1 m long detonation tube exhausting into atmospheric air with a conical diverging nozzle. The nozzle had a length of 0.3 m and an 8° half angle. The impulse measurements were obtained in ethylene-oxygen mixtures at 100 kPa initial pressure with different nitrogen dilutions. A ballistic pendulum arrangement was used and the tube contained internal obstacles to promote DDT in the diluted mixtures. A constant increase in impulse of approximately 1% over the plain tube case was observed for nitrogen dilutions between 0% and 40%.

Falempin et al. (2001) experimentally investigated the effect of diverging nozzles on impulse with a ballistic pendulum arrangement in ethylene-oxygen mixtures. They tested conical diverging nozzles, bell shaped nozzles, and straight extensions. The nozzles contained air at ambient conditions and they attributed the measured increase in impulse primarily due to the partial fill effect.

Additional studies have investigated the effect of ejectors on performance (Allgood and Gutmark, 2002, Allgood et al., 2004). Allgood and Gutmark (2002) carried out two-dimensional, reactive numerical calculations of ejectors on detonation tubes predicting the thrust as a function of the ejector dimensions. Allgood et al. (2004) carried out an experimental study using a high-speed shadowgraph imaging system to visualize the flow from their two-dimensional ejector. No experimental thrust measurements were obtained for the different ejector configurations in the later work of Allgood et al. (2004). Ejectors are designed to entrain additional environment air into the flow to increase the exhaust gas momentum and the thrust. While the use of ejectors attached to the end of detonation tubes is an interesting problem, it is out of the scope of this work.

The behavior of detonations propagating through variable area geometries has also been investigated. In particular, Tzuk et al. (1993) and Grigor'ev (1996) have experimentally studied the expansion of detonation products through diverging noz-

zles that were seeded with particles in order to visualize the flow. They both observed an increase in particle velocities as the flow expanded through the diverging nozzle. As in our experiments, the combustible mixture in their experiments did not fill the nozzle, however they did not measure thrust. An experimental study carried out by Thomas and Williams (2002) investigated the behavior of a detonation wave in two-dimensional curved channels and diverging nozzles. The channels and nozzles were completely filled with the combustible mixture and sooted foils were used to record the detonation behavior as the geometry changed. Akbar et al. (1995) studied the propagation of detonations through converging channels and extended Whitham's method of shock dynamics to the detonation case in order to design the channel. In the work of Thomas and Williams (2002) and Akbar et al. (1995), there was no effort to measure impulse.

While the studies of Cambier and Tegner (1998), Eidelman and Yang (1998), Yang et al. (2001), Guzik et al. (2002), Morris (2004), Cooper et al. (2002), and Falempin et al. (2001) have studied nozzles on detonation tubes, this experimental data is the first to take a systematic look at the effect of nozzles on impulse under varying environment pressures. With the nozzles tested here, the effect of divergence angle, volumetric fill fraction, and nozzle length are investigated.

5.2 Experimental data

The next sections present the experimental impulse data obtained with the converging, diverging nozzles, and converging-diverging nozzles. A brief description of each nozzle is also included. Each nozzle was attached to the detonation tube and the impulse was measured as the environment pressure varied between 100 and 1.4 kPa. The combustible mixture was stoichiometric ethylene-oxygen at an initial pressure of 80 kPa and the thickest diaphragm of 105 μm was used to improve experimental repeatability at low environment pressures. The results for the are presented in the following sections.

5.2.1 Converging nozzles

Two converging nozzles were tested to determine their effect on impulse as the environment pressure was varied between 100 kPa and 1.4 kPa. An illustration of the detonation tube with a converging nozzle appears in Fig. 5.1. The nozzle described as "Noz-0.50" had an area ratio $A_t/A = 0.50$ and the nozzle described as "Noz-0.75" had an area ratio $A_t/A = 0.75$. Additional nozzle details appear in Table 2.1. The measured impulse data is presented in Fig. 5.2.

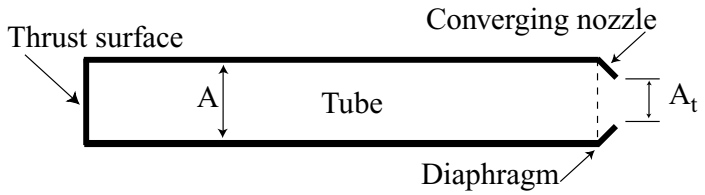

Figure 5.1: Illustration of a converging nozzle on the detonation tube.

The effect of the converging nozzles on impulse is modest. The relatively short length of the nozzles as compared to the length of the detonation tube $L/L^0 = 0.9$ results in volumetric fill fractions for both nozzles of 0.96. The nozzle with the largest exit area (Noz-0.75) is observed to increase the impulse 2.3% at 100 kPa environment pressure over the plain tube case. For this volume ratio, the partial fill model predicts an increase of 2%. The impulse from the nozzle with the smallest exit area (Noz-0.75) is observed to slightly decrease below the plain tube case at 100 kPa environment pressure. This is due to the pressure acting on the internal surface of the nozzle generating a pressure force in the direction opposite of that generated by the pressure force across the thrust surface. These results are in agreement with other studies on short converging nozzles (Eidelman and Yang, 1998, Yang et al., 2001).

As the environment pressure is decreased, the tamper mass in the nozzle goes to zero and the partial fill effect is eliminated. The impulse is observed to increase for both nozzles over the plain tube case and this can be attributed to the quasi-steady flow through the restriction that delays the rate of pressure decrease at the thrust

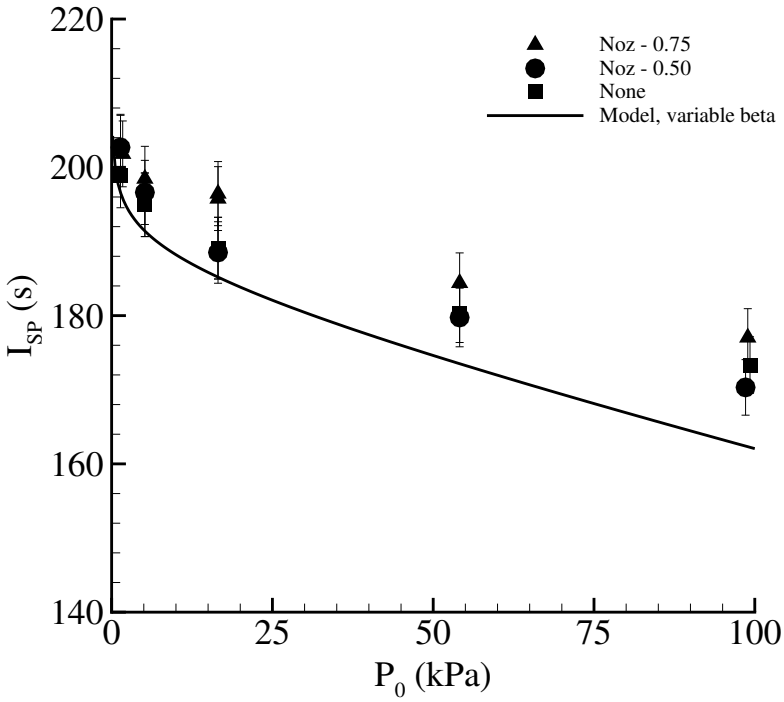

Figure 5.2: Specific impulse for the converging nozzles as a function of the environment pressure. Data for the tube without a nozzle is also plotted along with the modified impulse model (Eq. 4.13).

surface. Thrust surface pressure histories from the plain tube and the nozzle with the smallest exit area (Noz-0.50) are plotted in Fig. 5.3 for environment pressures of (a) 100 kPa and (b) 1.4 kPa. Multiple wave reflections due to the convergent geometry of the nozzle are observed during the pressure decay process.

5.2.2 Diverging nozzles

Three conical diverging nozzles and the straight extension were added to the detonation tube and their effect on the impulse was measured for environment pressures between 100 kPa and 1.4 kPa. An illustration of the detonation tube with a diverging nozzle appears in Fig. 5.4. The nozzles had half angles ϕ ranging from 0 to 12 and lengths of 0.3 m and 0.6 m (Table 2.2). Over the range of tested environment pressures, the addition of a diverging nozzle always increased the specific impulse over the case of a plain tube. The effect of each nozzle on the impulse is discussed in the

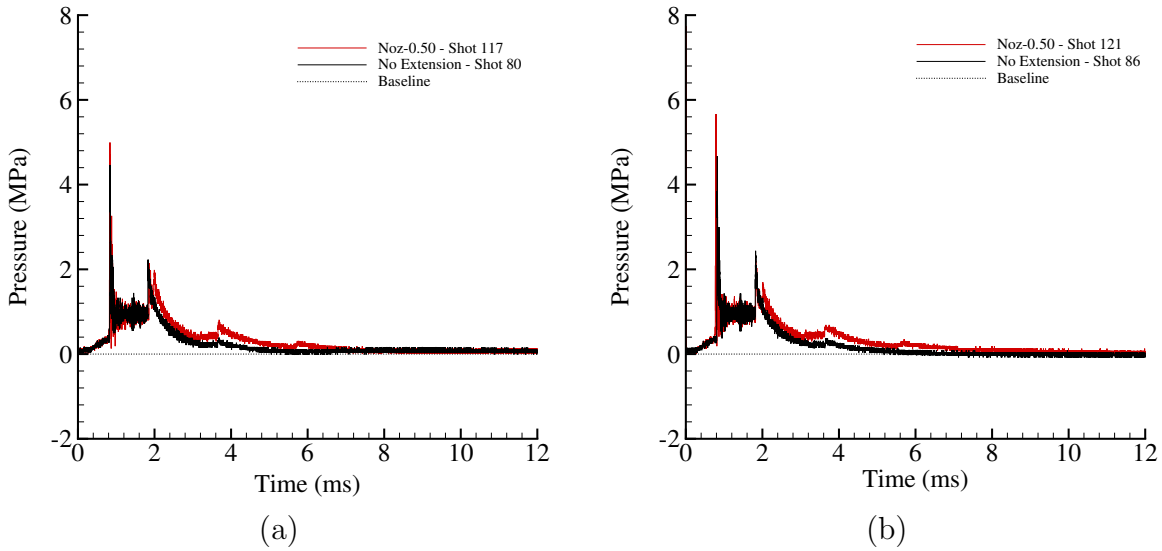

Figure 5.3: Thrust surface pressure histories for the plain tube and the converging nozzle with an area ratio $A_t/A = 0.50$ at an environment pressure of (a) 100 kPa and (b) 1.4 kPa.

following sections.

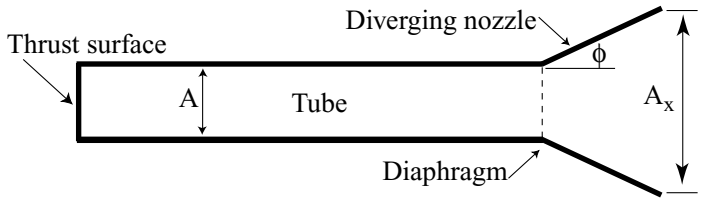

Figure 5.4: Illustration of the detonation tube with a diverging nozzle.

5.2.2.1 0°-0.6 m nozzle

The impulse obtained with the straight extension (characterized as a diverging nozzle with a 0° half angle) is plotted as a function of the environment pressure in Fig. 5.5. The percent increases in the specific impulse I_{sp} over the case of a tube without nozzle I_{sp}^0 at each environment pressure are tabulated in Table 5.1.

At 100 kPa, the largest increase in specific impulse over the plain tube case is observed. This can be attributed to the partial fill effect and the presence of the

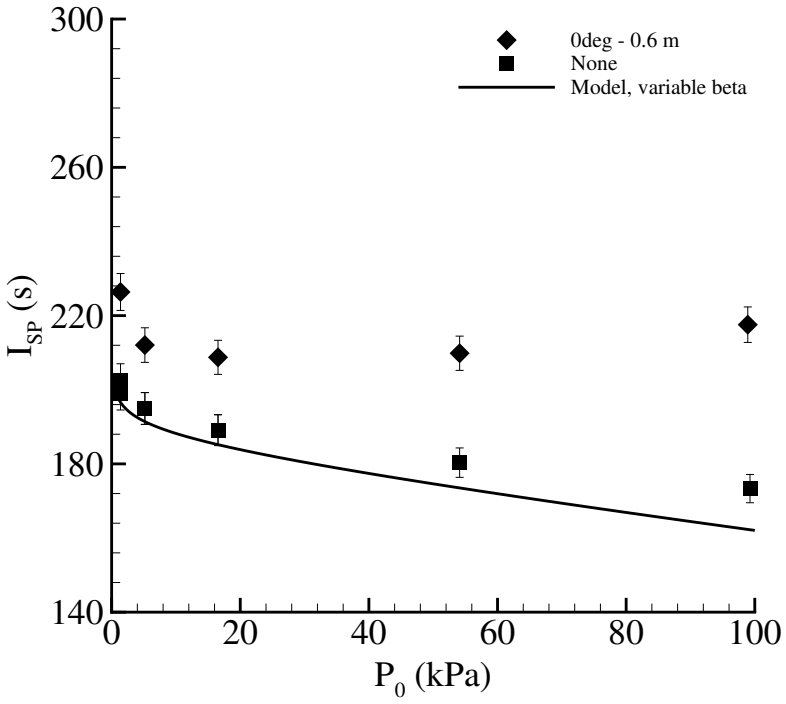

Figure 5.5: Specific impulse for the 0°-0.6 m nozzle as a function of the environment pressure. Data for the tube without a nozzle is also plotted along with the modified impulse model (Eq. 4.13).

P_0 (kPa)	Tamper Mass Ratio N/C	Mass Fraction $C/(N+C)$	$\Delta I_{sp}/I_{sp}^0$ Measured From Fig. 5.5(%)
100	0.73	0.58	26
54 .5	0.39	0.72	16
16.5	0.12	0.89	10
5.2	0.04	0.96	9
1.4	0.01	0.99	13

Table 5.1: Percent increases in specific impulse for the 0°-0.6 m nozzle.

tamper that is exhausted from the tube in addition to the detonation products. As the environment pressure decreases, a corresponding decrease in the tamper mass results and the impulse decreases as predicted by the partial fill model. For the lowest environment pressure $P_0 = 1.4$ kPa, the tamper mass has gone to zero ($C/(N+C) \rightarrow 1$). In this case, the increase in impulse does not go to zero but instead increases by 13% over the case of a plain tube. Now, the extension acts to confine the exhaust flow and slow the rate of pressure decrease at the thrust surface.

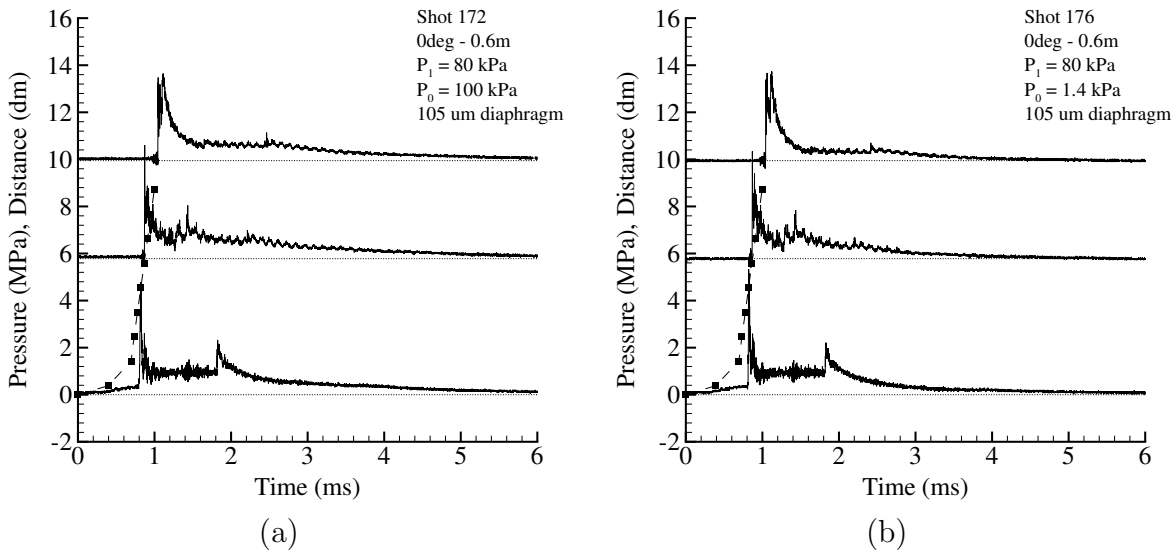

Figure 5.6: Pressure traces obtained with the 0°-0.6 m nozzle for P_0 equal to (a) 100 kPa and (b) 1.4 kPa.

Figure 5.6 plots the experimental pressure traces along the tube length at an environment pressure of 100 kPa and 1.4 kPa. Differences in the traces are difficult to distinguish unless the two thrust surface pressure histories are superimposed as in Fig. 5.7. In Fig. 5.7, a faster pressure decay from the P_3 value is observed at the lower environment pressure of 1.4 kPa than at 100 kPa. Additionally, the pressures are observed to reach different limiting values at large times, greater than 10 ms, due to the different environment pressures.

5.2.2.2 8°-0.3 m nozzle

The impulse obtained with the 8°-0.3 m diverging nozzle is plotted as a function of the environment pressure in Fig. 5.8. The percent increases in the impulse over the case of a tube without nozzle are tabulated at each environment pressure in Table 5.2.

Although this nozzle has half the length of the straight extension, it has a similar mass fraction at an environment pressure of 100 kPa. While the partial fill model predicts that the same impulse should result from the two nozzles, only a 6.4% increase in impulse is observed with the 8°-0.3 m nozzle whereas the straight extension observed a 26% increase. This illustrates that the partial fill effect is more efficient at

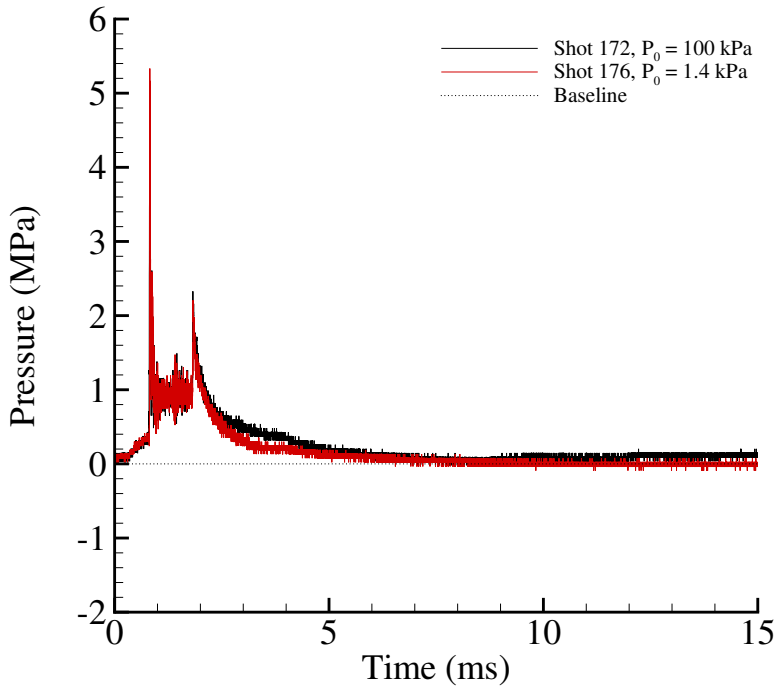

Figure 5.7: Thrust surface pressure history obtained with the 0°-0.6 m nozzle for P_0 equal to 100 kPa and 1.4 kPa.

increasing the impulse in one-dimensional geometries than two-dimensional geometries. Unlike the straight extension, the impulse of the 8°-0.3 m nozzle increases as P_0 decreases. At $P_0 = 1.4$ kPa, the impulse increases 29% over the plain tube and 16% over the straight extension.

P_0 (kPa)	Tamper Mass Ratio N/C	Mass Fraction $C/(N+C)$	$\Delta I_{sp}/I^0_{sp}$ Measured From Fig. 5.8(%)
100	0.65	0.61	6.4
54.5	0.41	0.71	10
16.5	0.13	0.89	19.8
5.2	0.038	0.96	25
1.4	0.016	0.99	29

Table 5.2: Percent increases in specific impulse for the 8°-0.3 m nozzle.

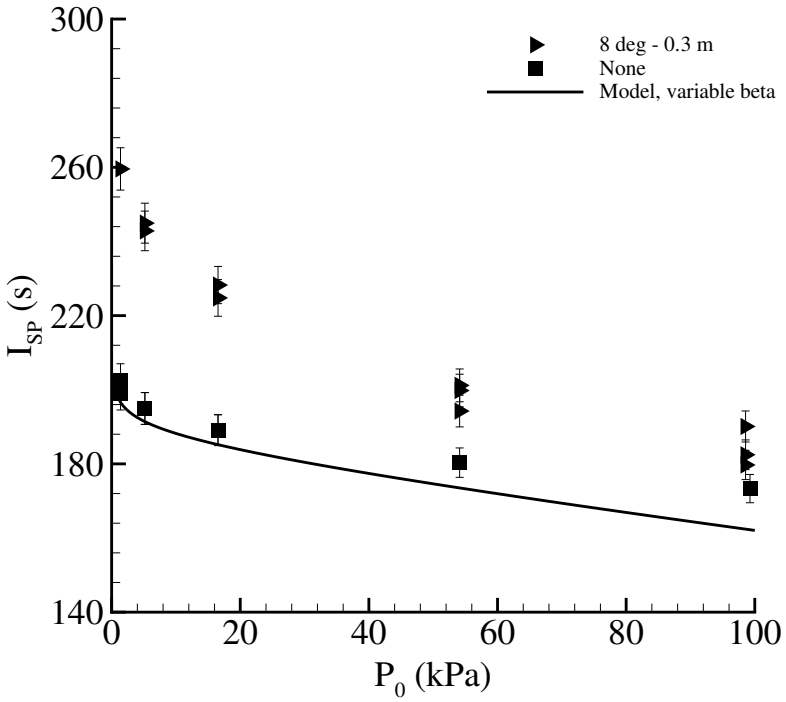

Figure 5.8: Specific impulse for the 8°-0.3 m nozzle as a function of the environment pressure. Data for the tube without a nozzle is also plotted along with the modified impulse model (Eq. 4.13).

5.2.2.3 12°-0.3 m nozzle

The impulse obtained with the 12°-0.3 m diverging nozzle is plotted as a function of the environment pressure in Fig. 5.9. The percent increases in the impulse over the case of a tube without nozzle are tabulated at each environment pressure in Table 5.3.

P_0 (kPa)	Tamper Mass Ratio N/C	Mass Fraction $C/(N+C)$	$\Delta I_{sp}/I^0_{sp}$ Measured From Fig. 5.9(%)
100	1.17	0.46	26
54.5	0.63	0.61	22
16.5	0.20	0.83	28
5.2	0.058	0.94	31
1.4	0.016	0.98	36

Table 5.3: Percent increases in specific impulse for the 12°-0.3 m nozzle.

The impulse with the 12°-0.3 m nozzle remains constant as the environment pres-

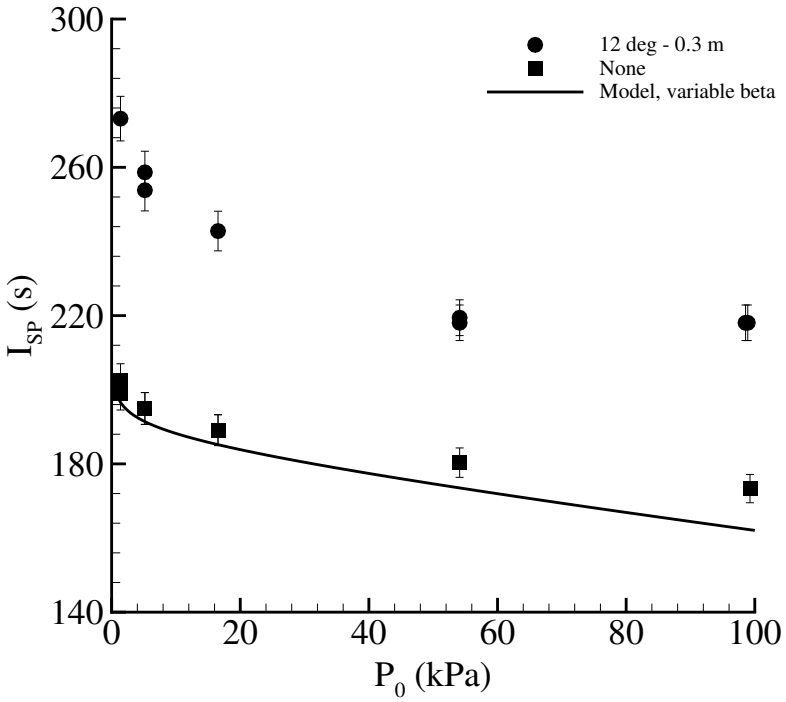

Figure 5.9: Specific impulse for the 12°-0.3 m nozzle as a function of the environment pressure. Data for the tube without a nozzle is also plotted along with the modified impulse model (Eq. 4.13).

sure decreases from 100 kPa to 54 kPa. As previously observed with the straight extension, the impulse is affected by the tamper mass contained in the nozzle. As the environment pressure decreases, the tamper mass N decreases and does so at a faster rate the larger the nozzle volume.

$$\Delta N = \frac{\Delta P_0 V}{R T_0} \tag{5.1}$$

Thus, for a given decrease in the environment pressure P_0, the change in the tamper mass is greater for the larger nozzle volume. When the environment pressure has decreased sufficiently and the tamper is small, quasi-steady flow exists in the nozzle. It is the competition between these two effects that ultimately determine the impulse. In the case of the 12°-0.3 m nozzle, as the environment pressure decreases from 100 kPa to 54 kPa these two effects are balanced and no net change in the measured specific impulse is observed.

As the environment pressure decreases below 54 kPa, the tamper mass is sufficiently low and the effect of quasi-steady flow within the nozzle acts to increase in the impulse over the case of the plain tube. At the lowest environment pressure of $P_0 = 1.4$ kPa, the 12° half angle nozzle generates more impulse than the smaller nozzle with an 8° half angle and the same length.

Sample pressure traces for the 12°-0.3 m nozzle appear in Fig. 5.10 for environment pressures of (a) 100 kPa and (b) 1.4 kPa. The thrust surface pressure histories are superimposed in Fig. 5.11. The only noticeable deviation is in the final values due to the different environment pressures.

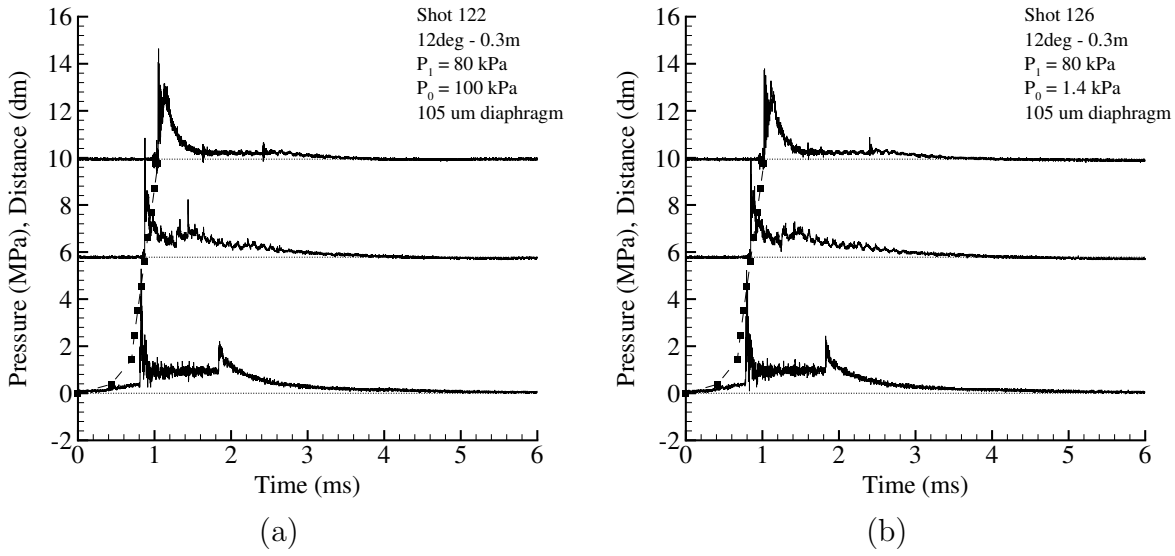

Figure 5.10: Pressure traces obtained with the 12°-0.3 m nozzle for P_0 equal to (a) 100 kPa and (b) 1.4 kPa.

5.2.2.4 12°-0.6 m nozzle

The impulses obtained with the 12°-0.6 m diverging nozzle are plotted as a function of the environment pressure in Fig. 5.12. The percent increases in the impulse over the case of a tube without nozzle are tabulated at each environment pressure in Table 5.4.

Sample pressure traces for the 12°-0.6 m nozzle appear in Fig. 5.13 for environment pressures of (a) 100 kPa and (b) 1.4 kPa. The thrust surface pressure histories are

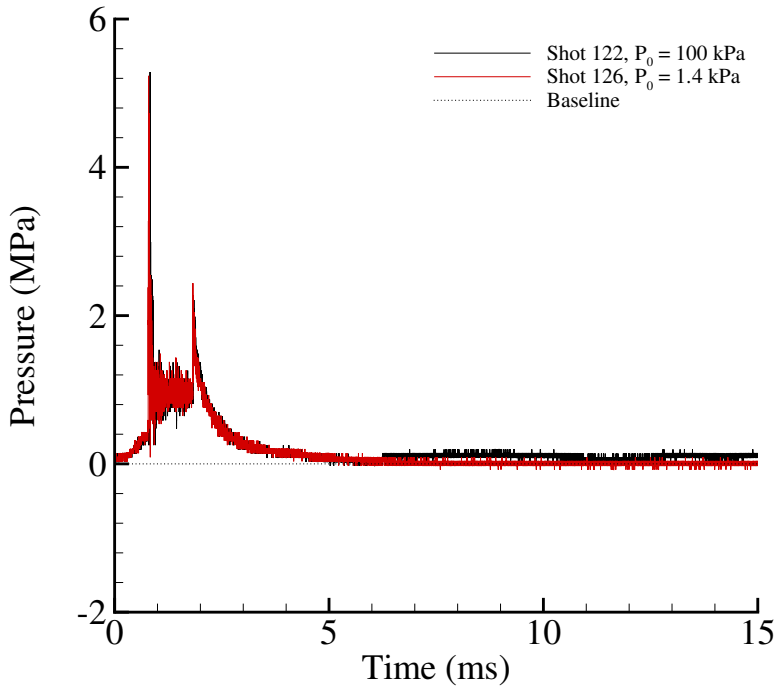

Figure 5.11: Thrust surface pressure history obtained with the 12°-0.3 m nozzle for P_0 equal to 100 kPa and 1.4 kPa.

superimposed in Fig. 5.14. The only noticeable deviation is in the final values due to the different environment pressures.

The 12°-0.6m nozzle has the largest volume of all the nozzles tested and also generates the largest increases in impulse. At an environment pressure of 100 kPa, a 72% increase in impulse is observed and this is due to the large tamper mass contained in the nozzle. As P_0 decreases, the tamping action of the nozzle gas decreases and the impulse decreases. This was observed previously with the 0°-0.6 m nozzle and

P_0 (kPa)	Tamper Mass Ratio N/C	Mass Fraction $C/(N+C)$	$\Delta I_{sp}/I_{sp}^0$ Measured From Fig. 5.12(%)
100	5.0	0.17	72
54.5	2.7	0.27	59
16.5	0.9	0.54	43
5.2	0.3	0.80	39
1.4	0.1	0.93	43

Table 5.4: Percent increases in specific impulse for the 12°-0.6 m nozzle.

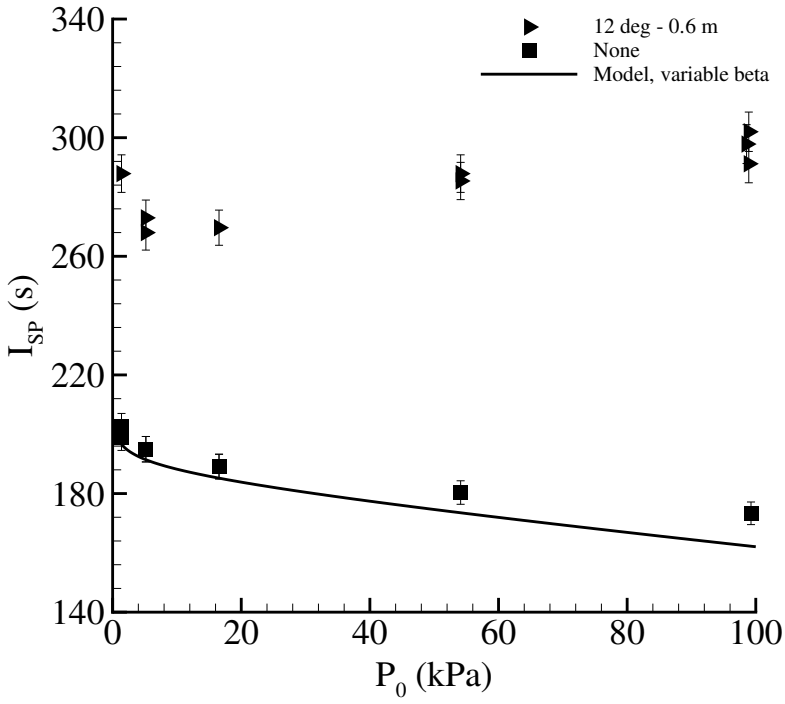

Figure 5.12: Specific impulse for the 12°-0.6 m nozzle as a function of the environment pressure. Data for the tube without a nozzle is also plotted along with the modified impulse model (Eq. 4.13).

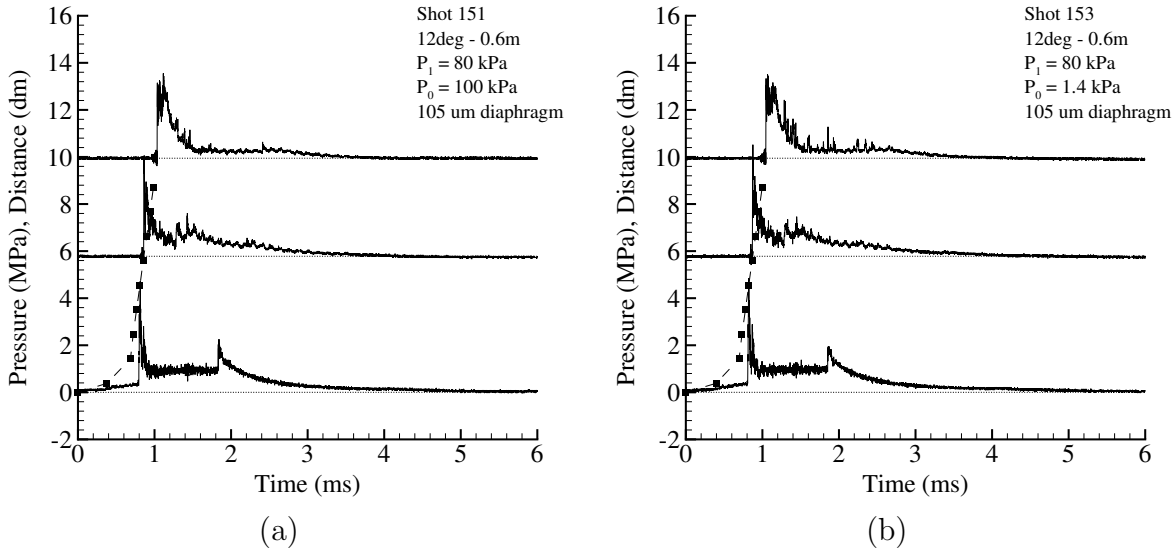

Figure 5.13: Pressure traces obtained with the 12°-0.6 m nozzle for P_0 equal to (a) 100 kPa and (b) 1.4 kPa.

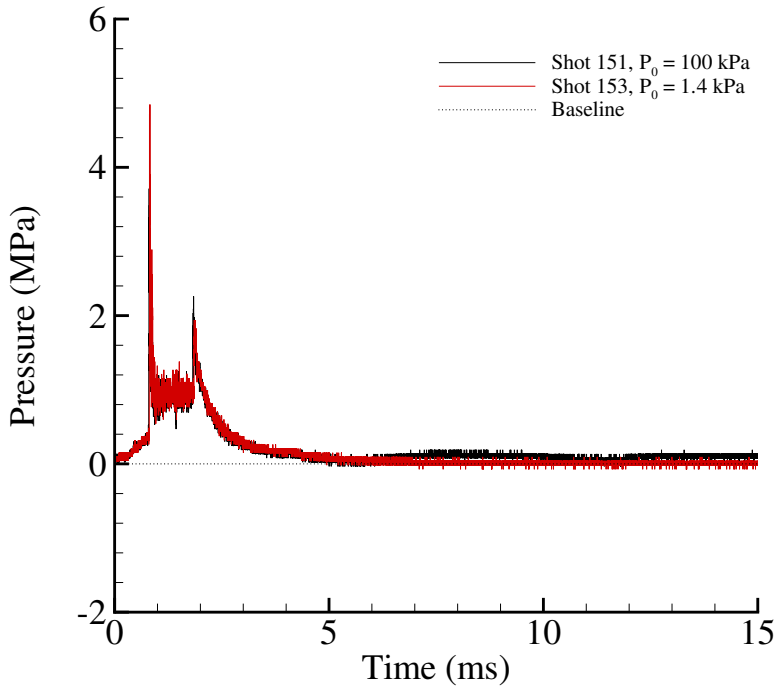

Figure 5.14: Thrust surface pressure history obtained with the 12°-0.6 m nozzle for P_0 equal to 100 kPa and 1.4 kPa.

the shorter 12° half angle nozzle. However, a smaller change in impulse was observed in response to a change in the environment pressure as compared to the 12°-0.6m nozzle because of their smaller volumes. When the environment pressure reaches approximately 10 kPa, the impulse is observed to reach a minimum. At this point the tamper mass is sufficiently small such that the partial fill effect is negligible. The nozzle expands the flow and the walls of the nozzle experience a positive pressure difference which also contributes to increase the impulse. For environment pressures less than 10 kPa, the impulse increases with decreasing environment pressure. As expected, the shorter 12° half angle nozzle expands the flow less than that longer one does. Note that the maximum increase in impulse due to flow expansion at the lowest P_0 is less than the increase in impulse due to the partial fill effect at $P_0 = 100$ kPa. This is likely due to significant flow separation from the nozzle walls at $P_0 = 100$ kPa as is discussed in §5.3.4

5.2.3 Converging-diverging nozzles

The two diverging nozzles with a 12° half angle were tested with the three converging-diverging sections described in §2.5.3. The experimental data appears in Fig. 5.15 for the 0.3 m nozzle and in Fig. 5.16 for the 0.6 m nozzle as a function of the environment pressure.

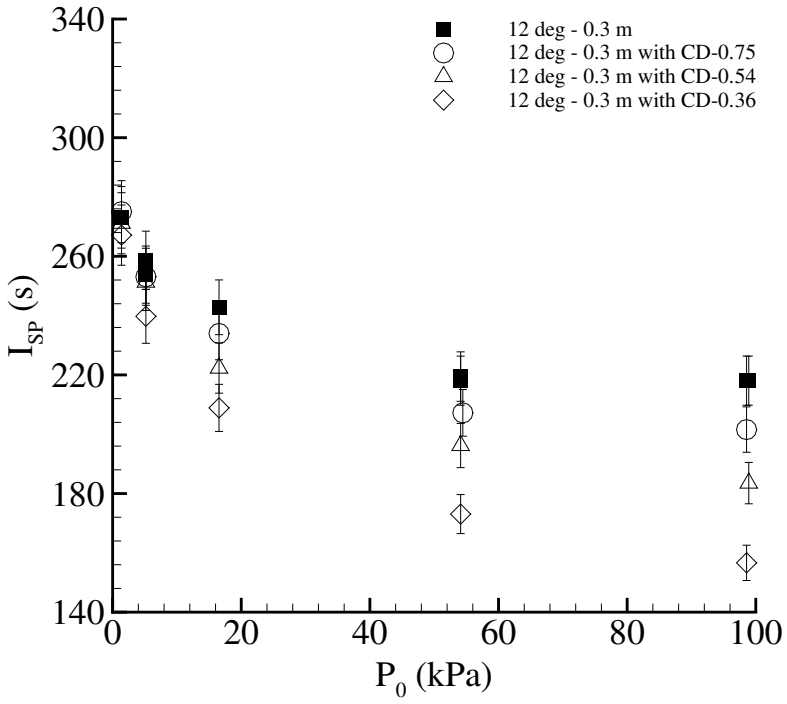

Figure 5.15: Specific impulse data for the 12° half angle nozzles with converging-diverging sections as a function of the environment pressure.

Analyzing the control volume shown in Fig. 5.17 for the case with a converging-diverging nozzle requires consideration of the nozzle surfaces that have x-direction components such as the thrust surface A_{TS}, the converging portion of the nozzle A_C, and the diverging portion of the nozzle A_D. The total force on the tube depends not only on the time-varying pressure on the thrust surface, but also the time-varying

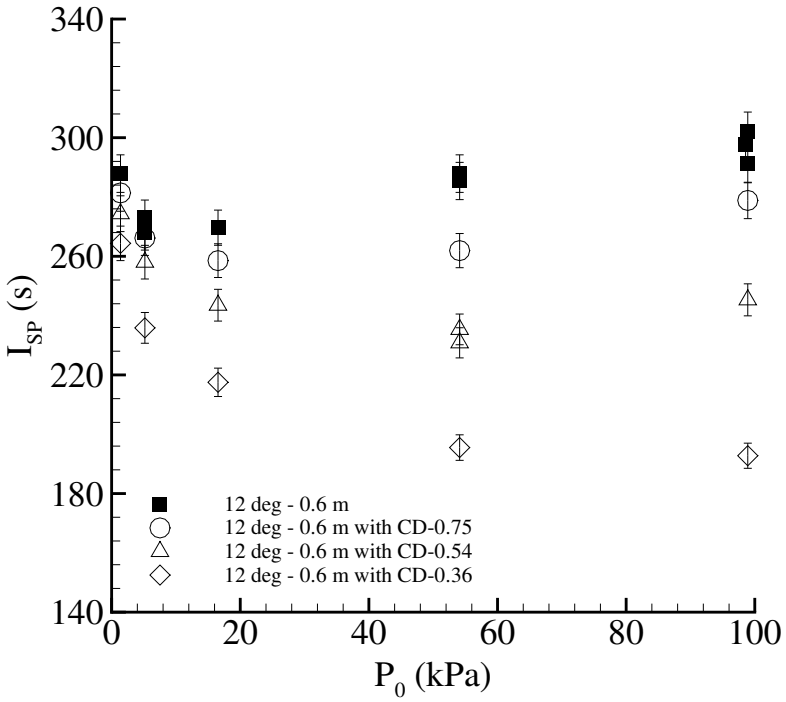

Figure 5.16: Specific impulse data for the 12° half angle nozzles with converging-diverging sections as a function of the environment pressure.

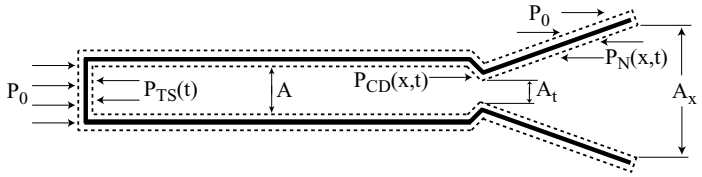

Figure 5.17: Control volume for a tube with a converging-diverging nozzle.

pressure on these additional areas.

$$
\begin{aligned}
I = & \iint_{A_{TS}} [P_{TS}(t) - P_0]\hat{x} \cdot \hat{n} \; dAdt \\
& + \iint_{A_C} [P_0 - P_C(t)]\hat{x} \cdot \hat{n} \; dAdt \\
& + \iint_{A_D} [P_D(t) - P_0]\hat{x} \cdot \hat{n} \; dAdt
\end{aligned} \tag{5.2}
$$

Where pressure P_C acts on area A_C, pressure P_D acts on area A_D, $\hat{n}$ is a unit vector

normal to each surface, $\hat{x}$ is a unit vector aligned with the x-axis which is the desired direction of motion.

The relative size of these three force contributions determines the impulse. When the environment pressure is large, the impulse decreases as the throat area decreases. This can be attributed to the presence of large regions of separated flow in the diverging portion of the nozzle and so the contribution of the third term in Eq. 5.2 is small. The second term is negative and increases in absolute magnitude as the throat becomes smaller resulting in a net decrease in impulse. For the nozzle with a length of 0.3 m, a maximum loss impulse of 27% was observed with the most restrictive converging-diverging section whereas a 42% loss in impulse was observed for the 0.6 m long nozzle. Estimating the loss in impulse by decreasing the throat area by 36% (as is the case for the data of CD-0.36 in Figs. 5.15 and 5.16) results in a 36% loss in impulse if the impulse model is used $I = KV/U_{CU}(P_3 - P_0)$ where $V = AL$ and the state 3 pressure is assumed to equal the pressure on the convergent portion of the nozzle A_C.

As the environment pressure decreases, the effect of the converging-diverging restrictions decreases such that at $P_0 = 1.4$ kPa, each nozzle configuration gives approximately the same value of impulse. In this situation, the large pressure ratio across the nozzle dominates the impulse. While the second term of Eq. 5.2 acts to decrease the impulse, the flow expansion and a positive pressure differential across the diverging nozzle walls is significantly greater and the third term of Eq. 5.2 acts to increase the impulse.

Sample thrust surface pressure histories are presented in Fig. 5.18 for the 12°-0.3 m nozzle with the most and least restrictive converging-diverging sections and environment pressures of (a) 100 kPa and (b) 1.4 kPa. Multiple wave reflections are observed for the most restrictive converging-diverging section.

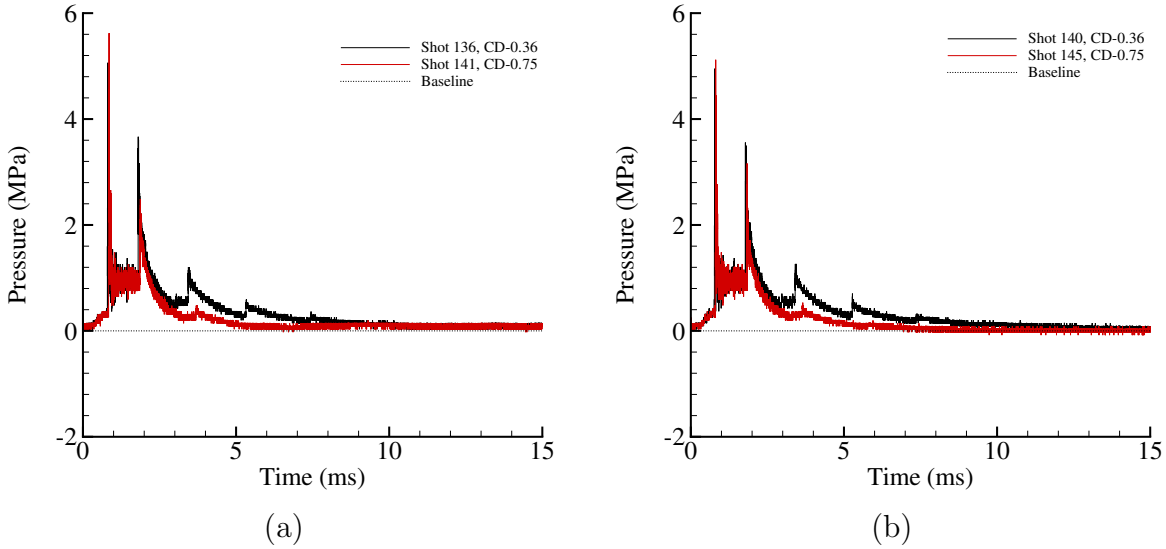

Figure 5.18: Specific impulse data for the 12°-0.3 m nozzles with converging-diverging sections for environment pressures of (a) 100 kPa and (b) 1.4 kPa.

5.2.4 Comparisons

The diverging nozzles with the 8° and 12° half angles are plotted together in Fig. 5.19 illustrating the effect of the half angle (compare data for the 8°-0.3 m and 12°-0.3 m nozzles) and the effect of nozzle length (compare data for the 12°-0.3 m and 12°-0.6 m nozzles).

The partial fill effect has been previously observed for the different nozzles as the environment pressure decreases from 100 kPa. The nozzle with the largest volume generates the largest increases in impulse over the baseline case of a plain tube. As previously observed, the nozzle dimensions also affect how quickly the impulse decreases as the environment pressure decreases. For example, the impulse from the 12°-0.6 m with the largest volume experiences the largest decrease in impulse as compared to the other diverging nozzles when the environment pressure decreases from 100 to 54.5 kPa. The impulse from the 12°-0.3 nozzle which has the second largest volume is actually observed to remain constant as the environment pressure decreases from 100 to 54.5. The impulse from the 8°-0.3m nozzle which has the smallest volume of the diverging nozzles is just observed to increase as the environment pressure de-

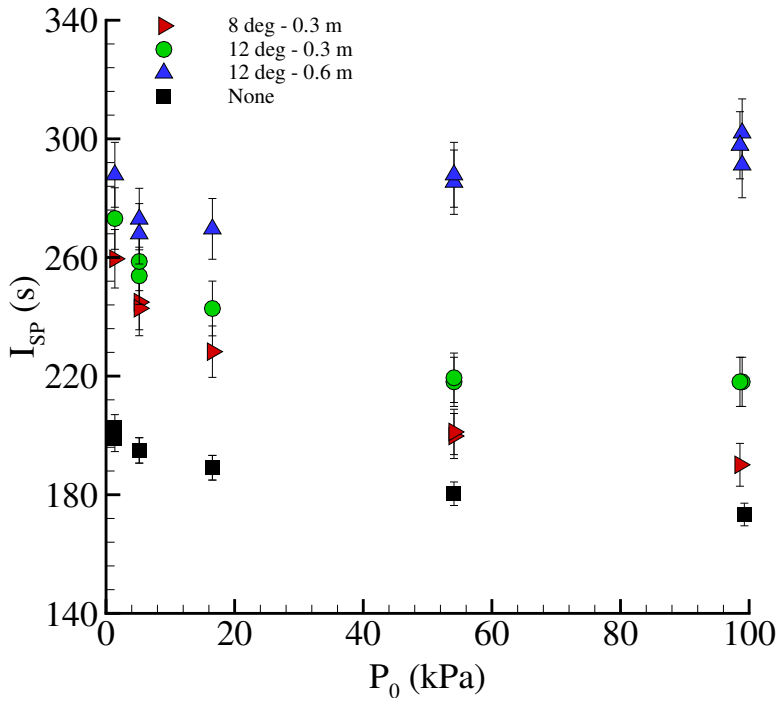

Figure 5.19: Specific impulse as a function of environment pressure for detonation tubes with diverging nozzles.

creases. In this case, the increase in impulse due to the increased pressure differential across the thrust surface is sufficiently large enough to exceed the decrease in impulse caused by a reduction in the tamper mass as the environment pressure decreases from 100 to 54.5 kPa.

For each diverging nozzle there is an environment pressure where neither the tamper mass or the flow expansion of the nozzle dominate the impulse. This point is observed most clearly for the large 12°-0.6m nozzle between environment pressures of 16.5 and 5.2. For the shorter 12°-0.3m nozzle this occurs between 100 and 54.5 kPa. This point is not observed for the 8°-0.3m nozzle as the expansion by the nozzle seems to always dominate the impulse.

Comparison of the 8°-0.3m nozzle and the straight extension clearly show the effect of these competing processes for two nozzles with the same volume. Their impulse data are plotted in Fig. 5.20. These two nozzles have approximately the same explosive mass fraction at $P_0 = 100$ kPa, yet the straight extension generates

a higher impulse. As P_0 decreases and the tamper mass goes to zero, the diverging nozzle generates higher values of impulse due to the flow expansion provided by the divergent shape.

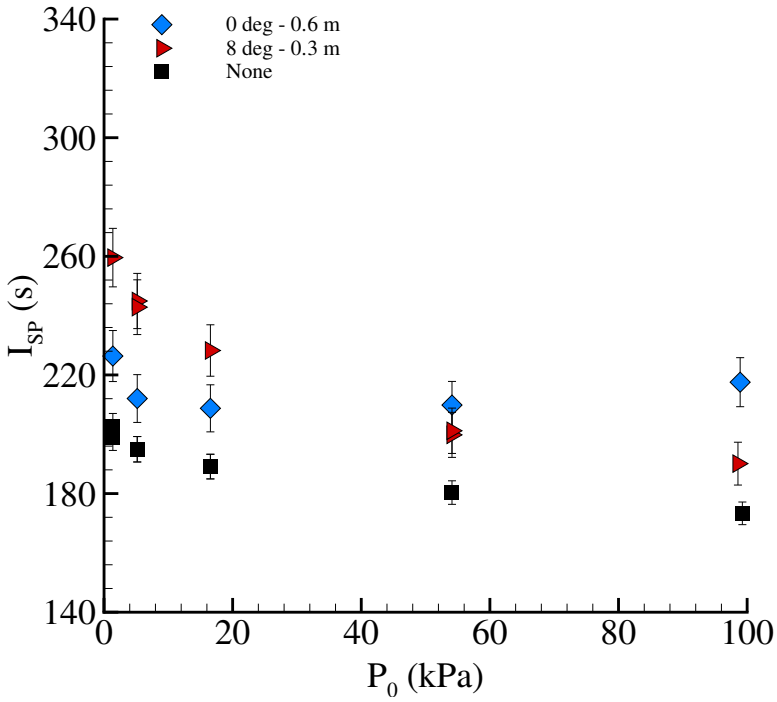

Figure 5.20: Specific impulse as a function of environment pressure for detonation tubes with the straight extension and the 8°-0.3 m nozzle.

5.3 Data analysis assuming quasi-steady nozzle flow

The experimental impulse data suggests that quasi-steady flow expansion occurs within the nozzles at the lowest environment pressures tested where the partial fill effects due to the tamper mass are negligible (Fig. 5.19). Based on this observation and the lack of other analysis methods for nozzles on detonation tubes, it is of value to analyze the measured impulse data assuming that quasi-steady nozzle flow is established. For this analysis to be reasonable, several crucial assumptions have be made about the detonation tube nozzle flow.

First, it is assumed that quasi-steady flow is established within the nozzle for a

significant portion of the blowdown process. This implies a rapid startup time and that the time of unchoking at the nozzle inlet occurs late in the blowdown process. The startup time is defined as the time between when the transmitted shock enters the nozzle inlet until the establishment of quasi-steady flow and is known (Amann, 1969, Smith, 1966) to depend on the initial nozzle pressure ratio. At large values of P_0 where the pressure ratio P_3/P_0 is small, the establishment of quasi-steady nozzle flow is not expected to occur. However, at the lowest values of P_0 and large values of P_3/P_0, rapid startup of the nozzle is expected and the majority of the blowdown process proceeds with quasi-steady nozzle flow.

Second, it is assumed that the decrease in pressure upstream of the nozzle inlet does not significantly affect the quasi-steady nozzle flow and that this pressure decrease can be modeled. In steady flow devices with constant-rate combustion occurring upstream of the nozzle, the nozzle inlet conditions are constant in time. This is not the case for a detonation tube which contains the unsteady processes of detonation propagation and the subsequent unsteady blowdown to ambient pressure.

If these effects are assumed to be minor or can be reasonably modeled, then the impulse from a detonation tube with a nozzle can be compared to the impulse from an ideal, steady flow nozzle with the same dimensions. In the case of a steady flow nozzle, the exhaust gas velocity at the nozzle exit plane determines the specific impulse if the exhaust gases are pressure matched to the environment and the total force on the engine equals $\dot{m}u_x$.

$$I_{sp} = \frac{I}{\int_0^t \dot{m}gdt} = \frac{\int_0^t \dot{m}u_x dt}{\int_0^t \dot{m}gdt} = \frac{u_x}{g} \tag{5.3}$$

This force is determined by drawing a control volume around the device as illustrated in Fig. 5.21 and recognizing that the mass flow of the exhaust $\dot{m}$ is constant in time.

When this same control volume is applied to a detonation tube, the unsteadiness of the flow must be considered. The general unsteady mass conservation for the control volume is

$$\frac{d\mathcal{M}}{dt} + \dot{m}(t) = 0 \tag{5.4}$$

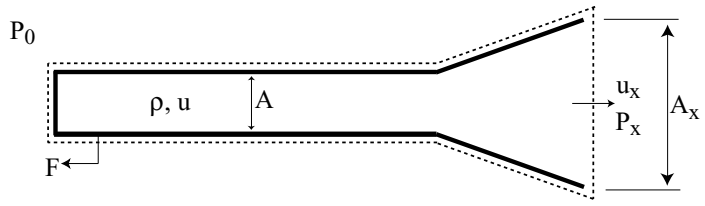

Figure 5.21: Control volume surrounding engine.

The general unsteady momentum conservation for the control volume consists of the pressure forces and the exhaust gas momentum.

$$F(t) = \dot{m}(t)u_x(t) + A_x[P_x(t) - P_0] + \frac{d}{dt}\int_V \rho u dV \tag{5.5}$$

When the nozzle inlet flow is choked, the mass flow rate depends on the throat area, the upstream pressure, and the product gas state $T_i/\mathcal{W}$. The detonation tube pressure decreases through the blowdown process and so the mass flow rate will also decrease. For pressure-matched nozzle exit conditions, the middle term of Eq. 5.5 is zero. The last term corresponds to the unsteady variation of momentum inside the control volume. This term is typically considered to be zero in steady flow devices where the combustion chamber cross section is large compared to the nozzle section. In this case, the nozzle approach velocity is typically small and the change in momentum due to this increase in velocity can be neglected (Sutton, 1992). In the case of a detonation tube, not only is the tube diameter equal to the nozzle inlet diameter but the unsteady waves inside the tube alter the gas momentum over time. The detonation wave increases the gas momentum which is subsequently decreased by expansion through the Taylor wave. Particles behind the Taylor wave are at state 3 and have zero velocity and their unsteady variation of momentum is zero. Their momentum is increased after they pass through the reflected wave from the open tube end and they accelerate away from the thrust surface and out of the tube. Thus, the third term of Eq. 5.5 is expected to be positive when considering a detonation tube but, for the later purpose of using the analysis of steady nozzle flows, this term is

assumed to be small.

As discussed, the assumptions that have been made are numerous but necessary in order to use the standard equations of ideal, steady flow analysis to analyze the experimental data for detonation tubes with nozzles. To do so, the experimental measurements of specific impulse are converted into an average exhaust velocity $\overline{u_x}$ with Eq. 5.3 that is comparable to the constant exhaust velocity u_x of the steady flow analysis. The merit of conducting this analysis is to generate an ultimate measure of performance for detonation tubes with nozzles. Analysis methods that consider all the unsteadiness of the device would require detailed numerical calculations for each specific configuration. Therefore, steady flow through the nozzle is presently assumed and the methods of calculation appear in the next section. The non-ideal processes such as the change in the nozzle inlet conditions, boundary layer separation, the partial fill effects, and the transient flow startup time that can be modeled or estimated are discussed in more detail in later sections.

5.3.1 Steady flow nozzle calculations

The inlet state to the detonation tube nozzle must be carefully chosen to facilitate an appropriate comparison between the calculated exhaust gas velocity from Eq. 5.3 using the experimental data and the predicted exhaust gas velocity based on steady flow expansion. This choice is complicated by the unsteady wave processes that propagate through the tube. In the case of a finite length tube, a reflected expansion wave is generated that propagates through the products towards the thrust surface once the detonation wave reaches the open end of the tube. This unsteady expansion accelerates the flow from zero velocity at state 3 to a nonzero velocity out of the tube. For a tube without a nozzle, the flow is accelerated to sonic conditions at the open end. When a nozzle is attached, sonic conditions are assumed to exist at the nozzle inlet. The flow velocity at this sonic point is calculated assuming the flow steadily and adiabatically expands from state 3 to sonic conditions such that the total enthalpy

remains constant and equal to the enthalpy at state 3.

$$u(P) = \sqrt{2[h_3 - h(P)]} \tag{5.6}$$

From the sonic point, the flow is steadily expanded by the nozzle and the thermodynamic states throughout the nozzle can be calculated in three ways. First, the extreme assumptions of either equilibrium or frozen flow can be made and thermodynamic computations carried out to obtain the enthalpy as a function of pressure on the isentrope. Second, elementary perfect gas relationships can be used to get analytic formulas for exhaust velocity as a function of pressure. Third, steady flow simulations with a detailed chemical reaction mechanisms for specific nozzle geometries can be carried out to find exit conditions and specific impulses.

With the extreme assumptions of either equilibrium or frozen composition, the nozzle flow is calculated using STANJAN (Reynolds, 1986). The results of flow velocity as a function of pressure are plotted in Fig. 5.22 starting from state 3, expanding to the sonic point, and then through the nozzle. A limiting velocity and specific impulse is predicted from the expansion to low pressures.

$$u \rightarrow u_{max} = \lim_{P \rightarrow 0} \sqrt{2[h_t - h(P)]} \tag{5.7}$$

In general, since $h = h(\mathbf{Y}, T)$, species and temperature variations need to be related to the pressure variation in order to predict h.

The second method for calculating the nozzle flow is with the perfect gas relationships, the result of which (Eq. 1.8) is rewritten in Eq. 5.8.

$$u_x = \sqrt{\frac{2\gamma}{\gamma - 1} R T_i \left[1 - \left(\frac{P_x}{P_i} \right)^{(\gamma-1)/\gamma} \right] + u_i^2} \tag{5.8}$$

Equation 5.8 can be solved for any known inlet conditions $P_i, u_i, \gamma, T_i/\mathcal{W}$. The corresponding temperature at any state is determined from the isentropic relation $T \sim P^{(\gamma-1)/\gamma}$ and the area is determined from the mass equation $d(\rho u A) = 0$. How-

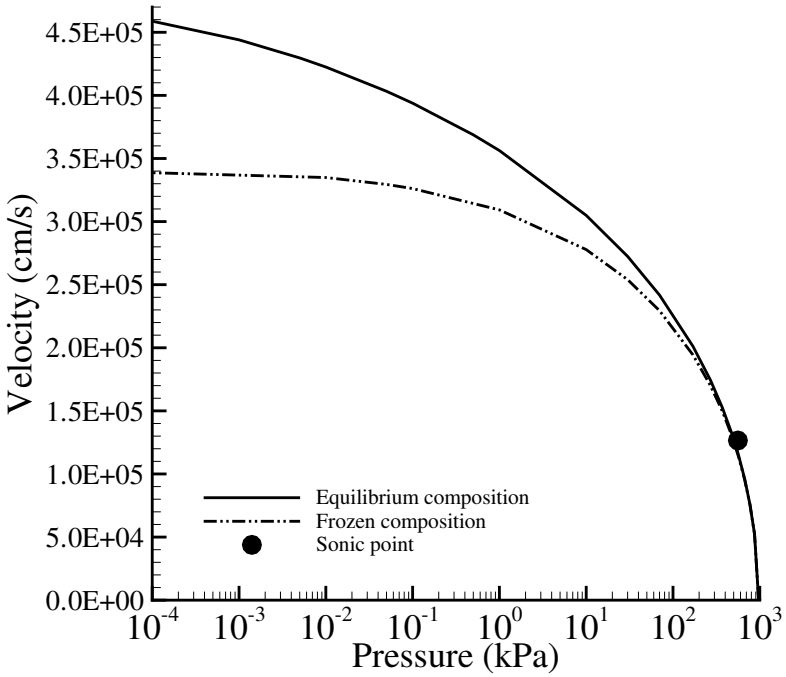

Figure 5.22: Acceleration of flow from state 3 through the sonic point and subsequent nozzle assuming either equilibrium or frozen composition.

ever, Eq. 5.8 uses a constant value of γ and product gas molecular weight, so the effect of species variation within the expansion is not considered.

Finally, the third method for calculating nozzle flows utilizes detailed chemical reaction mechanisms and finite rate kinetics. In the case of steady supersonic flow through rapidly diverging nozzles, the effects of finite rate kinetics can significantly affect the exit state and therefore, the measured impulse (Scofield and Hoffman, 1971). To evaluate this extent of chemical kinetics on the impulse in nozzles with dimensions similar to these experiments, the steady flow conservation equations in one-dimension with the species equation are solved.

$$\frac{d}{dx}\left(\rho u A\right) = 0 \tag{5.9}$$

$$\rho u \frac{du}{dx} + \frac{dP}{dx} = 0 \tag{5.10}$$

$$\frac{d}{dx}\left(h + \frac{u^2}{2}\right) = 0 \tag{5.11}$$

$$u\frac{dY_i}{dx} = \Omega_i \tag{5.12}$$

For an adiabatic change, the energy equation can be written in terms of the thermicity.

$$\frac{dP}{dt} = c^2\frac{d\rho}{dt} + \rho c^2\dot{\sigma} \tag{5.13}$$

The thermicity term $\dot{\sigma}$ corresponds to the pressure change due to chemical reaction and c is the frozen sound speed. In the absence of chemical reaction, Eq. 5.13 reduces to $dP = c^2 d\rho$, the usual relationship for nonreactive isentropic flow.

Equation 5.13 is substituted into Eqs. 5.9-5.12 and the derivatives with respect to position are converted into derivatives with respect to time with the transformation $dt = dx/u$ (Eqs. 5.14-5.17). This means that a single particle is tracked, recording its state as a function of time. Since the flow field is steady, all particles have the same history.

$$\frac{dP}{dt} = \frac{\rho u^2}{1 - M^2}\left(\frac{u}{A}\frac{dA}{dx} - \dot{\sigma}\right) \tag{5.14}$$

$$\frac{d\rho}{dt} = \frac{\rho}{1 - M^2}\left(M^2\frac{u}{A}\frac{dA}{dx} - \dot{\sigma}\right) \tag{5.15}$$

$$\frac{dY_i}{dt} = \Omega_i \tag{5.16}$$

$$\frac{dx}{dt} = u \tag{5.17}$$

The Mach number M equals u/c. The area terms are solved from the prescribed nozzle shape A_N normalized by the throat area which equals the tube cross-section

A is these experiments.

$$\frac{A_N(x)}{A} = \left(1 + \frac{x\tan(\alpha)}{R_0}\right)^2 \tag{5.18}$$

The equations 5.14-5.18 are simultaneously integrated and the GRI3Mech mechanism is used to obtain real gas enthalpies and reaction rates. A series of computations with different nozzle half angles between 2.5° and 13.2° were carried out for an ethylene-oxygen mixture with 80 kPa initial pressure. The starting condition for the calculation is the state parameters and species amounts at the sonic point (Fig. 5.22). The resulting gas velocity through the nozzle as the pressure decreases is plotted in Fig. 5.23 for the different half angles with the equilibrium and frozen composition results of Fig. 5.22.

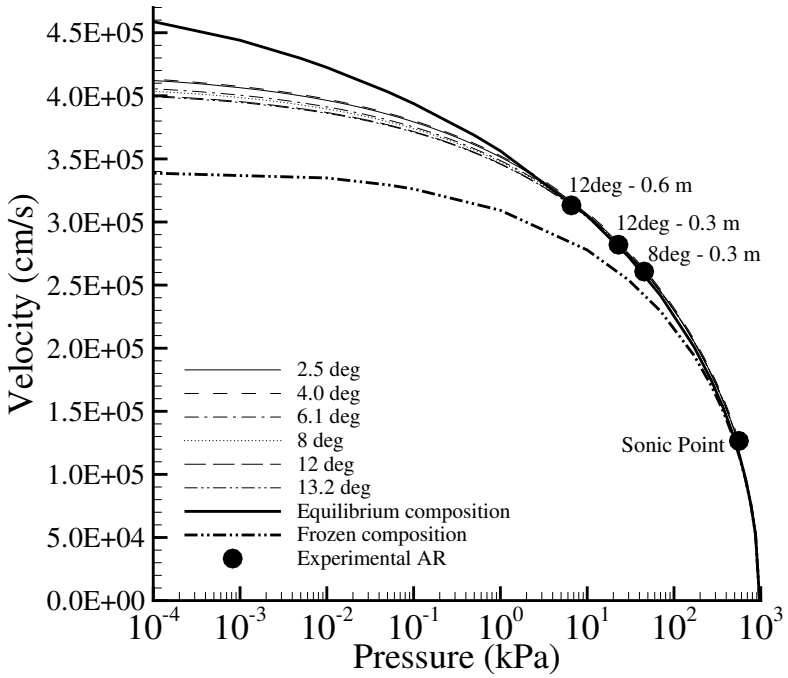

Figure 5.23: Comparison of flow velocity considering finite rate kinetics compared to thermodynamic calculations considering equilibrium and frozen composition as a function of pressure.

The flow expansion considering finite rate chemical kinetics follows that of the equilibrium predictions until the pressure has decreased to approximately 10 kPa. At

this point, the flow velocity calculated with finite rate kinetics is greater than the velocity predicted with frozen composition but less than the velocity predicted with equilibrium composition. Investigation of the species mole fractions as a function of pressure identify that the mole fractions of H_2O stop changing once the pressure reaches approximately 10 kPa and the mole fractions of CO_2 stop changing once the pressure reaches approximately 1 kPa (Fig. 5.24). As the pressure continues to decrease, these species amounts are frozen at values between 0.32 and 0.34 for H_2O and 0.25 and 0.30 for CO_2 depending on the nozzle half angle. Variations in the OH mole fractions (Fig. 5.25a) for the different nozzle half angles are small by comparison.

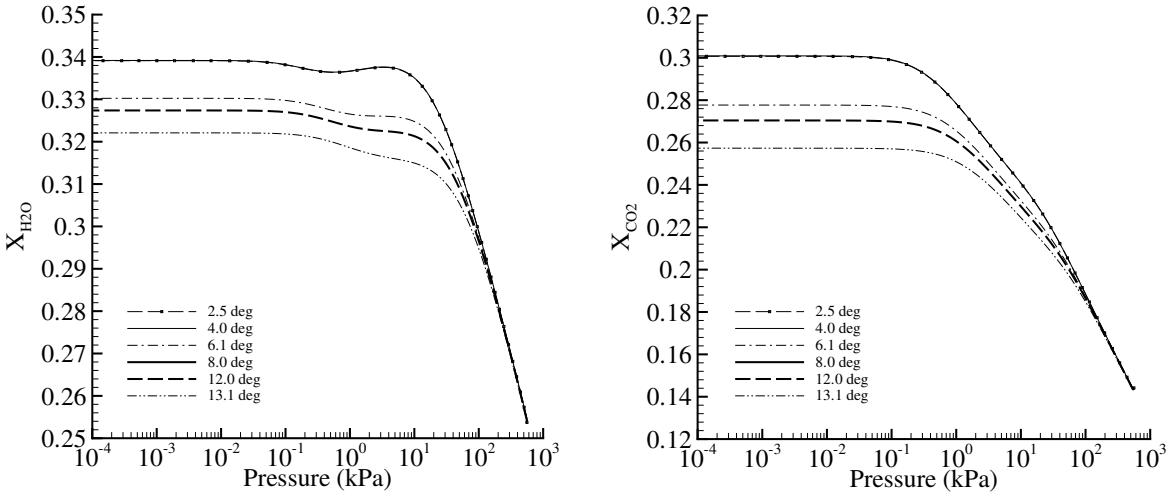

(a) (b)

Figure 5.24: Mole fractions of (a) H_2O and (b) CO_2 molecules as a function of pressure for different half angle diverging nozzles.

At equilibrium, the mole fractions for both H_2O and CO_2 should approach 0.5,

$$C_2H_4 + 3O_2 \rightarrow 2H_2O + 2CO_2$$

but this is not the case when the finite chemical reaction rates are considered as observed in Fig. 5.24. The nozzle with the smallest half angle of 2.5° yields the highest mole fractions for H_2O and CO_2 due to the slower rate of pressure decrease (Fig. 5.26) unlike that of the nozzle with a large half angle. As the flow expands, the recombination and dissociation reactions are important. The recombination reactions

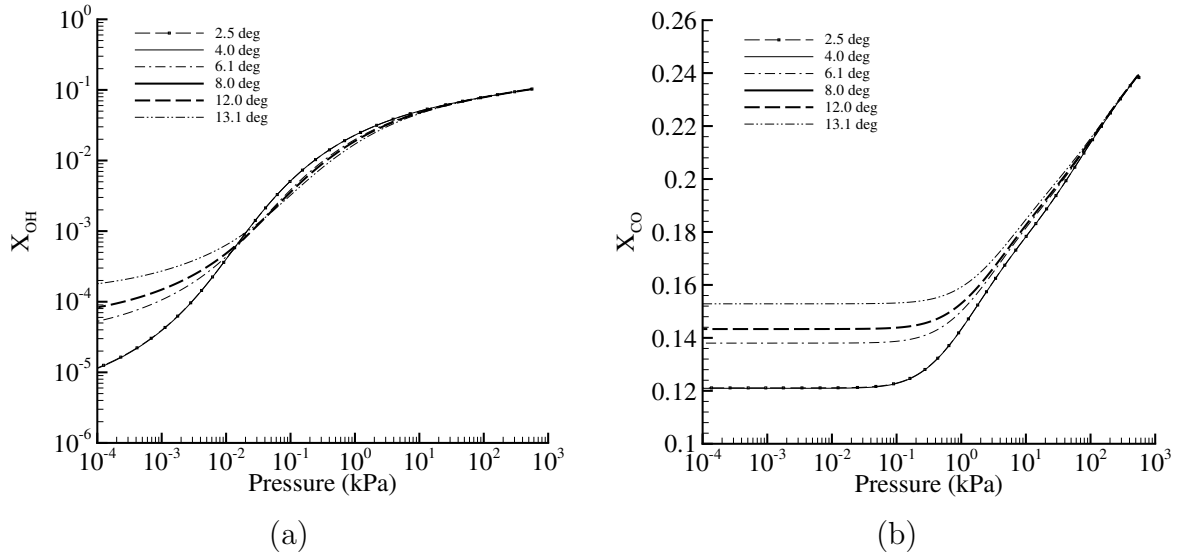

(a) (b)

Figure 5.25: Mole fractions of (a) OH and (b) CO molecules as a function of pressure for different half angle diverging nozzles.

release energy into the flow, elevating the temperature and pressure over the case with no chemical reaction. This recombination results in an increase in the amounts of H_2O and CO_2 (Fig. 5.24) and a decrease in the amount of OH and CO (Fig. 5.25). The mole fractions for the species of Figs. 5.24 and 5.25 do not sum to one for any of the half angles. The missing atoms are found to be in smaller amounts in the O, H, and O_2 species.

Also plotted on Fig. 5.23 are points corresponding to the area ratios of the experimental nozzles. These points indicate the predicted pressure and velocity of the product gases at the exit plane of each nozzle assuming steady expansion and pressure matched conditions. Their locations on the velocity-pressure curve indicate that, in the present experiments, the products are in equilibrium throughout the entire expansion process. Another method to estimate whether or not the products are in equilibrium throughout the nozzle is to predict the Damkohler numbers for each nozzle. The Damkohler number is used to describe the extent of chemical non-equilibrium in terms of the characteristic timescales of chemical reaction and fluid motion and is

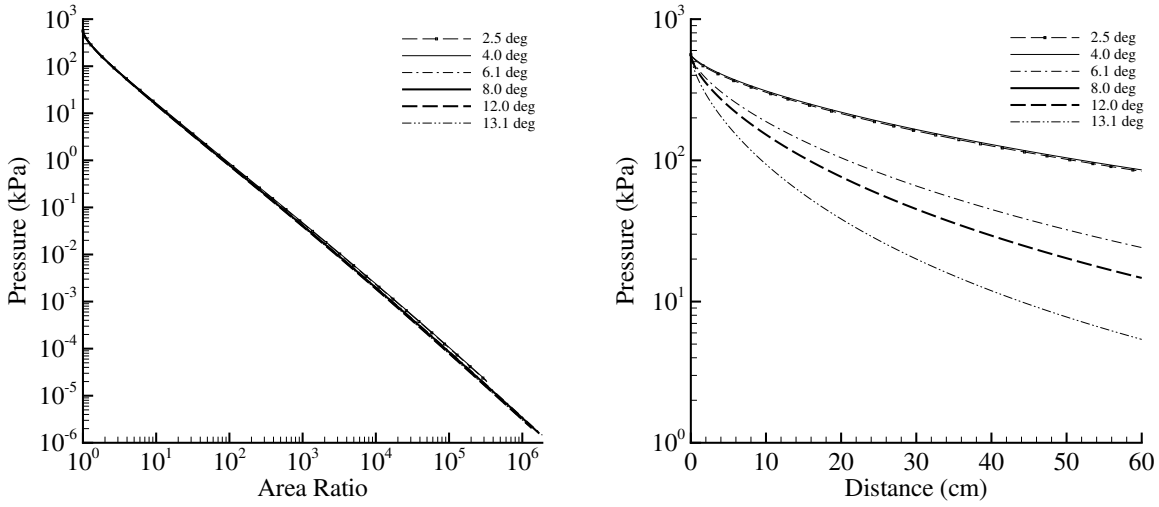

Figure 5.26: Pressure as a function of (a) area ratio and (b) distance from the nozzle throat for different half angles assuming finite reaction rates.

discussed in more detail in Chapter 6.

$$Da = \frac{t_{chem}}{t_{flow}} \tag{5.19}$$

High nozzle divergence results in fast flow expansion so the pressure decreases at a rate that is much faster than the time required for the chemical reactions to respond. The species amounts do not adjust, the flow is said to be chemically frozen, and $Da \gg 1$. Alternatively, low nozzle divergence results in slow expansion of the flow. Under this modest pressure decrease, the chemical reactions are able to adjust sufficiently fast and remain in near equilibrium. In this case, $Da \ll 1$. At the nozzle inlet the chemical timescale t_{chem} behind the detonation wave is estimated from the eigenvalue analysis with a method described in Chapter 6 and the timescale of fluid motion is estimated with c_3/L where L is the nozzle length (Table 5.5). The Damkohler numbers are less than one or close to one indicating that equilibrium composition is expected for the nozzles in this study, which is in agreement with Fig. 5.23.

The experimental values of $\overline{u_x}$ determined from the measured values of I_{sp} are plotted in Fig. 5.27 with the steady flow predictions of velocity as a function of

	$P_1 - 60$ kPa	$P_1 = 100$ kPa
t_{chem}	420 μs	160 μs
t_{flow} for $L = 0.3$ m	252 μs	249 μs
t_{flow} for $L = 0.6$ m	504 μs	498 μs
Da for $L = 0.3$ m	1.67	0.64
Da for $L = 0.6$ m	0.83	0.32

Table 5.5: Tabulated timescales in expanding flow through a nozzle.

pressure. The experimental values of $\overline{u_x}$ are observed to increase with decreasing environment pressure as do the predictions based on steady nozzle flow. However, as expected, the experimental values are lower than the steady predictions due to the unsteadiness of the flow and the fact that the exhaust gases are not pressure-matched to the environment pressure during the entire blowdown event as is assumed when using Eq. 5.3. The next sections discuss in more detail some of the non-ideal effects

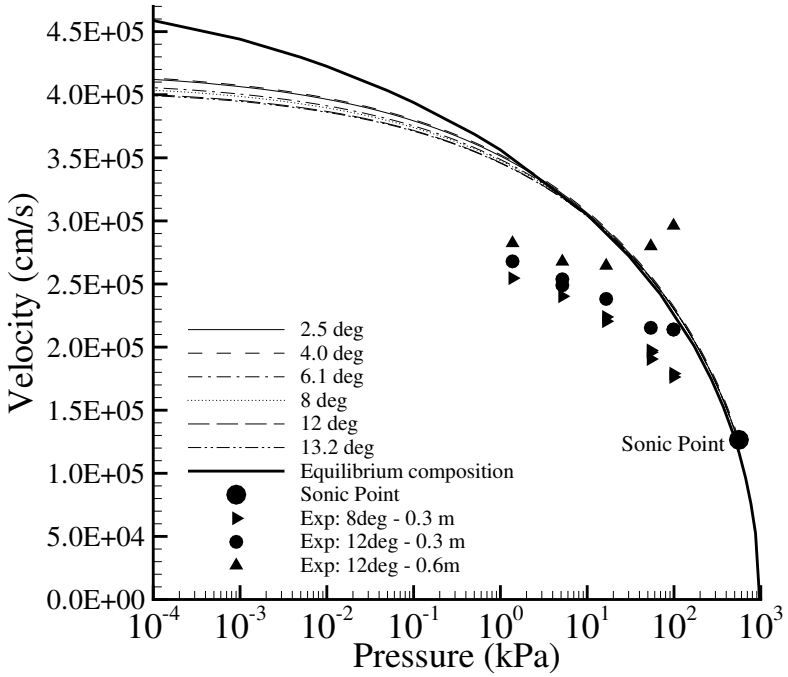

Figure 5.27: Steady flow predictions of velocity as a function of pressure. Also plotted are the experimental data of exhaust velocity calculated with Eq. 5.3.

present in detonation tube nozzles.

5.3.2 Changing nozzle inlet state

The unsteadiness of the detonation tube means that the nozzle inlet state that was previously based on state 3 is not constant in time. After the first characteristic of the Taylor wave reflects off the open tube end and reaches the thrust surface, the pressure is decreasing at all locations within the tube. Thus, calculation of the inlet state based on state 3 is not reasonable. A better choice from which to start the expansion to the sonic point is to determine an intermediate pressure that represents the average pressure within the tube over the entire cycle. Averaging the experimental pressure traces obtained for mixtures with an initial pressure of 80 kPa yields an intermediate value of 400 kPa. Starting the expansion with this average value for the pressure results in steady flow predictions that better represent the experimental data as shown in Fig. 5.28. Here it is significant to note that several of the data

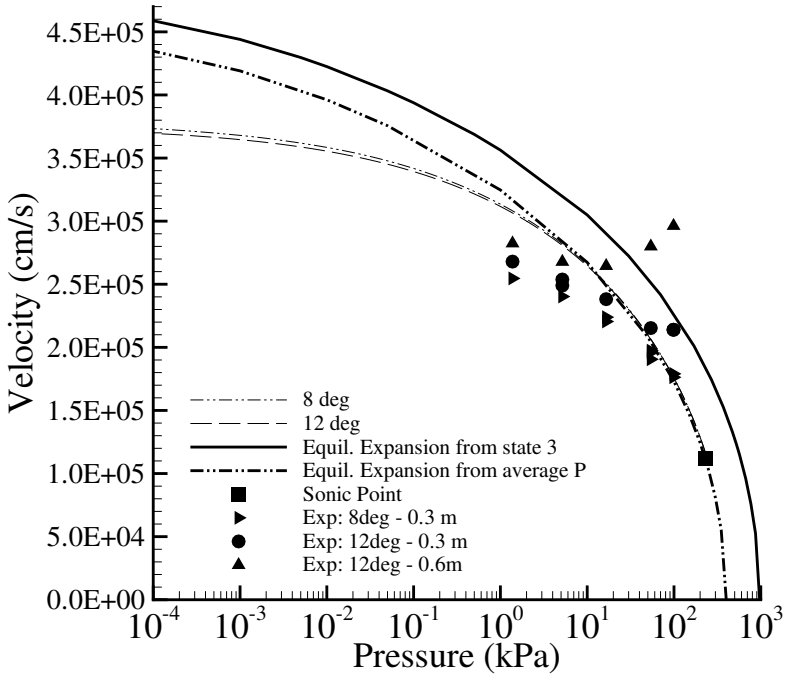

Figure 5.28: Equilibrium and finite rate calculations starting from an average tube pressure of 400 kPa compared with equilibrium calculations starting from the state 3 pressure of 970 kPa.

points, in particular those for the 12°-0.6m nozzle and pressures greater than 10 kPa

and those for the 12°-0.3m nozzle and pressures greater than 50 kPa, do not follow the trend of the other data for the same nozzle. For these data points, the tamper mass of the nozzle is large enough such that the partial fill effect discussed in Chapter 3 can be seen to dominate the impulse.

5.3.3 Partial fill effects

The explosive mass fractions for each nozzle and environment pressure were given in Tables 5.1-5.4 and the data is plotted with the Gurney model (Eq. 3.30) in Fig. 5.29. The experimental data with nozzles is normalized by $I_{sp}^{\circ} = 173$ s which is the experimentally measured value from a fully filled tube without a nozzle and a 105 μm thick diaphragm at an initial pressure of 80 kPa.

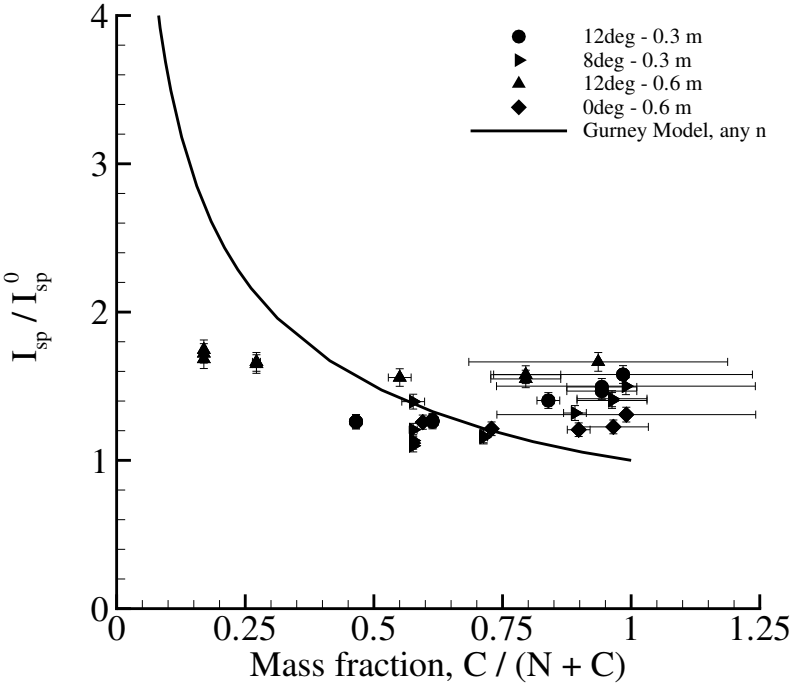

Figure 5.29: Normalized specific impulse as a function of the explosive mass fraction. The Gurney model of Eq. 3.30 is plotted with the experimental data for tubes with nozzles.

The experimental data of Fig. 5.29 can be divided into three groups. The first group has mass fractions less than 0.4. This data corresponds to the highest en-

vironment pressure and the largest nozzle. The partial fill model is based on one-dimensional geometries and overpredicts the impulse obtained with a tube and a diverging nozzle. Thus, when the partial fill effect of the tamper dominates the impulse a larger increase in impulse is gained with a straight extension rather than a diverging nozzle. For these cases of large nozzles and high environment pressures, the partial fill effect is of greatest importance. This effect lessens as the environment pressure decreases and the explosive mass fraction increases.

For intermediate mass fractions between 0.4 and 0.75, the partial fill model is in reasonable agreement with the data. This data corresponds to the nozzles with the smallest volumes where the effect of the divergent shape is minimized and the larger environment pressures. The data of the straight extension at the larger environment pressures is observed to be best predicted by the partial fill model for this range of explosive mass fractions.

The data at the highest mass fractions, greater than 0.75, correspond to all of the nozzles and the lowest environment pressures. It is obvious that the experimental results are uncorrelated with the explosive mass fraction for this situation. In this regime, quasi-steady flow is important and the analysis of the previous section applies. The partial fill model is not able to model the increased blowdown time and flow expansion that occurs within the nozzle.

5.3.4 Boundary layer separation

Sutton (1992) states that a rough criterion for jet separation is when the nozzle exit pressure is less than or equal to 0.4 times the environment pressure. In other words, as long as the nozzles exhaust at a pressure that is greater than $0.4 \times P_0$, then flow separation of the boundary layer from the nozzle walls is not expected. Sutton (1992) states that other factors such as the pressure gradient, nozzle contour, boundary layer, and flow stability affect separation in addition to the nozzle exit pressure and the environment pressure.

Due to the dearth of research of flow through detonation tube nozzles, the general

relationship for flow separation must suffice. An estimation of the nozzle exit pressure is obtained from the previous steady flow predictions with finite rate kinetics at the area ratios that correspond to the experimental nozzles. Since the results based on an average tube pressure for the nozzle inlet condition (Fig. 5.28) best represent the experimental data, these results are used to determine the pressure. The pressure decrease through the nozzle is plotted in Fig. 5.30 along with points corresponding to the area ratios of the experimental nozzles. The separation criteria for each of the experimentally tested environment pressures between 100 kPa and 1.4 kPa are also indicated.

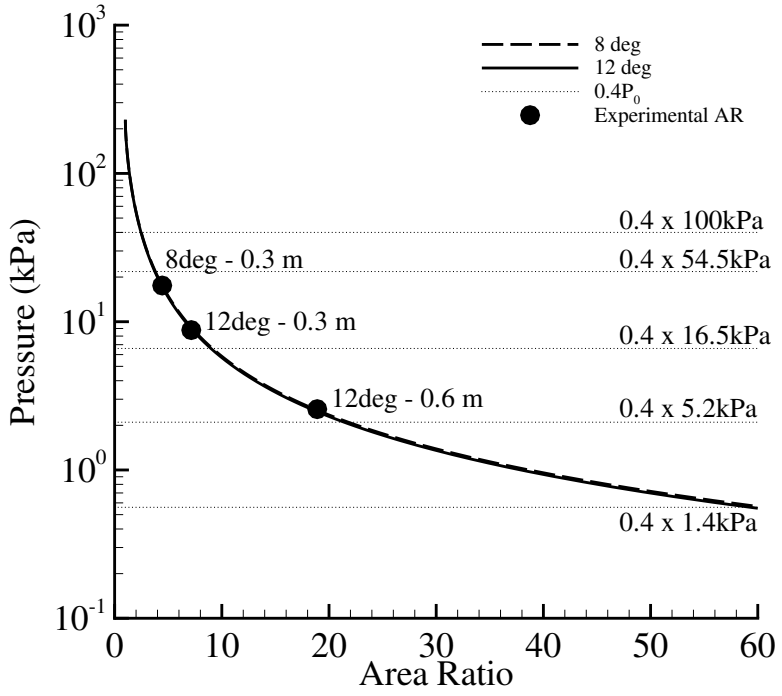

Figure 5.30: Pressure decay in nozzles assuming steady flow and comparisons to the expected separation pressure in the experimental tests.

It is important to note that the relationship between for the pressure-area ratio relationship of Fig. 5.30 is for a nozzle inlet pressure equal to the average tube pressure. Towards the end of the blowdown process this nozzle inlet pressure may be sufficiently lower than the average pressure such that Fig. 5.30 is no longer valid. Instead, the curve will be shifted to lower pressures increasing the likelihood that

separation will occur and to occur closer to the nozzle inlet. As the tube pressure continues to decrease, the separation point will travel closer to the nozzle throat. When the separation point passes through the nozzle inlet, unchoking occurs and the flowfield becomes entirely subsonic. This event is assumed to occur late in the blowdown process.

For the initial times when Fig. 5.30 applies, the 8°-0.3 m nozzle is expected to separate when operated in environment pressures of 54.5 kPa and greater. For all environment pressures below 54.5 kPa, Fig. 5.30 predicts that no separation will occur. These same results are also valid for the shorter 12° nozzle. The longer 12° nozzle is expected to separate when operated in all environment pressures greater than 5.2 kPa. Only at the two lowest environment pressures tested of 5.2 and 1.4 kPa is separation not expected.

Overexpansion of the flow is predicted for the 12°-0.3 m nozzle exhausting into $P_0 = 16.5$ kPa and for the 12°-0.6 m nozzle exhausting into $P_0 = 5.2$ kPa. This is observed by comparing the predicted nozzle exhaust pressure (indicated by the solid dots in Fig. 5.30) to the environment pressure P_0 and to the expected separation pressure $0.4 \times P_0$. If the predicted nozzle exit pressure lies between P_0 and $0.4 \times P_0$ then the flow overexpands in the nozzle. Overexpansion of the flow is not desirable because the established pressure differential across the nozzle walls generates a force in the opposite direction of the pressure differential across the thrust surface. For this reason, separation within the nozzle is often preferred. Sutton (1992) states that nozzles with high area ratios that are typically designed for high altitude flight actually have a larger thrust when operated at sea level when separation is present than when operated at the design altitude. This similar effect is observed in the experimental data (Fig. 5.12) for the 12°-0.6 m nozzle where the impulse at 100 kPa is an average of 300 s while at $P_0 = 5.2$ kPa the impulse is 275 s. However, when the flow is highly separated, a large portion of the nozzle is not utilized so flight performance will suffer due to the additional engine weight and size.

5.3.5 Startup time

The nozzle startup time is defined as the time from when the transmitted shock wave enters the nozzle throat until time when quasi-steady flow is established. The presence of this transient nozzle flow has previously been studied in shock tunnels and rocket nozzles. A shock tunnel, illustrated in Fig. 5.31, uses a driver tube containing high pressure gas and a driven tube containing a low pressure gas. The two chambers

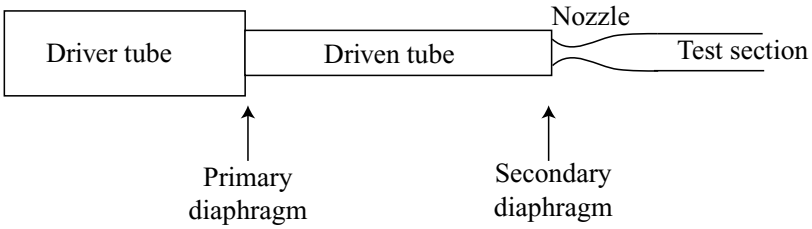

Figure 5.31: Schematic of shock tunnel facility.

are separated by the primary diaphragm that is ruptured generating a planar shock wave that is transmitted through the low pressure driven gas. This shock reaches the end of the driven tube and ruptures a second diaphragm at the nozzle inlet. This second diaphragm separates the low pressure gas in the driven tube from the evacuated conditions of the nozzle and test section.

Testing time is limited by the time needed to establish quasi-steady flow in the nozzle and the time when the contact surface between the driver and driven gases arrives at the nozzle inlet (Jacobs and Stalker, 1991). The time required for the contact surface to reach the nozzle inlet and contaminate the test gas depends on the dimensional specifics of the facility and the gas dynamics between the driver and driven tube. The nozzle startup time depends on the initial pressure ratio across the secondary diaphragm.

Early observations of the nozzle starting process were recorded in images taken by Amann (1969) and Smith (1966) in reflected shock tunnels. Successive shadowgraph images were used to measure the wave trajectories in the experiments of Amann (1969). The experiments were carried out in two–dimensional reflection nozzles with a 15° half angle. The nozzle inlet was either sharp or rounded. The incident shock

was of Mach 3. The schlieren images of Smith (1966) were taken downstream of the nozzle exit in an axisymmetric reflection nozzle with a 10° half angle with an incident shock wave of Mach 3.0 and 5.7. Wave trajectories were measured with thin-film heat transfer gauges and a pitot pressure gauge. In a more recent study by Saito and Takayama (1999), double exposure laser holographic interferometry was used to visualize the flow of a Mach 2.5 incident shock wave within a 15° half angle, two-dimensional reflection nozzle.

The starting processes observed in the nozzles were qualitatively similar in each study. Three important features observed in these flows are the primary shock, the secondary shock, and the contact surface. AMRITA simulations carried out with a Mach 3 incident shock wave and a 15° half angle nozzle illustrate these features (Fig. 5.32).

(a) (b) (c)

Figure 5.32: Frames from AMRITA inviscid simulation of starting process in a 15° half angle nozzle with an incident Mach 3 shock wave. Waves to note are the primary shock, contact surface, secondary shock, oblique expansions at throat, and forming of an incident shock in Frame c).

The transmitted primary shock and contact surface propagate through the nozzle with a decreasing velocity as a result of the divergent cross-section. Expansion fans originate behind the transmitted shock at the corners of the nozzle inlet and reflect on the nozzle axis. A secondary shock wave forms between the contact surface and nozzle inlet. This left-facing shock wave moves upstream relative to the fluid and is needed to match the high Mach number, low pressure flow exhausting from the inlet to the low Mach number, high pressure flow behind the primary shock. A model and subsequent calculation using the method of characteristics by Smith (1966) identifies

that an unsteady expansion must exist downstream of the nozzle inlet. Because the primary shock and contact surface decelerate, the characteristics in the post-shock flow rotate and become convergent resulting in the formation of the secondary shock at the tail of the unsteady expansion. Successful starting of the nozzle occurs when this secondary shock is swept downstream and out of the nozzle. At this time, quasi-steady flow exists within the nozzle. Failure of the nozzle to start occurs when the flow velocity coming from the inlet is not sufficient to prevent the secondary shock from reaching the nozzle inlet; the condition of sonic flow no longer exists at the throat and the downstream portion of the nozzle flow is completely subsonic.

Viscosity has also been shown to effect this starting process. The inviscid simulations of Igra et al. (1998) accurately model the experiments of Amann (1969) which lead them to conclude that the short startup time of their situation is not significantly affected by viscosity. However, in the experiments of Amann (1969) and Saito and Takayama (1999) which were also numerically simulated by Saito and Takayama (1999) and Tokarcik-Polsky and Cambier (1994), the secondary shock wave was observed to bifurcate at the wall creating a region of separated flow. While the numerical simulations correctly predicted the shock bifurcation at the wall, the downstream region of separated flow was not accurately modeled. This was attributed to the use of a laminar boundary layer model in the simulations. A Reynolds number calculation by Saito and Takayama (1999) suggests that the boundary layer is actually turbulent.

While shock tunnel experimenters strove to reduce the nozzle start time to maximize the test time, rocket nozzle developers sought to reduce the nozzle start time in order to prevent structural damage (Chen et al., 1994). Flow instabilities during engine startup and shutdown generate large pressure fluctuations along the nozzle walls that can ultimately damage the nozzle. The flow transient during rocket engine startup is different than that of shock tunnel startup. During rocket engine startup at sea level, the pressure ratio across the nozzle increases as the combustion chamber increases to its steady state operating value. The rate of this pressure increase affects the startup process. If this process occurs instantaneously, we would expect the starting process to be closer to that of a shock tunnel nozzle discussed previously. For

these flows in rocket engine nozzles during startup, the effect of viscosity is substantial. Numerical simulations by Chen et al. (1994) of the startup of 1/16-scale nozzle of a J-2S rocket engine using a time-accurate compressible Navier Stokes solver with a turbulence model predict the ratio of wall pressure to chamber pressure over the nozzle length for a range of nozzle pressure ratios. In these cases, the predicted point of flow separation at the wall strongly agrees with the experimental data and occurs near the nozzle inlet.

For detonation tube nozzle flows, the startup process is certainly affected by viscosity at the low pressure ratios and is likely to also be affected by the Taylor wave pressure profile that exists behind the shock wave after it just enters the nozzle inlet. For simplicity, an estimate of the detonation tube nozzle startup time is made from the time taken by a particle as it travels under steady flow conditions from the inlet to the exit of the nozzle. The startup time is assumed to equal three durations of this steady flow time which is then compared to the total single-cycle time of the detonation tube. The time duration from ignition to the end of the blowdown process is approximately 4000 μs for the 8°-0.3m nozzle, 4500 μs for the 12°-0.3m, 5000 μs for this 12°-0.6m. Three durations of the steady flow time determined from the previous finite rate calculations yield values of approximately 252 μs for the 8°-0.3m nozzle, 354 μs for the 12°-0.3m, 642 μs for this 12°-0.6m nozzle. Thus, the startup time is expected to range between 6% and 12% of the total cycle time. Visualization experiments or numerical simulations are required to better estimate the effect of viscosity and the nozzle flow field in order to obtain more reasonable estimates of the startup time as a function of the environment pressure.

Multi-cycle operation would reduce this nozzle startup time and also reduce the amount of pressure decay experienced at the end of each cycle such that the average exhaust velocity would be greater than in the single-cycle case. As a result, the performance would likely increase closer to the theoretical steady flow predictions.

5.3.6 Comparison of experiments and steady flow analysis

With calculation of the effective nozzle inlet state, the specific impulse from the predicted exhaust velocity is determined using Eq. 5.3. This is plotted with all experimental data for tubes with and without a nozzle as a function of the pressure ratio across the nozzle (P_3/P_0 for the detonation tube data and P_i/P_x for the steady flow predictions). The steady flow predictions are shown both for the nozzle inlet state based on state 3 (Fig. 5.23) and for the nozzle inlet state based on the average pressure during the cycle (Fig. 5.28).

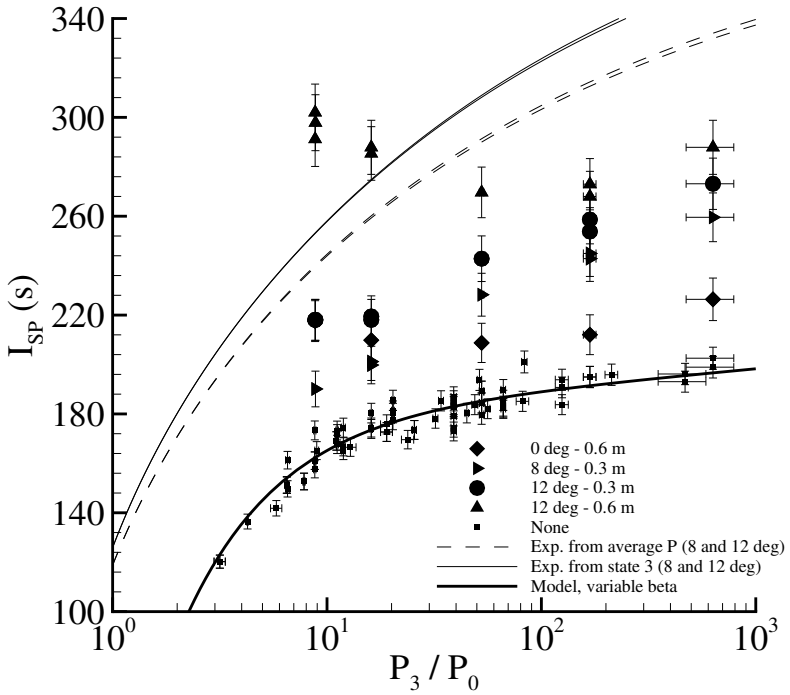

Figure 5.33: Specific impulse as a function of the nozzle pressure ratio. The steady flow predictions based on isentropic expansion are also plotted.

5.4 Summary

Experiments were carried out to measure the impulse from detonation tubes with exit nozzles as a function of the environment pressure. Adding a nozzle onto the tube was found to increase the impulse over the case of a tube without a nozzle at

all the environment pressures. Observations of the experimental data determined that the partial fill effect dominates the impulse for the largest environment pressures tested and that this effect decreases as the tamper mass and environment pressure decrease. In this case, a straight extension is more effective at increasing the impulse than a diverging nozzle for tubes with equivalent explosive mass fractions. At the lowest environment pressures, quasi-steady flow is established within the nozzle and the effect of the nozzle divergence expands the flow. In this case, a diverging nozzle is more effective at increasing the impulse over a straight extension.

To better understand the effect of nozzles on detonation tubes at low environment pressures, the experimental data was analyzed assuming that quasi-steady flow was established in the nozzle. This modeling is reasonable when the environment pressure is sufficiently low such that separation does not occur in the nozzle and the startup time is only a small fraction of the entire blowdown time. Because the detonation tube pressure upstream of the nozzle inlet decreases in time, the average tube pressure from which to determine the nozzle inlet condition was found to best represent the experimental data. Comparisons of the steady flow nozzle predictions based on the average detonation tube pressure modeled the data for all of the diverging nozzles at the lowest environment pressures. The steady flow predictions did not model the data for the larger nozzles at the largest environment pressures due to the influence of the tamper mass.

Thus, nozzles on detonation tubes have been shown to increase the impulse over the baseline case of a plain tube but their performance depends on the pressure ratio across the nozzle and the nozzle shape. Large nozzles operating under small initial pressure ratios are in the regime where unsteady gas dynamics and the partial fill effects of the tamper mass are important. This effect is of decreasing importance as the nozzle size is reduced. All nozzles operating under large initial pressure ratios are in the regime where quasi-steady flow exists in the nozzle and the usual steady flow analysis techniques can be used to predict upper bounds to the performance.

Chapter 6

Non-equilibrium chemical effects

6.1 Introduction

This chapter investigates the effect of finite rate chemistry in expanding detonation products. The motivation is to investigate the assumption made in the original impulse model (Wintenberger et al., 2003) that the detonation products can be represented by a polytropic equation of state throughout the Taylor wave. The goal is to develop bounding estimates based on realistic chemical kinetics for the thermodynamic state of detonation products and apply these to impulse calculations.

In the original impulse model of Wintenberger et al. (2003), a polytropic approximation $P \sim \rho^{\gamma}$ is used to represent the isentrope in the detonation products in order to analytically predict the impulse. This method has been previously used in other studies of nonsteady flow in equilibrium detonation products (Shepherd et al., 1991) and to compare computed blast and expansion waves with experimental data. The thermochemical basis of this approximation has been examined (Fomin and Trotsyuk, 1995, Zajac and Oppenheim, 1969, Nikolaev and Fomin, 1982) assuming "shifting" equilibrium in the products to compute the dependence of internal energy and molar mass on temperature and density for adiabatic flow. These studies demonstrate that there is a limited range of thermodynamic states over which the approximation of polytropic behavior is quantitatively reliable.

Previous studies have investigated the extent of equilibrium in detonation products (Borisov et al., 1991, Eckett, 2001). Borisov et al. (1991) first noted differences

between the cases of fuel-air and fuel-oxygen detonation and the extent of chemical equilibrium in the products. He investigated unconfined gaseous clouds, determining the critical radius at which the detonation products can be considered to be in equilibrium. We investigated this issue in cylindrical tubes closed at one end by numerically solving the species evolution based on detailed chemical kinetics and a prescribed pressure-time history approximated by the similarity solution for the Taylor wave following a detonation. This study looks at the extent of chemical equilibrium just through the Taylor wave expansion.

6.2 Ideal detonation waves and the CJ state

To begin the analysis, we consider the role of finite reaction rates in the detonation process itself. In the standard model of an ideal detonation wave, the shock and reaction zone are treated as a single front or discontinuity, and the chemical reactions are assumed to occur sufficiently fast (Fickett and Davis, 1979) such that the flow is in equilibrium before the expansion begins (Fig. 6.1). The properties behind the front

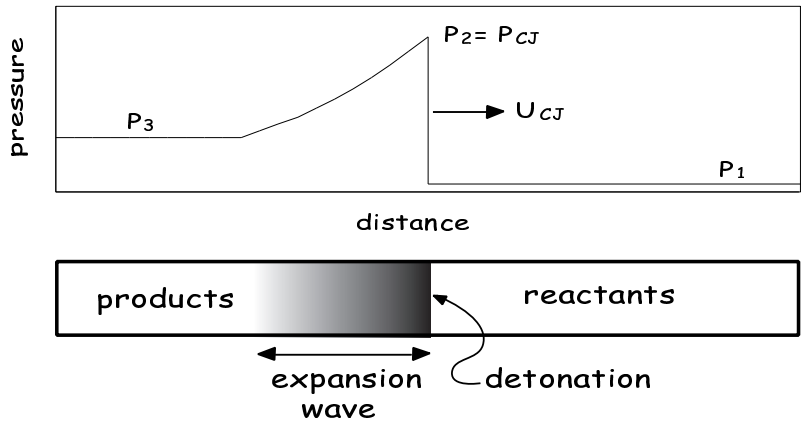

Figure 6.1: Detonation propagation in tube with a closed end.

are determined by solving conservation equations, also known as jump conditions, across the discontinuity. The equations are most conveniently solved in a coordinate system that moves with the detonation wave speed U_{CJ}. The velocity components

are

$$w_1 = U_{CJ} - u_1 \tag{6.1}$$

$$w_2 = U_{CJ} - u_2 \tag{6.2}$$

and the conservation of mass, momentum, and energy in this frame are

$$\rho_1 w_1 = \rho_2 w_2 \tag{6.3}$$

$$P_1 + \rho_1 w_1^2 = P_2 + \rho_2 w_2^2 \tag{6.4}$$

$$h_1 + \frac{w_1^2}{2} = h_2 + \frac{w_2^2}{2} \tag{6.5}$$

$$s_2 \geq s_1 \tag{6.6}$$

State 1 refers to the reactants and state 2 refers to the products. The products are described by the ideal gas equation of state $P = \rho RT$ where $R = \tilde{R}/\mathcal{W}$ for a mixture of species.

$$\mathcal{W} = \left(\sum Y_i/\mathcal{W}_i\right)^{-1} \tag{6.7}$$

$$h = \sum Y_i h_i(T) \tag{6.8}$$

$$s = \sum s_i(T, P, Y_i) \tag{6.9}$$

$$h_i = \Delta h_f + \int_{T^\circ}^{T} c_{p_i}(T')dT' \tag{6.10}$$

Combining the continuity (Eq. 6.3) and the momentum (Eq. 6.4) equations yields the Rayleigh line

$$P_2 - P_1 = -(\rho_1 w_1)^2 (v_2 - v_1) \tag{6.11}$$

which when substituted into the energy (Eq. 6.5) equation yields the Rankine-Hugoniot equation (Thompson, 1988).

$$h_2 - h_1 = 1/2(P_2 - P_1)(v_2 + v_1) \tag{6.12}$$

The species at state 2 are determined from an equilibrium computation where the species $Y_i = Y_i^{eq}(T, P)$. Complete definition of state 2 (P_2, T_2, Y_2^{eq}) requires that the the jump conditions (Eq. 6.11 and Eq. 6.12) and the equilibrium species be solved simultaneously given w_1. Because the slope of Eq. 6.11 in the $P - v$ plane is less than the slope of the isentropes, the detonation velocity w_1 is always supersonic. If $u_1 = 0$, this implies $w_1 \geq U_{CJ}$ and $w_1 \equiv U_{CJ}$ is the experimentally observed detonation velocity. At this CJ state, the Isentrope, Hugoniot, and Rayleigh lines are all tangent

$$\frac{P_2 - P_1}{v_2 - v_1} = \frac{\partial P}{\partial v}\Big)_{Hugoniot} = \frac{\partial P}{\partial v}\Big)_{s,Y^{eq}} \tag{6.13}$$

implying that the product velocities are *sonic relative to the detonation wave.*

$$w_2 = c_2^{eq} \qquad \text{or} \qquad M_2 = 1 \tag{6.14}$$

The value of U_{CJ} and P_2 and T_2 of the products are determined from a numerical solution of the jump conditions and an equilibrium computation that is based on realistic thermochemical properties for the mixture of relevant gas species in the reactants and the products. One such program is STANJAN (Reynolds, 1986) which utilizes realistic representations of the specific heat temperature dependence and enthalpies of formation. For detonations, it is important to include species such as O, H, and OH in the products in addition to the major species H_2O, CO_2, CO, H_2, and N_2 as is done in Schultz and Shepherd (2000). Generally, the relevant gas species at the CJ state depend on the types of atoms, the pressures, and the temperatures. For a wide range of hydrocarbons, the species mentioned above are adequate.

To eliminate the need for a detailed chemical thermodynamic model, the jump conditions of Eqs. 6.3, 6.4, and 6.5 are simplified by using the "2-γ model" of detonations. The level of modeling accuracy is influenced by the choice of parameters representing the upstream and downstream CJ conditions. Improper parameter selection can affect the computed CJ state and influence the subsequent product expansion through the Taylor wave (Fig. 6.1) resulting in predicting inaccurate values of P_3, c_3, and the impulse (Eq. 4.8).

6.2.1 2-γ Model

The 2-γ model is a simplification of the detonation jump equations in which the reactants and products are approximated as perfect gases with constant but distinct values of γ and c_p. A fixed specific energy difference q is assumed to exist between reactants and products.

$$h_1 = c_{p1} T_1 \tag{6.15}$$

$$h_2 = c_{p2} T_2 - q \tag{6.16}$$

$$P_1 = \rho_1 R_1 T_1 \tag{6.17}$$

$$P_2 = \rho_2 R_2 T_2 \tag{6.18}$$

$$c_{p1} = \frac{\gamma_1 R_1}{\gamma_1 - 1} \tag{6.19}$$

$$c_{p2} = \frac{\gamma_2 R_2}{\gamma_2 - 1} \tag{6.20}$$

Substituting these relations into the jump conditions of Eqs. 6.3, 6.4, and 6.5 and making use of the fact that $M_2 = 1$ yields the pressure ratio, density ratio, and temperature ratio across the detonation wave.

$$\frac{P_2}{P_1} = \frac{1 + \gamma_1 M_1^2}{1 + \gamma_2} \tag{6.21}$$

$$\frac{\rho_1}{\rho_2} = \frac{\gamma_2}{\gamma_1 M_1^2} \left(\frac{1 + \gamma_1 M_1^2}{1 + \gamma_2} \right) \tag{6.22}$$

$$\frac{T_2}{T_1} = \frac{\gamma_2 R_1}{\gamma_1 M_1^2 R_2} \left(\frac{1 + \gamma_1 M_1^2}{1 + \gamma_2} \right)^2 \tag{6.23}$$

Evaluation of the reactant (state 1) properties is straightforward since the composition is fixed and the standard thermodynamic relationships for an ideal gas mixture can be used.

The normalized effective heat release q/R_1T_1 can be computed

$$\frac{q}{R_1T_1} = \frac{\gamma_2}{\gamma_2 - 1}\frac{\gamma_2}{\gamma_1}\left(\frac{1+\gamma_1 M_{CJ}^2}{1+\gamma_2}\right)^2 \frac{\gamma_2+1}{2M_{CJ}^2} - \frac{\gamma_1}{\gamma_1 - 1}\left(1 + \frac{\gamma_1 - 1}{2}M_{CJ}^2\right) \tag{6.24}$$

given the value of $M_{CJ} = U_{CJ}/c_1$ which is found through the chemical equilibrium solution with realistic thermodynamic properties. The remaining CJ state parameters are computed with Eqs. 6.25-6.28. In these equations, knowledge of the downstream γ_2 and R_2 are required.

$$\frac{P_{CJ}}{P_1} = \frac{1+\gamma_1 M_{CJ}^2}{1+\gamma_2} \tag{6.25}$$

$$\frac{\rho_{CJ}}{\rho_1} = \frac{\gamma_1 M_{CJ}^2}{\gamma_2}\left(\frac{1+\gamma_2}{1+\gamma_1 M_{CJ}^2}\right) \tag{6.26}$$

$$\frac{T_{CJ}}{T_1} = \frac{P_{CJ}}{P_1}\frac{R_1\rho_1}{R_2\rho_{CJ}} \tag{6.27}$$

$$u_{CJ} = U_{CJ}\left(1 - \frac{\rho_1}{\rho_2}\right) \tag{6.28}$$

This model can be simplified further by using a common value of γ and R to represent the reactants and products. The resulting equations are calculated from Eqs. 6.24-6.28 where $\gamma_2 = \gamma_1$. Although this approximation is used in some analytical treatments of detonation, it is not sufficiently accurate for engineering models or analysis of laboratory experiments and so we do not discuss it further here.

6.3 Chemical reactions in expansion waves

We now consider the effect of chemical reaction in the flow (Fig. 6.1) behind the detonation front. The issue can be understood by considering a small mass of fluid, idealized as a point in the flow (x, t) but containing enough mass to be characterized by the state variables, as it passes from the CJ point to state 3. The state variables are changing through the Taylor wave and the chemical reaction rates $\mathbf{\Omega}(T, P, \mathbf{Y})$ are

known to be strong functions of these properties so that in general, the full set of equations for an adiabatic flow without diffusive transport,

$$\text{Mass:} \quad \frac{D\rho}{Dt} + \rho\nabla \cdot \underline{u} = 0 \tag{6.29}$$

$$\text{Momentum:} \quad \rho\frac{D\underline{u}}{Dt} + \nabla P = 0 \tag{6.30}$$

$$\text{Energy:} \quad \rho\frac{Dh}{Dt} = \frac{DP}{Dt} \tag{6.31}$$

$$\text{Species:} \quad \rho\frac{D\mathbf{Y}}{Dt} = \mathbf{\Omega} \tag{6.32}$$

have to be solved simultaneously to determine the flow field $P(x,t)$, $\rho(x,t)$, $T(x,t)$, $\mathbf{Y}(x,t)$, and $u(x,t)$. The vector $\mathbf{Y}$ has components Y_i corresponding to the species i.

There are two limiting cases for chemical reaction:

1. Frozen composition ($\mathbf{Y} = \mathbf{Y}^\circ = Y_i^\circ = \text{constant}$)

This occurs when the reaction rates are so *slow* that $\mathbf{\Omega} \equiv 0$ for all species. In this case,

$$C_p = \frac{\partial h}{\partial T}\Big)_P = \sum Y_i^\circ C_{p_i}(T) \qquad \text{since} \qquad \sum h_i \frac{\partial Y_i^\circ}{\partial T}\Big)_P = 0 \tag{6.33}$$

where Y_i° represents the constant mass fraction of species i.

2. Equilibrium composition ($\mathbf{Y} = \mathbf{Y}^{eq} = Y_i^{eq}(T,P)$)

This occurs when disturbances from equilibrium re-adjust so *fast* that $|Y_i - Y_i^{eq}(T,P)|$ remains relatively small.

$$\left| \frac{Y_i - Y_i^{eq}(T,P)}{Y_i^{eq}(T,P)} \right| \ll 1 \tag{6.34}$$

$$C_p = \frac{\partial h}{\partial T}\Big)_P = \sum Y_i^{eq} C_{p_i}(T) + \sum h_i \frac{\partial Y_i^{eq}}{\partial T}\Big)_P \tag{6.35}$$

6.3.1 Non-equilibrium flow

Each element of fluid described by the conservation equations 6.29, 6.30, 6.31 is assumed locally to be in partial thermodynamic equilibrium with respect to all degrees

of freedom except chemical reaction (Fickett and Davis, 1979). Thus, temperature, pressure, and in general $\mathbf{Y}^{eq}$ depend on x and t. This is a generalization of the usual idea of thermodynamic equilibrium which occurs only after a long time and therefore makes sense for processes that have a time-independent, spatially-uniform final state.

Consider an element of fluid that is initially in chemical equilibrium. If the state of the fluid (T, P) is suddenly changed as illustrated in Fig. 6.2(a), then a finite amount of time t_{chem} is required for the chemical reactions to adjust the species mass fractions back to local equilibrium. In this case, the chemical timescale is significantly larger

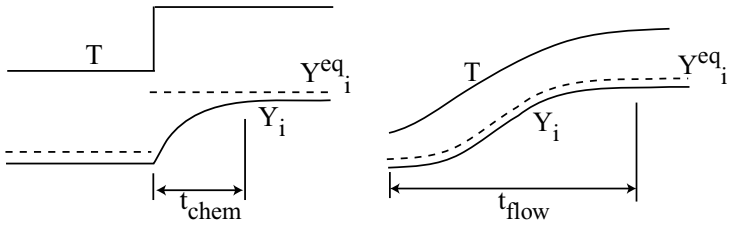

Figure 6.2: Schematic of (a) rapid flow changes and (b) continuous flow changes with the corresponding chemical transient.

than the timescale of fluid motion t_{flow}.

Now consider the opposite situation where the state of the fluid (T, P) changes in a very slow, continuous fashion as illustrated in Fig. 6.2(b). As long as the characteristic time of fluid motion is significantly greater than the time required by the chemical reactions to adjust, the composition will be in local thermodynamic equilibrium (LTE).

The extent of chemical non-equilibrium is most conveniently specified in terms of the Damkohler number,

$$Da = \frac{t_{chem}}{t_{flow}} \tag{6.36}$$

where $Da \gg 1$ implies frozen flow and $Da \ll 1$ implies equilibrium flow. We evaluate t_{chem} in ethylene-oxygen and ethylene-air mixtures by reformulating the species equation assuming that the flow is nearly in equilibrium and then examining the response to a small disturbance. The specifics are discussed in the following sections.

6.4 Polytropic approximation

Adiabatic expansion of the detonation products is modeled with a single value for γ. This simple polytropic model of the gas behavior,

$$P\rho^{-\gamma} = \text{constant} \tag{6.37}$$

where γ is a fitting parameter chosen to best approximate the actual behavior of the mixture, must be checked in each individual case. As discussed previously, the two limiting cases are to either assume shifting equilibrium composition $\gamma = \gamma_e$ or frozen composition $\gamma = \gamma_f$ in the products.

The equilibrium γ_e and the frozen γ_f are each associated with a corresponding sound speed c. In the context of the classical Chapman-Jouguet model of detonation, c_2 (Eq. 6.14) is the *equilibrium* sound speed c_e.

$$c_e^2 = \frac{\partial P}{\partial \rho}\Big)_{s,Y_i^{eq}} \tag{6.38}$$

In shifting equilibrium, changes in the state variables result in a shift in the species compositions so that chemical equilibrium is restored $Y_i = Y_i^{eq}(T, P)$. This is what all standard thermochemical programs such as STANJAN (Reynolds, 1986) use to compute the CJ state and is equivalent to determining the minimum wave speed U_{CJ} that will satisfy the conservation relations for a steady supersonic wave. The corresponding γ_e is then

$$\gamma_e = \frac{\rho}{P} c_e^2 \tag{6.39}$$

The equilibrium sound speed is distinct from the *frozen* sound speed c_f, in which the differentiation is carried out with fixed species amounts $Y_i = Y_i^0$.

$$c^2 = \frac{\partial P}{\partial \rho}\Big)_{s,Y_i^0} \tag{6.40}$$

The corresponding γ_f is then

$$\gamma_f = \frac{\rho}{P} c_f^2 = \frac{C_p(T)}{C_v(T)} \tag{6.41}$$

The value of γ_e (and the corresponding c_e) is smaller than the value of γ_f (and the corresponding c_f) by an amount that depends on the degree of dissociation in the gas and the Gibbs energy of reaction associated with the dissociation-recombination reactions (Fickett and Davis, 1979). The differences between the equilibrium and frozen states are much more significant for the high-temperature, low-pressure mixtures of detonation products generated from the fuel-oxygen mixtures used in laboratory experiments than for low-temperature, high-pressure mixtures of combustion products generated from the fuel-air mixtures used in engine combustors.

We calculate the fitting parameter γ in Eq. 6.37 required to model the equilibrium and frozen isentropes from the CJ state in an ethylene-oxygen and an ethylene-air mixture initially at 1 bar and 300 K. The parameter γ can be interpreted as the slope of the isentrope in logarithmic coordinates.

$$\gamma = \frac{\partial \ln P}{\partial \ln v} \tag{6.42}$$

The isentropes, plotted in Fig. 6.3 in the P-v plane, Fig. 6.4 in the T-v plane, and Fig. 6.5 in the P-T plane, were computed with STANJAN (Reynolds, 1986) using a set of 31 species (AR, CH4, C4H10, H2O2, CH, CO, C8H18, N, CH2, CO2, H, NO, CH2O, C2H, HCO, NO2, CH2OH, C2H2, HO, N2, CH3, C2H4, HO2, O, CH3O, C2H6, H2, O2, CH3OH, C3H8, H2O).

Equations 6.43-6.45 are derived from Eq. 6.37 and are used to calculate γ from Figs. 6.3 - 6.5. The results are tabulated in Table 6.1.

$$\ln P = -\gamma \ln v + \text{constant} \tag{6.43}$$

$$\ln T = (1 - \gamma) \ln v + \text{constant} \tag{6.44}$$

$$\ln P = \frac{\gamma}{\gamma - 1} \ln T + \text{constant} \tag{6.45}$$

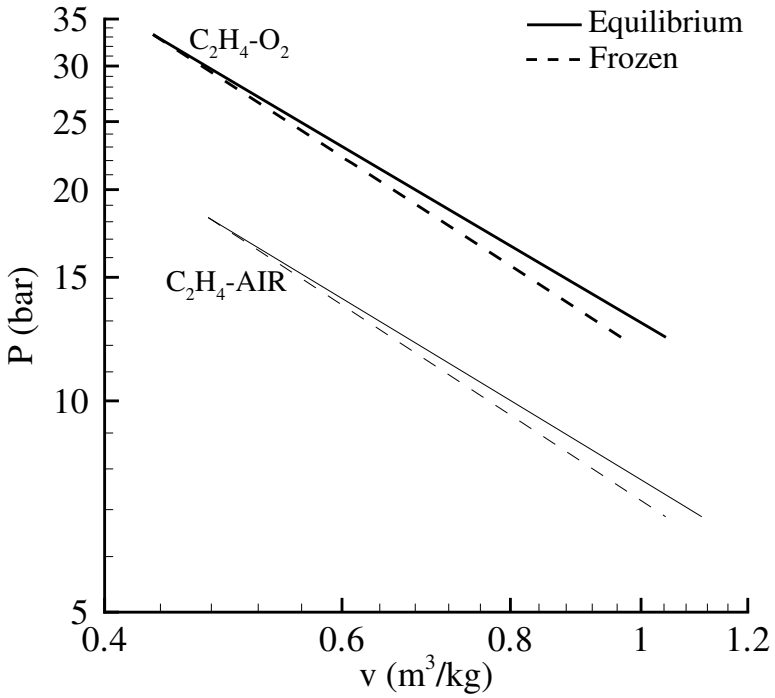

Figure 6.3: P versus v for an ethylene-oxygen and ethylene-air mixture with an initial pressure of 1 bar and an initial temperature of 300 K. The solid lines correspond to shifting equilibrium composition and the dashed lines correspond to frozen composition.

The γ determined by the pressure-volume fit is closest in value to γ_e at the CJ

γ	$C_2H_4 + 3O_2$	C_2H_4 + AIR
γ_f at CJ state	1.2356	1.1717
γ_e at CJ state	1.1397	1.1611
γ from P-v fit of eq. isentrope	1.1338	1.1638
γ from T-v fit of eq. isentrope	1.0967	1.1466
γ from T-P fit of eq. isentrope	1.0853	1.1260

Table 6.1: Tabulated values of γ determined by fitting isentropes with either equilibrium or frozen composition in ethylene-oxygen or -air mixtures.

state. For most simple detonation problems, it is sufficient to have an approximate representation of the equation of state of the products in the vicinity of the isentrope that originates at the CJ state. The usual practice is to approximate the products as being in chemical equilibrium at each point along the isentrope. The molar mass of the products will change as the composition shifts with pressure and temperature but

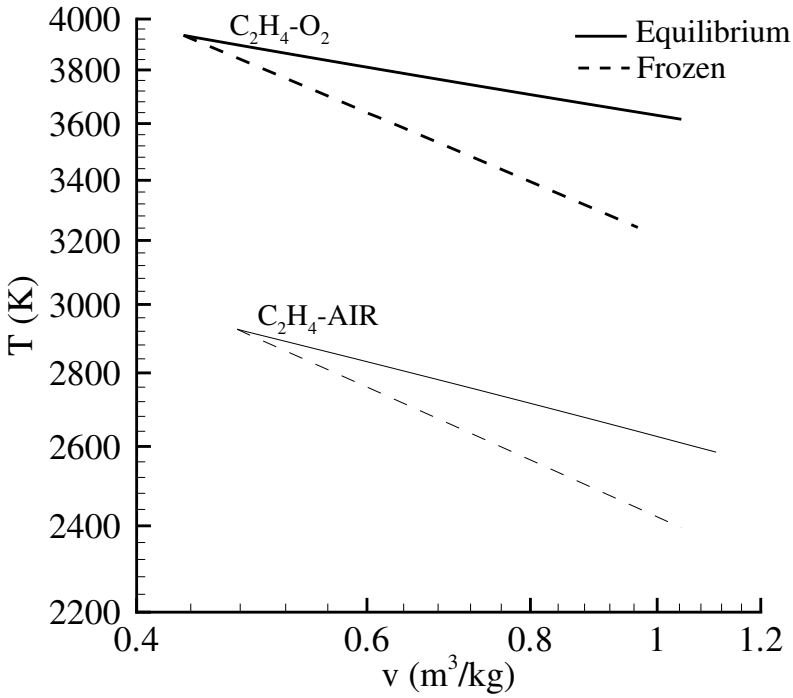

Figure 6.4: T versus v for an ethylene-oxygen and ethylene-air mixture with an initial pressure of 1 bar and an initial temperature of 300 K. The solid lines correspond to shifting equilibrium composition and the dashed lines correspond to frozen composition.

for the present purposes, we assume the composition is fixed at the values obtained for the CJ state.

From Table 6.1, we see that in general it is not possible to approximate the properties of the expanding detonation products in the Taylor wave region as a polytropic process with a single, unique value of γ. In particular, due to the importance of energy exchange in recombination-dissociation equilibrium, the values of γ_e for the $T - v$ and $T - P$ relationships are significantly different than for the $P - v$ relationship, particularly for the ethylene-oxygen case. Since the pressure only changes by a factor of two in the Taylor wave, a common short cut is to simply use γ_e at the CJ state for γ. To validate this assumption for different mixtures, we carried out a study to compare the chemical reaction times assuming finite reaction rates to the characteristic times of fluid motion throughout the Taylor wave calculated with the similarity solution (Fickett and Davis, 1979). In §6.6 below, we compare the

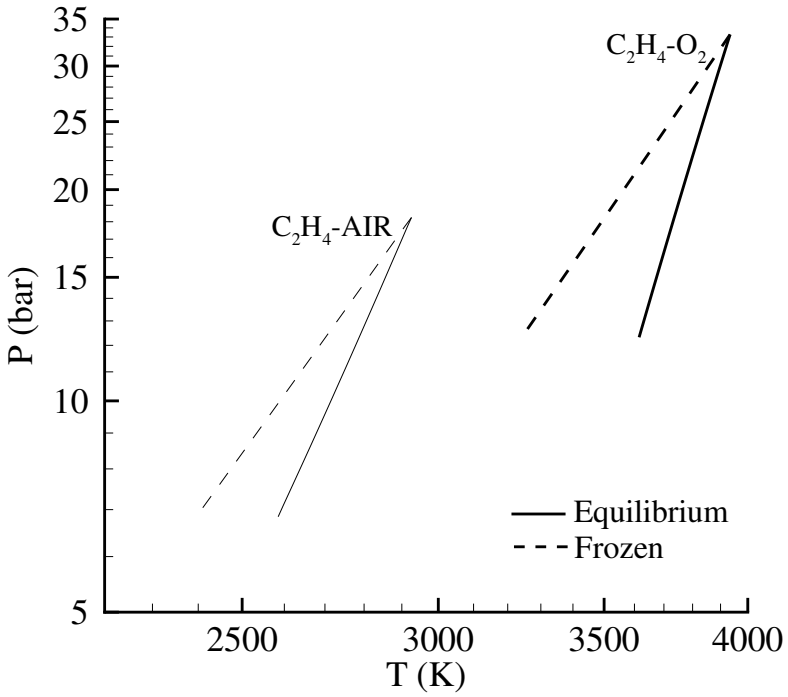

Figure 6.5: P versus T for an ethylene-oxygen and ethylene-air mixture with an initial pressure of 1 bar and an initial temperature of 300 K. The solid lines correspond to shifting equilibrium composition and the dashed lines correspond to frozen composition.

timescales between ethylene-oxygen and ethylene-air mixtures with initial temperatures of 300 K and initial pressures of 20, 60, and 100 kPa. If the expansion of the products to lower pressures is important, a more elaborate treatment, including the possibility of "freezing" of the composition, may need to be undertaken. Additionally, in situations where strong shock waves may occur in the products, then a more sophisticated approach needs to be taken.

6.5 Taylor-Zeldovich expansion wave

The Taylor wave expands the moving flow behind the detonation wave to zero velocity at the closed tube end as illustrated on the distance-time diagram of Fig. 6.6. Here we assume an ideal detonation traveling at the CJ velocity with instantaneous detonation initiation. The decrease in flow velocity is associated with a corresponding decrease

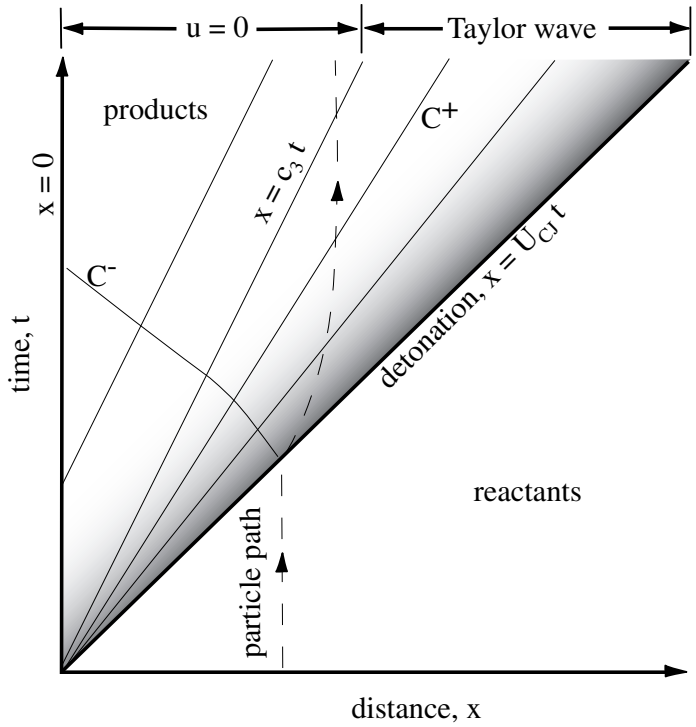

Figure 6.6: Schematic of Taylor wave showing characteristics and a representative particle path through a detonation propagating from the closed end of a tube into stationary gas.

in pressure (Figure 6.1) and a growing region of fluid at rest extends behind the end of the Taylor wave to the closed end of the tube. The properties within the expansion wave are calculated assuming a similarity solution using the method of characteristics for this case of planar flow (Taylor, 1950, Zel'dovich, 1940). Similarity solutions also exist in cylindrical and spherical flows behind ideal detonations initiated instantaneously from a point. These flow fields can be computed by numerical solution of the governing equations in similarity coordinates as discussed by Taylor (1950), Sedov (1971-72), Stanyukovich (1960), and other textbooks.

Although our previous discussion has shown that a single value of γ defining the polytropic relationship may not be a good assumption for all mixtures, especially those far from equilibrium, we assume that the approximation is adequate so that the usual gas dynamic equations apply in order for us to be able to model the flow through the Taylor wave. There are two relevant sets of characteristics, C^+ and C^-,

defined by

$$C^+ : \qquad dx/dt = u + c \tag{6.46}$$

$$C^- : \qquad dx/dt = u - c \tag{6.47}$$

The detonation front and some representative characteristics in the products are shown on Fig. 6.6. On the C^+ characteristics,

$$\frac{dx}{dt} = \begin{cases} x/t = c_3 & \text{for} \quad 0 < x/t < c_3 \\ \\ u + c = x/t & \text{for} \quad c_3 < x/t < U_{CJ} \end{cases} \tag{6.48}$$

where state 3 defines the region from the end of expansion wave $x = c_3 t$ to the wall at $x = 0$. The flow in this region is uniform and stationary with constant properties.

The Riemann invariant J^- is constant on the C^- characteristics that span the region between the detonation $x = U_{CJ}t$ and state 3.

$$J^- = u - \int_{P_{CJ}}^{P} \frac{dP}{\rho c} \tag{6.49}$$

Given numerical solutions for $\rho(P)$ and $c(P)$, Eq. 6.49 can be integrated from the CJ reference state to state 3 where the flow velocity is zero to determine $u(P)$ in the Taylor wave. From the polytropic relation $P \sim \rho^\gamma$ and $\mathbf{\Omega} = 0$, the integral in Eq. 6.49 can be reduced to $2c/(\gamma - 1)$.

$$J^- = u - \frac{2}{\gamma - 1}c = -\frac{2}{\gamma - 1}c_3 = u_2 - \frac{2}{\gamma - 1}c_2 \tag{6.50}$$

Equation 6.50 is solved for c_3 as a function of the CJ parameters where $u_2 = U_{CJ} - c_2$ or alternatively, the flow velocity u through the Taylor wave.

$$c_3 = \frac{\gamma + 1}{2}c_2 - \frac{\gamma - 1}{2}U_{CJ} \tag{6.51}$$

$$u = \frac{2}{\gamma - 1}(c - c_3) \tag{6.52}$$

At this point, we introduce the similarity variable $\eta = x/c_3 t$ which equals $\eta = U_{CJ}/c_3$ at the CJ state and decreases to one at the end of the Taylor wave. Starting with the C^+ Riemann invariant relationship of Eq. 6.48, the sound speed is evaluated at an arbitrary point in the flow by substituting Eq. 6.52 for u.

$$\begin{aligned} x/t &= u + c \\ x/t &= \frac{2}{\gamma - 1}(c - c_3) + c \\ c/c_3 &= \frac{2}{\gamma + 1} + \left(\frac{\gamma - 1}{\gamma + 1}\right)\eta \end{aligned} \tag{6.53}$$

For all distances behind the detonation wave, the sound speed in the products is written as

$$c = \begin{cases} c_3 & \text{for} \quad 0 < x/t < c_3 \\ \\ c_3\left[2/(\gamma+1) + (\gamma-1)/(\gamma+1)\eta\right] & \text{for} \quad c_3 < x/t < U_{CJ} \end{cases} \tag{6.54}$$

and is plotted for the ethylene-oxygen and ethylene-air mixtures in Fig. 6.7 as a function of η through the Taylor wave.

The flow velocity is calculated by substituting Eq. 6.54 into Eq. 6.52.

$$\begin{aligned} u &= \frac{2}{\gamma - 1}\left[\left(\frac{c}{c_3}\right)c_3 - c_3\right] \\ &= \frac{2}{\gamma - 1}\left[\frac{2}{\gamma + 1} + \left(\frac{\gamma - 1}{\gamma + 1}\right)\eta\right]c_3 - \frac{2}{\gamma - 1}c_3 \\ &= \frac{2c_3}{\gamma + 1}(\eta - 1) \end{aligned} \tag{6.55}$$

As before, the piecewise function of the flow velocity behind the detonation wave can be written explicitly and is plotted in Fig. 6.8 as a function of η through the Taylor

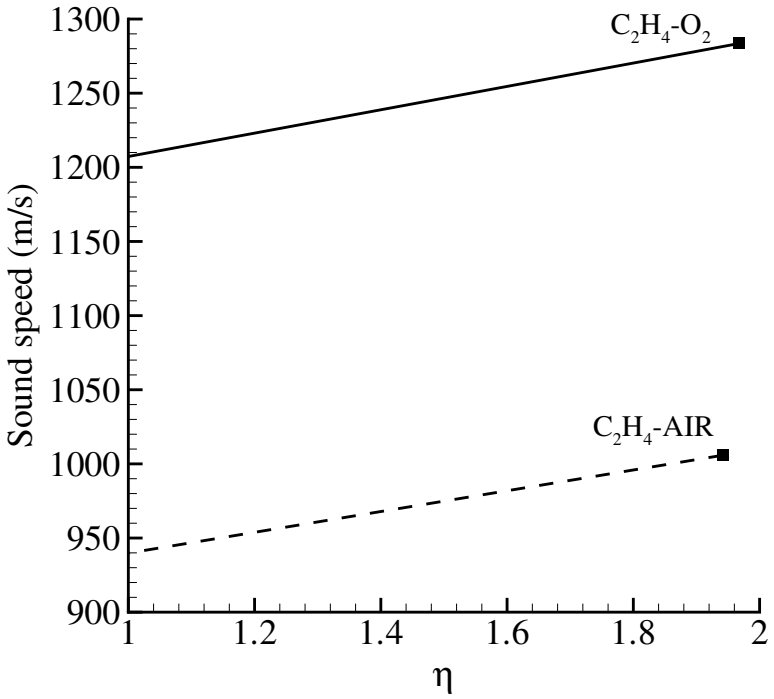

Figure 6.7: Sound speed versus η through the Taylor wave calculated with γ_e and fixed composition for an ethylene-oxygen and ethylene-air mixture with an initial pressure of 100 kPa. The solid square symbols correspond to the CJ state.

wave for the two mixtures considered.

$$u = \begin{cases} 0 & \text{for} \quad 0 < x/t < c_3 \\ \\ 2c_3\left(\eta - 1\right)/(\gamma + 1) & \text{for} \quad c_3 < x/t < U_{CJ} \end{cases} \tag{6.56}$$

The flow velocity within the Taylor wave decreases linearly with increasing distance behind the detonation front. The location where the flow velocity decreases to zero is located a distance of c_3/U_{CJ} behind the detonation wave. From the detonation jump conditions and the Riemann invariant relation, this distance is

$$\frac{c_3}{U_{CJ}} = \frac{\gamma + 1}{2}\frac{\rho_1}{\rho_2} - \frac{\gamma - 1}{2} \tag{6.57}$$

In limit of large M_{CJ}, the density ratio is given by $\rho_1/\rho_2 = \gamma/(\gamma + 1)$ and the end

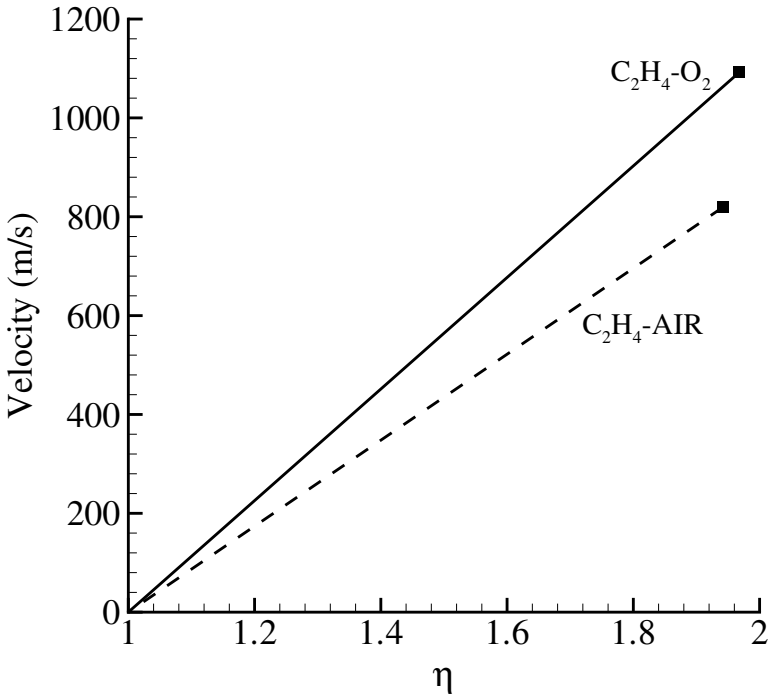

Figure 6.8: Velocity versus η through the Taylor wave calculated with γ_e and fixed composition for an ethylene-oxygen and ethylene-air mixture with an initial pressure of 100 kPa. The solid square symbols correspond to the CJ state.

of the Taylor wave is located exactly half-way between the detonation and the wall. Experience with computations using realistic values of the properties indicates that this is a fairly reliable rule of thumb for the extent of the Taylor wave.

The remaining flow properties for the temperature T, density ρ, and pressure P are found from the following isentropic relations where $c \sim \sqrt{T}$, $P \sim \rho^{\gamma}$, and $T \sim \rho^{\gamma-1}$ are all constant. For example, the pressure P is related to the sound speed by

$$P = \begin{cases} P_{CJ}\left(c_3/c_2\right)^{2\gamma/(\gamma-1)} & \text{for} \quad 0 < x/t < c_3 \\ \\ P_3\left[2/(\gamma+1) + (\gamma-1)/(\gamma+1)\eta\right]^{2\gamma/(\gamma-1)} & \text{for} \quad c_3 < x/t < U_{CJ} \end{cases} \tag{6.58}$$

and is plotted in Fig. 6.9.

A characteristic timescale of fluid motion is determined from the rate of change

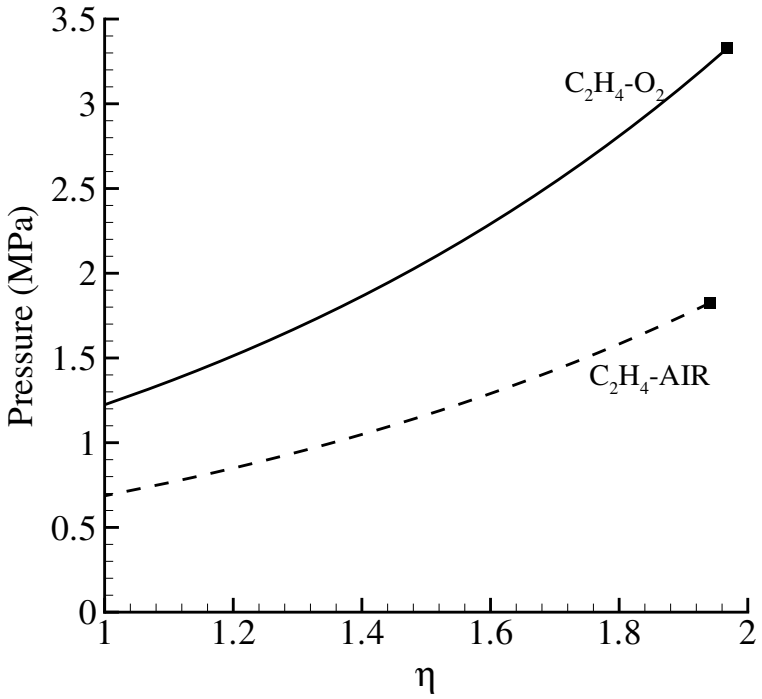

Figure 6.9: Pressure versus η through the Taylor wave calculated with γ_e and fixed composition for an ethylene-oxygen and ethylene-air mixture with an initial pressure of 100 kPa. The solid square symbols correspond to the CJ state.

of pressure along a particle path (sketched in Fig. 6.6)

$$t_{flow} = -\frac{P}{DP/Dt} \tag{6.59}$$

where the pressure-time derivative is computed from the similarity solution with the chain rule.

$$\frac{DP}{Dt} = \frac{dP}{d\eta}\frac{D\eta}{Dt} \tag{6.60}$$

From the definition of η, we have

$$\frac{D\eta}{Dt} = -\frac{1}{t}\left(\eta - \frac{u}{c_3}\right) \tag{6.61}$$

Replacing u in Eq. 6.61 with Eq. 6.52 results in an ordinary differential equation in

terms of η and t.

$$\begin{aligned}\frac{D\eta}{Dt} &= -\frac{1}{t}\left[\eta - \frac{2}{\gamma+1}\left(\frac{c}{c_3} - 1\right)\right] \\ &= -\frac{2}{t(\gamma+1)}\left[\frac{(\gamma-1)}{2}\eta + 1\right]\end{aligned} \tag{6.62}$$

Integrating Eq. 6.62 results in Eq. 6.63 which is used to calculate the six different particle paths of Figs. 6.10(a) and 6.10(b).

$$\eta = \frac{2}{\gamma+1}\left[\left(\frac{t}{t_{CJ}}\right)^{-(\gamma-1)/(\gamma+1)}\left(\frac{\gamma-1}{2}\frac{U_{CJ}}{c_3} + 1\right) - 1\right] \tag{6.63}$$

A path is determined from the initial particle location in the tube. For example, consider a particle that is initially located a distance X from the thrust surface. The particle does not move, as noted by a vertical line in the distance-time plots, until the detonation wave reaches the particle at time $t_{CJ} = X/U_{CJ}$. For times greater than t_{CJ} the particle is instantaneously accelerated by the detonation wave and then decelerated by the Taylor wave to zero flow velocity where the particle path is a vertical line for all later times. Six particle paths, for initial positions $X = 0.05, 0.25, 0.5, 1, 2.5, 5$ m from the thrust surface, were determined using Eq. 6.63 for the two mixtures investigated. The particle initially located the furthest ($X = 5$ m) from the thrust surface remained in the Taylor wave longer than the particles initially located closer to the thrust surface.

From Eq. 6.58, the derivative of P with respect to η is taken,

$$\frac{dP}{d\eta} = \frac{2P_3\gamma}{\gamma-1}\left(\frac{2}{\gamma+1} + \frac{\gamma-1}{\gamma+1}\eta\right)^{(\gamma+1)/(\gamma-1)} \tag{6.64}$$

and then combining with Eq. 6.62 yields the variation of pressure along a particle path.

$$\frac{DP}{Dt} = -\frac{2}{t(\gamma+1)}\left[\frac{(\gamma-1)}{2}\eta + 1\right]\frac{2P_3\gamma}{\gamma-1}\left(\frac{2}{\gamma+1} + \frac{\gamma-1}{\gamma+1}\eta\right)^{(\gamma+1)/(\gamma-1)} \tag{6.65}$$

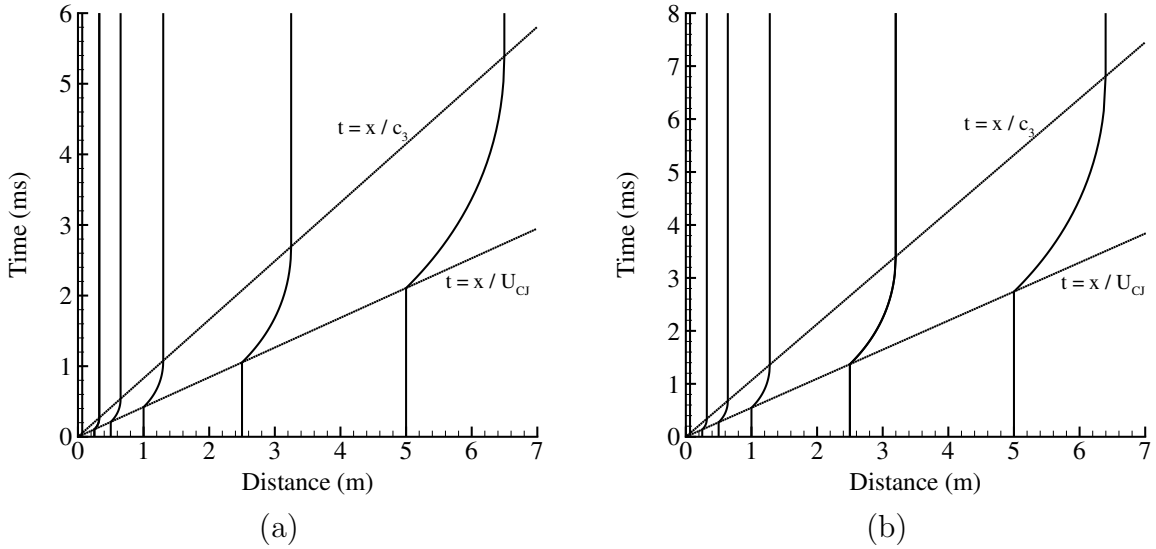

Figure 6.10: Paths of six particles that travel through the Taylor wave plotted on a distance-time diagram for an (a) ethylene-oxygen and (b) ethylene-air mixture with initial pressure of 100 kPa and initial temperature of 300 K.

The results are plotted in Fig. 6.11 as a function of η for the ethylene-air mixture.

Each particle experiences the largest rate of change of pressure just behind the detonation wave ($\eta = U_{CJ}/c_3$). As η decreases and the particle moves through the Taylor wave, the rate of change of pressure decreases (becomes less negative). Additionally, the extent of the Taylor wave grows as the detonation wave propagates down the tube so that the rate of change of pressure is highest for those particles initially located closest to the thrust surface.

Integrating Eq. 6.65 yields the variation of pressure with respect to time along a particle path. The pressure-time curves plotted in Fig. 6.12 for the six particle paths studied are normalized by P_{CJ} and time shifted by t_{CJ} for comparison. This means that a particle initially at position X, which is not processed by the detonation wave until $t = t_{CJ} = X/U_{CJ}$, is time-shifted to the left by t_{CJ} seconds.

Now, the characteristic timescales of fluid motion are plotted in Fig. 6.13 and later compared to the chemical timescales. Just behind the detonation wave, the flow times are at a minimum and they increase through the Taylor wave.

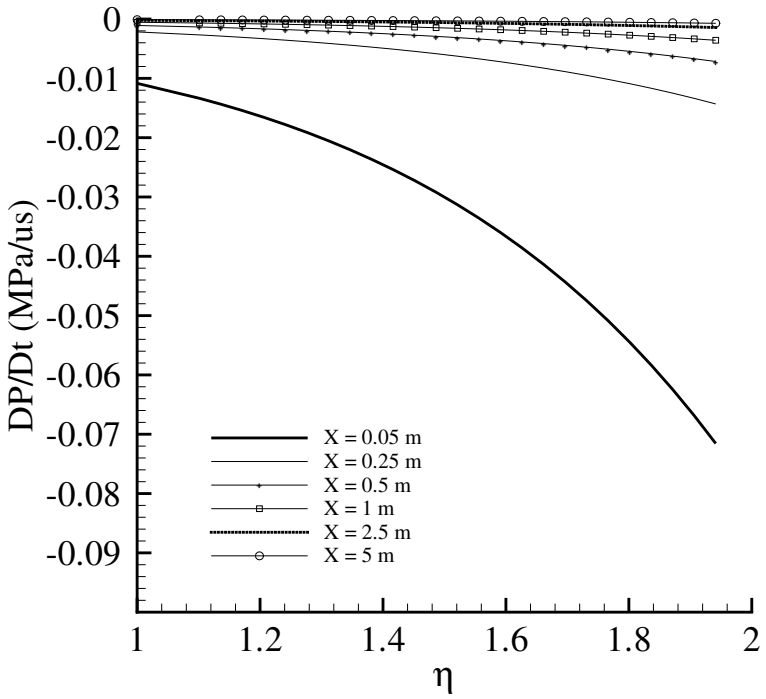

Figure 6.11: Variation of the rate of change of pressure in an ethylene-air mixture with an initial pressure of 1 bar along a particle path through the Taylor wave as a function of the similarity variable η. The equilibrium γ was used in the calculations and the solid symbols correspond to the CJ state.

6.5.1 Computing the chemical timescale

In this section we describe the method used to compute the characteristic timescales for relaxation to equilibrium due to the finite rate chemical reactions. The species equation (Eq. 6.32) can be reformulated (Eq. 6.68) by assuming that only small deviations $\mathbf{Y}' = \mathbf{Y} - \mathbf{Y}^{eq}$, where $|\mathbf{Y}'| \ll |\mathbf{Y}^{eq}|$, from equilibrium exist. For LTE, $\mathbf{\Omega}^{eq} = 0$.

$$\rho \frac{D\mathbf{Y}}{Dt} = \mathbf{\Omega}(\mathbf{Y}, T, P) \tag{6.66}$$

$$\rho \frac{D(\mathbf{Y}' + \mathbf{Y}^{eq})}{Dt} = \mathbf{\Omega}(\mathbf{Y}' + \mathbf{Y}^{eq}, T, P) = \mathbf{\Omega}' + \mathbf{\Omega}^{eq} \tag{6.67}$$

$$\rho \frac{D\mathbf{Y}'}{Dt} = \mathbf{\Omega}' \tag{6.68}$$

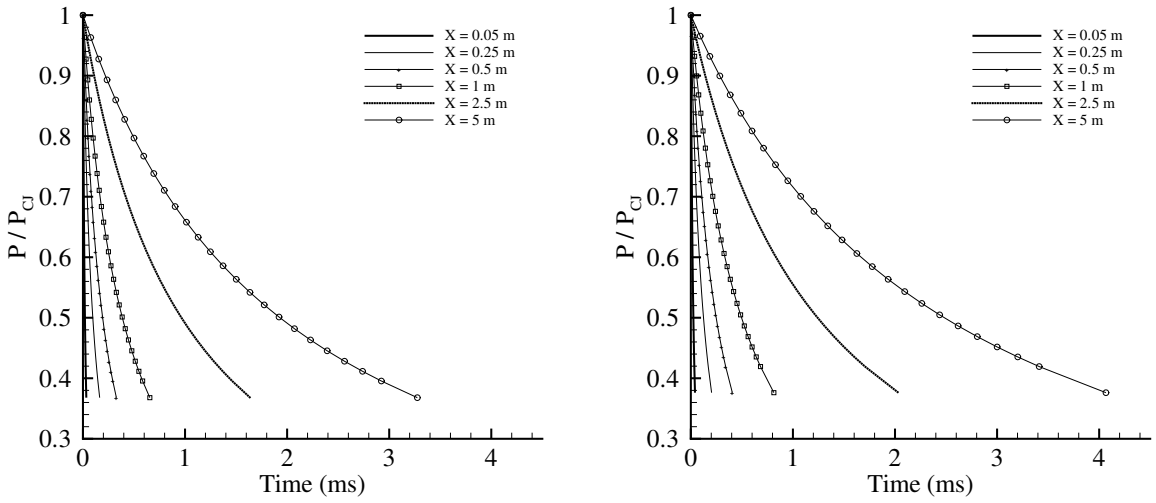

Figure 6.12: Normalized pressure versus time through the Taylor wave along six different particle paths corresponding to particles at different initial positions along the tube in an (a) ethylene-oxygen and (b) ethylene-air mixture.

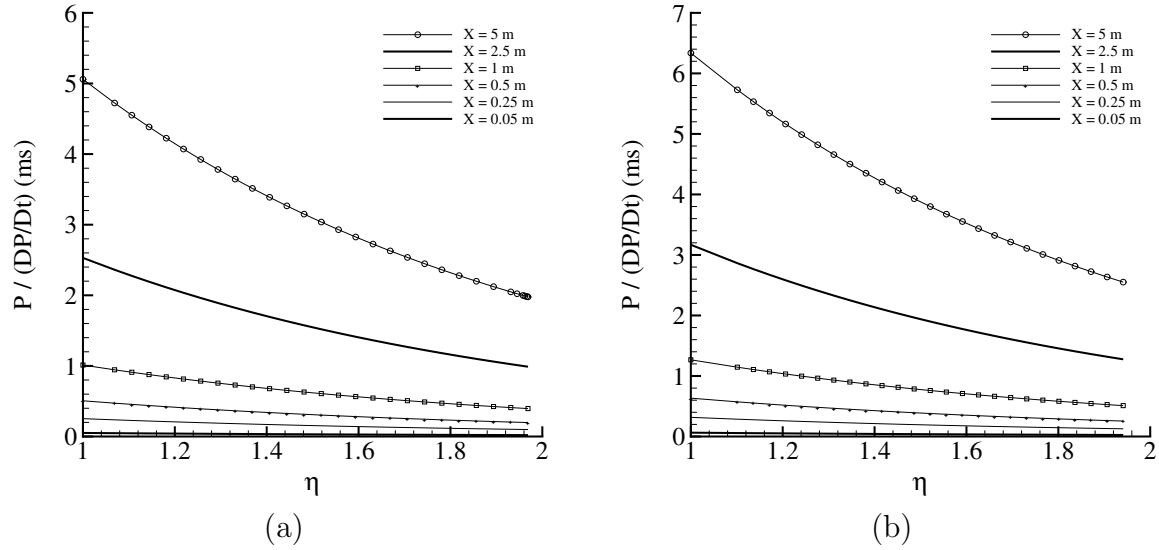

Figure 6.13: Characteristic times of fluid motion through the Taylor wave along six different particle paths corresponding to particles at different initial positions along the tube in an (a) ethylene-oxygen and (b) ethylene-air mixture.

Expanding $\mathbf{\Omega}$ in a Taylor series in $\mathbf{Y}$ yields

$$\mathbf{\Omega} \approxeq \sum \frac{\partial \Omega_i}{\partial Y_k}(Y_k') + ... \tag{6.69}$$

Combining the leading term in the Taylor series of Eq. 6.69 with Eq. 6.68 yields

$$\rho \frac{D\mathbf{Y}'}{Dt} = \sum \frac{\partial \Omega_i}{\partial Y_k} Y_k' \tag{6.70}$$

which can be written as a matrix equation

$$\rho \frac{D\mathbf{Y}'}{Dt} = \mathcal{J}\mathbf{Y}' \tag{6.71}$$

where $\mathcal{J}_{\rangle\|} = \partial\Omega_i/\partial Y_k$ is the Jacobian matrix. This matrix specifies how the reaction rates Ω_i vary in response to changes in the mass fractions and can be diagonalized, $det(\mathcal{J} - \lambda\mathbf{I}) = 0$ to obtain a set of eigenvalues λ_i. The number of nonzero eigenvalues, or independent reaction progress variables, is equal to the difference between the number of species and the number of atoms. The real parts of the nonzero eigenvalues equal the reciprocals of the characteristic time t_{chem} determining the time required for the associated progress variables to relax to equilibrium after a disturbance. In general, a distinct value of t_{chem} is associated with each of the 31 and 48 independent progress variables considered for the ethylene-oxygen and ethylene-air mixtures in this study for each time increment through the Taylor wave.

Comparison of these chemical timescales to the flow timescale (Eq. 6.59) is used to test the assumption of chemical equilibrium as discussed in §6.3.1. The calculated values of Da for each time increment through the Taylor wave are based on the corresponding, instantaneous values of t_{chem} and t_{flow} and are presented in the next section for the ethylene-oxygen and ethylene-air mixtures investigated at different initial pressures.

6.6 Results

The extent of non-equilibrium and the chemical timescales were computed by numerical simulation of chemical reaction and energy conservation on a particle path

through the Taylor wave. The energy equation (Eq. 6.31)

$$\rho \frac{dh}{dt} = \frac{dP}{dt} \tag{6.72}$$

is written in terms of the temperature derivative where h is comprised of contributions from all the species

$$h = \sum h_i(T) Y_i \tag{6.73}$$

$$\rho \sum Y_i \frac{dh_i}{dT} \frac{dT}{dt} + \rho \sum h_i \frac{dY_i}{dt} = \frac{dP}{dt} \tag{6.74}$$

$$C_p \frac{dT}{dt} = -\sum h_i \frac{dY_i}{dt} + \frac{1}{\rho} \frac{dP}{dt} \tag{6.75}$$

and the species are determined by integrating the rate equations

$$\rho \frac{dY_i}{dt} = \Omega_i(T, P, \mathbf{Y}) \ . \tag{6.76}$$

In general, P has to be determined by simultaneously solving the energy equation with the equations of motion. To avoid this complication and estimate the effect of chemical reactions within the Taylor wave, we use the pressure decrease from the similarity analysis to solve the energy equation. An approximate form of the pressure profile for each particle path is obtained by fitting

$$\ln \left(\frac{P}{P_{CJ}} \right) = At^2 + Bt + C \tag{6.77}$$

to each particle path in Figs. 6.12(a) and 6.12(b). The $\Omega_i = dY_i/dt$ term in the energy equation is obtained from a detailed model of the chemical kinetics using the local temperature and pressure. The reaction mechanism, GRIMech 3.1 in this case, includes all the relevant product species, elementary reactions, and corresponding rate constants. The calculation is initiated from the CJ state given the species, species mole fractions, CJ temperature, and CJ pressure. The species mass fractions

and state parameters (T, ρ) as a function of time are determined through the Taylor wave.

A total of six cases were investigated: ethylene-air and ethylene-oxygen mixtures at an initial temperature of 300 K and initial pressures of 100 kPa (Fig. 6.14), 60 kPa (Fig. 6.15), and 20 kPa (Fig. 6.16). Visual comparison of the state changes along a specific particle path to the frozen and equilibrium isentropes highlight the effect that finite rate chemical kinetics can have on fluid particles as they are expanding.

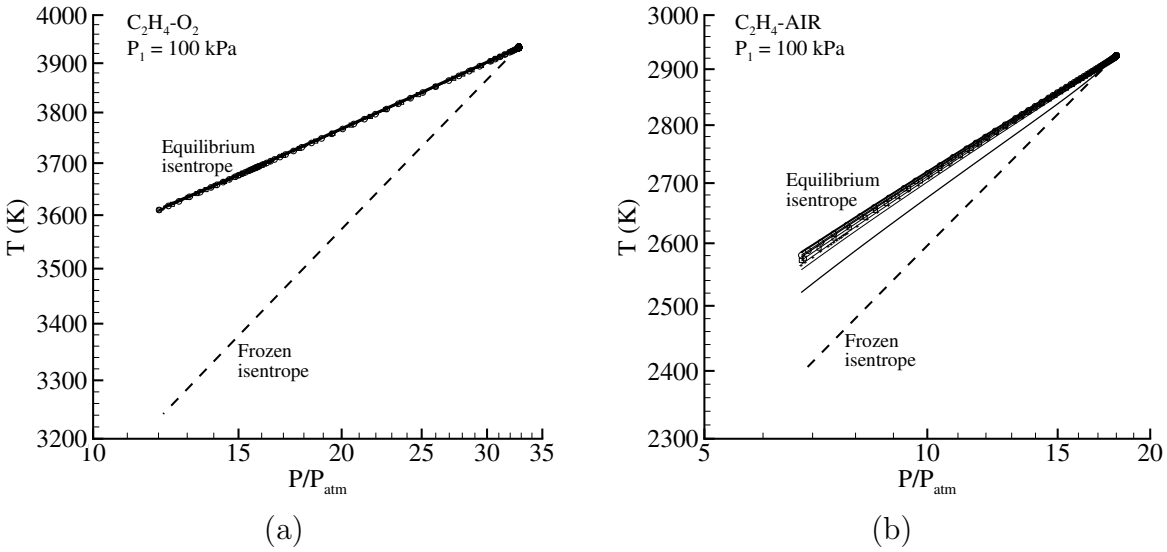

Figure 6.14: Temperature versus pressure for the six particle paths through the Taylor wave for an (a) ethylene-oxygen and (b) ethylene-air mixtures at an initial pressure of 100 kPa. Also plotted are the frozen and equilibrium isentropes.

The expanding detonation products in the ethylene-oxygen mixtures (Figs. 6.14(a), 6.15(a), and 6.16(a)) effectively lie on the equilibrium isentrope and only a slight deviation from equilibrium is observed when $P_1 = 20$ kPa. The effect of pressure is also observed through comparison of the air mixtures (Figs. 6.14(b) , 6.15(b), and 6.16(b)) where the CJ temperature only varies on the order of 100 K. The particles deviate more from equilibrium than in the oxygen mixtures. As the pressure decreases, the particle paths are not modeled by the equilibrium isentrope such that when $P_1 = 20$ kPa (Fig. 6.16(b)), the particles initially located closest to the thrust surface are better modeled by the frozen isentrope.

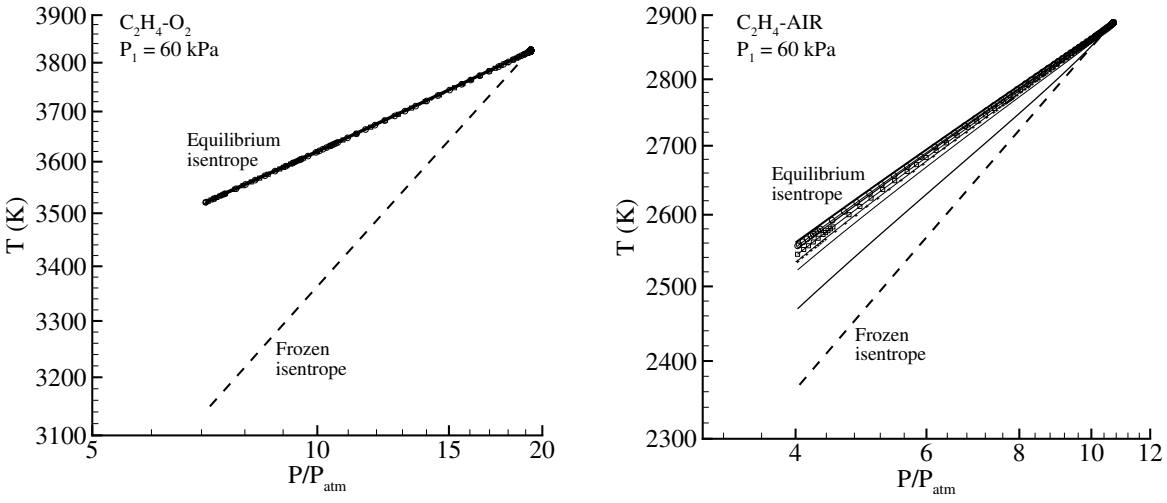

Figure 6.15: Temperature versus pressure for the six particle paths through the Taylor wave for an (a) ethylene-oxygen and (b) ethylene-air mixtures at an initial pressure of 60 kPa. Also plotted are the frozen and equilibrium isentropes.

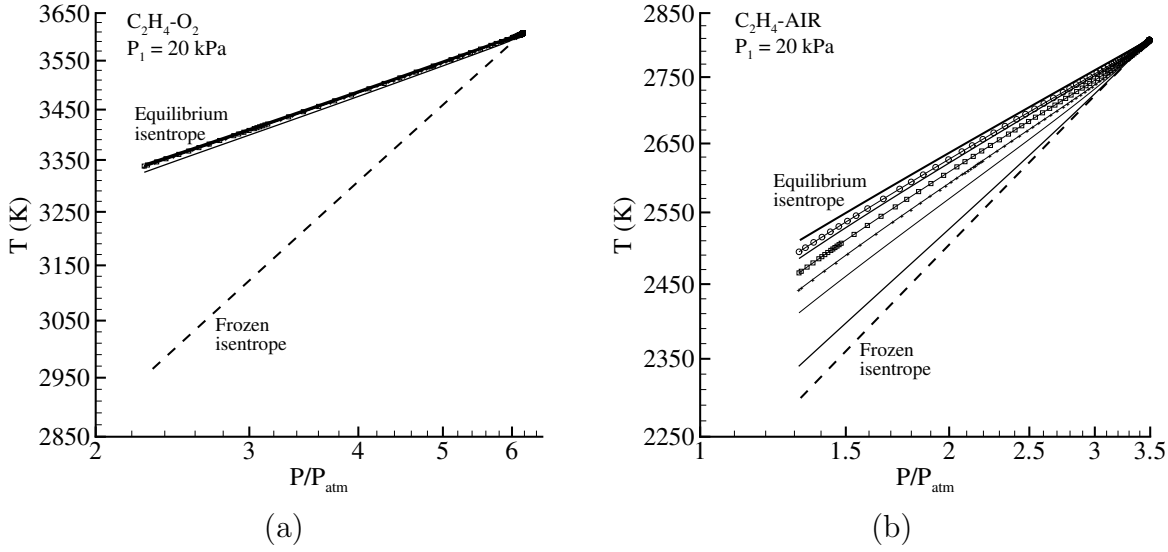

Figure 6.16: Temperature versus pressure for the six particle paths through the Taylor wave for an (a) ethylene-oxygen and (b) ethylene-air mixtures at an initial pressure of 20 kPa. Also plotted are the frozen and equilibrium isentropes.

The mole fractions at the end of the Taylor wave for the oxygen (Table 6.2) and the air (Table 6.3) mixtures are compared. Since the oxygen mixtures can be modeled with the equilibrium isentrope, differences in the final species amounts for different

particle paths at the same initial pressure are not observed but rather, only depend on the initial pressure.

X [m]	P_1 [kPa]	H_2	H	O	O_2	OH	H_2O	CO	CO_2
1	100	0.054	0.049	0.061	0.105	0.110	0.244	0.246	0.131
1	20	0.057	0.064	0.069	0.108	0.106	0.227	0.248	0.122
0.05	100	0.054	0.049	0.061	0.105	0.110	0.244	0.246	0.131
0.05	20	0.057	0.064	0.071	0.108	0.105	0.227	0.247	0.121

Table 6.2: Tabulated mole fractions for ethylene-oxygen mixtures, different particles and different initial pressures.

In contrast, the species amounts at the end of the Taylor wave in the ethylene-air mixtures (Table 6.3) yield more variation than the oxygen mixtures. This is expected since the state changes along a particle path approximate the equilibrium isentrope if $X = 5$ m and $P_1 = 100$ kPa, whereas the state changes along a particle path approximate the frozen isentrope if $X = 0.05$ m and $P_1 = 20$ kPa.

X [m]	P_1 [kPa]	H_2	H	O	O_2	OH	H_2O	CO	CO_2	NO	N_2
1	100	0.006	0.000	0.000	0.008	0.006	0.121	0.025	0.105	0.008	0.720
1	20	0.006	0.003	0.003	0.014	0.008	0.115	0.034	0.095	0.008	0.714
0.05	100	0.006	0.000	0.000	0.011	0.006	0.119	0.028	0.099	0.011	0.720
0.05	20	0.006	0.003	0.003	0.014	0.008	0.115	0.034	0.095	0.008	0.714

Table 6.3: Tabulated mole fractions for ethylene-air mixtures, different particles and different initial pressures.

At each time step, the values of t_{chem} found from the eigenvalues of the Jacobian (§6.5.1) are divided by the timescale of fluid motion yielding the Damkohler number for each reaction progress variable through the Taylor wave. These results are plotted for all progress variables for two initial particle positions of $X = 0.05$ m and $X = 5$ m in the ethylene-oxygen and ethylene-air mixtures with initial pressures of 20 kPa (Fig. 6.17) and 100 kPa (Fig. 6.18).

The Damkohler numbers for the ethylene-oxygen mixtures at 100 kPa (Fig. 6.18(c)) are much less than one for particles with initial positions greater than 1 m from the thrust surface, indicating that they are equilibrium (Refer to Appendix A for additional plots of Damkohler numbers for all cases analyzed). For the initial particle positions less than 1 m from the thrust surface (Fig. 6.18(a)), there is a single progress

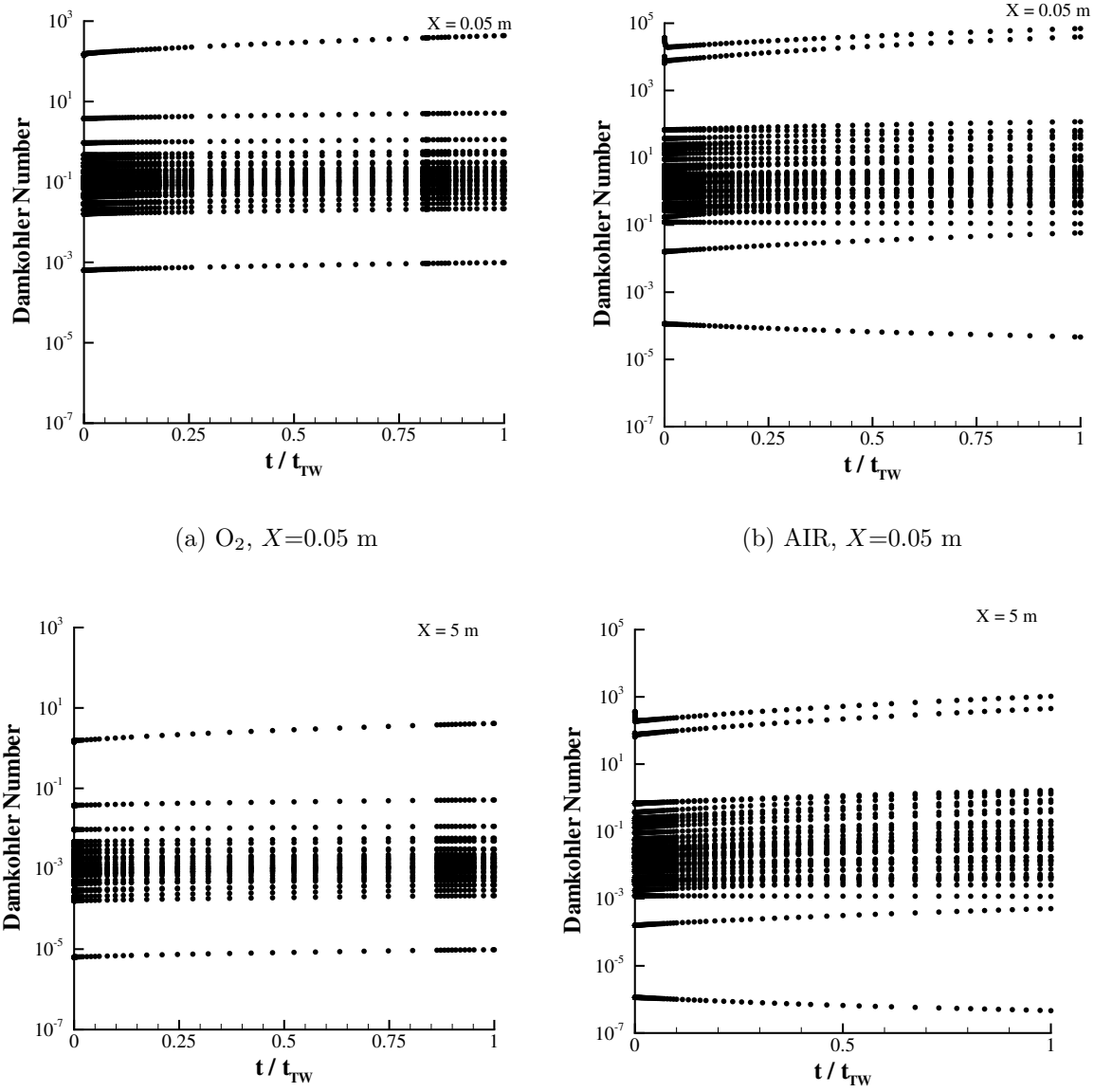

(a) O_2, X=0.05 m

(b) AIR, X=0.05 m

(c) O_2, X=5 m

(d) AIR, X=5 m

Figure 6.17: Damkohler numbers for each reaction progress variable in ethylene-oxygen and ethylene-air mixtures through the Taylor wave. The initial pressure is 20 kPa. The x-axis is time normalized by the total time each particle takes to travel through the Taylor wave.

variable that is not in equilibrium. Having a single progress variable not in equilibrium does not imply that the state variables will approximate the frozen isentrope (Fig. 6.14), but rather that a critical number of non-equilibrated progress variables must exist for this to occur. At the lower pressure of 20 kPa, it is only for particles

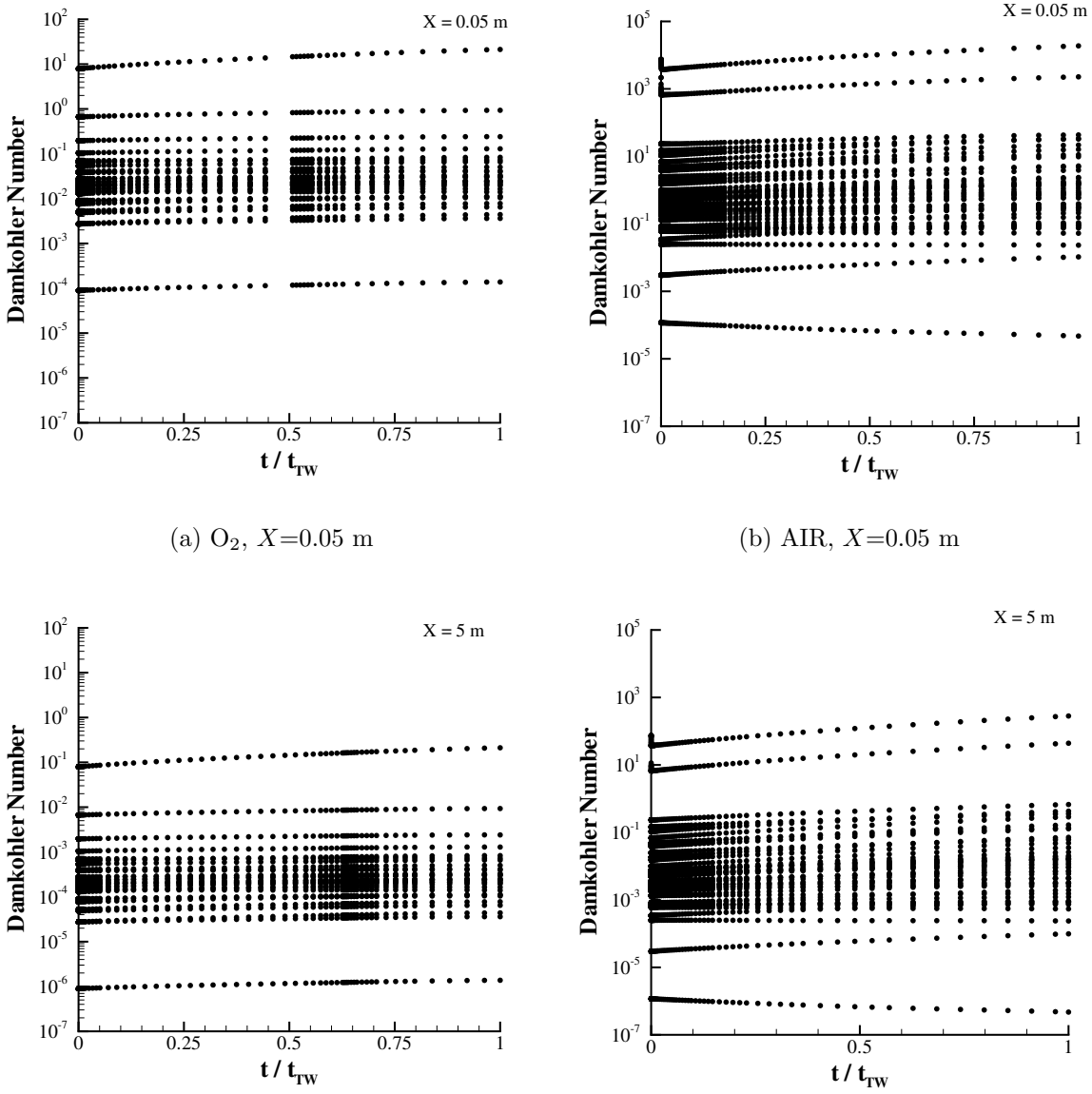

(a) O_2, X=0.05 m

(b) AIR, X=0.05 m

(c) O_2, X=5 m

(d) AIR, X=5 m

Figure 6.18: Damkohler numbers for each reaction progress variable in ethylene-oxygen and ethylene-air mixtures through the Taylor wave. The initial pressure is 100 kPa. The x-axis is time normalized by the total time each particle takes to travel through the Taylor wave.

initially at $X = 0.05$ m (Fig. 6.17(a)), does a departure from equilibrium appear (Fig. 6.14). Thus, based on the chemical reaction mechanism used, slight deviations from equilibrium can exist and the state can still be effectively modeled assuming equilibrium since only a small fraction of the Damkohler numbers are greater than

one.

The same trends are observed for the ethylene-air mixtures, but now the number of nonequilibrated reaction progress variables are greater than in the oxygen cases. At an initial pressure of 100 kPa and an initial particle position of $X = 0.05$ m (Fig. 6.18(b)), at least ten of the reaction progress variables have not equilibrated. This trend is more prominent when $P_1 = 20$ kPa such that now, over half of the Damkohler numbers are greater than one (Fig. 6.17(b)). This reinforces the visual observation that the particle behavior more closely approximates the frozen isentrope in Fig. 6.16(b).

The reaction progress variable with the smallest eigenvalue has the largest t_{chem} which we define as t^*_{chem} and it is of interest to determine the species that influence the long equilibration time. These are determined from the eigenvectors of the Jacobian. The eigenvectors themselves do not vary significantly for different initial pressures and the same mixture, only the corresponding eigenvalues change. As a result, Table 6.4 lists the magnitude of t^*_{chem} averaged over the six particles analyzed at each pressure and mixture. Variations in t^*_{chem} less than 1% were observed over the range of initial positions. Alternatively, the values of t_{flow} do not vary with pressure, but depend on the initial particle position (Table 6.5).

Oxidizer	P_1 [kPa]	t^*_{chem} (ms)
O_2	20	22.1
O_2	60	2.8
O_2	100	1.1
Air	20	5491.3
Air	60	2262.9
Air	100	1522.0

Table 6.4: Tabulated t^*_{chem} for ethylene-oxygen and ethylene-air mixtures. Values are averaged over the six initial positions at each initial pressure.

The species combinations corresponding to the values of t^*_{chem} in the ethylene-oxygen mixtures is

$$0.17\ H_2 + 0.36\ H + 0.38\ O + 0.15\ O_2 + 0.24\ OH + 0.45\ CO \leftrightarrows 0.46\ H_2O + 0.45\ CO_2$$

and in the ethylene-air mixtures is

X (m)	O_2: t_{flow} (ms)	Air: t_{flow} (ms)
5	0.1	0.1
2.5	0.3	0.3
1	0.5	0.6
0.5	1.0	1.3
0.25	2.6	3.2
0.05	5.1	6.4

Table 6.5: Tabulated t_{flow} for ethylene-oxygen and ethylene-air mixtures, different particles averaged over the initial pressures analyzed.

$$0.08\ H_2 + 0.02\ H + 0.37\ CO + 0.74\ NO \leftrightarrows 0.37\ N_2 + 0.15\ O_2 + 0.09\ H_2O + 0.37\ CO_2\ .$$

These relationships are comprised of several common dissociation/recombination reactions for H_2-O_2 and CO-CO_2. For example, the mole fractions of carbon in the reaction suggests the equilibrium relation $CO \rightleftarrows CO_2 + O$. The H_2O molecules may be in equilibrium based on either $H_2O \rightleftarrows OH + H$ or $H_2O \rightleftarrows H_2 + 1/2\ O_2$. The remaining OH, H_2, and O_2 molecules are likely in equilibrium as specified by $2\ OH \rightleftarrows H_2 + O_2$, $H_2 \rightleftarrows 2H$, and $O_2 \rightleftarrows 2O$. In the case of the ethylene-air mixtures, these same equilibrium reactions for the C, H_2O, and OH species exist, in addition to equilibrium relations for the nitrogen species. The Zeldovich mechanism for NO is the most likely and consists of three relations: $O + N_2 \rightarrow NO + N$, $N + O_2 \rightarrow NO + O$, $N + OH \rightarrow NO + H$. This NO mechanism is known to be slow compared to the other equilibrium relations and it is the cause for the largest values of t^*_{chem} in Table 6.4.

The Damkohler numbers are plotted in Fig. 6.19 for the values of t^*_{chem} at the end of the Taylor wave as a function of initial particle position. As noted before, the particles initially located closer to the thrust surface experience the greatest rate of pressure decrease and many chemical reactions have not equilibrated at this point. The percentage of the total progress variables not in equilibrium by the end of the Taylor wave is plotted in Fig. 6.20. This percentage increases as the initial mixture pressure decreases. In a 1-m tube, 20% of the progress variables have not reached equilibrium in the detonation products of a low-pressure ethylene-air mixture, whereas only 4% have not equilibrated in the products of a low-pressure ethylene-oxygen mixture.

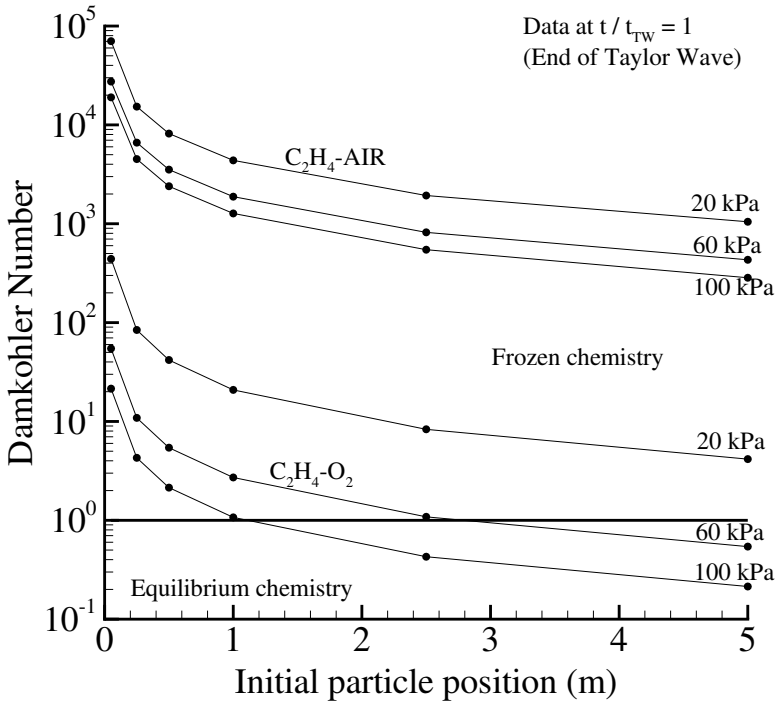

Figure 6.19: Damkohler numbers at the end of the Taylor wave for the values of t^*_{chem} as a function of the initial particle position.

6.7 Conclusions

An analysis of expanding detonation products through the Taylor wave in a tube that is closed at one end and open at the other has been presented. Ethylene-oxygen and ethylene-air mixtures at three initial pressures were considered and a total of six particles with different initial positions along the tube were tracked to determine the time rate of change in their state parameters. Using an eigenvalue analysis of the species equation, the chemical timescales and associated progress variables were computed.

The fuel-oxygen detonation products are hotter than the fuel-air products and so it is generally appropriate to assume equilibrium composition. However, significant differences between the values of γ in these hotter mixtures exist due to the much higher degree of dissociation. While the values of γ are similar for the fuel-air mixtures, these detonation products are not as close to equilibrium because their colder

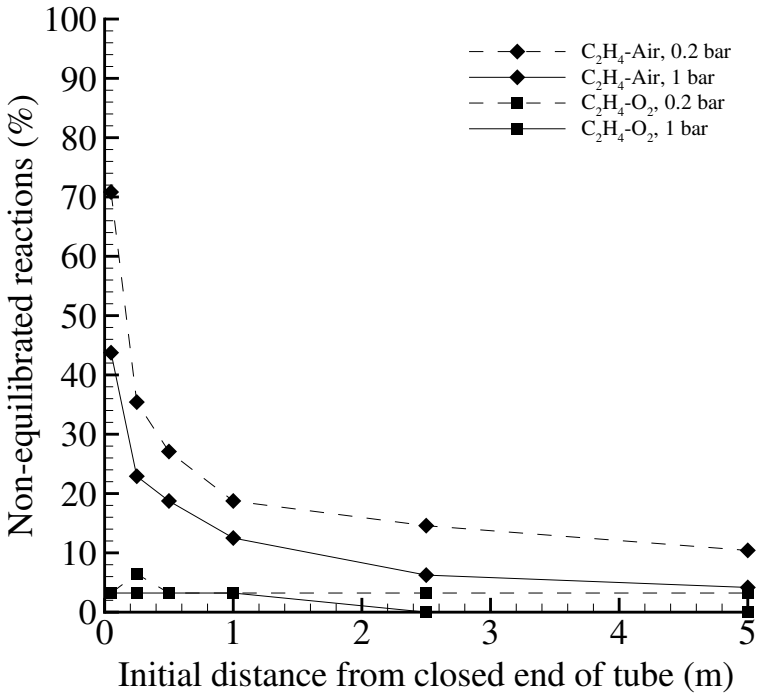

Figure 6.20: The percentage of independent reaction progress variables in non-equilibrium by the end of the Taylor wave in ethylene-oxygen and ethylene-air mixtures with initial pressures of 0.2 bar and 1 bar as a function of the initial particle position.

temperatures.

In fact, substantial non-equilibrium exists in fuel-air mixtures, especially for particles located near the thrust surface. The percentage of the total progress variables that have not equilibrated by the end of the Taylor wave increases as the initial mixture pressure decreases. In a 1-m tube, 20% of the progress variables have not reached equilibrium in the detonation products of a low-pressure ethylene-air mixture, whereas only 4% have not equilibrated in the products of a low-pressure ethylene-oxygen mixture. This means that ethylene-oxygen mixtures can be accurately modeled using the equilibrium flow assumption, but that significant departures from equilibrium are present for low-pressure ethylene-air mixtures, especially in short (< 1 m) detonation tubes. However, only modest variations in the effective polytropic exponent occur due to non-equilibrium in the ethylene-air mixtures. Additional departures from equilibrium are expected if further flow expansion is obtained through a nozzle at the tube

exit.

Chapter 7

Conclusions

This work is an experimental and analytical study of impulse generation by detonation tubes. It was motivated by the lack of experimental data and scientific understanding on what operating parameters affect impulse. The main topics that are addressed include quantification of the impulse obtained from partially filled tubes operating in atmospheric conditions, fully filled tubes operating in sub-atmospheric conditions, and tubes with exit nozzles.

A new understanding of the mechanisms that contribute to the increase in specific impulse when the tube is partially filled have been presented through new analysis of the detonation tube in terms of the masses and with the development of a "bubble" model that is valid in the limit of a nearly empty tube. Together these models can be used to correlate the available experimental and numerical data of impulse for a wide range of combustible mixtures and inert gases. In the case of partially filled detonation tubes exhausting into 1 atm environments, previous research determined that the specific impulse increases if only a fraction of the tube contains the explosive mixture. Through analysis of all the available published data it was determined that a correlation based solely on the volumetric fill fraction (Zhdan et al., 1994, Li and Kailasanath, 2003) does not correctly predict the specific impulse when the densities of the explosive and inert gases are significantly different, such as in the case of hydrogen-oxygen mixtures exhausting into air at standard conditions. Consideration of the principles of energy conservation indicate that the specific impulse depends primarily on the chemical energy of the explosive and the relative mass ratios. As a result,

correlating the specific impulse with the explosive mass fraction and by compiling all the available experimental and numerical data from partially filled detonation tubes showed that the data can be predicted by a single unifying relationship.

This mass-based relationship clearly fails in the limit when the explosive mass fraction goes to zero because the impulse is dominated by unsteady gas dynamics. An analytical model of an expanding "bubble" of hot, constant-volume combustion products in an infinitely long tube was developed to successfully predict the theoretical maximum specific impulse from an arbitrary explosive-inert gas combination. The maximum specific impulse was found to depend on the sound speed ratio between the hot expanding products and the inert gas, the ratio of specific heats of the expanding hot products, and the pressure decay at the thrust surface. With one-dimensional gas dynamics, the contact surface trajectory was predicted as the hot products expanded which determined the pressure decay at the thrust surface. A plot of the non-dimensional pressure decay integral was determined for a variety of initial pressure ratios and values for the specific heat ratio in the products. These predictions, along with the new model, are new contributions to the PDE community for which no other models of this kind exist. The predictions are in good agreement with the available numerical data that exists for ethylene-oxygen and hydrogen-oxygen mixtures.

Detonation tubes exhausting into sub-atmospheric pressures were studied through the first experimental study directly measuring impulse with the ballistic pendulum as the environment pressure varied. Previously, only a few numerical studies have predicted the impulse under these conditions. The detonation tube was installed within the dump tank of Caltech's T5 hypersonic wind tunnel facility. This enabled tests to be carried out in environment pressures from 100 to 1.4 kPa and with initial pressures between 100 to 30 kPa in the ethylene-oxygen mixtures. The results showed that the impulse increases as the environment pressure deceases. For example, at an initial mixture pressure of 80 kPa, decreasing the environment pressure from 100 to 1.4 kPa increases the impulse by 15%. The increase in impulse is attributed to an increase in the pressure differential across the thrust surface and the blowdown time.

With the database of new experimental results, the increase in blowdown time was quantified and used to improve the original impulse model of Wintenberger et al. (2003). This model is capable of accurate predictions of the impulse for a variety of mixtures, initial pressures, equivalence ratios, and now for a variety of environment pressures.

The first experiments determining the effect of nozzles on detonation tube impulse were also carried out. As before, the impulse was measured as the environment pressure varied generating the first set of experimental data proving that nozzles can increase the impulse over the case of a plain tube at all sub-atmospheric environment pressures. Previous studies have investigated nozzles, but these were carried out with the tube exhausting into 100 kPa air and only a few nozzle designs were tested. A total of twelve different nozzles including converging, diverging, converging-diverging, and a straight extension were tested in this study.

The effect of incomplete product gas expansion is observed when all of the impulse data are plotted in terms of the nozzle pressure ratio P_3/P_0 and compared to the steady flow impulse predictions assuming isentropic expansion. The straight detonation tube with no exit nozzle generated the lowest values of impulse. Adding a nozzle successfully increases the impulse over the baseline case, yet how the nozzle affects the impulse depends on the pressure ratio. Figure 5.33 is the first demonstration that a nozzle on an unsteady device has two operating regimes. At large pressure ratios, a quasi-steady flow regime is established and the nozzle divergence expands the flow. Here the impulse values are ordered in terms of increasing nozzle exit area ratio. At small pressure ratios, the unsteady gas dynamics previously investigated in the partially filled detonation tubes are observed. Here the impulse values are ordered in terms of their mass fractions and are even observed to produce impulse values greater than the steady flow impulse predictions.

A final numerical study was carried out to investigate the effect of chemical non-equilibrium on expanding flows of detonation products by solving the species evolution based on detailed chemical kinetics and a prescribed pressure-time history approximated by the similarity solution for the Taylor wave following a detonation

propagating from the closed end of a tube. An eigenvalue analysis of the Jacobian matrix $\mathcal{J} = \partial\Omega_i/\partial Y_k$ determined the characteristic time required for the associated progress variables to relax to equilibrium after a disturbance. Comparison of these chemical timescales to the flow timescale (based on the rate of pressure decrease) tested the assumption of chemical equilibrium. Substantial non-equilibrium exists in fuel-air mixtures, especially for particles located near the closed end of the tube. The percentage of the total progress variables that have not equilibrated by the end of the Taylor wave increases as the initial mixture pressure decreases. In a 1 m tube, 20% of the progress variables have not reached equilibrium in the detonation products of a low-pressure ethylene-air mixture, whereas only 4% have not equilibrated in the products of a low-pressure ethylene-oxygen mixture. This means that ethylene-oxygen mixtures can be accurately modeled using the equilibrium flow assumption, but that significant departures from equilibrium are present for low-pressure ethylene-air mixtures, especially in short (< 1 m) detonation tubes.

7.1 Future work

When the detonation wave enters the divergent nozzle section, a decaying shock wave is established. The role of this decaying shock wave under different environment pressures and nozzle divergence angles would be of interest to investigate experimentally in a two-dimensional facility capable of taking high speed movies of the shock trajectory and possible boundary layer separation along the nozzle walls. At very large pressure ratios, such as those in hypersonic wind tunnel facilities, the presence of a secondary shock is well known. It would be of interest to investigate the role of this secondary shock in relation to the unsteady exhaust flow from a detonation tube. We would expect these shock structures to be qualitatively different between the previously observed nozzle operating regimes.

The extent of the Taylor wave behind the detonation wave may also have an effect on the nozzle flow and subsequent impulse. All of these tests were carried out in a tube 1 m in length. From predictions of the internal flow field following a detonation

propagating in a tube closed at one end, a detonation wave that has propagated a long distance has a long expansion region and comparatively low rate of pressure decrease behind it as compared to a detonation wave that has only propagated a very short distance from the closed tube end. A study investigating the effect of nozzle performance as a function of tube length and environment pressure would be of interest.

Bibliography

M. Ahmadian, R. J. Appleton, and J. A. Norris. Designing magneto-rheological dampers in a fire out-of-battery recoil system. *IEEE Transactions on Magnetics*, 39(1):480–485, 2003.

R. Akbar, D. W. Schwendeman, J. E. Shepherd, R. L. Williams, and G. O. Thomas. Wave shaping channels for gaseous detonations. In R. Brun and L. Z. Dumitrescu, editors, *Shock Waves at Marseille IV*. Springer-Verlag, Berlin, 1995.

R. Akbar, P. A. Thibault, P. G. Harris, L. S. Lussier, F. Zhang, S. B. Murray, and K. Gerrard. Detonation properties of unsensitized and sensitized JP-10 and Jet-A fuels in air for pulse detonation engines. 36th AIAA/ASME/SAE/ASEE Joint Propulsion Conference and Exhibit, July 16–19, Huntsville, AL, AIAA 2000–3592, 2000.

D. Allgood and E. Gutmark. Effects of exit geometry on the performance of a pulse detonation engine. 40th AIAA Aerospace Sciences Meeting and Exhibit, January 14–17, Reno, NV, AIAA2002-0613, 2002.

D. Allgood, E. Gutmark, A. Rasheed, and A. J. Dean. Experimental investigation of a pulse detonation engine with a 2D ejector. 42nd AIAA Aerospace Sciences Meeting and Exhibit, January 5–8, Reno, NV, AIAA2004-0864, 2004.

H. O. Amann. Experimental study of the starting process in a reflection nozzle. *The Physics of Fluids Supplement*, I:150–153, 1969.

M. Arens. Flow separation in overexpanded contoured nozzles. *AIAA Journal*, 1(8): 1945–1955, 1963.

M. Arens and E. Spiegler. Shock-induced boundary layer separation in overexpanded conical exhaust nozzles. *AIAA Journal*, 1(3):578–581, 1963.

J. M. Austin and J. E. Shepherd. Detonations in hydrocarbon fuel blends. *Combustion and Flame*, 132(1-2):73–90, 2003.

A. K. Aziz, H. Hurwitz, and H. M. Sternberg. Energy transfer to a rigid piston under detonation loading. *Phys. of Fluids*, 4(3):380–384, 1961.

L. H. Back and G. Varsi. Detonation propulsion for high pressure environments. *AIAA Journal*, 12(8):1123–1130, 1974.

Philip R. Bevington. *Data Reduction and Error Analysis in the Physical Sciences*. McGraw-Hill, 1969.

A. A. Borisov, S. A. Gubin, and V. A. Shargatov. Applicability of a chemical equilibrium model to explosion products. In *Prog. Astronaut. Aeronaut.*, volume 134, pages 138–153, 1991.

C. E. Brennen. *Cavitation and Bubble Dynamics*. Oxford University Press, 1995.

C. M. Brophy and D. W. Netzer. Effects of ignition characteristics and geometry on the performance of a JP-10/O_2 fueled pulse detonation engine. 35th AIAA/ASME/SAE/ASEE Joint Propulsion Conference and Exhibit, June 20–24, 1999, Los Angeles, CA, AIAA 99-2635, 1999.

J. L. Cambier and J. K. Tegner. Strategies for pulsed detonation engine performance optimization. *Journal of Propulsion and Power*, 14(4):489–498, 1998.

T. W. Chao. *Gaseous detonation-driven fracture of tubes*. PhD thesis, California Institute of Technology, 2004.

C. L. Chen, S. R. Chakravarthy, and C. M. Hung. Numerical investigation of separated nozzle flows. *AIAA Journal*, 32(9):1836–1843, 1994.

M. Cooper, S. Jackson, J. Austin, E. Wintenberger, and J. E. Shepherd. Direct experimental impulse measurements for deflagrations and detonations. 37th AIAA/ASME/SAE/ASEE Joint Propulsion Conference, July 8–11, 2001, Salt Lake City, UT, AIAA 2001-3812, 2001.

M. Cooper, S. Jackson, J. Austin, E. Wintenberger, and J. E. Shepherd. Direct experimental impulse measurements for detonations and deflagrations. *Journal of Propulsion and Power*, 18(5):1033–1041, 2002.

M. Cooper, S. Jackson, and J. E. Shepherd. Effect of deflagration-to-detonation transition on pulse detonation engine impulse. GALCIT Report FM00-3, Graduate Aeronautical Laboratories, California Institute of Technology, Pasadena, CA 91125, 2000.

M. Cooper and J. E. Shepherd. The effect of nozzles and extensions on detonation tube performance. 38th AIAA/ASME/SAE/ASEE Joint Propulsion Conference and Exhibit, July 7–10, 2002, Indianapolis, IN, AIAA 02–3628, 2002.

M. Cooper and J. E. Shepherd. Experiments studying thermal cracking, catalytic cracking, and pre-mixed partial oxidation of JP-10. 39th AIAA/ASME/SAE/ASEE Joint Propulsion Conference and Exhibit, Huntsville, AL, 2003-4687, 2003.

M. Cooper and J. E. Shepherd. Effect of porous thrust surface on transition to detonation and impulse. *J. Propulsion and Power*, 20(3), 2004. in print.

P. W. Cooper. *Explosives Engineering*. Wiley-VCH, Inc., New York, NY, 1996.

J. Corner. *Theory of the Interior Ballistics of Guns*. Wiley, New York, 1950.

D. F. Davidson, D. C. Horning, M. A. Oehlschlaeger, and R. K. Hanson. The decomposition products of JP-10. 37th AIAA/ASME/SAE/ASEE Joint Propulsion Conference and Exhibit, July 8–11,Salt Lake City, UT, AIAA 2001–3707, 2001.

W. C. Davis. Introduction to explosives. In J. A. Zukas and W. P. Walters, editors, *Explosive Effects and Applications*. Springer-Verlag, New York, 1998.

W. Doering. On detonation processes in gases. *Ann. Phys.*, 43:421–436, 1943.

S. Dorofeev, V. P. Sidorov, M. S. Kuznetzov, I. D. Matsukov, and V. I. Alekseev. Effect of scale on the onset of detonations. *Shock Waves*, 10:137–149, 2000.

S.B. Dorofeev, M.S. Kuznetsov, V.I. Alekseev, A.A. Efimenko, and W. Breitung. Evaluation of limits for effective flame acceleration in hydrogen mixtures. *Journal of Loss Prevention in the Process Industries*, 14(6):583–589, 2001.

G. E. Duvall, J. O. Erkman, and C. M. Ablow. Explosive acceleration of projectiles. *Israel Journal of Technology*, 7(6):469–475, 1969.

C. A. Eckett. *Numerical and analytical studies of the dynamics of gaseous detonation.* PhD thesis, California Institute of Technology, 2001.

S. Eidelman and X. Yang. Analysis of the pulse detonation engine efficiency. 34th AIAA/ASME/SAE/ASEE Joint Propulsion Conference and Exhibit, July 13–15, 1998, Cleveland, OH, AIAA 98–3877, 1998.

T. Endo, T. Yatsufusa, S. Taki, J. Kasahara, A. Matsuo, S. Sato, and T. Fujiwara. Homogeneous-dilution model of partially-fueled pulse detonation engines. 42nd AIAA Aerospace Sciences Meeting and Exhibit, January 5–8, 2004, Reno, NV, AIAA2004-1214, 2004.

F. Falempin, D. Bouchaud, B. Forrat, D. Desbordes, and E. Daniau. Pulsed detonation engine possible application to low cost tactical missile and to space launcher. 37th AIAA/ASME/SAE/ASEE Joint Propulsion Conference and Exhibit, July 8–11, 2001, Salt Lake City, UT, AIAA 2001–3815, 2001.

R. Farinaccio, P. Harris, R. A. Stowe, R. Akbar, and E. LaRochelle. Multi-pulse detonation experiments with propane-oxygen. 38th AIAA/ASME/SAE/ASEE Joint Propulsion Conference and Exhibit, July 7–10, Indianapolis, IN, AIAA2002–4070, 2002.

W. Fickett. Motion of a plate driven by an explosive. *J. Appl. Phys.*, 62(12):4945–4946, 1987.

W. Fickett and W. C. Davis. *Detonation*. University of California Press, Berkerely, CA, 1979.

P. A. Fomin and A. V. Trotsyuk. An approximate calculation of the isentrope of a gas in chemical equilibrium. *Fizika Goreniya i Vzryva*, 31(4):59–62, 1995.

M. Frey and G. Hagemann. Restricted shock separation in rocket nozzles. *J. Propulsion and Power*, 16(3):478–484, 2000.

Jerry H. Ginsberg and Joseph Genin. *Dynamics*. West Publishing Company, Minneapolis/St. Paul, second edition, 1995.

R. J. Green, S. Nakra, and S. L. Anderson. Breakdown behavior of fuels for pulse detonation engines. Office of Naval Research, Energy Conversion and Propulsion Program, August 2001.

V. V. Grigor'ev. Use of a nozzle in particle acceleration by a flow of gas detonation products in tubes. *Combustion, Explosion, and Shock Waves*, 32(5):492–499, 1996.

R. W. Gurney. The initial velocites of fragments from bombs, shells, and grenades. Technical report, Army Ballistic Research Laboratory, 1943. Report BRL 405.

S. Guzik, P. G. Harris, and A. De Champlain. An investigation of pulse detonation engine configurations using the method of characteristics. 38th AIAA/ASME/SAE/ASEE Joint Propulsion Conference and Exhibit, July 7-10, 2002, Indianapolis, IN, AIAA2002-4066, 2002.

P. G. Harris, R. Farinaccio, R. A. Stowe, A. J. Higgins, P. A. Thibault, and J. P. Laviolette. The effect of ddt distance on impulse in a detonation tube. 37th AIAA/ASME/SAE/ASEE Joint Propulsion Conference and Exhibit, July 8–11, 2001, Salt Lake City, UT, AIAA 2001–3467, 2001.

I. G. Henry. The Gurney formula and related approximations for high-explosive deployment of fragments. Technical report, AD813398, Hughes Aircraft Co., 1967. Report PUB-189.

P. G. Hill and C. R. Peterson. *Mechanics and Thermodynamics of Propulsion*. Addison-Wesley, second edition, 1992.

J. B. Hinkey, J. T. Williams, S. E. Henderson, and T.R. A. Bussing. Rotary-valved, multiple-cycle, pulse detonation engine experimental demonstration. 33rd AIAA/ASME/SAE/ASEE Joint Propulsion Conference and Exhibit, July, Seattle, WA, AIAA97-2746, 1997.

B. Hitch. The effect of autoignition-promoting additives on deflagration-to-detonation transition. 38th AIAA/ASME/SAE/ASEE Joint Propulsion Conference and Exhibit, July 7–10, Indianapolis, IN, AIAA 2002–3719, 2002.

N. Hoffman. Reaction propulsion by intermittent detonative combustion. German Ministry of Supply, AI152365 Volkenrode Translation, 1940.

O. Igra, L. Wang, J. Falcovitz, and O. Amann. Simulation of the starting flow in a wedge-like nozzle. *Shock Waves*, 8:235–242, 1998.

S. I. Jackson, M. Grunthaner, and J. E. Shepherd. Wave implosion as an initiation mechanism for pulse detonation engines. 39th AIAA/ASME/SAE/ASEE Joint Propulsion Conference and Exhibit, July 20-23, 2003, Huntsville, AL, AIAA2003-4820, 2003.

P. A. Jacobs and R. J. Stalker. Mach 4 and Mach 8 axisymmetric nozzles for a high–enthalpy shock tunnel. *Aeronautical Journal*, 95:324–334, Nov. 1991.

S. J. Jacobs. The energy of detonation. NAVORD Report 4366, U.S. Naval Ordnance Laboratory, White Oak, MD. Available as NTIS AD113271 – Old Series, 1956.

G. E. Jones, J. E. Kennedy, and L. D. Bertholf. Ballistics calculations of R. W. Gurney. *American Journal of Physics*, 48(4):264–269, 1980.

S.A.S. Jones and G. O. Thomas. Pressure hot-wire and laser doppler anemometer studies of flame acceleration in long tubes. *Combustion and Flame*, 87:21–32, 1991.

K. Kailasanath. A review of PDE research - performance estimates. 39th AIAA Aerospace Sciences Meeting and Exhibit, January 8–11, 2001 Reno, NV, AIAA2001-0474, 2001.

K. Kailasanath and G. Patnaik. Performance estimates of pulsed detonation engines. In *Proceedings of the 28th International Symposium on Combustion*, pages 595–601. The Combustion Institute, 2000.

J. Kasahara. Experimental analysis of pulse detonation engine performance by pressure and momentum measurements. AIAA2003-0893, 2003.

James E. Kennedy. The gurney model of explosive output for driving metal. In Jonas A. Zuker and William P. Walters, editors, *Explosive Effects and Applications*, chapter 7, pages 221–257. Springer, New York, 1998.

C. B. Kiyanda, V. Tanguay, A. J. Higgins, and J. H. S. Lee. Effect of transient gas dynamic processes on the impulse of pulse detonation engines. *J. of Propulsion and Power*, 18(5):1124–1126, 2002.

R. Knystautas, J.H.S. Lee, J. E. Shepherd, and A. Teodorczyk. Flame acceleration and transition to detonation in benzene-air mixtures. *Combustion and Flame*, 115: 424–436, 1998.

R. A. Lawrence and E. E. Weynand. Factors affecting flow separation in contoured supersonic nozzles. *AIAA Journal*, 6(6):1159–1160, 1968.

C. Li and K. Kailasanath. Performance analysis of pulse detonation engines with partial fuel filling. *Journal of Propulsion and Power*, 19(5):908–916, 2003.

R. P. Lindstedt and H. J. Michels. Deflagration to detonation transitions and strong deflagrations in alkane and alkene air mixtures. *Combustion and Flame*, 76:169–181, May 1989.

K. McManus, E. Furlong, I. Leyva, and S. Sanderson. Mems based pulse detonation engine for small scale propulsion applications. 37th AIAA/ASME/SAE/ASEE Joint Propulsion Conference and Exhibit, July 8–11, 2001, Salt Lake City, UT, AIAA 2001–3469.

C. I. Morris. Numerical modeling of pulse detonation rocket engine gasdynamics and performance. 42nd AIAA Aerospace Sciences Meeting and Exhibit, Reno, NV, January 5–8, 2004–0463, 2004.

J. A. Nicholls, H. R. Wilkinson, and R. B. Morrison. Intermittent detonation as a thrust-producing mechanism. *Jet Propulsion*, 27(5):534–541, 1958.

Yu. A. Nikolaev and P. A. Fomin. Analysis of equilibrium flows of chemically reacting gases. *Fizika Goreniya i Vzryva*, 18(1):66–72, 1982.

J. J. Quirk. AMRITA - a computational facility (for CFD modeling). VKI 29th CFD Lecture Series, edited by H. Deconind, von Karman Inst. for Fluid Dynamics, Belgium, 1998.

M. I. Radulescu, C. I. Morris, and R. K. Hanson. The effect of wall heat loss on the flow fields in a pulse-detonation wave engine. 42nd AIAA Aerospace Sciences Meeting and Exhibit, January 5–8, 2004, Reno, NV, AIAA 2004–1124, 2004.

A. Rasheed, V. E. Tangirala, C. L. Vandervort, A. J. Dean, and C. Haubert. Interactions of a pulsed detonation engine with a 2D turbine blade cascade. 42nd AIAA Aerospace Sciences Meeting and Exhibit, Reno, NV, January 5–8, 2004–1207, 2004.

W. C. Reynolds. The element potential method for chemical equilibrium analysis: Implementation in the interactive program stanjan, version 3. Technical report, Dept. of Mechanical Engineering, Stanford University, Stanford, CA, January 1986.

Benjamin Robbins. *New Principles of Gunnery.* London Royal Society, London, a new edition by charles hutton edition, 1805.

C. S. Robinson. *The Thermodynamics of Firearms.* McGraw-Hill, New York, 1943.

G. L. Romine. Nozzle flow separation. *AIAA Journal*, 36(9):1618–1625, 1998.

T. Saito and K. Takayama. Numerical simulations of nozzle starting process. *Shock Waves*, 9:73–79, 1999.

S. Sato, A. Matsuo, J. Kasahara, and T. Endo. Numerical investigation of the PDRE performance with detailed chemistry. 42nd AIAA Aerospace Sciences Meeting and Exhibit, January 5–8, 2004, Reno, NV, AIAA2004-0464, 2004.

F. Schauer, J. Stutrud, and R. Bradley. Detonation initiation studies and performance results for pulsed detonation engines. 39th AIAA Aerospace Sciences Meeting and Exhibit, January 8–11, 2001, Reno, NV, AIAA 2001-1129, 2001.

E. Schultz and J.E. Shepherd. Validation of detailed reaction mechanisms for detonation simulation. Technical Report FM99-5, Graduate Aeronautical Laboratories, California Institute of Technology, February 2000.

M. P. Scofield and J. D. Hoffman. Maximum thrust nozzles for nonequilibrium simple dissociating gas flows. *AIAA Journal*, 9(9):1824–1832, 1971.

L. I. Sedov. *A Course in Continuum Mechanics*. Groningen, Wolters-Noordhoff, 1971-72.

J. E. Shepherd. *Dynamics of vapor explosions: rapid evaporation and instability of butane droplets exploding at the superheat limit*. PhD thesis, California Institute of Technology, Pasadena, California, 1980.

J. E. Shepherd and M. Kaneshige. Detonation database. Technical report, Graduate Aeronautical Laboratories, California Institute of Technology, July 1997, rev. 2001. Report FM97-8.

J. E. Shepherd, A. Teodorczyk, R. Knystautas, and J. H. Lee. Shock waves produced by reflected detonations. *Progress in Astronautics and Aeronautics*, 134:244–264, 1991.

C. E. Smith. The starting process in a hypersonic nozzle. *J. Fluid Mechanics*, 24: 625–640, 1966. part 4.

K. P. Stanyukovich. *Unsteady Motion of Continuous Media*, pages 142–196. Pergamon Press, 1960.

George P. Sutton. *Rocket Propulsion Elements*. John Wiley and Sons, Inc., New York, NY, sixth edition, 1992.

G. I. Taylor. The dynamics of the combustion products behind plane and spherical detonation fronts in explosives. *Proc. Roy. Soc.*, A200:235–247, 1950.

G. O. Thomas and R. Ll. Williams. Detonation interaction with wedges and bends. *Shock Waves*, 11:481–492, 2002.

P. A. Thompson. *Compressible Fluid Dynamics*, pages 347–359. Rensselaer Polytechnic Institute Bookstore, Troy, NY, 1988.

S. Tokarcik-Polsky and J. Cambier. Numerical study of transient flow phenomena in shock tunnels. *AIAA J.*, 32(5):971–978, 1994.

Y. Tzuk, I. Bar, and S. Rosenwaks. Dynamics of the detonation products of lead azide. IV. laser shadowgraphy of expanding species. *J. Appl. Phys.*, 74(9):5360–5365, 1993.

J. von Neumann. Theory of detonation waves. In A. J. Taub, editor, *John von Neumann, Collected Works*. Macmillan, New York, 1942.

R. P. Welle, B. S. Hardy, J. W. Murdock, A. J. Majamaki, and G. F. Hawkins. Separation instabilities in overexpanded nozzles. 39th AIAA/ASME/SAE/ASEE Joint Propulsion Conference and Exhibit, Huntsville, AL, 2003-5239, 2003.

E. Wintenberger. *Application of steady and unsteady detonation waves to propulsion*. PhD thesis, California Institute of Technology, 2004.

E. Wintenberger, J. Austin, M. Cooper, S. Jackson, and J. E. Shepherd. An analytical model for the impulse of a single-cycle pulse detonation engine. 37th AIAA/ASME/SAE/ASEE Joint Propulsion Conference, July 8–11, 2001, Salt Lake City, UT, AIAA 2001-3811, 2001.

E. Wintenberger, J. Austin, M. Cooper, S. Jackson, and J. E. Shepherd. An analytical model for the impulse of a single-cycle pulse detonation engine. *Journal of Propulsion and Power*, 19(1):22–38, 2003.

E. Wintenberger, J. M. Austin, M. Cooper, S. Jackson, and J. E. Shepherd. Impulse of a single-pulse detonation tube. Technical report, Graduate Aeronautical Laboratories, California Institute of Technology, 2002. Report FM00-8.

Y. Wu, F. Ma, and V. Yang. System performance and thermodynamic cycle analysis of air-breathing pulse detonation engines. *Journal of Propulsion and Power*, 19(4): 556–567, 2003.

V. Yang, Y. H. Wu, and F. H. Ma. Pulse detonation engine performance and thermodynamic cycle analysis. ONR Propulsion Meeting, 2001, 2001.

L. J. Zajac and A. K. Oppenheim. Thermodynamics computations for the gasdynamic analysis of explosion. *Combust. Flame*, 13(5):537–550, 1969.

Ya. B. Zel'dovich. On the theory of the propagation of detonations in gaseous systems. *JETP*, 10:542–568, 1940. Available in translation as NACA TM 1261 (1950).

S. A. Zhdan, V. V. Mitrofanov, and A. I. Sychev. Reactive impulse from the explosion of a gas mixture in a semi-infinite space. *Combustion, Explosion and Shock Waves*, 30(5):657–663, 1994.

R. Zitoun and D. Desbordes. Propulsive performances of pulsed detonations. *Comb. Sci. Tech.*, 144(1):93–114, 1999.

Appendix A

Damkohler Data

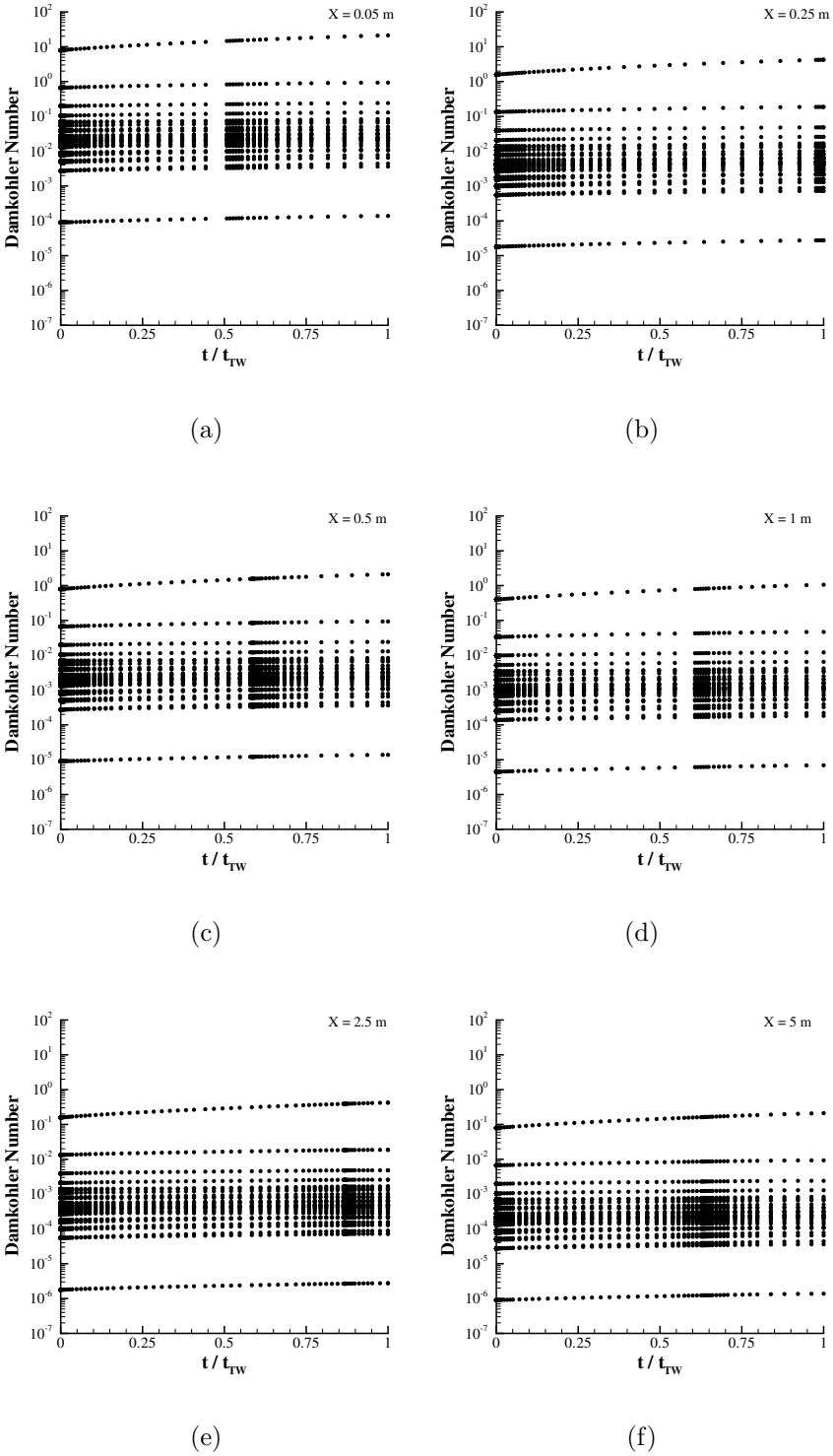

Figure A.1: Damkohler numbers for particles with varying initial position. Initial mixture is C_2H_4-O_2 at 100 kPa. x-axis is time normalized by the total time each particle takes to travel through the TW.

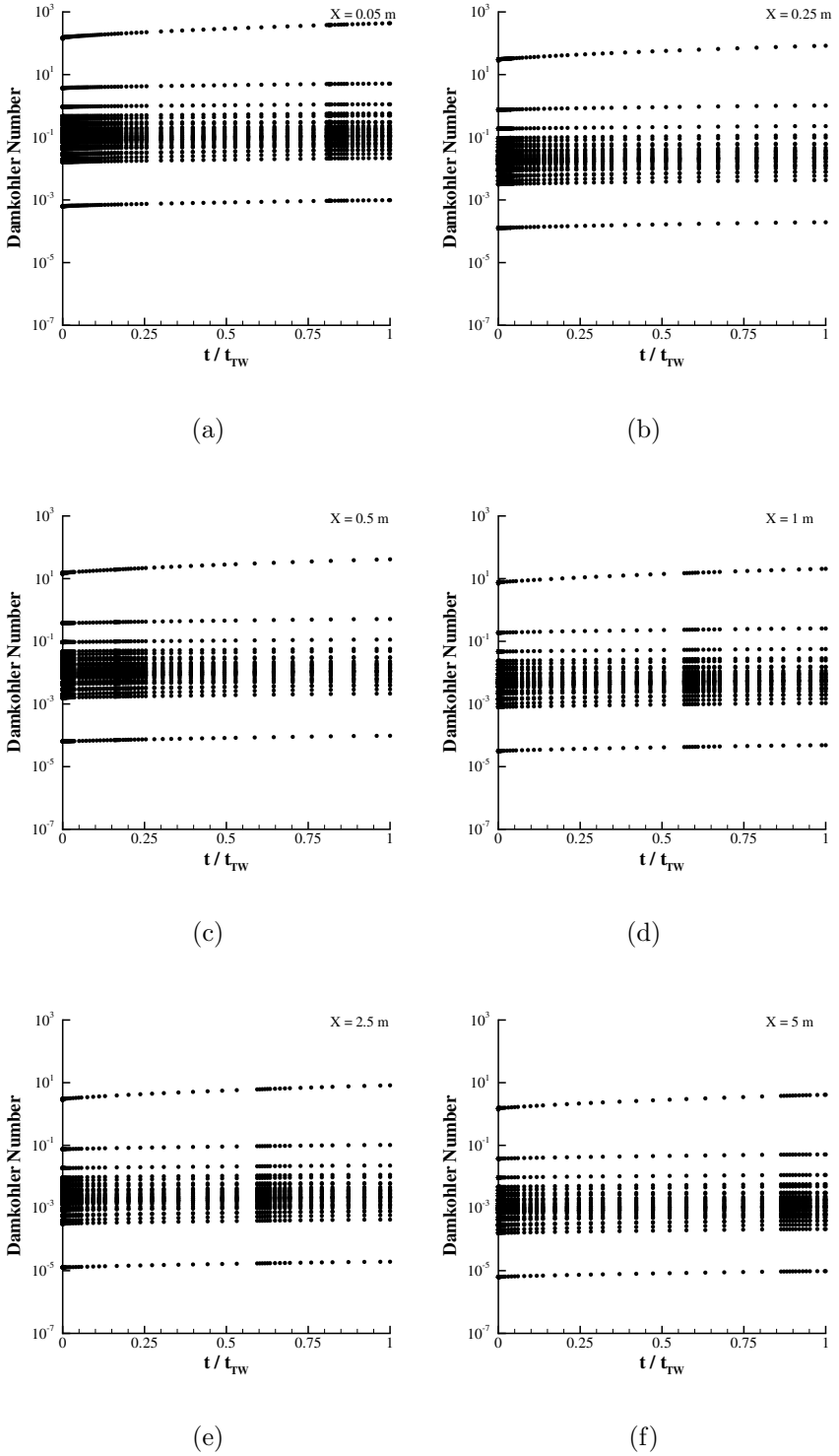

Figure A.2: Damkohler numbers for particles with varying initial position. Initial mixture is C_2H_4-O_2 at 20 kPa. x-axis is time normalized by the total time each particle takes to travel through the TW.

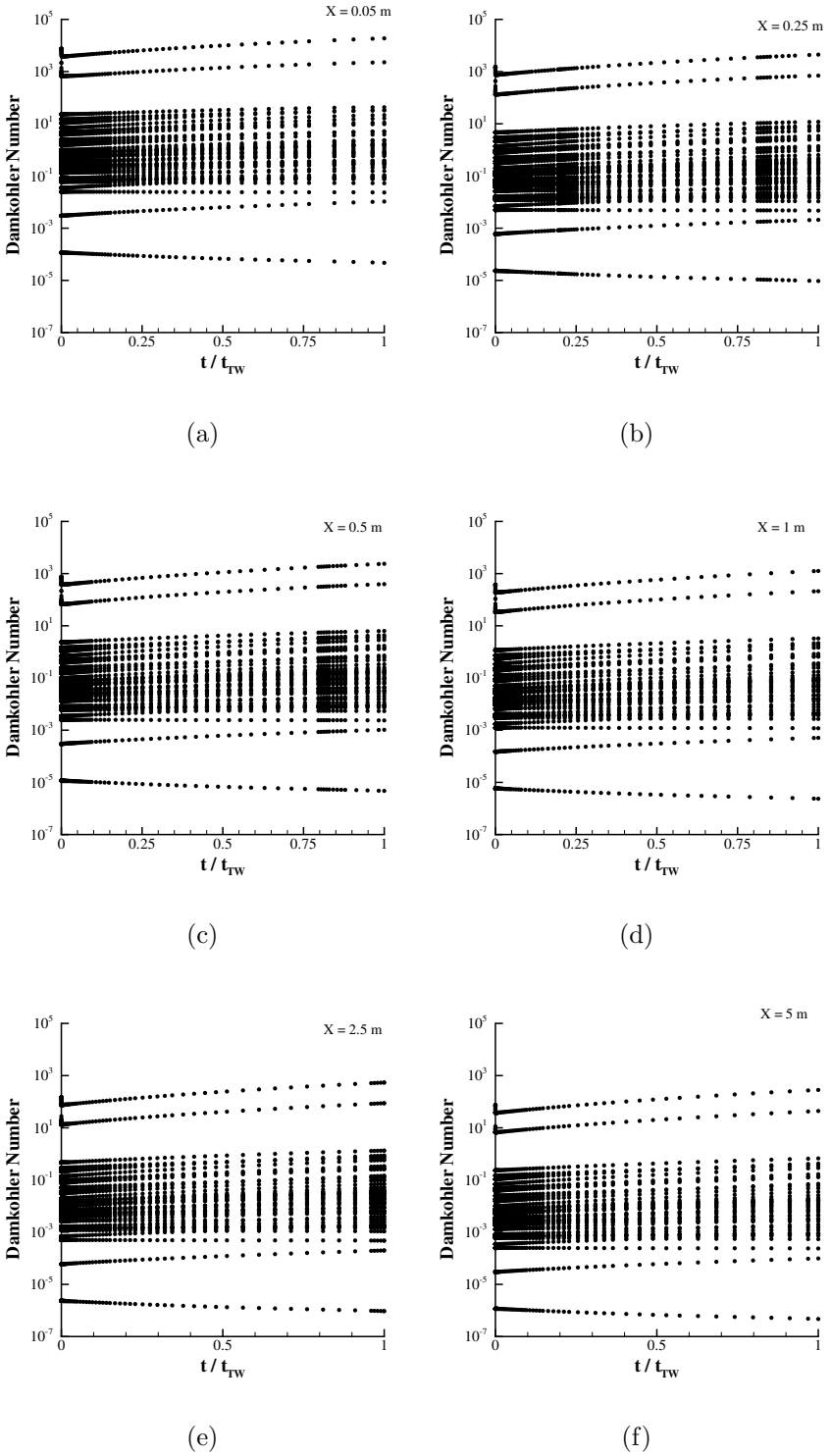

Figure A.3: Damkohler numbers for particles with varying initial position. Initial mixture is C_2H_4-AIR at 100 kPa. x-axis is time normalized by the total time each particle takes to travel through the TW.

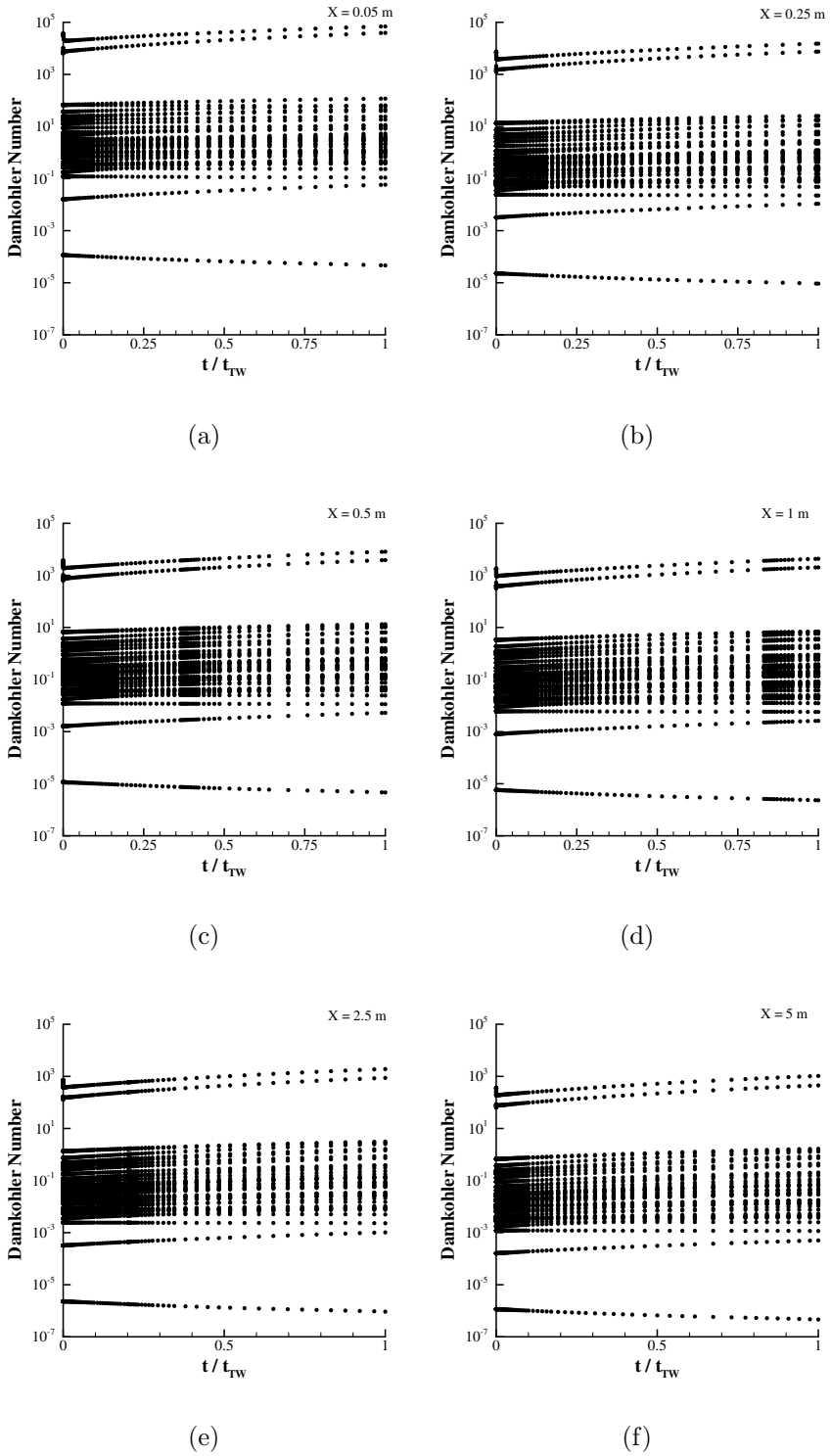

Figure A.4: Damkohler numbers for particles with varying initial position. Initial mixture is C_2H_4-AIR at 20 kPa. x-axis is time normalized by the total time each particle takes to travel through the TW.

Appendix B

List of experiments

Shot No.	P_1 (kPa)	P_0 (kPa)	I_V (kg m^2/s)	I_{SP} (s)	DDT (μs)	Diap.	Exit Condition
2	60	100	1115	151	–	1	–
3	60	100	1115	151	773	1	–
4	60	100	1115	151	817	1	–
5	40	100	671	137	1148	1	–
6	20	100	–	–	None	1	–
7	30	100	443	120	1532	1	–
8	80	100	1549	158	758	1	–
9	100	100	2078	169	520	1	–
10	30	100	443	120	1647	1	–
11	100	100	2078	169	552	1	–
12	80	100	1584	161	704	1	–
28	100	54.1	2216	180	510	1	–
29	80	54.1	1710	174	725	1	–
30	60	54.1	1218	165	805	1	–
31	40	54.1	750	153	1195	1	–
32	30	54.1	523	142	1626	1	–
33	100	16.5	2251	183	546	1	–
34	80	15.5	1790	182	742	1	–
35	100	54.1	2228	181	541	1	–
37	100	16.5	2245	183	669	1	–
38	60	16.5	1286	175	781	1	–
40	40	16.5	853	174	1137	1	–
41	30	16.5	637	173	1887	1	–
42	60	16.5	1321	179	811	1	–
43	60	16.5	1275	173	810	1	–
44	80	16.5	1767	180	710	1	–
45	40	16.5	853	174	1203	1	–
46	30	16.5	637	173	1491	1	–
49	40	54.1	750	153	1156	1	–
53	41	16.5	830	165	–	1	–
54	100	16.5	2239	182	–	1	–
55	30	16.5	648	176	1824	1	–
56	60	5.2	1355	184	779	1	–
57	40	5.2	910	185	1187	1	–
60	60	16.5	1355	184	802	2	–
61	60	16.5	1349	183	814	2	–
62	100	16.5	2280	186	538	2	–

Table B.1: Shot list for experiments with low environment pressure. Initial mixture is CH_4-$3O_2$. Diaphragm thicknesses are specified as "1" for 25 μm, "2" for 51 μm, and "3" for 105 μm thicknesses.

Shot No.	P_1 (kPa)	P_0 (kPa)	I_V (kg m^2/s)	I_{SP} (s)	DDT (μs)	Diap.	Exit Condition
63	80	16.5	1813	185	753	2	–
65	54.5	5.2	1275	191	806	2	–
66	80	16.5	1813	185	723	2	–
68	80	54.1	1716	175	712	2	–
69	80	1.4	1957	199	743	3	–
70	60	16.5	1378	187	797	3	–
71	60	5.2	1429	194	797	3	–
72	90	0.53	2158	195	655	3	–
74	80	5.2	1917	195	718	3	–
75	80	16.5	1859	189	739	3	–
76	80	16.5	1859	189	733	3	–
77	100	16.5	2332	190	682	3	–
78	60	16.5	1366	185	816	3	–
79	80	5.2	1917	195	751	3	–
80	80	100	1704	173	752	3	–
81	80	100	1584	161	744	2	–
82	80	54.1	1773	180	726	3	–
83	100	5.2	2407	196	666	3	–
84	80	1.4	1991	203	712	3	–
85	60	1.4	1446	196	787	3	–
86	80	1.4	1956	199	731	3	–
87	70	1.4	1710	199	722	3	–
88	85	1.4	2124	203	726	3	–
89	60	100	1189	161	804	3	–
90	60	100	1104	150	798	2	–
91	60	54.1	1286	175	801	3	–
92	60	1.4	1423	193	829	3	–
93	100	100	2060	168	680	2	–
94	100	100	2130	173	–	3	–
95	100	54.1	2280	186	685	3	–
96	60	5.2	1406	191	737	3	–
97	100	54.1	2181	178	553	2	–
98	100	100	2112	172	536	3	–
99	60	54.1	1229	167	788	2	–
100	80	100	1869	190	729	3	8°–0.3m
101	77.8	100	1733	181	719	2	8°–0.3m
102	80	100	1767	180	753	2	8°–0.3m

Table B.2: Shot list for experiments with low environment pressure. Initial mixture is CH_4-$3O_2$. Diaphragm thicknesses are specified as "1" for 25 μm, "2" for 51 μm, and "3" for 105 μm thicknesses.

Shot No.	P_1 (kPa)	P_0 (kPa)	I_V (kg m^2/s)	I_{SP} (s)	DDT (μs)	Diap.	Exit Condition
103	80	54.1	1910	194	724	2	8°–0.3m
104	80	54.1	1978	201	742	3	8°–0.3m
105	80	16.5	2210	225	733	2	8°–0.3m
106	80	16.5	2244	228	735	3	8°–0.3m
107	80	1.4	2552	260	749	3	8°–0.3m
108	80	54.1	1964	200	736	3	8°–0.3m
109	80	5.2	2408	245	707	3	8°–0.3m
110	80	5.2	2387	243	751	3	8°–0.3m
111	80	100	1741	177	751	3	Noz-0.75
112	80	54.1	1813	185	689	3	Noz-0.75
113	80	16.5	1931	197	748	3	Noz-0.75
114	80	5.2	1951	199	730	3	Noz-0.75
115	80	1.4	1984	202	714	3	Noz-0.75
116	80	16.5	1925	196	698	3	Noz-0.75
117	80	100	1674	170	746	3	Noz-0.50
118	80	54.1	1767	180	732	3	Noz-0.50
119	80	16.5	1853	189	729	3	Noz-0.50
120	80	5.2	1933	197	734	3	Noz-0.50
121	80	1.4	1993	203	703	3	Noz-0.50
122	80	100	2148	219	736	3	12°–0.3m
123	80	54.1	2148	219	724	3	12°–0.3m
124	80	16.5	2392	244	747	3	12°–0.3m
125	80	5.2	2501	255	735	3	12°–0.3m
126	80	1.4	2691	274	711	3	12°–0.3m
128	80	5.2	2548	259	733	3	12°–0.3m
129	80	100	2148	219	690	3	12°–0.3m
130	80	54.1	2162	220	717	3	12°–0.3m
131	80	100	1804	184	730	3	12°–0.3m-CD-0.54
132	80	54.1	1929	196	737	3	12°–0.3m-CD-0.54
133	80	16.5	2185	222	693	3	12°–0.3m-CD-0.54
134	80	5.2	2470	251	550	3	12°–0.3m-CD-0.54
135	80	1.4	2666	271	680	3	12°–0.3m-CD-0.54
136	80	100	1540	157	725	3	12°–0.3m-CD-0.36
137	80	54.1	1702	173	735	3	12°–0.3m-CD-0.36
138	80	16.5	2054	209	732	3	12°–0.3m-CD-0.36
139	80	5.2	2357	240	741	3	12°–0.3m-CD-0.36
140	80	1.4	2626	267	700	3	12°–0.3m-CD-0.36

Table B.3: Shot list for experiments with low environment pressure. Initial mixture is CH_4-$3O_2$. Diaphragm thicknesses are specified as "1" for 25 μm, "2" for 51 μm, and "3" for 105 μm thicknesses.

Shot No.	P_1 (kPa)	P_0 (kPa)	I_V (kg m^2/s)	I_{SP} (s)	DDT (μs)	Diap.	Exit Condition
141	80	100	1974	201	761	3	12°–0.3m-CD-0.75
142	80	54.1	2029	207	743	3	12°–0.3m-CD-0.75
143	80	5.2	2478	252	735	3	12°–0.3m-CD-0.75
144	80	16.5	2291	233	722	3	12°–0.3m-CD-0.75
145	80	1.4	2693	274	722	3	12°–0.3m-CD-0.75
147	80	100	2969	302	715	3	12°–0.6m
148	80	54.1	2831	288	717	3	12°–0.6m
149	80	16.5	2651	270	705	3	12°–0.6m
150	80	5.2	2635	268	688	3	12°–0.6m
151	80	100	2863	291	722	3	12°–0.6m
152	80	54.1	2806	286	726	3	12°–0.6m
153	80	1.4	2831	288	733	3	12°–0.6m
154	80	5.2	2684	273	712	3	12°–0.6m
155	80	100	2929	298	687	3	12°–0.6m
156	80	100	2742	279	754	3	12°–0.6m-CD-0.75
157	80	54.1	2575	262	746	3	12°–0.6m-CD-0.75
158	80	5.2	2617	266	743	3	12°–0.6m-CD-0.75
159	80	16.5	2542	259	715	3	12°–0.6m-CD-0.75
160	80	1.4	2767	282	719	3	12°–0.6m-CD-0.75
161	80	100	2412	246	693	3	12°–0.6m-CD-0.54
162	80	16.5	2394	244	717	3	12°–0.6m-CD-0.54
163	80	54.1	2314	236	619	3	12°–0.6m-CD-0.54
164	80	5.2	2537	258	755	3	12°–0.6m-CD-0.54
165	80	1.4	2698	275	719	3	12°–0.6m-CD-0.54
166	80	54.1	2270	231	730	3	12°–0.6m-CD-0.54
167	80	100	1895	193	745	3	12°–0.6m-CD-0.36
168	80	54.1	1922	196	612	3	12°–0.6m-CD-0.36
169	80	16.5	2138	218	735	3	12°–0.6m-CD-0.36
170	80	5.2	2319	236	730	3	12°–0.6m-CD-0.36
171	80	1.4	2599	265	732	3	12°–0.6m-CD-0.36
172	80	100	2139	218	730	3	0°–0.6m
173	80	54.1	2063	210	695	3	0°–0.6m
174	80	16.5	2052	209	730	3	0°–0.6m
175	80	5.2	2085	212	709	3	0°–0.6m
176	80	1.4	2226	227	732	3	0°–0.6m

Table B.4: Shot list for experiments with low environment pressure. Initial mixture is CH_4-$3O_2$. Diaphragm thicknesses are specified as "1" for 25 μm, "2" for 51 μm, and "3" for 105 μm thicknesses.

Appendix C

Experimental pressure traces

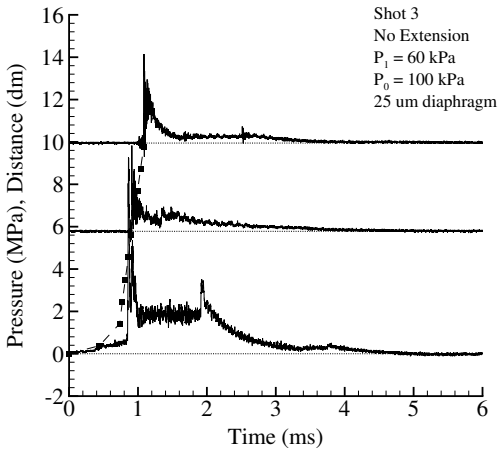

Shot 3

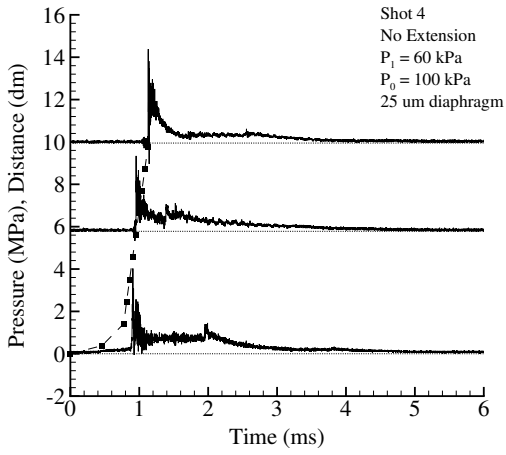

Shot 4

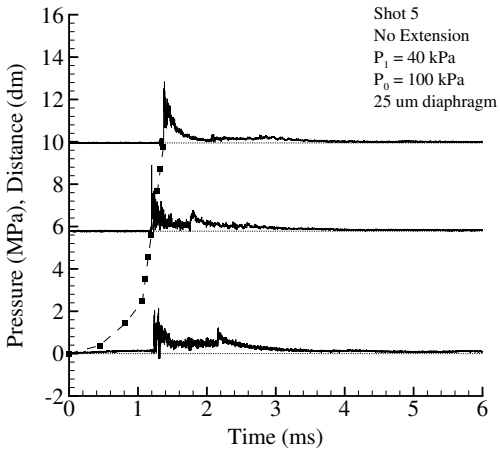

Shot 5

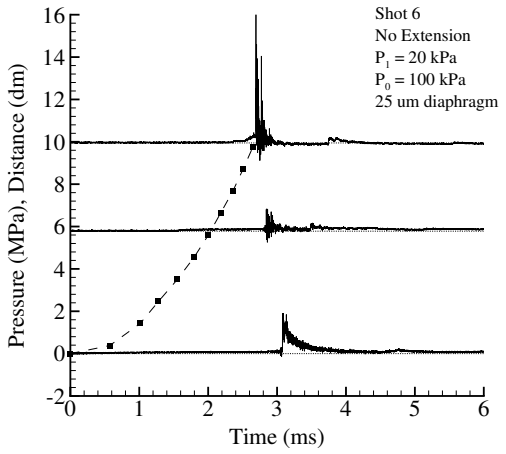

Shot 6

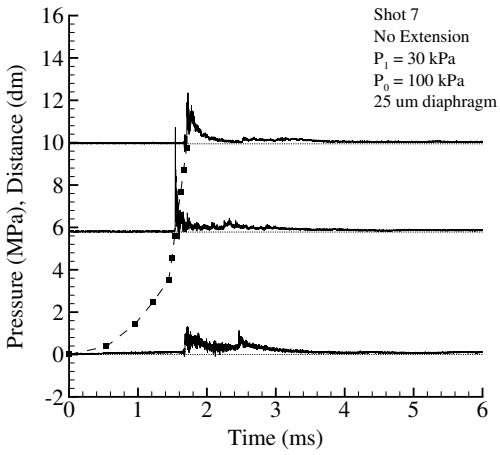

Shot 7

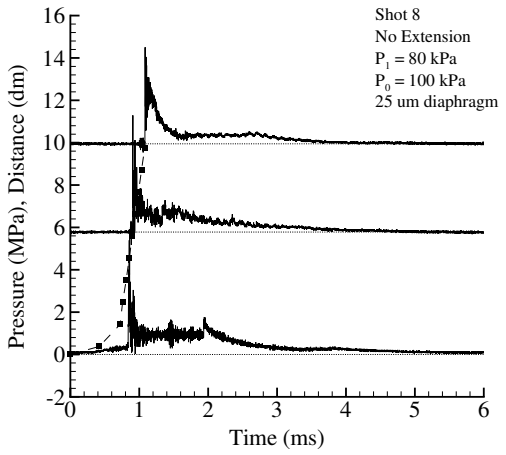

Shot 8

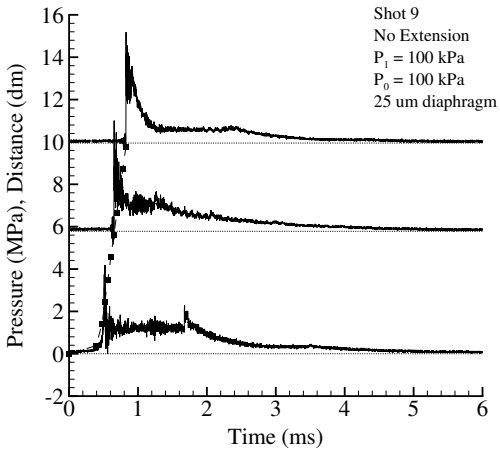

Shot 9

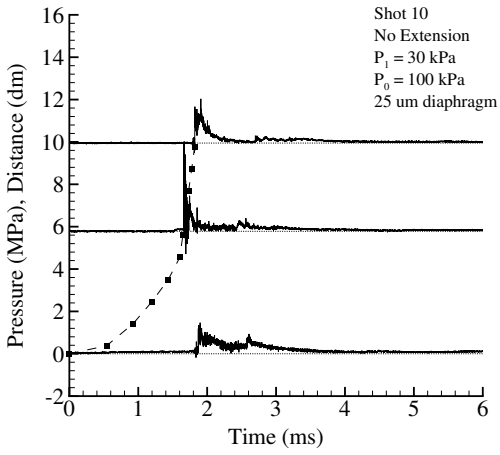

Shot 10

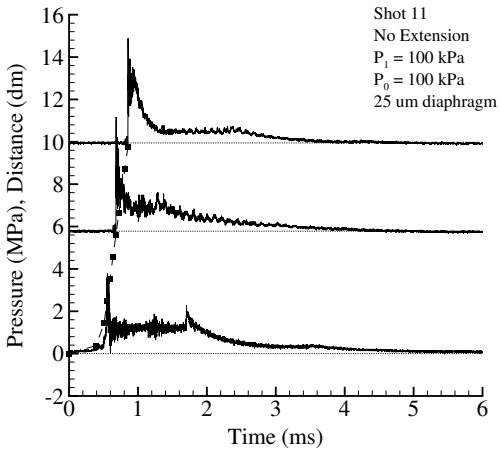

Shot 11

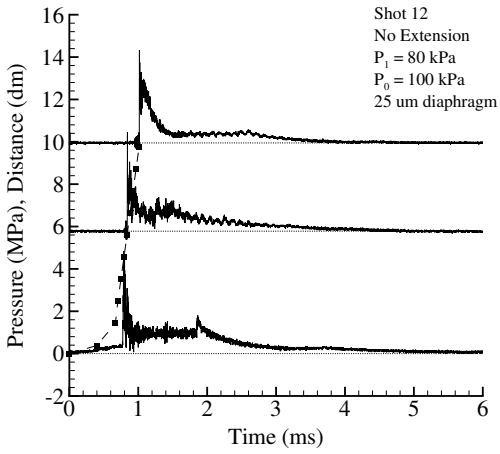

Shot 12

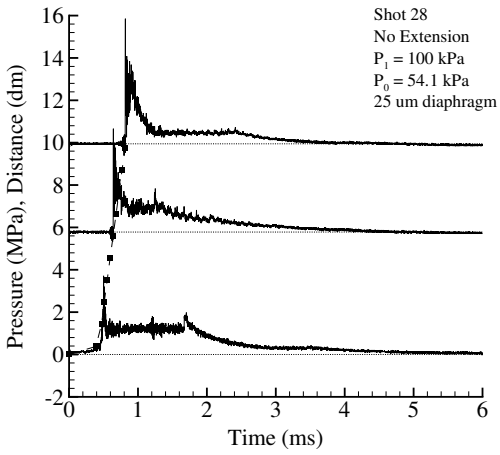

Shot 28

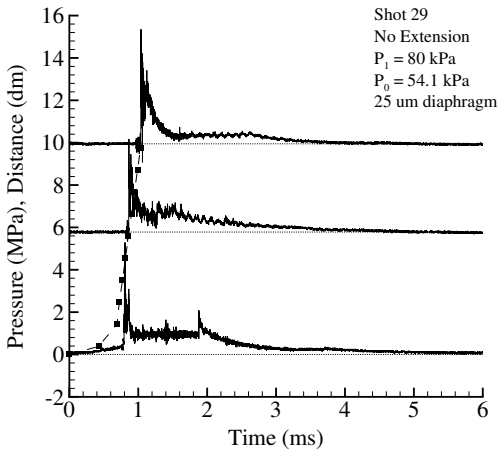

Shot 29

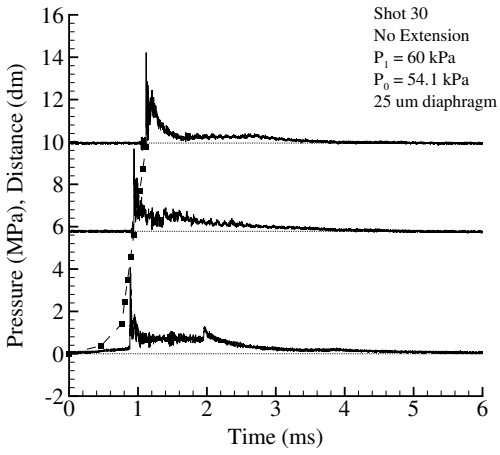

Shot 30

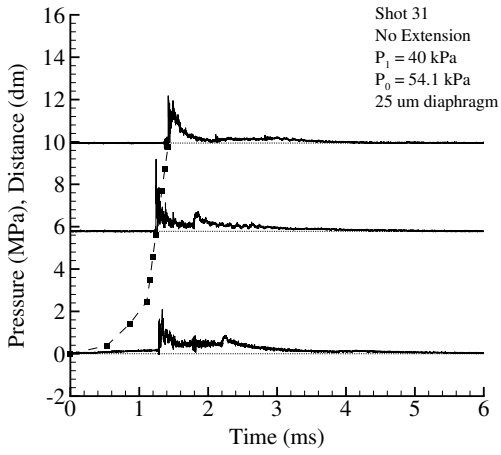

Shot 31

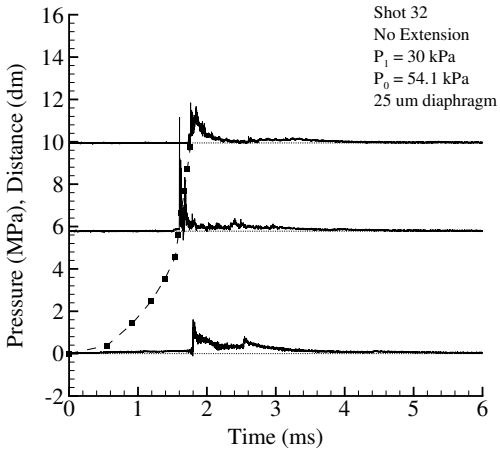

Shot 32

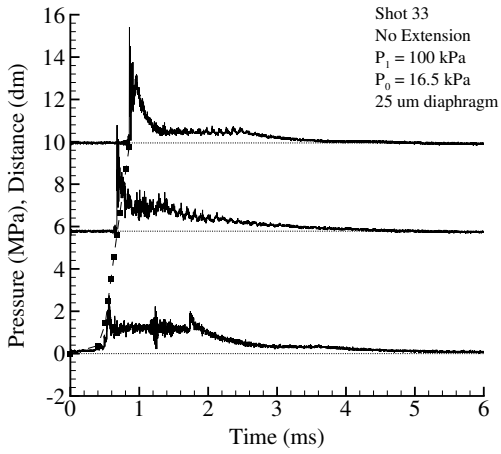

Shot 33

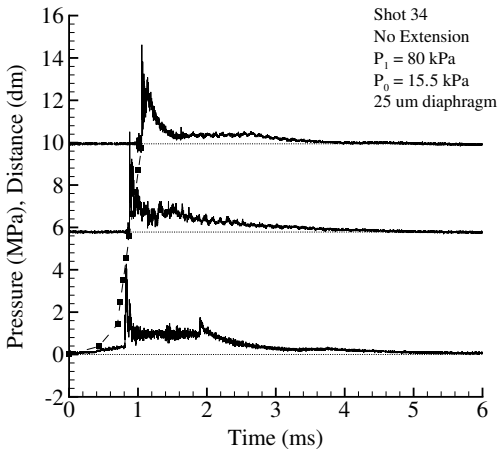

Shot 34

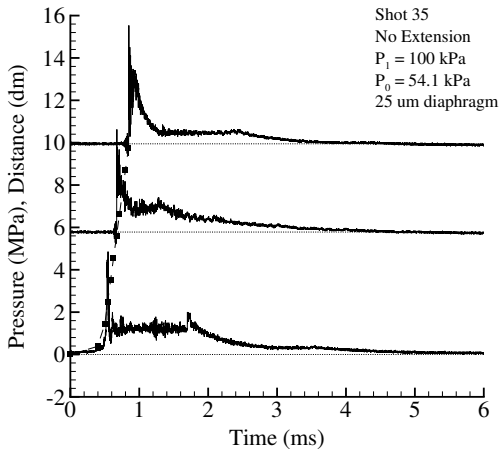

Shot 35

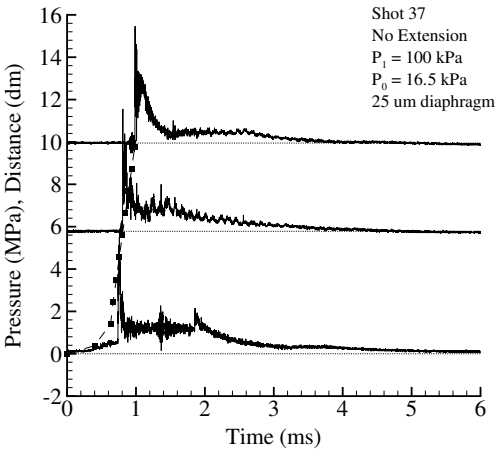

Shot 37

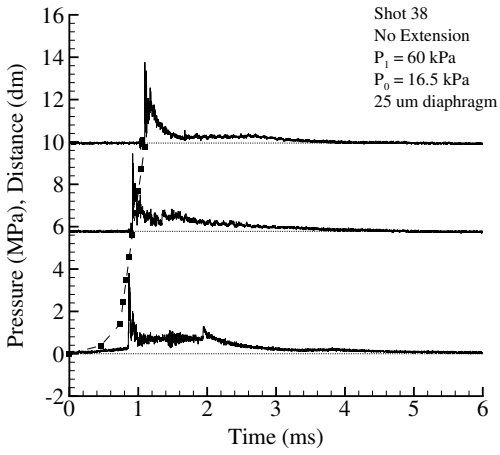

Shot 38

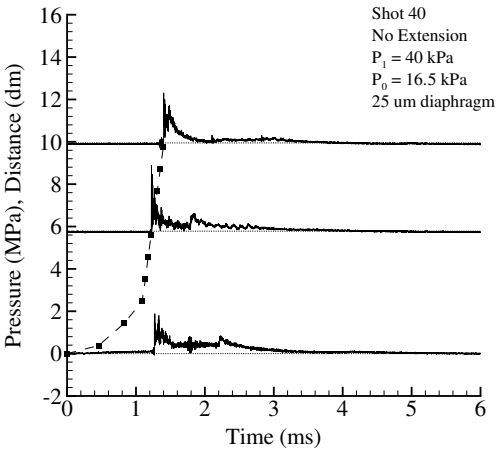

Shot 40

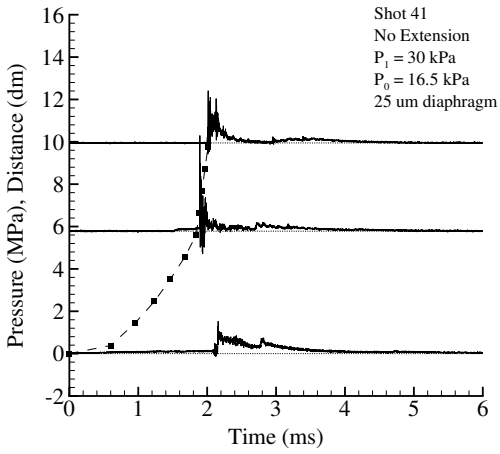

Shot 41

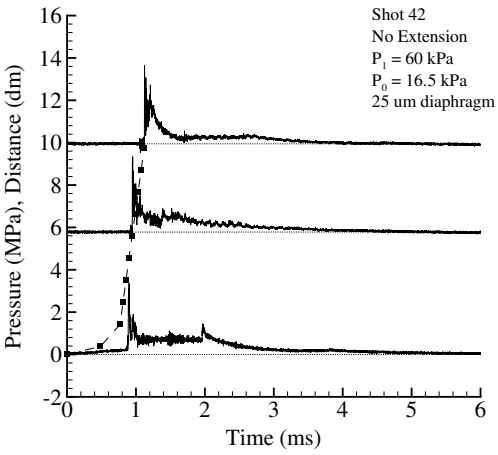

Shot 42

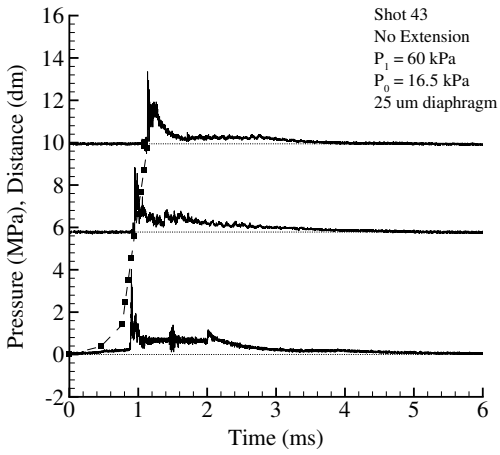

Shot 43

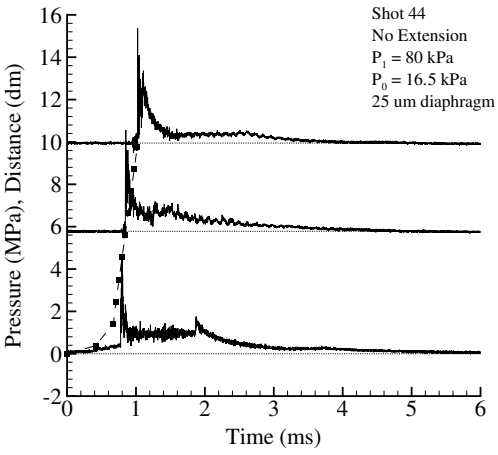

Shot 44

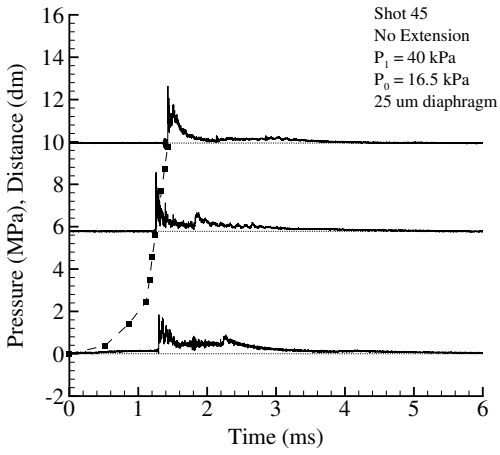

Shot 45

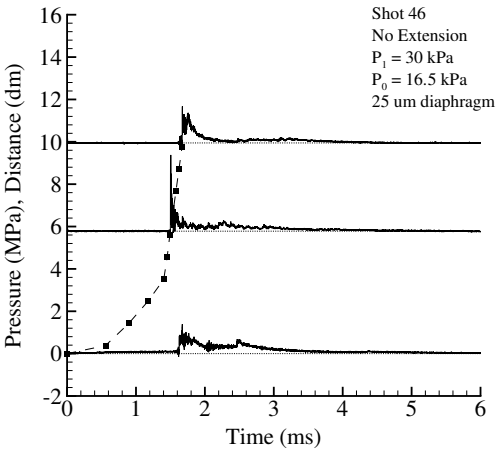

Shot 46

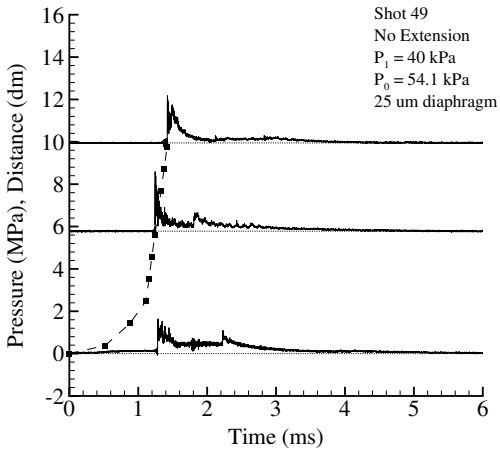

Shot 49

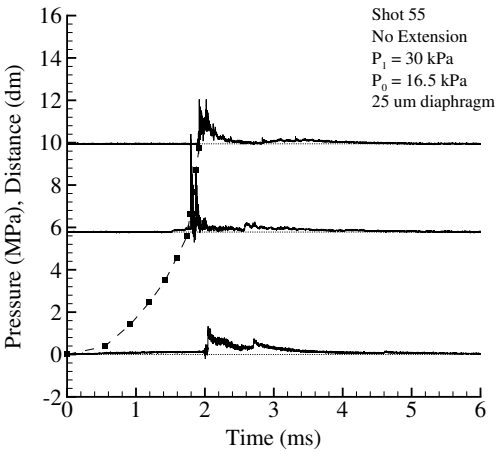

Shot 55

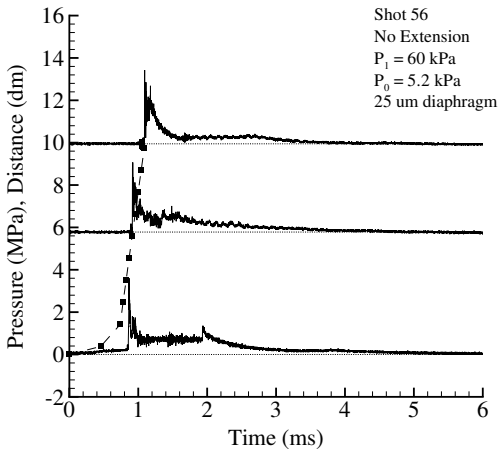

Shot 56

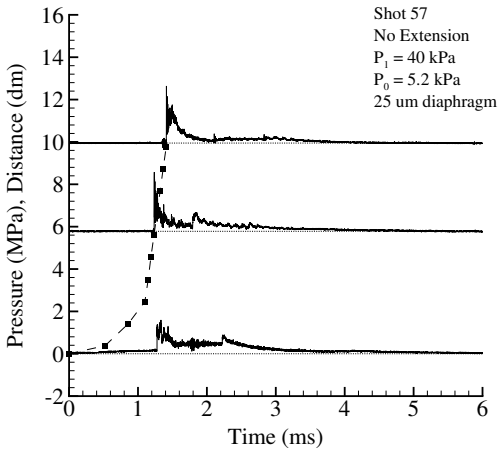

Shot 57

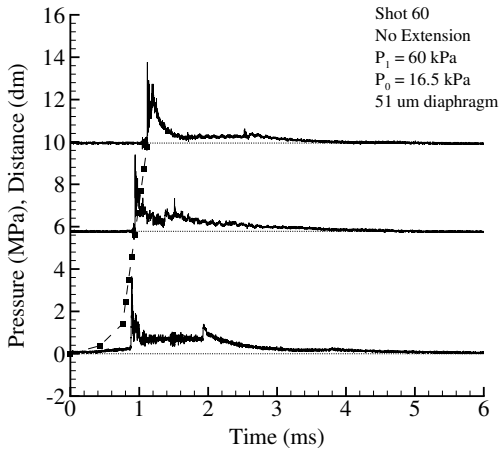

Shot 60

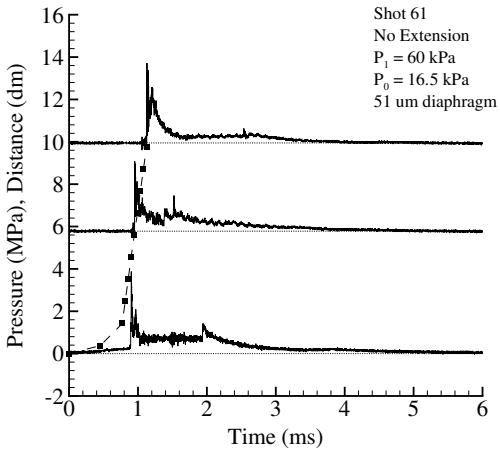

Shot 61

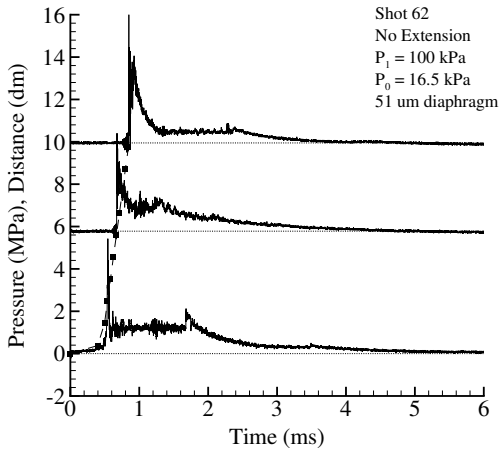

Shot 62

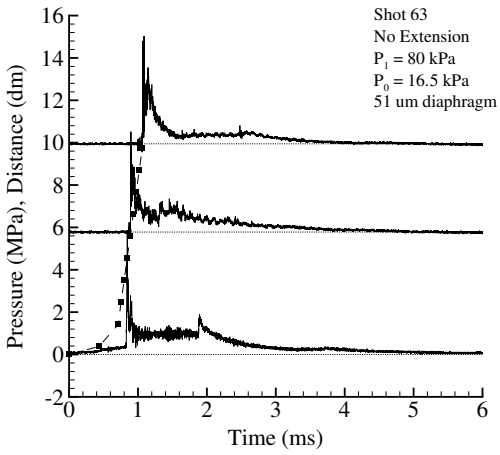

Shot 63

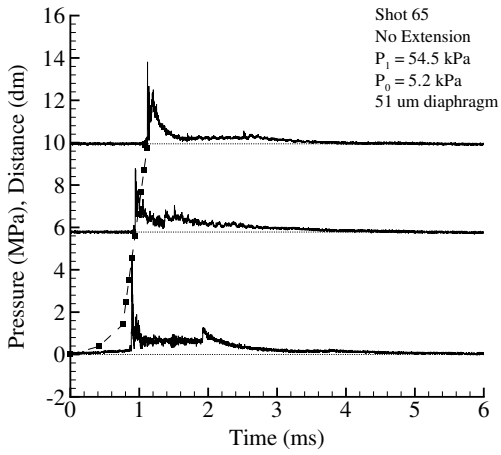

Shot 65

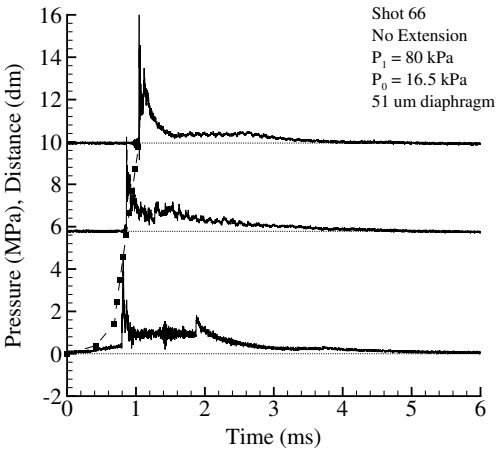

Shot 66

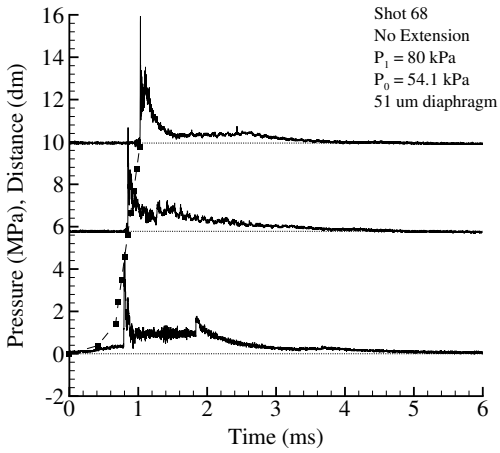

Shot 68

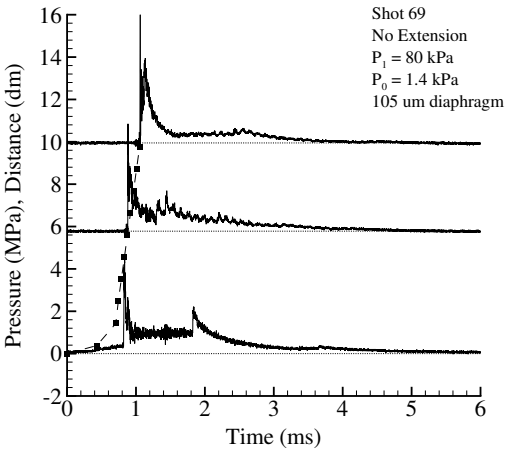

Shot 69

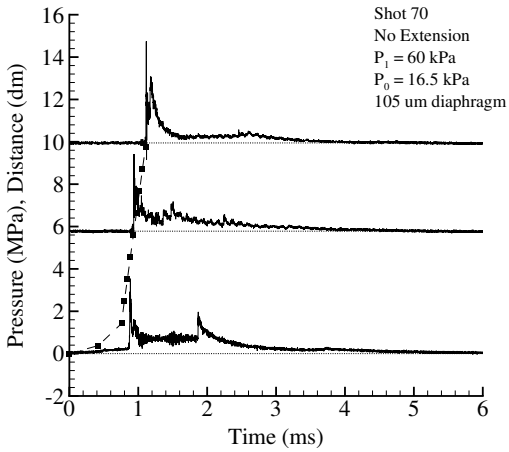

Shot 70

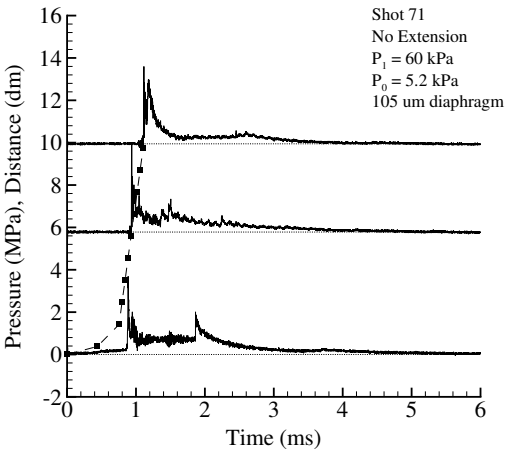

Shot 71

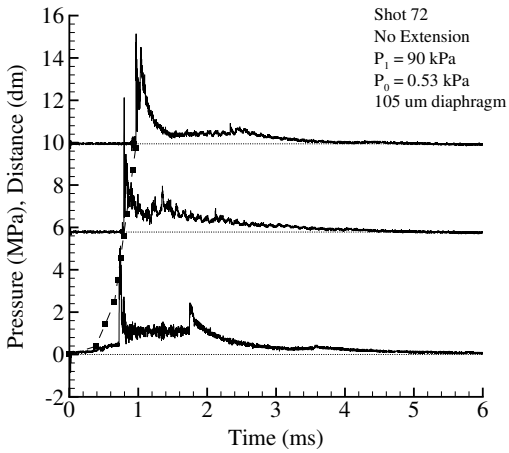

Shot 72

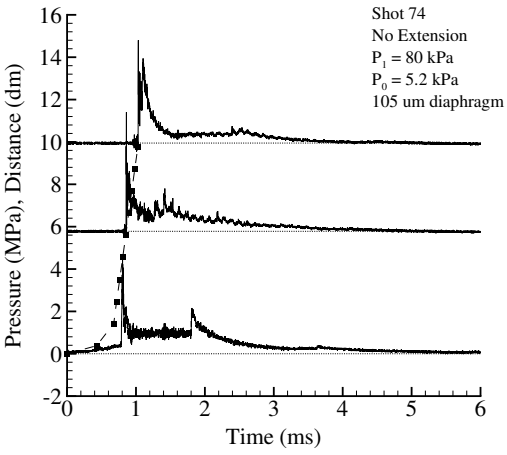

Shot 74

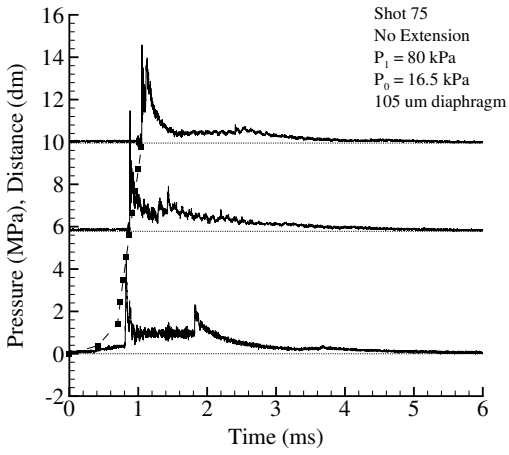

Shot 75

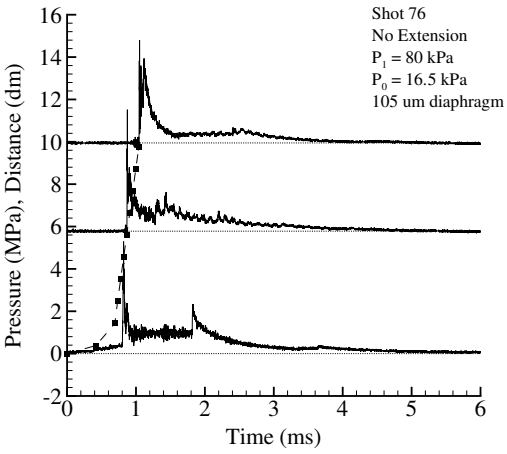

Shot 76

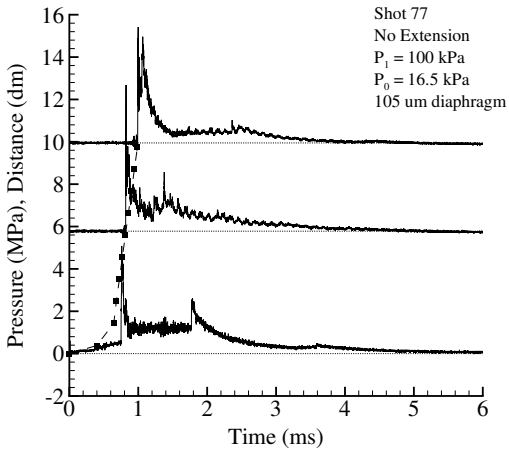

Shot 77

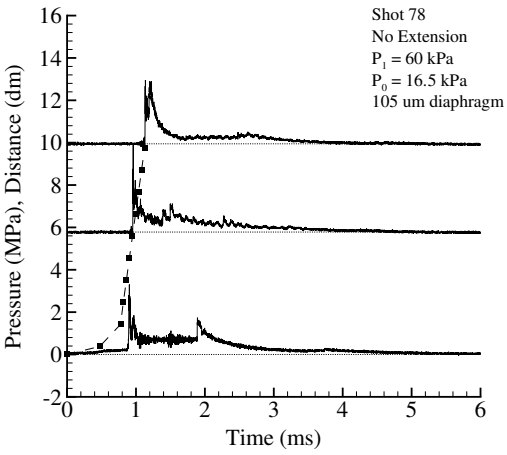

Shot 78

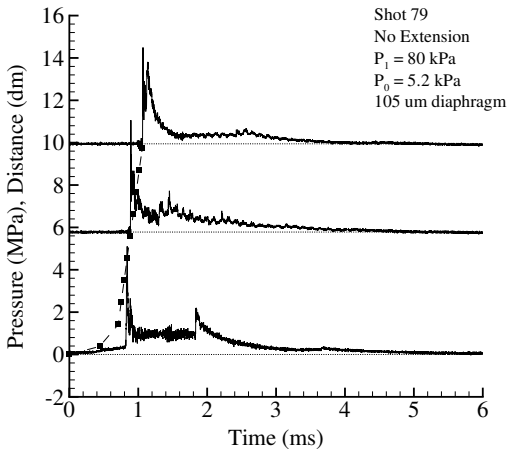

Shot 79

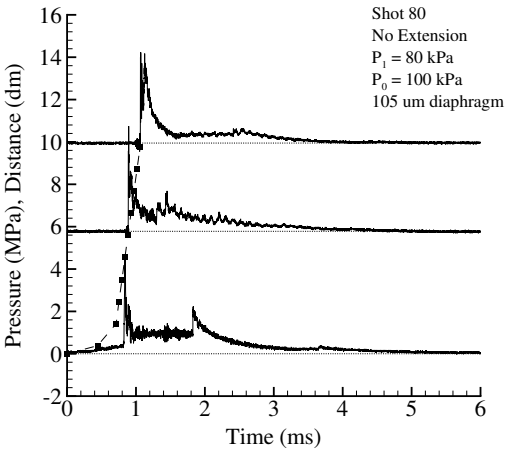

Shot 80

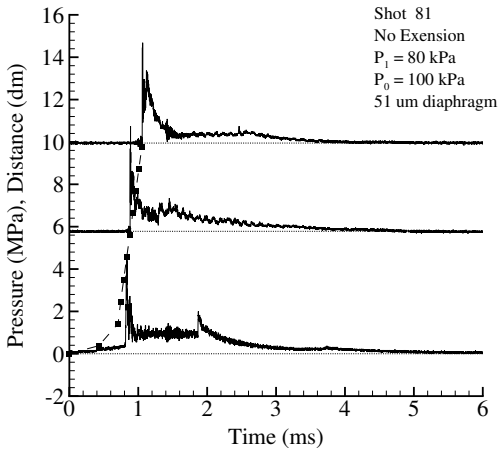

Shot 81

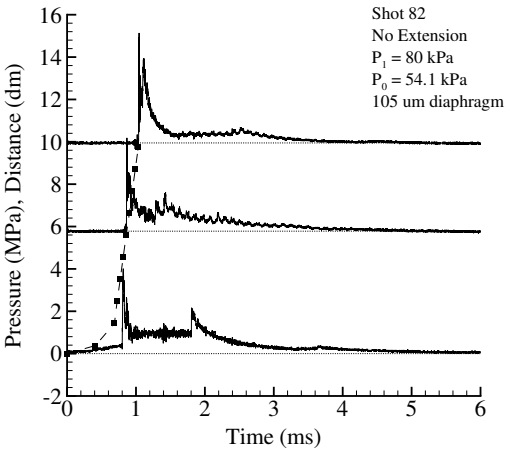

Shot 82

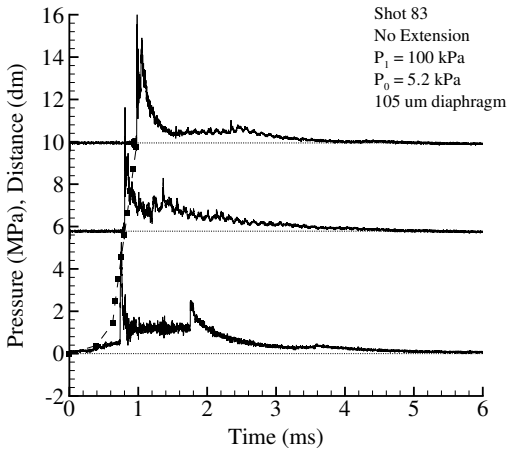

Shot 83

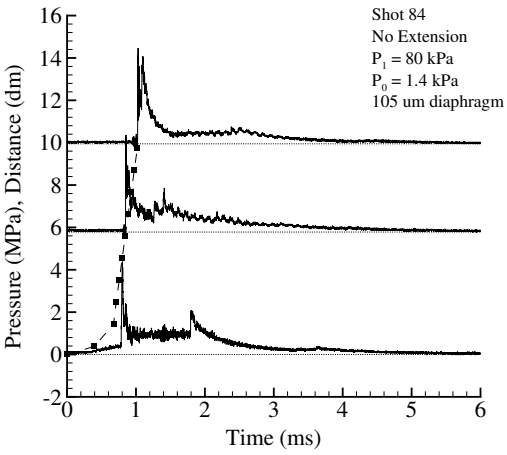

Shot 84

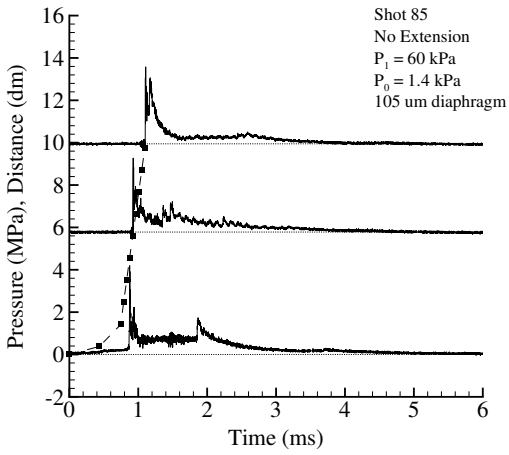

Shot 85

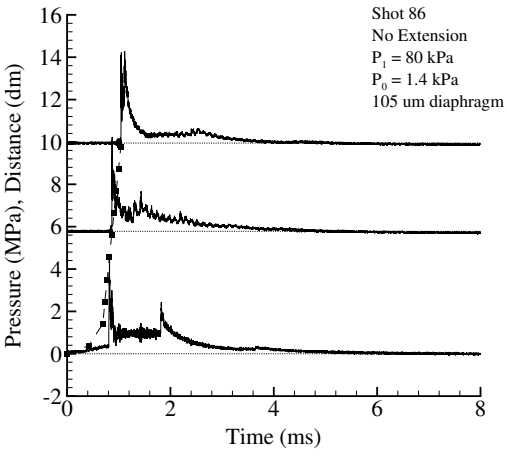

Shot 86

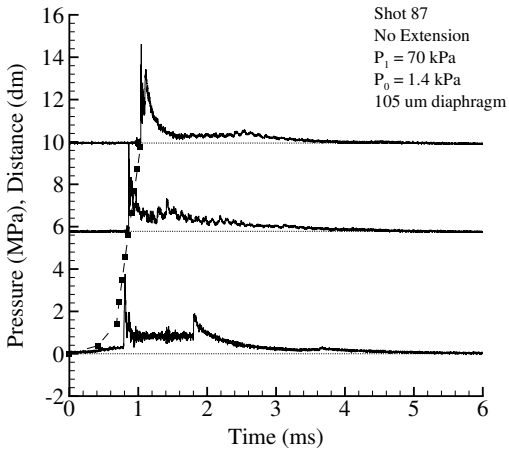

Shot 87

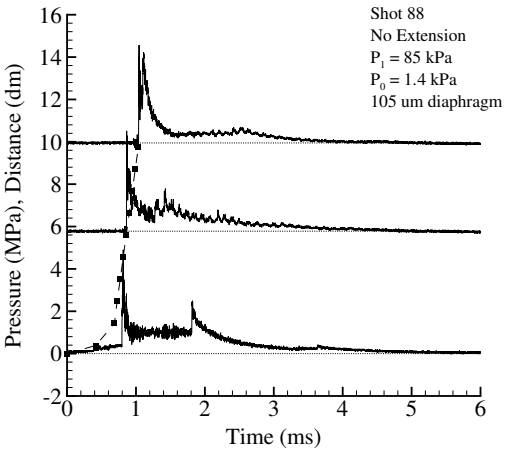

Shot 88

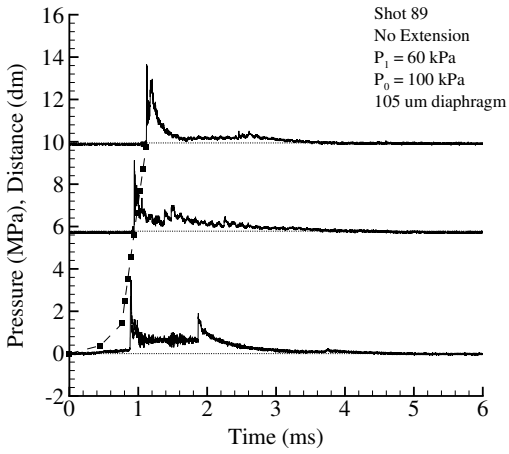

Shot 89

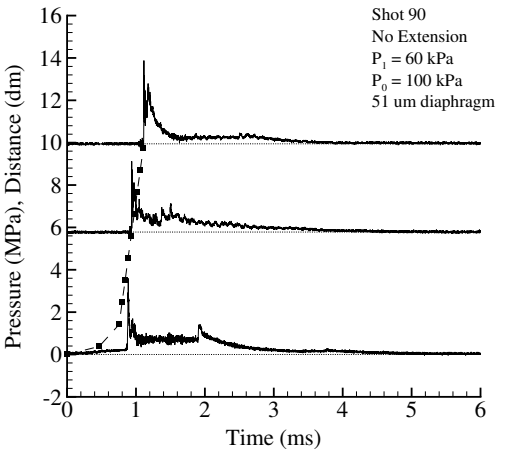

Shot 90

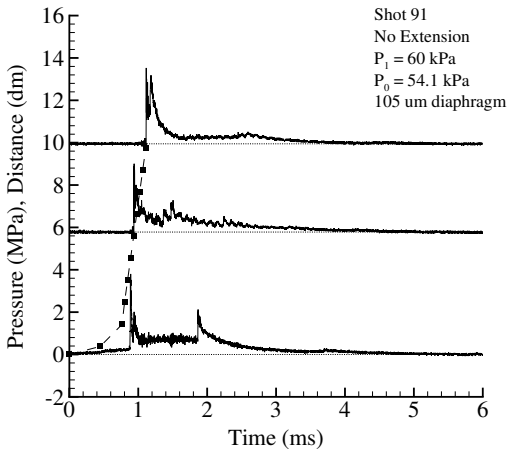

Shot 91

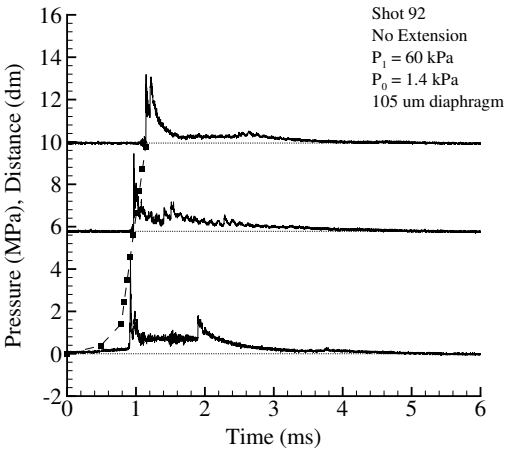

Shot 92

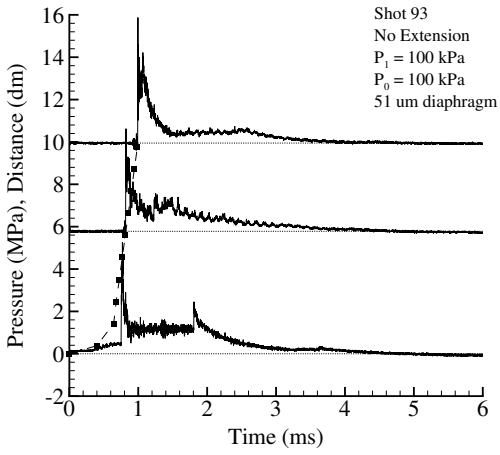

Shot 93

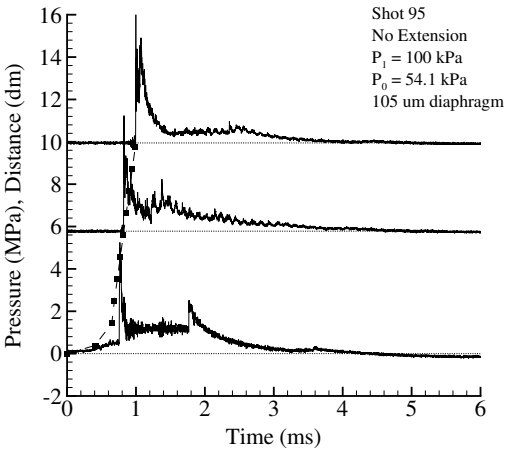

Shot 95

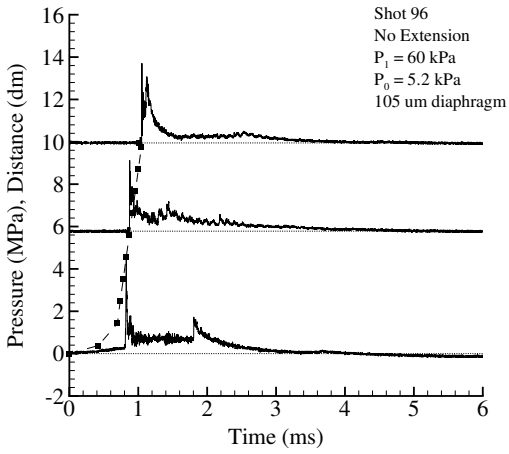

Shot 96

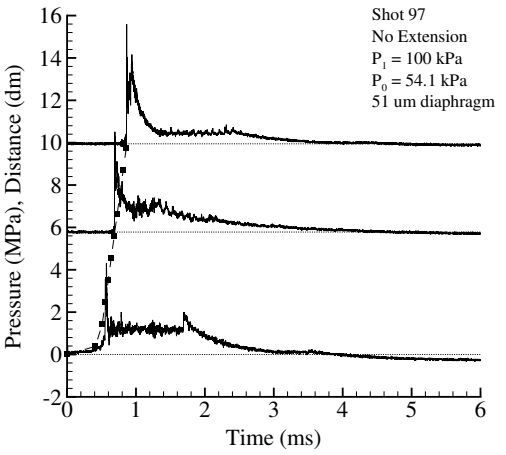

Shot 97

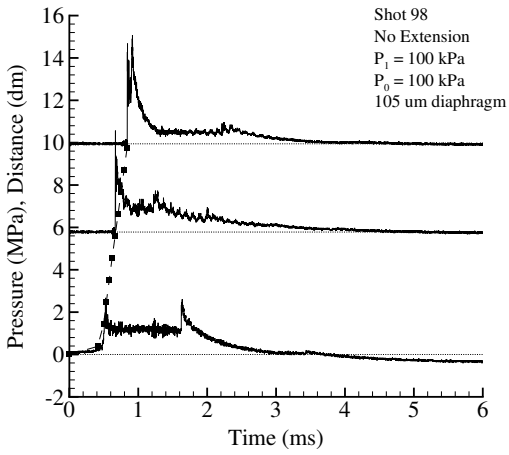

Shot 98

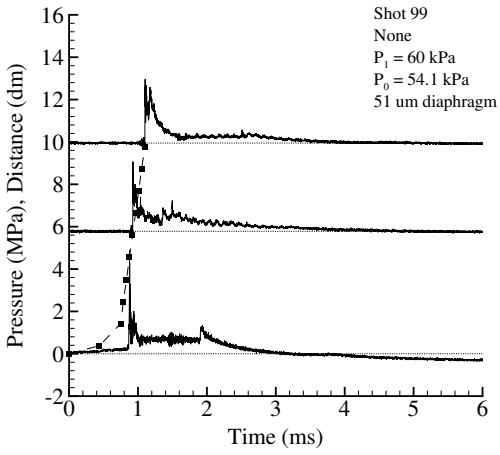

Shot 99

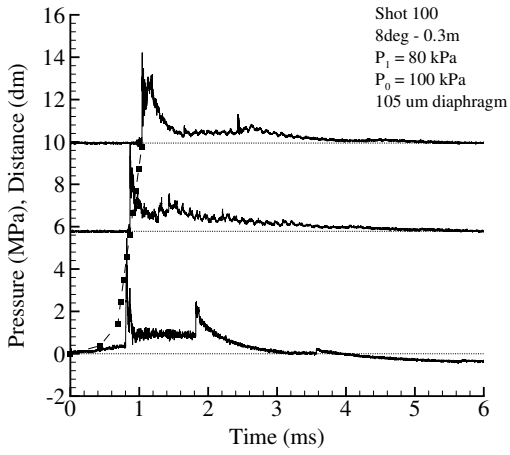

Shot 100

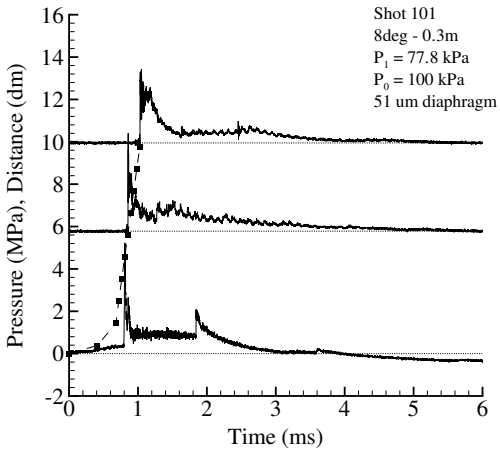

Shot 101

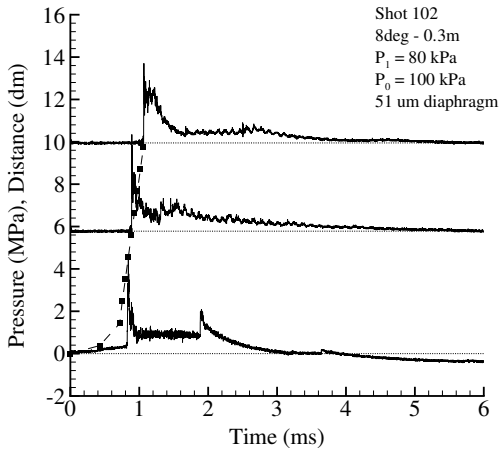

Shot 102

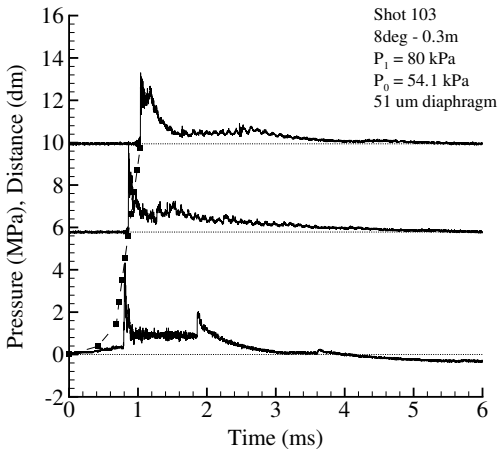

Shot 103

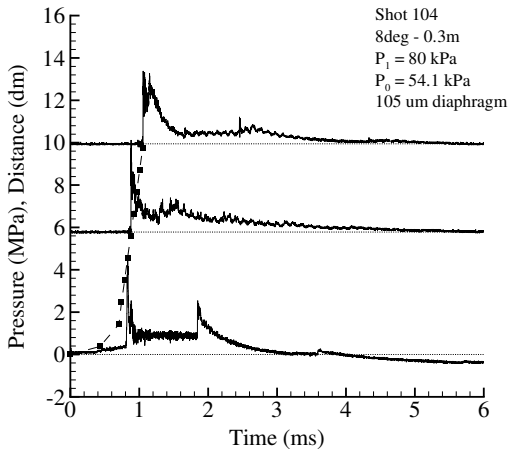

Shot 104

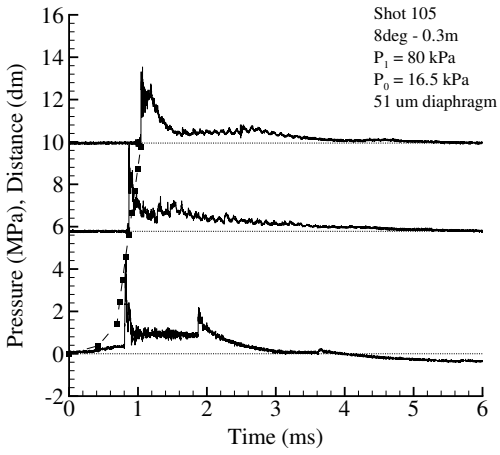

Shot 105

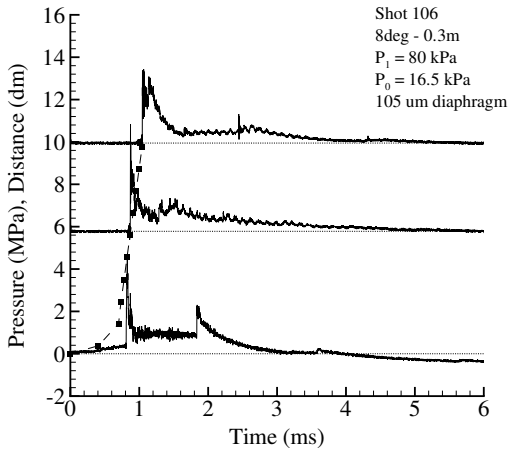

Shot 106

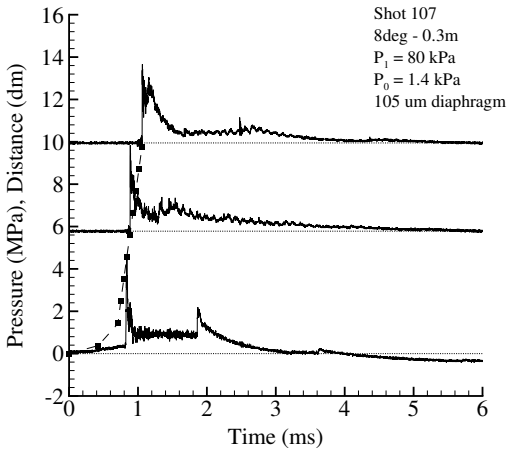

Shot 107

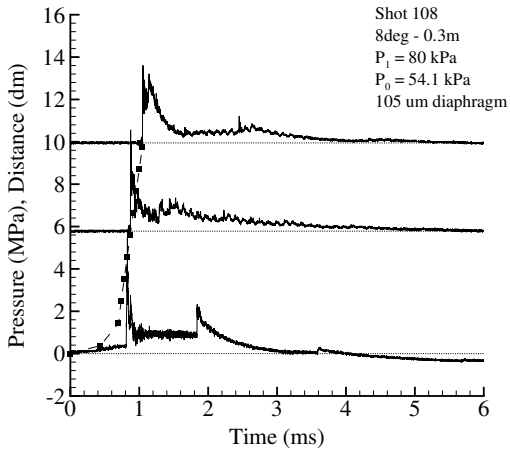

Shot 108

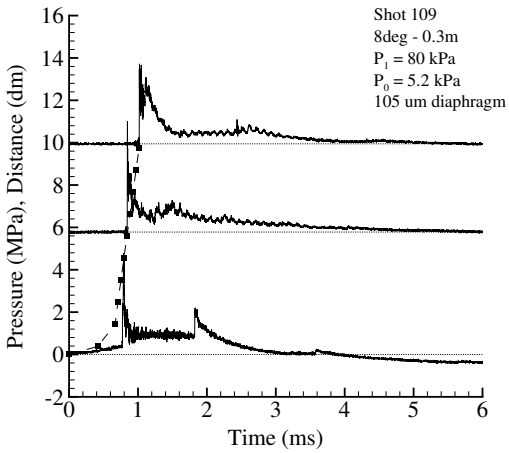

Shot 109

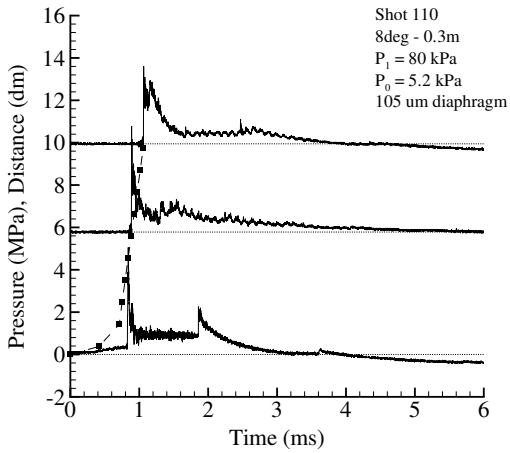

Shot 110

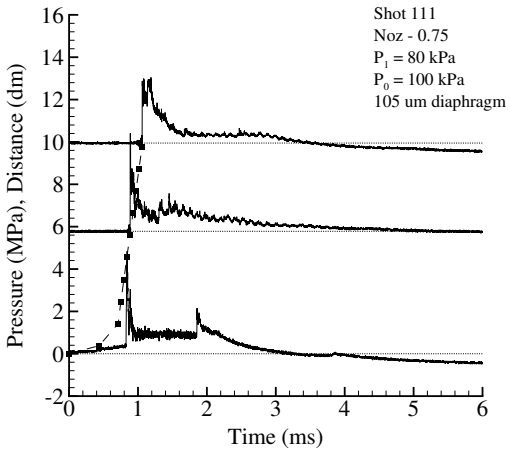

Shot 111

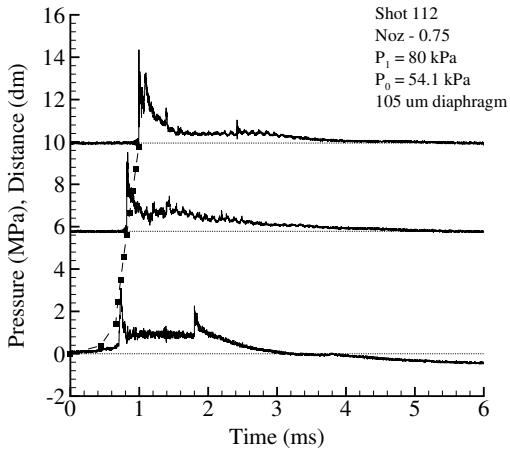

Shot 112

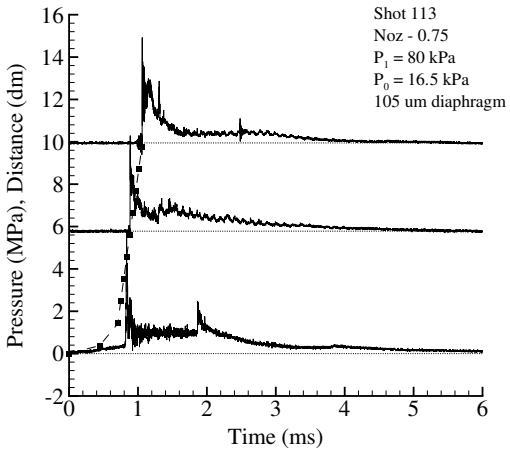

Shot 113

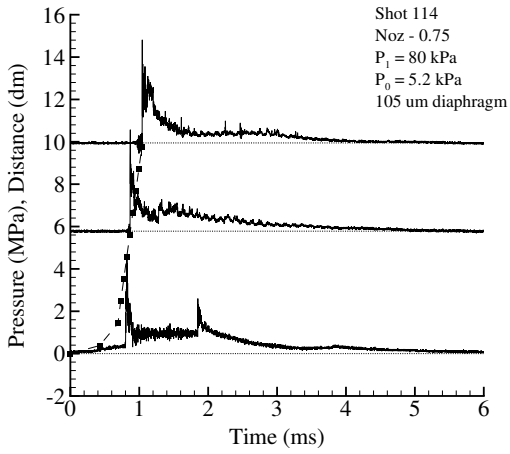

Shot 114

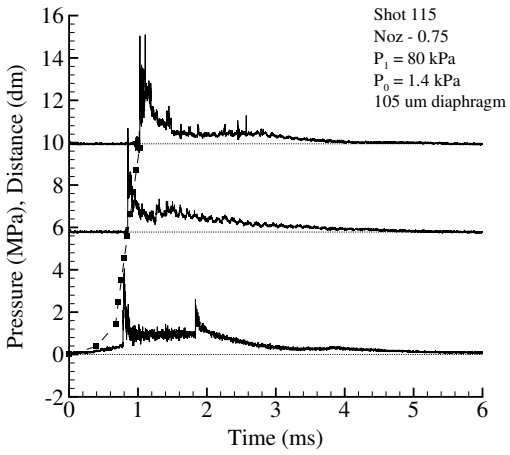

Shot 115

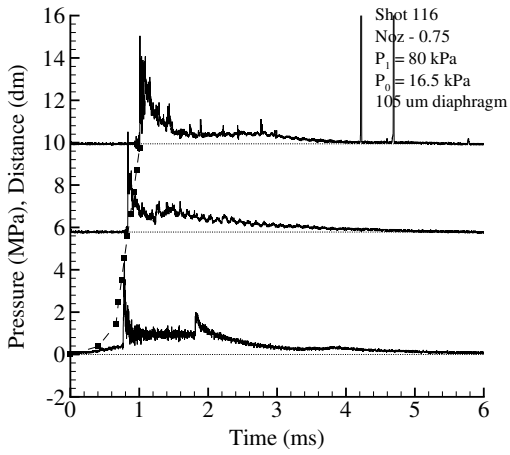

Shot 116

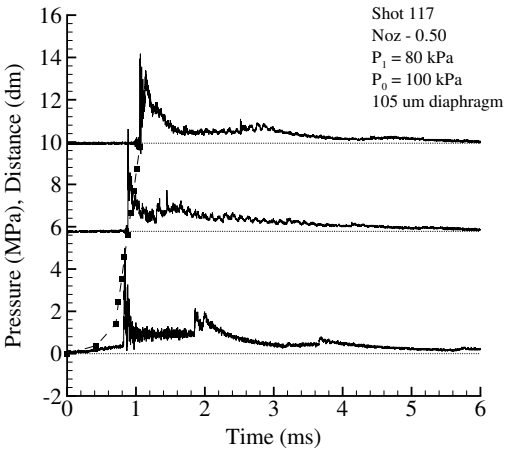

Shot 117

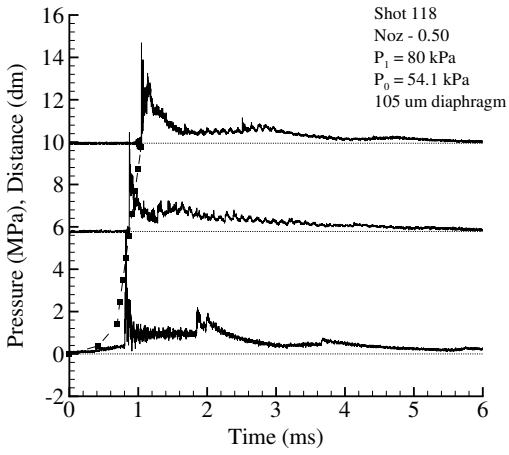

Shot 118

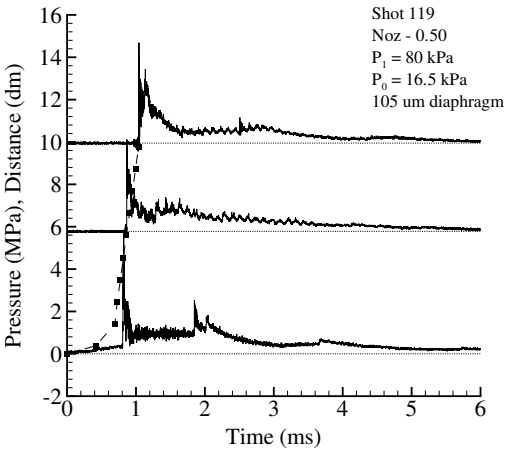

Shot 119

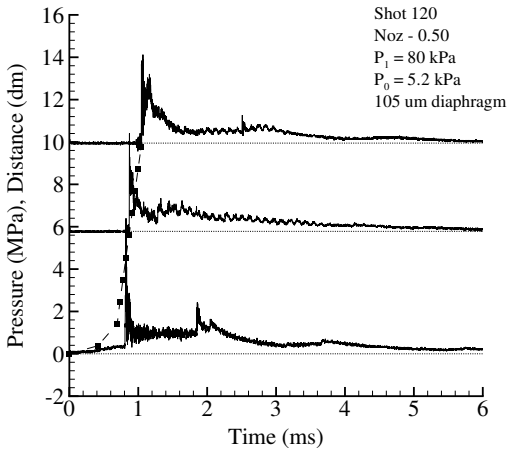

Shot 120

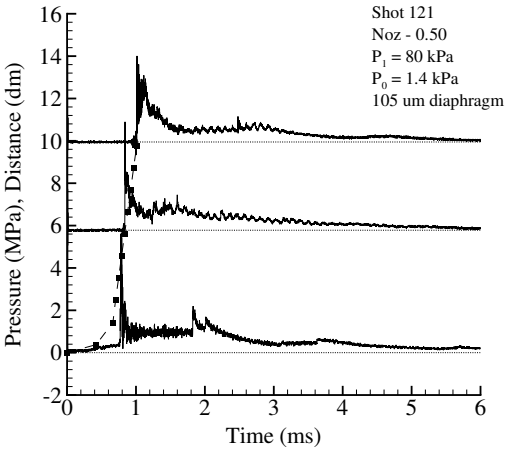

Shot 121

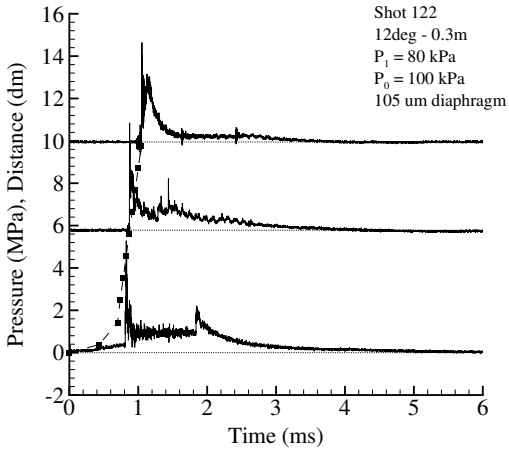

Shot 122

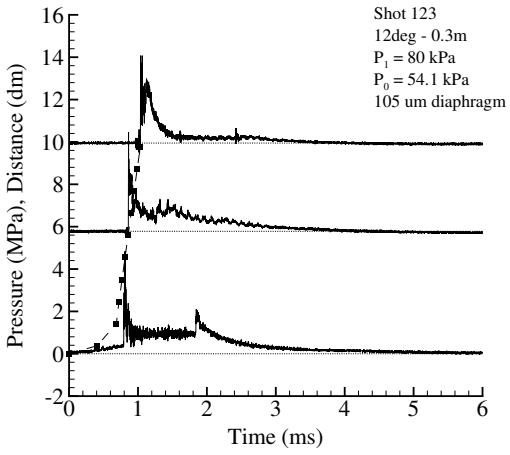

Shot 123

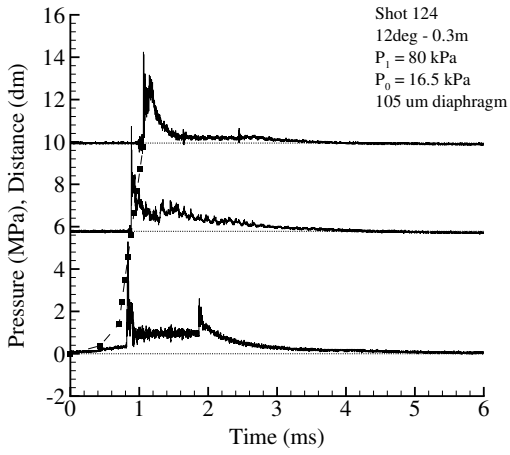

Shot 124

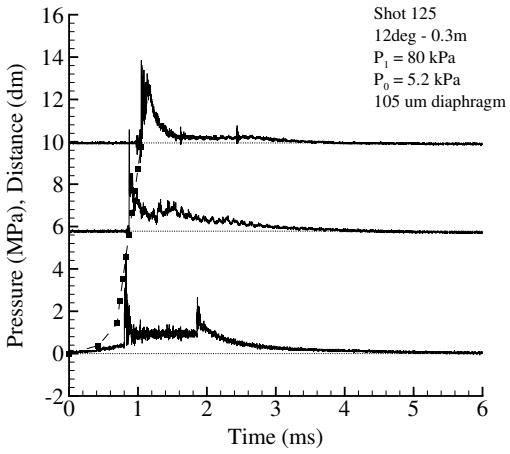

Shot 125

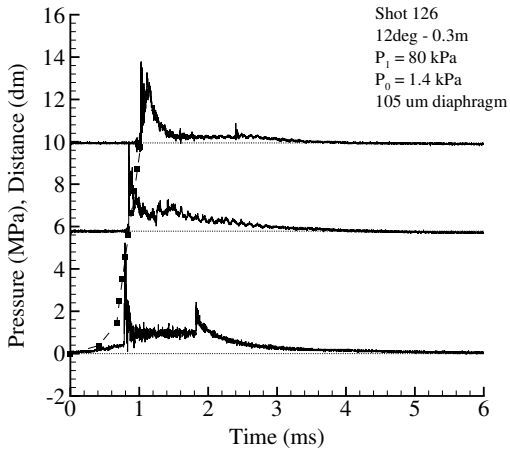

Shot 126

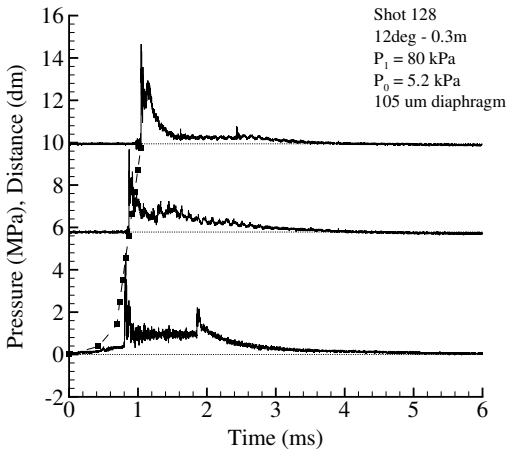

Shot 128

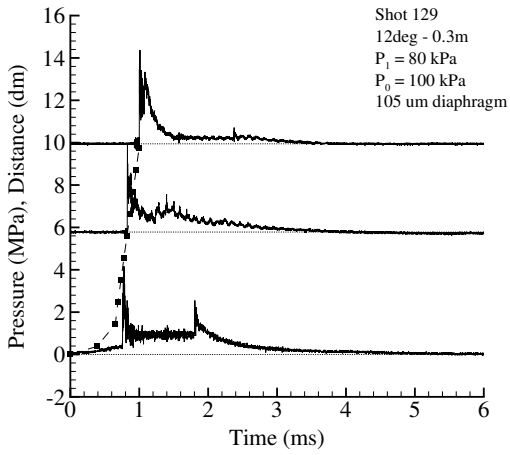

Shot 129

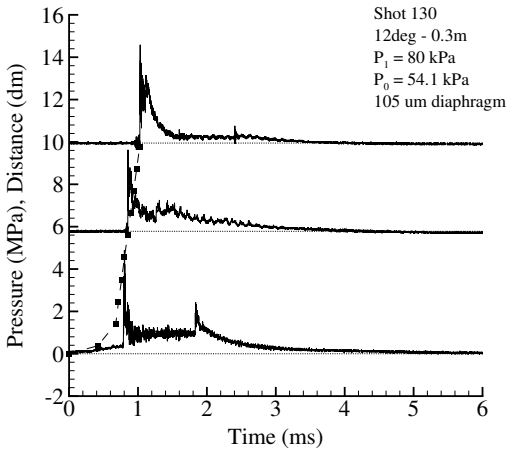

Shot 130

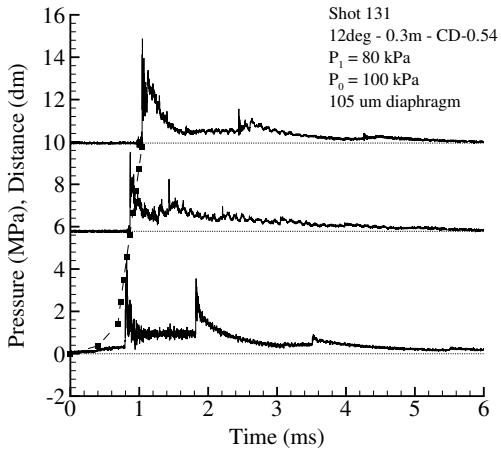

Shot 131

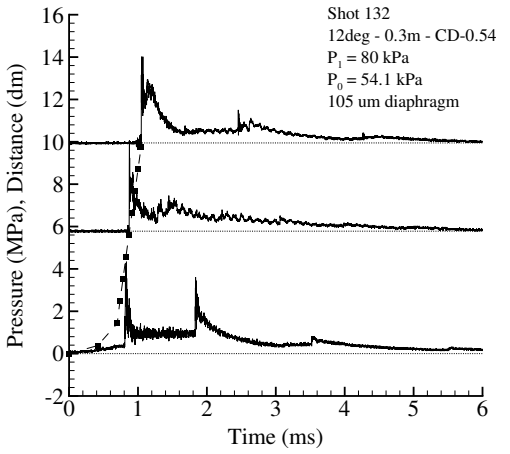

Shot 132

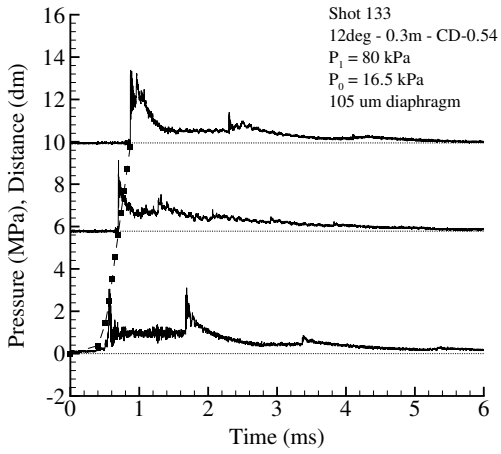

Shot 133

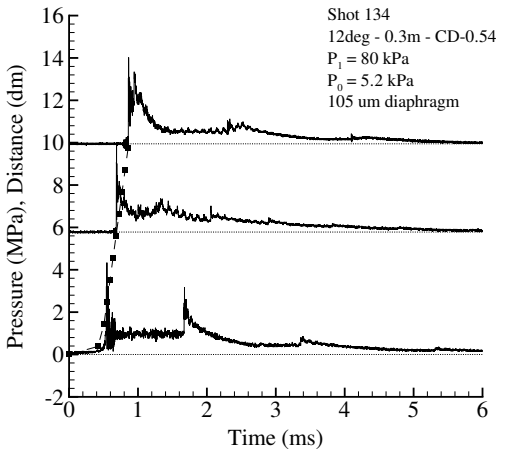

Shot 134

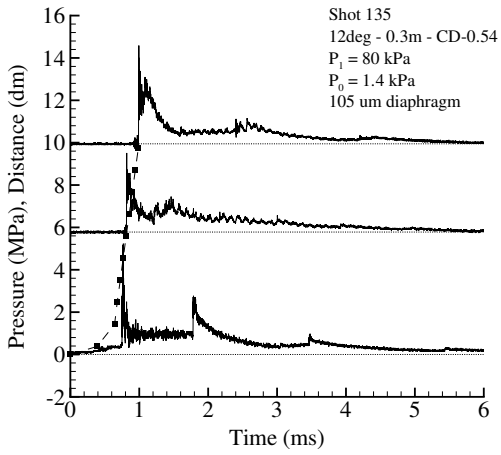

Shot 135

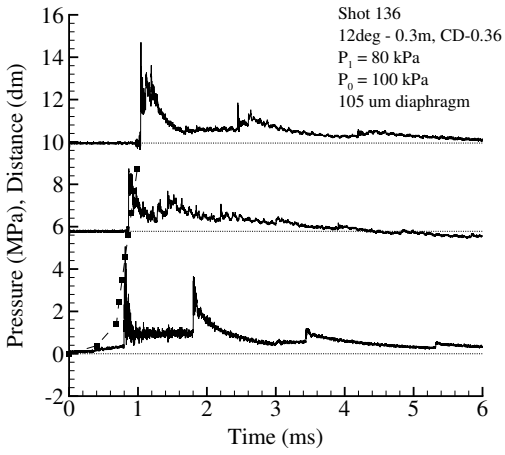

Shot 136

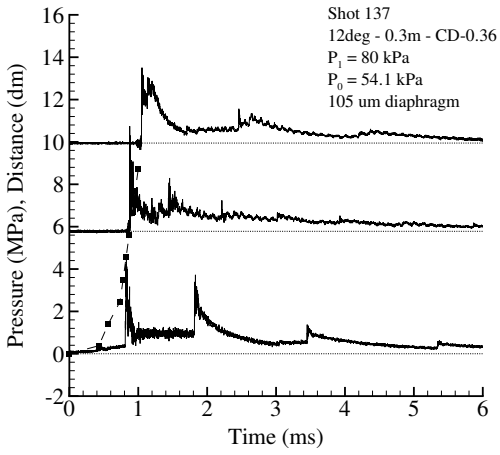

Shot 137

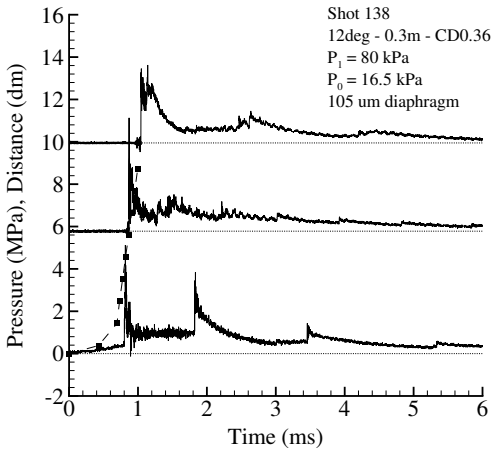

Shot 138

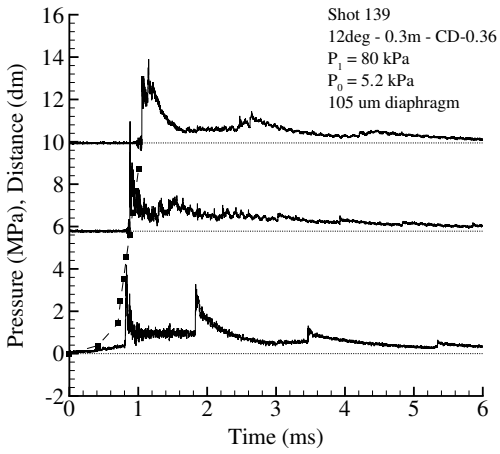

Shot 139

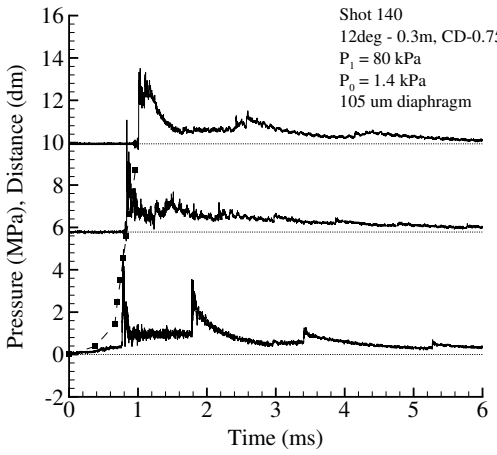

Shot 140

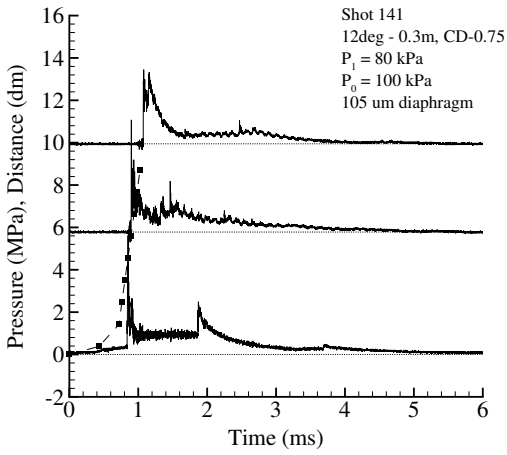

Shot 141

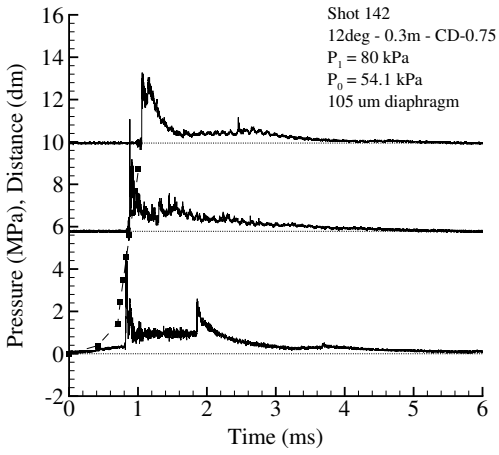

Shot 142

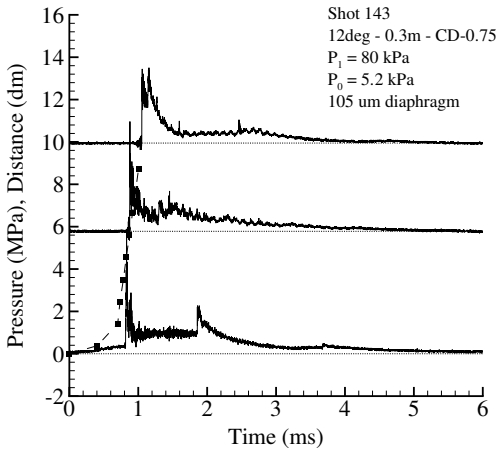

Shot 143

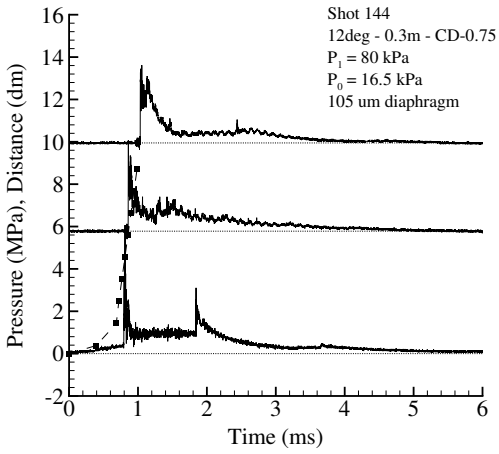

Shot 144

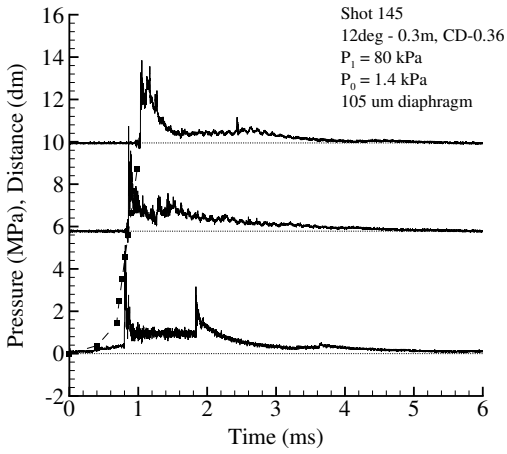

Shot 145

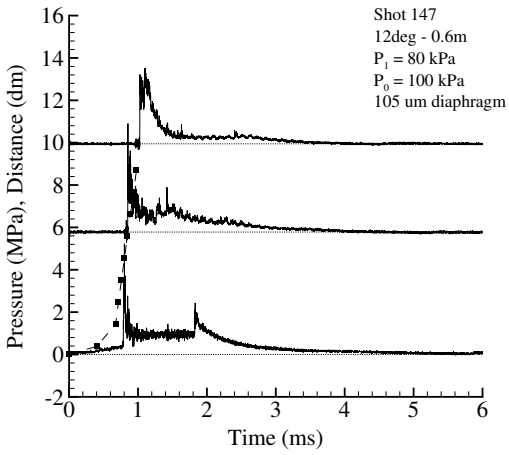

Shot 147

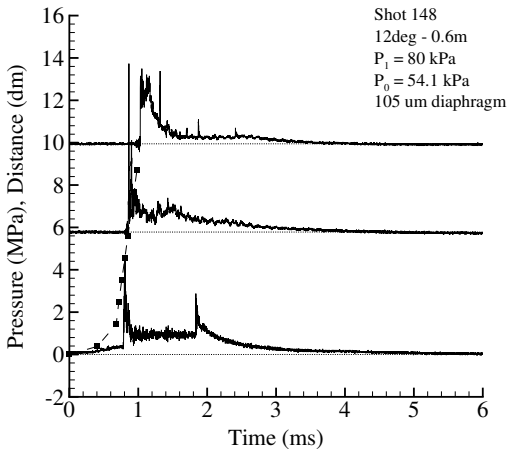

Shot 148

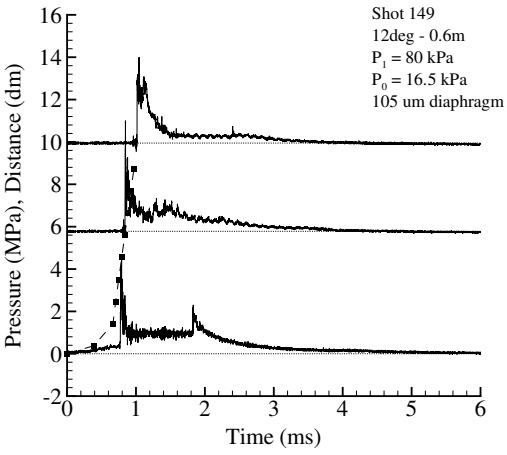

Shot 149

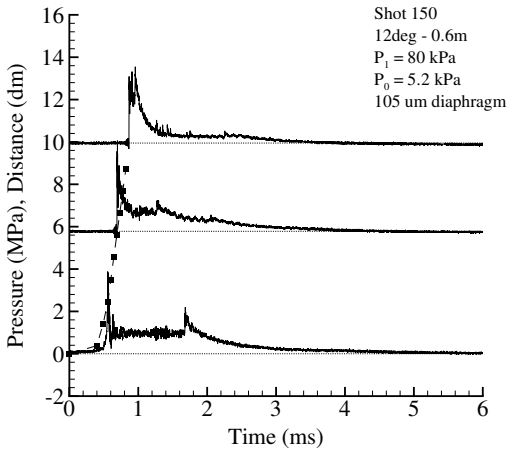

Shot 150

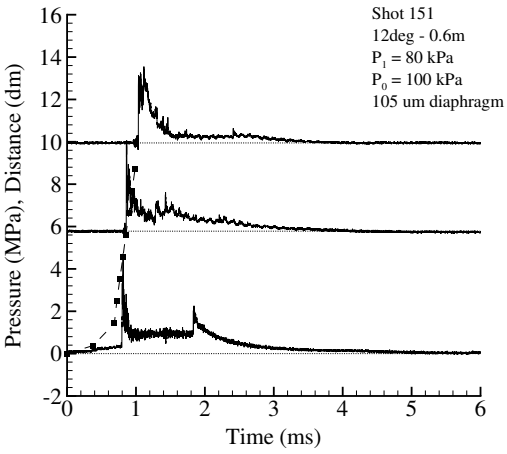

Shot 151

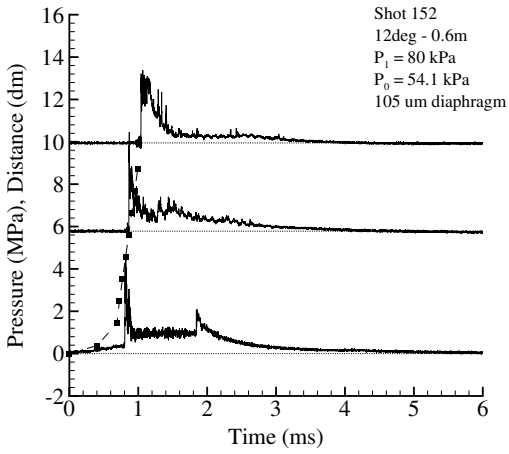

Shot 152

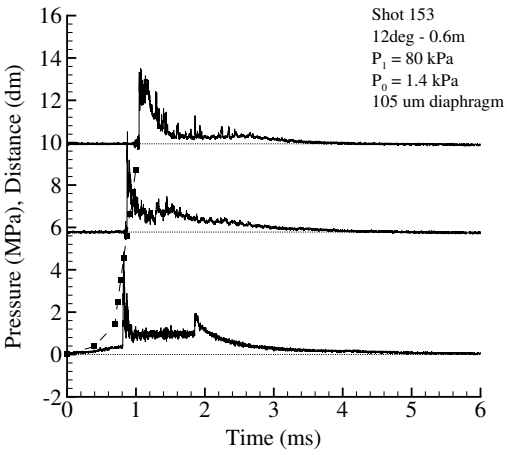

Shot 153

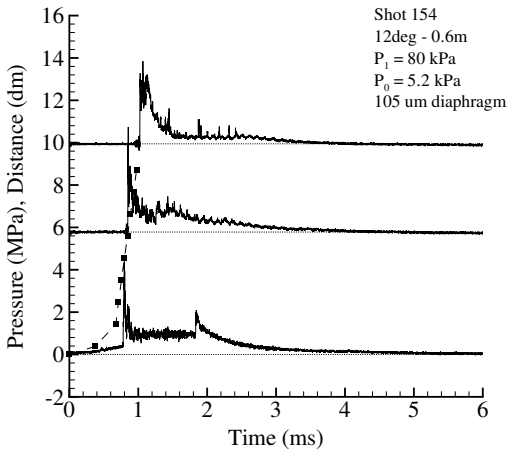

Shot 154

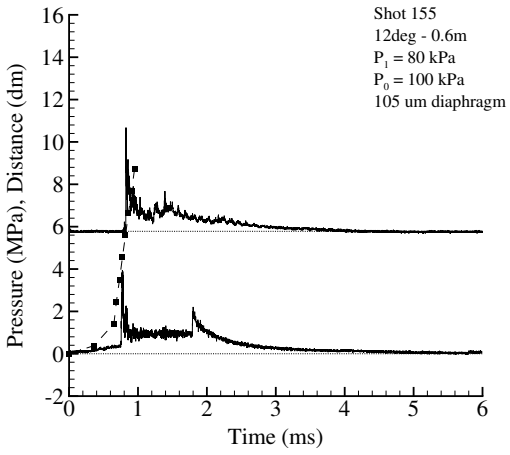

Shot 155

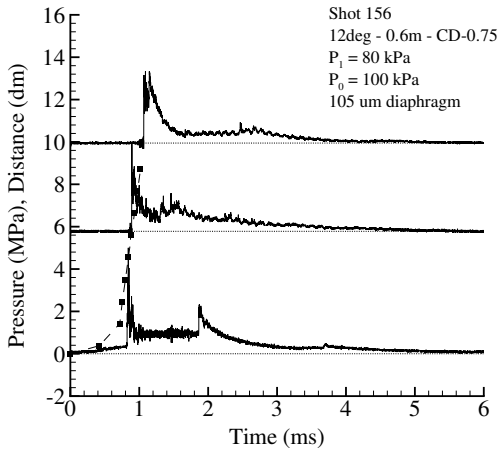

Shot 156

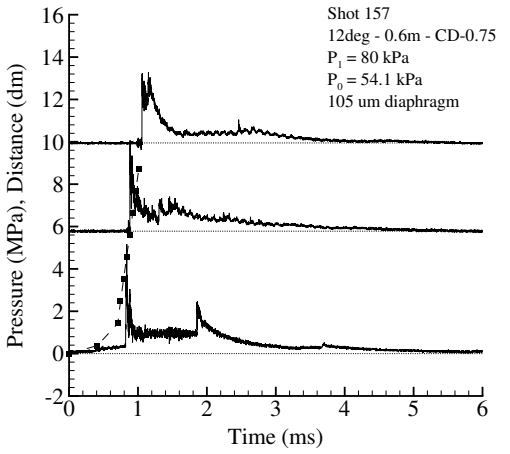

Shot 157

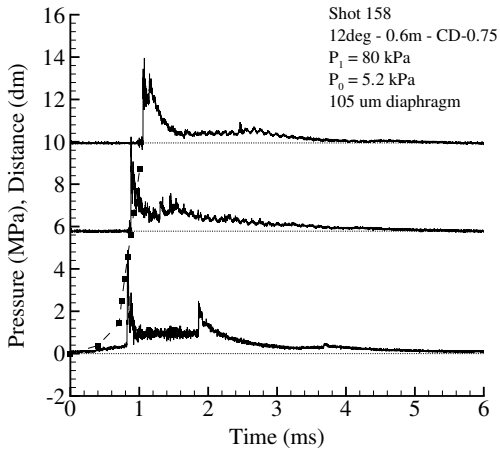

Shot 158

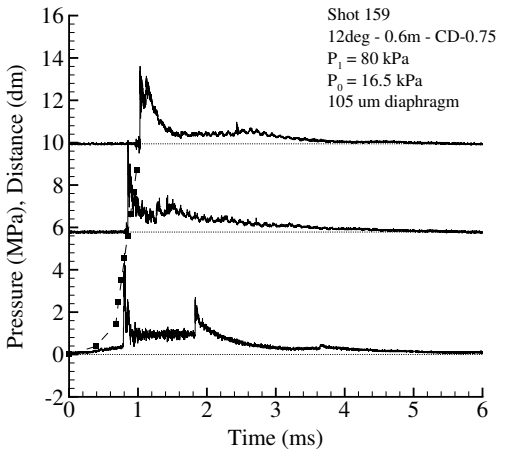

Shot 159

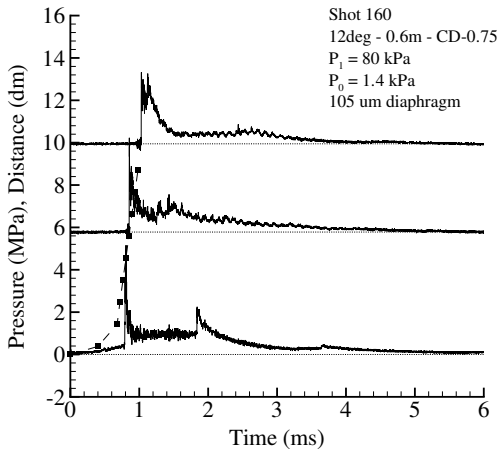

Shot 160

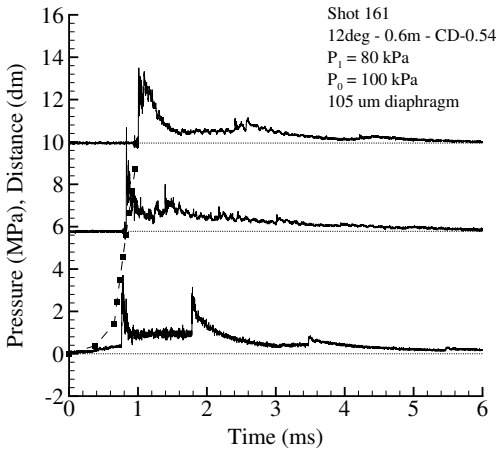

Shot 161

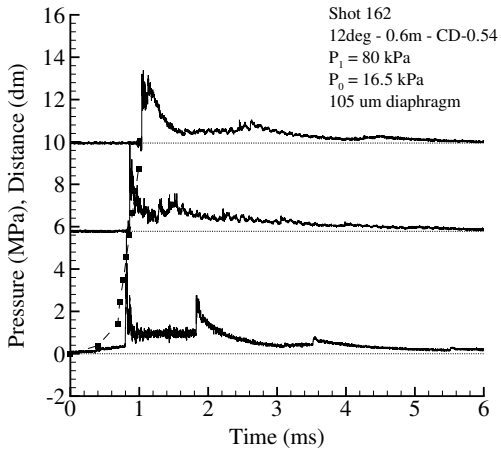

Shot 162

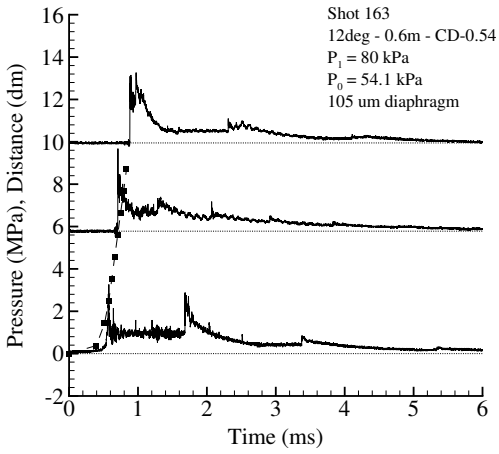

Shot 163

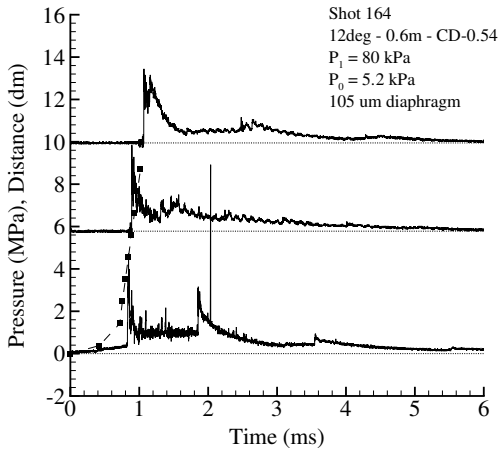

Shot 164

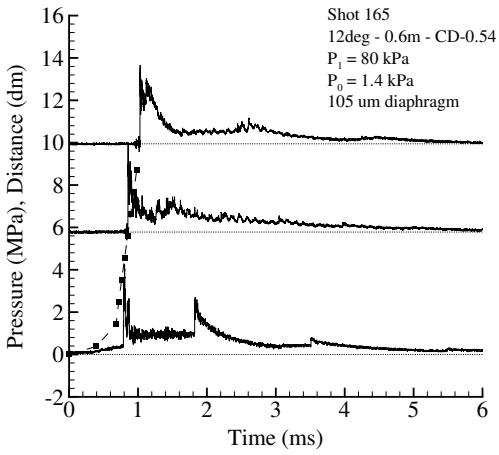

Shot 165

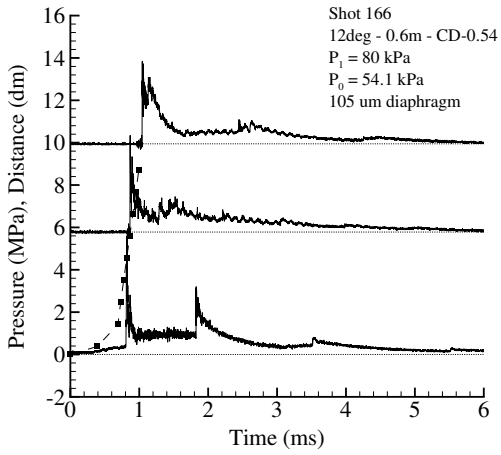

Shot 166

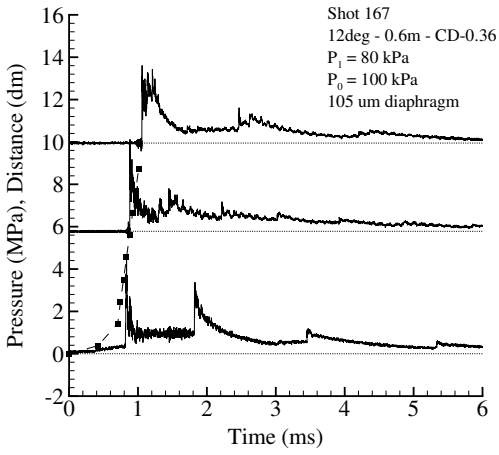

Shot 167

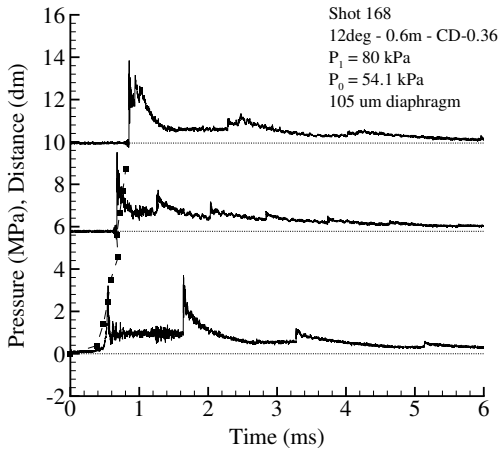

Shot 168

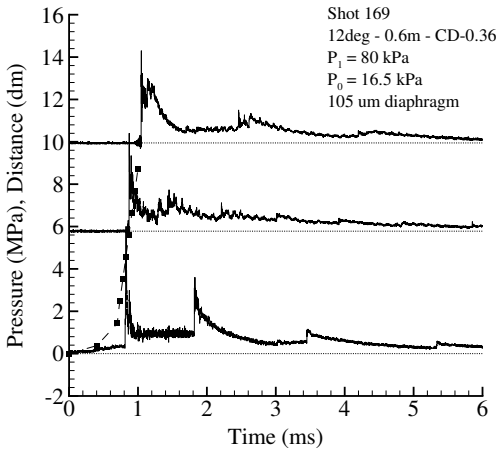

Shot 169

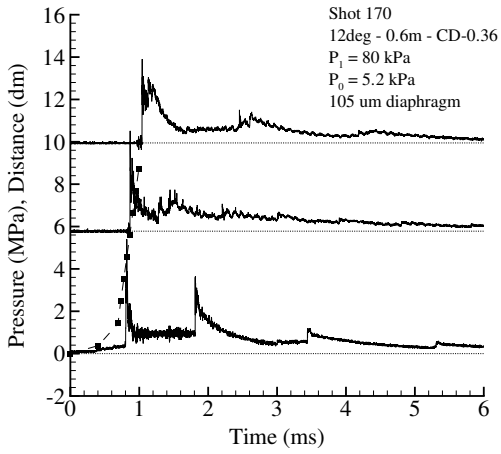

Shot 170

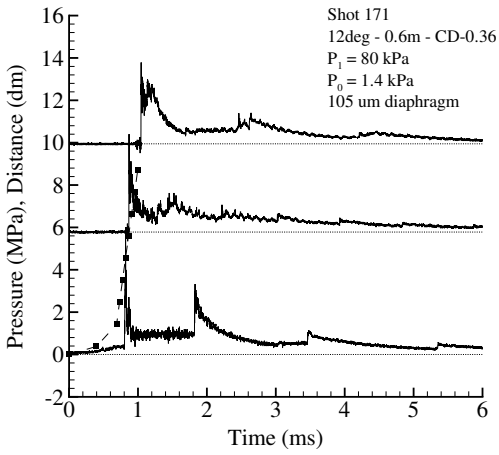

Shot 171

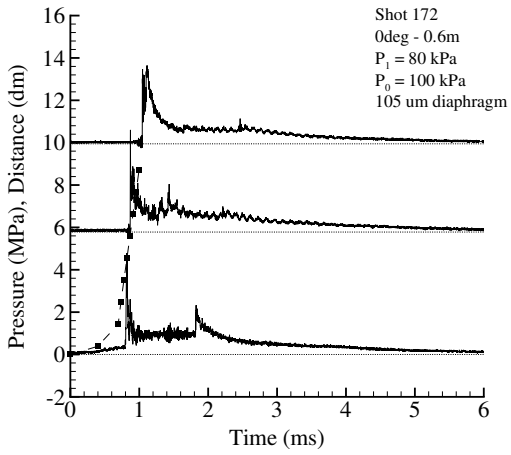

Shot 172

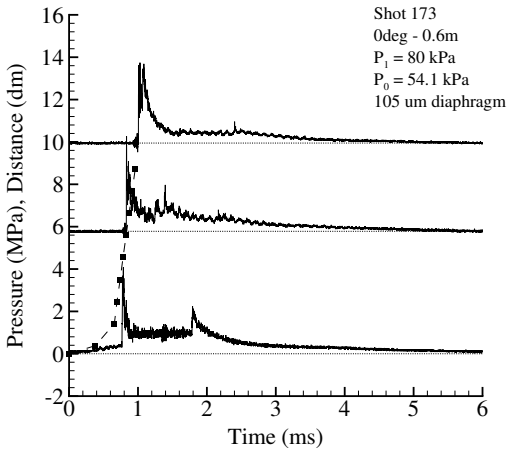

Shot 173

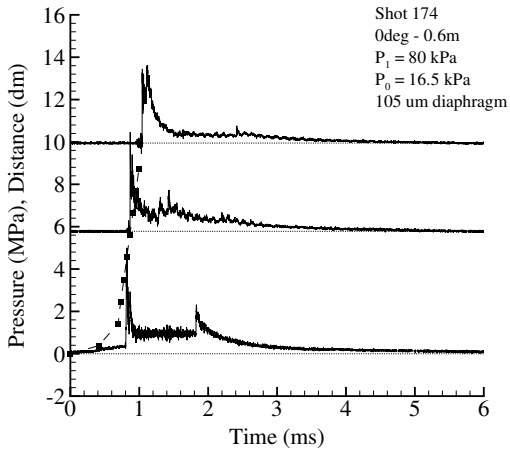

Shot 174

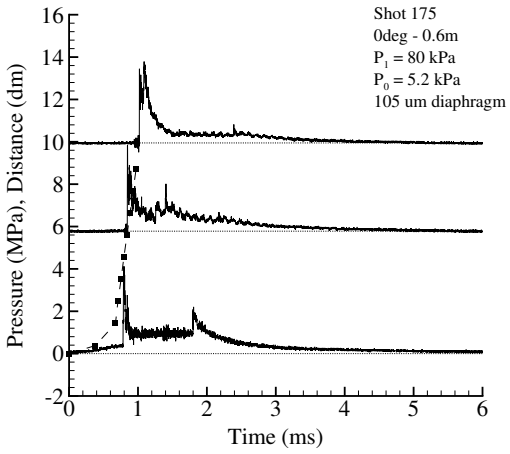

Shot 175

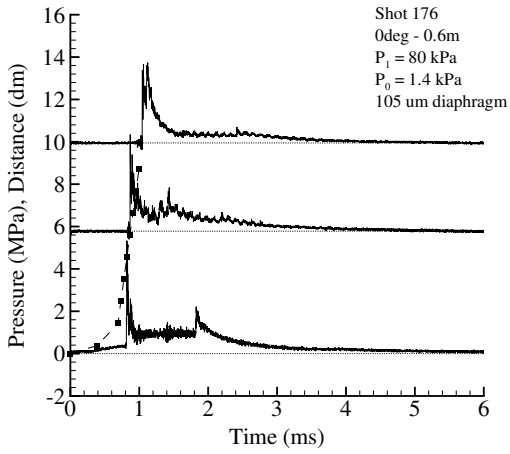

Shot 176